Measuring gaseous species emissions from ships and wetlands using FAAM BAe-146 research aircraft

Dominika Zofia Pasternak

Doctor of Philosophy

University of York
Chemistry

July 2023

Abstract

This work discusses novel airborne measurements of emissions from shipping and wetlands. Both parts focus on testing and developing methods for quantification of emissions using a large research aircraft, FAAM's BAe-146.

Shipping is the major source of anthropogenic sulphur affecting both air quality and climate. In coastal areas, shipping causes serious pollution problem affecting human health and contributing to acidification of the local environment. However, it is also thought to be a negative climate forcer due to its effect on cloud properties. From 2020 International Maritime Organisation requires all ships in international waters to reduce their sulphur emissions from 3.5% to 0.5% of apparent fuel content.

This work is the first airborne study of ship plumes in open water aiming to verify compliance to the regulations and to establish the framework for future measurements. A decrease in sulphur fuel content was seen between measurements in 2020 (2.34% ± 1.09% 1σ), 2021 (0.27% ± 0.50% 1σ) and 2022 (0.12% ± 0.21% 1σ).

Methane is a more potent greenhouse gas than carbon dioxide, yet there are still large gaps in understanding the global methane budget. Wetlands are thought to be the biggest single source, but their emissions bear 50% uncertainty, largely because there is few studies of tropical wetlands worldwide and nearly none on the entire continent of Africa.

This work shows the first successful airborne eddy covariance (AEC) measurement on board of a large research aircraft and first large scale quantification of methane emissions from Zambian wetlands. It also presents other attempts of deploying the technique and provides a guide for future AEC experiments. For the two most successful wetlands - Kafue Flats and Lukanga Swamp the average methane flux estimated with AEC was 23.0 (± 1.57) mg CH_4 m^{-2} h^{-1} and 27.9 (± 1.67) mg CH_4 m^{-2} h^{-1}, respectively.

Contents

List of Figures

List of Tables

Acknowledgements

I would like to thank James for being a great supervisor, always having time for me and giving me amazing opportunities. Even though it was not an easy time, looking back I am happy and proud of the work I did with your support.

Thank you to my co-supervisors: Jim and Sarah, for very useful feedback and for helping me to find direction for my work. I would also like to thank Adam for teaching me everything I know about airborne eddy covariance. Thank you to FAAM, Avalon and Airtask teams for the amazing time chasing ships on board of BAe-146.

Huge thank you to my ‘disruptive row’ and Zumba tribe: Becky, Beth, Loren, Maggie, Pete, Sari, Ryan, Stuart L, Stuart Y. and Will. You were always there to reassure me and then drag me to pub, which I always appreciated. You have also taught me everything I know about data analysis and without you I would never have completed my project. I am so grateful to be a part of such a great community.

I want to thank Joe for never stopping to believe in me. Thanks to you I learned to worry less about things out of my control and I grew so much as a person. I am grateful for your love and understanding. A massive thank you to Aleks, Cameron, Heather, Kristiina and Nuala for reminding me that life outside of academia exists and cheering me up when I was overwhelmed.

Last but not least I would like to thank my Parents for your support and patience. Knowing I can always count on you made me push through the most difficult moments of my PhD and thrive in the best ones.

COVID-19 statement

The initial timeline of my PhD assumed that I should have a complete ACRUISE dataset by the end of the 1st year, however the global pandemic postponed any further fieldwork till the beginning of my 3rd year. ACRUISE-2 took place in September 2021 and ACRUISE-3 in May 2022 (LNG focused). From then, I had to wait to receive ACRUISE-2 calibrated chemistry data from FAAM until October 2022 and ACRUISE-3 calibrated data until January 2023. That meant that until the end of my 3rd year I had only low quality data from ACRUISE-1 (June 2019), which made publishing first author paper during my PhD impossible and substantially delayed my work. Development of the peak integration code finished only in September 2022. The chapter on eddy covariance is a separate piece of work originating from my Master project and aimed to replace part of the ACRUISE work that would not be possible with the delays caused by COVID-19. Additionally, since I had to start working from home early on in my PhD and had limited support, it slowed down my work and affected my wellbeing.

Author's declaration

I declare that this thesis is a presentation of original work and I am the sole author. This work has not previously been presented for an award at this, or any other, University. All sources are acknowledged as References.

During the ACRUISE project I was involved in all three measurement campaigns: during first one as an instrument operator, during the second and third one also as a mission scientist. As an instrument operator I was responsible for the FAAM's core gas measurements suite and later for the whole air sampler. As a mission scientist I was involved with developing measurements strategy and mitigating restrictions relating to the COVID-19 pandemic in the planning phase. During the fieldwork I flew on board of BAe-146 leading scientific flights. On the ground I have provided the flying crew with live locations of ships of interest and kept track of measured ships.

I was not involved in raw data calibration and post processing and I do not take credit for the development of the peak integration code, although I was involved in the testing and refining process. I implemented the peak integration code on all three ACRUISE datasets and analysed the obtained data. I have also processed and analysed the whole air samples for VOCs. The ADMS 3 and STEAM models were kindly set up and run for me; for the latter I used the data for comparisons with the measurements.

For the MOYA and ZWAMPS project I implemented and characterised the first upgrade of the Fast Greenhouse Gas Analyser as a part of my Master project. This enabled acquisition of data suitable for eddy covariance. I had no part in developing the eddy4R code base and I was supported with the initial setup and filtering criteria, however the final analysis is my individual work.

Outline

Due to delays caused by the COVID-19 pandemic to the ACRUISE project focusing on sulphur emissions from ships, this work consists of two separate airborne measurements projects.

The main objective of the ACRUISE project is improving understanding of the impact of the global reduction in sulphur emissions from ships. The reduction was a result of a change in IMO regulations, so the first step was verifying the levels of compliance to the new limits by measuring the apparent sulphur fuel content. Moreover, the role in global sulphur budget as well as the effect on cloud formation and hence on climate were studied. Finally an attempt was made to understand the ship plume composition. An overview of the role of sulphur the atmosphere is presented in Chapter 1 and detailed study of sulphur (and other gaseous species) emissions from ship is presented in Chapters 2 to 4.

The second part of this work is a proof of concept study of airborne eddy covariance of methane emissions from Zambian, Uganda and Sápmi. The main objective was establishing if airborne eddy covariance can be calculated based on data from a large aircraft, here BAe-146. And if so, what are the requirements for the data quality, flight pattern and meteorological conditions. Since the work was successful in case of Zambian wetlands it also provided more insight into spacial distribution of methane emissions. The work is described in Chapters 4, 6 and 7 and a description of methane in the atmosphere and tropical wetlands can be found in Chapter 5.

The projects seem very different, however both utilise FAAM's BAe-146 as a measurement platform for gaseous species. This means that in terms of flight planning, data handling, capacities and limitations they actually have plenty in common.

Chapter 1

Introduction: Atmospheric sulphur and role of shipping

> *There is a ship at the nose steaming along quite merrily*
>
> Steve the Pilot

1.1 Sulphur in the atmosphere

Atmospheric sulphur comes predominantly from the anthropogenic sources, especially in the more populated and damaged by human activity Northern Hemisphere, however there is a fraction of atmospheric sulphur that comes from natural sources. Sulphur is present in different forms, but its reduced states usually get oxidised on the course of their journey through the atmosphere. The most abundant compounds are sulphur dioxide and sulphate, however hydrogen sulphide, carbonyl sulphide and dimethyl sulphide aerosol (DMS) also have a substantial contribution to the sulphur budget [1].

The two main removal mechanisms for atmospheric sulphur are wet deposition (precipitation):

$$SO_2 + H_2O_{(l)} \longrightarrow H_2SO_{4(aq)}$$

and dry deposition (physical processes). Both are harmless when it comes to low levels of atmospheric sulphur occurring naturally but in case of extreme emission events such as volcano eruption they can lead to acidification of the area downwind of the event and pose a threat to animals and plants alike. SO_2 can be also oxidised by OH radical:

$$SO_2 + OH + M \longrightarrow HOSO_2 + M$$
$$HOSO_2 + O_2 \longrightarrow HO_2 + SO_3$$
$$SO_3 + H_2O \longrightarrow H_2SO_4$$

where M is any molecule, or react with NO_x:

$$SO_2 + 2NO_2 + H_2O \longrightarrow HNO_3 + H_2SO_4$$
$$SO_2 + NO \longrightarrow NO_2 + SO$$
$$SO_2 + NO + H_2O \longrightarrow HNO_2 + H_2SO_4$$

Cullin and Hirshler [2] highlight following natural contributors to the global atmospheric sulphur budget:

Geothermal emissions, which are dominated by volcanoes. Sulphur emitted from geothermal sources takes form of sulphur dioxide and hydrogen sulphide. Volcanoes are capable of ejecting sulphur high enough for it to be transported to polar regions in stratosphere. Since large eruptions are relatively infrequent (globally about 5 a year [3]) and localised events, on average volcanoes are a relatively small source. It is also not the case that volcanic activity increases in the few hundred years - such myth was created as a misinterpretation of increased reporting of smaller volcanic eruptions thanks to modern communication means [3].

Sea spray introduces sulphur chloride in an aerosol form to the atmosphere. Most of sulphur introduced this way is soon deposited again, however about 10% stays in the air long enough to make it to the land. Sea spray is a greater source than volcanoes by about an order of magnitude (44 Tg S a^{-1} vs 5 Tg S a^{-1}).

Biogenic emissions usually relate to anaerobic processes. Large amounts of sulphur are emitted by phytoplankton, marine algae, sulphate reducing bacteria as well as decomposing vegetation or soils. Phytoplankton is particularly worth mentioning, since it is rather famous for emitting DMS which dominates oceanic sulphur budget. It is readily oxidized to SO_2 by hydroxyl radical and from there it can be further oxidized to sulphate. In the 1980s and 90s it was hypothesised that DMS as the dominant source of cloud condensation nuclei (CCN) in remote oceanic environments, hence affecting cloud properties and having key influence on cloud albedo [4]. The CLAW model (CLAW standing for the autors: Charlson, Lovelock, Andreae and Warren) was criticised already at its creation [5], more recent studies prove that DMS is not the only CCN source and the cloud response is far less straight forward [6]. Wetlands of all kind also can emit DMS and H_2S [1].

Humans are responsible for the emission of the majority of the atmospheric sulphur, which in nature is not particularly abundant [7]. These emissions come mostly from the Northern Hemisphere, however in the South Hemisphere they are also the dominant source of sulphur [1]. The south - north divide is confirmed by ice cores: ones from Greenland show increasing burden with anthropogenic sulphates while ones from Antarctica show no such trend [8].

In the last two hundred years atmospheric sulphur trends were determined by anthropogenic emissions. Intense coal and, subsequently, oil usage began during the Industrial Revolution (1760 - 1840, starting in the UK), and the increasing levels of sulphates can be traced using ice cores. Schwikowski et al. [8] studied cores from Monte Rosa glacier in the Italian Alps, using among others volcanic eruptions signatures to date the cores (high sulphate to calcium ratio and high sulphate in general). While no trend was found in the sulphate originating from sea-salt and mineral dust, anthropogenic sulphate showed clear increase in post-Industrial Revolution years, resolving even features like dips during the World Wars, sharp increase in 1950s due to increase in oil usage and slow decrease since 1970s when regulations against air pollution started being introduced. Until the end of 19th century trends coincided with black carbon trends hence it can be suspected that the bulk of sulphate comes from domestic combustion of wood or coal.

After peaking in 1970 [7] a substantial reduction in SO_2 emissions was observed globally from 1980s to 2000s. It was driven by legislation limiting sulphur emissions in Europe and North America, who were the major contributors at the time. Years 2000-06 saw an increase due to growth of emissions in China, which however were soon addressed and reduced, bringing the global trend back to decreasing. Currently India is the major SO_2 emitter and China the second largest. Overall trends between 1990 and 2015 are shown in Figure 1.1 [9]. It is important to make clear that both countries are among the largest in the world and are centers of production of goods largely consumed in Europe and North America, hence emissions of any pollutants or greenhouse gases are also dependent on Western consumption and politics.

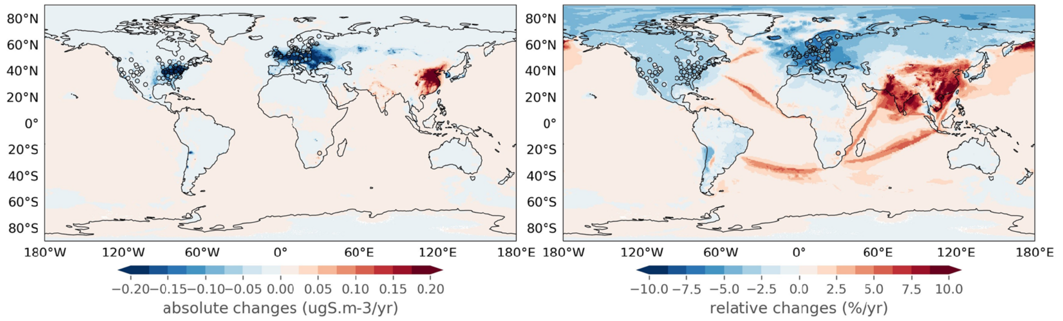

Figure 1.1: Changes in SO_2 air concentration in years 1990-2015 based on EMEP MSC-W model (map colouring) and observations (in circles). Source: Aas et al. [9].

Smith et al. [7] highlight following areas of anthropogenic emission in post-industrial revolution era: fossil fuels combustion and processing (coal, petroleum, natural gas, shipping bunker fuels), biomass combustion, metal smelting, pulp and paper processing and agricultural waste burning. The major terrestrial source of SO_2 is coal combustion (2-5% sulphur content), followed by oil combustion (1-2% sulphur content) [1]. Part of sulphur gets removed in the refining process, but where poorer quality oil derived fuel is used the content can be higher. Natural gas is lower in sulphur content, but still contains a not negligible amount of sulfur compounds, particularly hydrogen sulfide that are turned into SO_2 during flaring or turned into commercial products [7]. Sulphur might be more abundant in fossil fuels than in non-pressurised vegetation, yet biomass combustion, pulp and paper production and agricultural waste combustion introduce significant amount of SO_2 to the atmosphere. Metal smelting emissions depend strongly on the sulphur content in the ore and removal methods, both of which are often not reported in inventories [7]. Sulphur emissions from ships fall under the fossil fuel umbrella, but in the Northern Hemisphere shipping is responsible for approximately half of the total of SO_2 atmospheric input [10, 11].

Models and forecasts rely on observation networks, which tend to be heavily biased towards global North, and inventories. Liu et al. [12] point out, that most studies use bottom-up estimations which are prone to high uncertainty. Satellite data, on the other hand, is very useful for studying large sources and trends, however due to resolution issues it is not sufficient to provide a complete inventory. Merging classic bottom-up inventories with satellite based estimates is an important step in reducing these uncertainties and validate any assumptions taken.

Large amounts of sulphur in the atmosphere have detrimental effect on human health and the environment. SO_2 effect on health is often understudied compared to PM2.5 or NO_x. Its exact effect on human health is hard to separate from that of other pollutants, since usually high pollution events are driven by more than one species. In a recent study of SO_2 pollution in Bejing Wu et al. [13] highlight the need to model and forecast high SO_2 pollution events to mitigate their effects on Bejings inhabitants health. Sulphur (and other pollutants) emissions from shipping affect greatly the coastal areas, especially that only 30% of ship traffic occurs further than 400 km from the land lading to approximately 400 thousand premature deaths per year [14].

It is a common knowledge that sulphur in the atmosphere has a ‘cooling effect’ on the climate. However, the exact magnitude and mechanisms of the negative climatic response to sulphur have been debated for years. Even nowadays there are many unanswered questions about details of sulphur induced high albedo cloud formation [15].

Shipping affects the climate mainly through emissions of sulphur and greenhouse gases. The former has negative forcing effect, the latter positive. Shipping is estimated to be responsible for 13% of global SO_2 emissions [16]. Atmospheric sulphur is greatly affected by shipping, since the shift to clean fuels came to shipping much later than to land based engines. Ships remain a major emitter of PM and sulphur (mostly as SO_2). This is because particles and aerosols are cloud precursors and depending on their features, they can affect the characteristics of the cloud formed, e.g. albedo or lifetime. Clouds are crucial for climate, since they reflect sunlight having a cooling effect on the Earth’s surface. The relationship between aerosols and clouds is very complex and not fully understood, but it is widely believed that sulphur containing ship aerosols increase the number of cloud droplets producing more optically thick clouds which are referred to as ship tracks [17]. The extent of this effect is debated and varies greatly between models with satellite observations remaining ambiguous [18, 19].

1.2 Shipping

1.2.1 History

The history of shipping stretches back a long way. It is estimated that as long as 50 thousand years ago our ancestors used little barges to cross large water bodies between islands in the East Asia [20]. Scarce archaeological records makes it difficult to pinpoint the exact time when humans started building waterborne vessels, but genetic analysis of human remains suggests that navigation on water was essential for the rapid migration all over the world. Evidence suggests, that around 4000 BC small barges were used on the Nile river for trade and transportation purposes of any sort of goods. With increasing technical innovation, sailing became a common mean of transport by 3000 BC. By the 15th century AD 3 masted ships with up to 6 sails per mast navigated on shipping routes between Asia and Europe [21]. As the industrial revolution took place on land, steam engines were used in experimental steamboats in the early 19th century. These steamboats used wood as fuel, however as coal became readily available at lower price, it replaced wood [22].

In the early ages of shipping, the shipping industry had its place as a mean of transport for people and goods. With further progression of the industrial revolution and the industrialisation of energy resources, it became necessary to transport fuels internationally. This led to the invention of the first oil tankers, which transported large amounts of oil. Before tankers, oil was transported in small barrels which were prone to breaking during transportation [23]. Although these boats transported oil in large quantities, they were still powered by coal and the transition on to oil powered ships took until 20th century, as initially no real advantage was seen in using oil over the still widely available and cheap coal. They oil they transported was mostly oil for lamps [24].

In the wake of World War I, prototypes for oil powered ships were developed and the technology was soon well understood, but the choice for one or the other fuel type was given by availability, strategic thinking and political decisions [24]. Soon it became obvious that coal was a heavier, dirtier, and more labour intensive fuel in both transport and production, compared to oil. Moreover coal contained a lot of impurities in comparison to a highly refined fuel such as oil, which can be largely standardised. Furthermore coal had a lower thermal efficiency and emitted higher amounts of sulphur dioxide during combustion. This led to the political promotion of hydrocarbons and the limiting of pollution from coal combustion. In many ports the hazard to health and environment became concerning for authorities and general public alike. From 1950s air quality regulations started to be introduces, which sealed the destiny of coal fueled ships [25]. Looking at data from the worldwide marine sales of international marine bunkers, after World War II the change from coal to oil went rather rapidly and by the 1960s coal was only marginally used and completely vanished from the market by the 1970s [26].

In the beginning of the 1960's nuclear powered vessels were developed, but with a very few exceptions remained mostly used for non-civil purposes as the nuclear fuel was problematic in handling and posed high danger in case of engine or ship failure [27]. As new methods to store gas were researched, the liquefaction of natural gas was developed to store it during periods of low demand and gasify it during high demand. It did not took long for companies to search for methods to transport this liquefied gas [28]. The first LNG tanker with a couple of thousand cubic meters of LNG left the USA in 1959 and sailed to the United Kingdom. Today LNG tankers have capacities up to 266.000 cubic meters [29]. LNG is not only transported by ships but can also be used as a fuel, which is advertised as a cleaner and more environment friendly solution. In 2023 there was already a fleet of 355 LNG fueled ships, notably some cruise ships which are frequently in coastal areas having high impact on the air quality in such areas. Furthermore, orders for over 500 more LNG powered ships were already placed despite rise in gas prices [30]. LPG powered ships also exist, but are less popular.

In efforts to reduce both CO_2 and SO_2 emissions, more alternative fuels and techniques are being developed and put on the market, so far with mixed results. For example fuel water emulsion (FEW) and Humid Air Motor (HAM), both aim to be 'greener', but offer only slightly lower emissions at much higher costs of purchase and maintenance. There are also attempts to use fuels or biological origin, such as palm, coconut, rapeseed or soya oil.

But all of them are very expensive to produce and have other devastating ecological consequences, so in reality, they just move the problem elsewhere. So far only marine gas turbines offer a high decrease of all emissions when compared to a standard ship fuel. Perhaps instead of looking for alternative fuels, the research of alternative energy sources all together would prove more efficient and come at a cheaper price. Solar cells, wind power or electric fuel cells are already applied to small passenger boats, but are long way from taking over the global market. Long term, using combination of alternative sources of energy and cleaner fuels seems like the most viable option [31].

1.2.2 Sulphur emissions and regulations

The International Maritime Organisation (IMO) [32] was established as the Inter-Governmental Maritime Consultative Organization in 1948 to:

> provide machinery for cooperation among Governments in the field of governmental regulation and practices relating to technical matters of all kinds affecting shipping engaged in international trade; to encourage and facilitate the general adoption of the highest practicable standards in matters concerning maritime safety, efficiency of navigation and prevention and control of marine pollution from ships [32].

IMO is responsible for regulating shipping emissions [33]. From the late 1980s IMO started creating Special Areas, where for oceanographical or ecological reasons additional measures are taken to prevent pollution from oil, sewage or garbage. The first such area created was the Gulf of Aden. From 2005 Emission Control Areas (ECA) started being introduced e.g. in the North Sea, Baltic Sea or Caribbean Sea. The legal basis for all of these areas is the International Convention for the Prevention of Pollution from Ships (MARPOL) which came into force in 1983 [33]. SECAs limit predominantly sulphur emissions but some have also NO_x regulations. From

2015 sulphur content in fuel by mass in these areas should not exceed a strict limit of 0.1%. In the past this limit was more relaxed: 1.5% until 2010 and 1.0% until 2015. However, IMO also regulates sulphur emissions in international waters, setting the sulphur content limits at 4.5% until 2012, 3.5% until 2020 and currently 0.5%.

Any legislation has to be enforceable, so a method of remote measuring of the amount of sulphur emitted by ships is necessary. A number of studies quantify the apparent sulphur fuel content (SFC). In general the amount of emitted sulphur is compared to the amount of emitted carbon, with assumption that carbon constitutes 87 ± 1.5 % [34, 35] of typical ship fuel. The exact methods of quantifying the SFC vary.

DLR's FALCON was deployed to measure particulate emissions from ships in the English Channel and Bay of Biscay as early as 2004. The study was preceded by a ground test with an engine rig. Unfortunately, the authors did not attempt quantifying SFC, perhaps since it was already known to be 2.4% in the targeted ship [36].

Lack et al. [37, 38] used NOAA's WP-3D aircraft to target a Maersk Line ship entering Californian waters as it changed fuel from 3.15% to 0.07% sulphur content. The intercepted plume was about 2-5 min old. They used CO_2 balance to derive emission factors.

Kattner et al. [35] performed ground measurements in Hamburg harbour and analysed over 1400 ship plumes of 2-10 min age. NO was used as a plume indicator, as the most distinct and strongest signal. Equation 1.1 was used to quantify the emissions, relying on the assumption that all sulphur is emitted as SO_2 and all carbon is emitted as CO_2. This assumption is a simplification, however with limited instrumentation it is still legitimate.

$$\mathrm{SFC}[\%] = \frac{\mathrm{SO_2[ppb]}}{\mathrm{CO_2[ppm]}} \times 0.232[\%] \tag{1.1}$$

where SO_2 and CO_2 are peak areas for each species expressed in ppb and ppm, respectively. 0.232 is mass conversion factor for fuel content derived by Kattner [35]. Uncertainty was calculated as root sum of squares of the calibration uncertainties and signal-to-noise (SNR) uncertainties. For CO_2 SNR smaller than 5 were excluded, for SO_2 assumed to be zero.

1.2.3 Other species in ship plumes

Apart from being the main anthropogenic source of sulphur in the atmosphere, ships emit large volumes of NO_x affecting the local air quality. Burgard and Bria [39] used a remote sensing system originally designed to measure on land vehicles emissions to show that ships emit typically 72 ± 24 g NO_x per kg of fuel burned. Values in literature generally range from 60 to 90 g NO_x per kg of fuel burned for both remote and on board studies. Interestingly some airborne studies showed lower values (20-40 g NO_x per kg of fuel burned), but it was likely down to small sample size.

Alternatively NO_x to CO_2 ratios are used as a measure of emissions per unit of fuel which makes them more comparable with other vessels or vehicles [40]. Schlager et al. [41] report NO_x/ CO_2 ratios of 32-34 for younger plumes and 18 for older plumes. These values were consistent with inventories at the time of the experiment (2004). Meanwhile ratios for road vehicles fall around 0.002 - 0.008 for cars or 0.004 - 0.016 for HGVs [40].

For that reason IMO also introduced NO_x emission limits [33]. NO_x emissions can be actively controlled [42] either by optimising fuel combustion or by after-treatment of the exhausts i.e. catalytic removal.

Another class of species emitted by ships are volatile organic compounds (VOCs). They can be emitted by engines and generators as a part of the ship plume or from cargo in case of e.g. oil tankers as fugitive emissions. The former can be controlled to some extent by vapour recovery [42]. Currently IMO regulates only emissions from tankers' cargo [33].

In an analysis of the plumes of container ship at berth in Jingtang Port

(China) Xiao et al. [43] show consistency with diesel land vehicles emissions. Ship plumes however, tend to be richer in heavy alkanes (7+ carbon). The GC-MS analysis was done on air sampled directly at auxiliary engine exhaust, hence the plumes were 'fresh'. Most significant contributions come from alkanes, aromatic compounds - mainly benzene and toluene, acetone and dichloromethane. The latter two show significant variation.

Wu et al. [13] show how reducing one pollutant can potentially increase another one, shifting the problem. They find that the change of IMO's SFC regulations coincided with 15 times increase in the VOCs emissions in the Pearl River Delta Emission Control Area. There increase is attributed to shift in fuel use to low-sulfur diesel or heavy oils, which might contain less sulphur but are richer in short chain hydrocarbons which are precursors to VOCs. Hence the reduction in sulphur (and particulate mater) might have accidentaly led to increase in VOCs emissions, which in turn contribute to the thropospheric ozone production.

1.3 LNG tankers

Liquefied natural gas (LNG) is often considered the cleanest of fossil fuels because of its relatively low CO_2 emission per unit of combustion energy [44]. Its popularity is growing, also as a promising fuel for shipping (lower SO_2, NO_x and PM), which currently are subject to stricter pollution regulations [45]. However, LNG consists mainly of methane so its transport and handling are crucial in reducing its climatic impact.

There are not many studies of LNG shipping-related methane emissions, but it is estimated that LNG carriers use considerably more energy than pipeline transport [45] and have worse environmental impact [46]. Figure 1.2 shows possible routes the transported methane can escape to the atmosphere. Lowell et al. [45] assessed the sustainability of LNG as shipping fuel for International Council on Clean Transportation. The authors suggest that the majority of methane is emitted during regasification and processing. Storage, in turn is not considered as a significant source of methane, even though storage units always require venting.

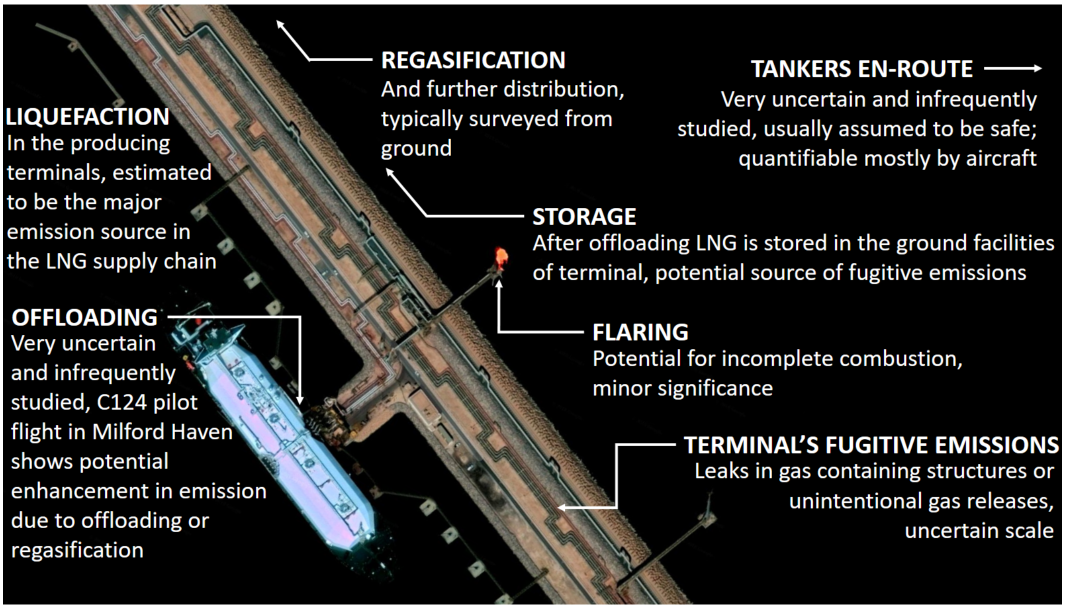

REGASIFICATION
And further distribution, typically surveyed from ground

TANKERS EN-ROUTE →
Very uncertain and infrequently studied, usually assumed to be safe; quantifiable mostly by aircraft

LIQUEFACTION
In the producing terminals, estimated to be the major emission source in the LNG supply chain

STORAGE
After offloading LNG is stored in the ground facilities of terminal, potential source of fugitive emissions

OFFLOADING
Very uncertain and infrequently studied, C124 pilot flight in Milford Haven shows potential enhancement in emission due to offloading or regasification

FLARING
Potential for incomplete combustion, minor significance

TERMINAL'S FUGITIVE EMISSIONS
Leaks in gas containing structures or unintentional gas releases, uncertain scale

Figure 1.2: Potential methane emission sources within LNG facilities. The fugitive emissions issue was first noticed by Howarth et al. [47] in 2011 and since remains a controversy. Along with offloading, regasification and en-route CH_4 release they are a potential subject of an airborne campaign using the modified FGGA. [48–50]

One of the first studies including LNG tankers emissions from 2001 analyses CO_2 and CH_4 emissions from LNG delivery chain in Japan [48]. The authors deem liquefaction as the major source of methane, however they do not analyse shipping in great depth. The outcomes of the study were confirmed several years later [50]. A detailed natural gas supply chain emissions analysis by Balcombe et al. [49] emphasises that "there is limited transparency of the sources of these emissions [i.e. leaks and venting] and there is very little detail in particular on fugitive emissions". Hence, independent measurements of methane emissions from LNG facilities is an urgent matter, that should not be ignored especially in the context of the Paris Agreement and other measures to lower GHG emissions.

To the best of my knowledge the only attempt to quantify methane from

LNG tankers comes from a very recent study by Balcombe et al. [51]. They monitored emissions from loading, laden voyage, unloading, and ballast voyage of an LNG tanker focusing on exhaust stacks (including frequently overlloked generator engines), vents, and fugitives. That tanker was built in 2021 Gaslog Galveston on it's second journey transporting LNG from the US to Belgium and returning in ballast. They found that venting and fugitive emissions had relatively low contribution to the GHG budget of the journey, but that the methane slip from engines plays the crucial role consuming 0.1% of the transported LNG. They also found that the slip is worse at low engine loads used during the journey (approx. 40%) and could be improved by running engines at 80% load. The authors note that this is a very modern ship and it might not be representative of the rather heterogenous LNG fleet.

1.4 ACRUISE project

Atmospheric **C**omposition and **R**adiative forcing changes due to **UN** **I**nternational **S**hip **E**missions regulations (ACRUISE) is a project [18] funded by NERC*. The project's time frame is January 2019 to January 2024 including a COVID-19 pandemic related funding extension and the parties involved are: Plymouth Marine Laboratory, University of Manchester, University of York, University of Oxford and University of Leeds. Upon granting of the funding in 2018 the project was facing four main unknowns [18]:

- Ship plumes composition, evolution and apparent sulphur fuel content before and after the change of legislation
- Levels of compliance to the pre- and post-2020 regulations, use of scrubbers and cleaner fuel especially for ships is in open water rather than a coastal areas

---

*`https://gotw.nerc.ac.uk/list_full.asp?pcode=NE%2FS005390%2F1`

- Influence of reduced shipping emissions on the marine atmosphere sulphur burden, especially when compared to DMS background
- Cloud response to the sulphur emissions change and how that affects climate on the global scale

In short, ACRUISE project aims to address all the uncertainties linked to the drastic global change of sulphur emissions from shipping caused by the 2020 IMO regulations change.

The last question was answered improving understanding of so called ship tracks, i.e. distinct clouds formed due to the influence of ship aerosol in satellite images. Previously there was a lot of speculations whether or not these clouds can actually be attributed to ships and if so how to classify them as ship track or just a cloud. ACRUISE project led to development of a machine learning based framework of ship track recognition in satellite photos [16, 52]. This method allows not only to detect the ship tracks visible for human eye but also ship-induced changes in properties of completely inconspicuous clouds. this work allowed establishing that estimate 80% reduction of sulphur emissions after IMO 2020 regulation change let to 25% reduction in number of detected ship tracks. This is due to a logarithmic relationship between the number of condensation nuclei and the number of cloud droplets.

The three first questions are still under investigation and some of the findings are discussed further in this work. The research conducted as parts of ACRUISE is interdisciplinary. Long term aerosol measurements are conducted at Penlee Point Atmospheric observatory facing one of the busiest straits in the world - English Channel. Looking back the huge advantage of these measurements is that they could be conducted throughout the COVID-19 pandemic unlike the airborne campaigns using FAAM's BAe-146 as a measurement platform (described in detail below). Finally regional and global modelling is used as a comparison to the observations.

Chapter 2

Methods: Gaseous emissions from ships

2.1 Instrumentation

2.1.1 Airborne measurements

The use of an aircraft to take atmospheric measurements was first proposed in 1907 and the first systematic airborne temperature record was taken during World War I. Since 1942, the British Met Office has used a research aircraft to monitor atmospheric processes in the United Kingdom and abroad on a regular basis [53]. Following the development of available technologies and demand for atmospheric measurements, the Facility for Airborne Atmospheric Measurements (FAAM) was created in 2001 as a 'flying laboratory' using a newly adapted BAe-146-301 jet aircraft.

2.1.2 FAAM

During each of the three ACRUISE field campaigns a different configuration of gas analysers was deployed. The non-atmospheric composition measurements were acquired using FAAM core instruments. The position, heading and roll angle were measured with Applanix POS AV 410 GPS-aided Inertial Navigation System, while altitude was measured with Thales AHV16 Radar Altimeter. Temperature and three-dimensional wind components were measured from the aircraft's nose using, respectively, a Rosemount 102 Total Air Temperature probe and a nose-mounted five-port turbulence probe. The true airspeed (dry-air) was derived based on data from the turbulence probe, the on-board Air Data Computer and the Total Air Temperature probe. Static pressure from the on-board Air Data Computer was also used.

Details of gaseous species measured during each campaign are summarised in Table 2.1. The overall layout of the Core Chemistry rack is shown in Figure 2.1.

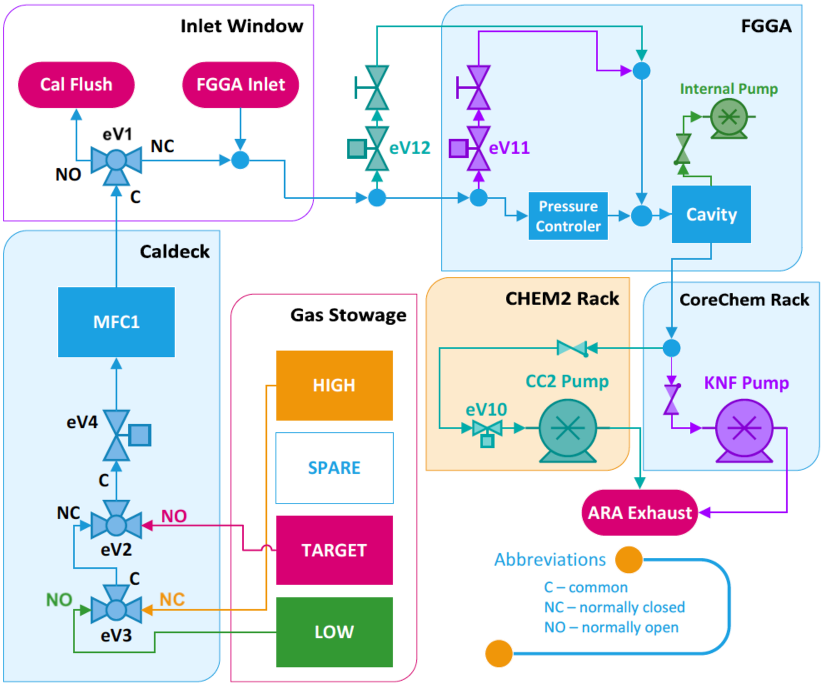

Figure 2.1: Core Chemistry rack scheme in the 2019 setup.

Species	Campaign		
	ACRUISE-1	ACRUISE-2	ACRUISE-3
TEi43i SO_2 [54, 55]	1Hz, greater of 5% or 4 ppb	1Hz, greater of 9% or 3 ppb	1Hz, greater of 9% or 3 ppb 5 Hz, 300 ppt LOD (LIF [56]) 4 Hz, 1.5 ppb LOD (CIMS [57])
FGGA CO_2 [58]	1 Hz, 0.393 ppm (old)	10 Hz, 0.599 ppm (new)	10 Hz, 0.574 ppm (new)
FGGA CH_4 [58, 59]	1 Hz, 2.55 ppb (old)	10 Hz, 3.1 ppb (new)	10 Hz, 3.3 ppb (new)
Core NO_x [60]	10 Hz, 3.52%	X	X
AL5005 CO [61]	1 Hz, 1.5 ppbat 150ppb	1 Hz, 1.5 ppbat 150ppb	1 Hz, 1.5 ppbat 150ppb
O_3 2BTECH [62]	0.5 Hz, greater of 3% or 5 ppb	0.5 Hz, greater of 3% or 5 ppb	0.5 Hz, greater of 3% or 5 ppb

Table 2.1: ACRUISE gas measurements with their uncertainties or LODs where uncertainties are not yet confirmed.

The instrument measuring CO_2 and CH_4 crucial to this work was the Fast Greenhouse Gas Analyser (FGGA, Los Gatos Research Inc.) using Near-IR Off-Axis Integrated Cavity Output Spectroscopy (near-IR OA-ICOS). Two models are certified to fly onboard FAAM's BAe-146: model 907-0010 from 2009 and model 907-0011 from 2017. The younger FGGA had capacity of sampling with a cavity pressure of either 140 or 50 Torr, the former providing faster flow the latter increasing ceiling altitude. The near-IR OA-ICOS technique is based on extending laser path using an optical cavity with mirrors on its ends reflecting the laser beam. There are two lasers set to 1.603 µm for CO_2 and 1.651 µm for CH_4 and H_2O (see Figure 2.2). Subsequently, the FGGA's software performs spectral fitting against the High-Resolution Transmission Molecular Absorption Database (HITRAN) spectra for all three gases and measures absorption to quantify their amount in sampled air. The mixing ratios in ppm are output in real time to the aircraft main data visualisation system. The quality of the measurement is defined in terms of ring-down time for each laser, which is a measure of cavity mirrors reflectively, which slowly degrades by contamination of the cavity optics. It is measured in µs for every acquired data point using a non-absorbing wavelength [63]. The inlet was window-mounted rearward facing 1/4" PFA tube housed in 3/8" stainless steel tube, located at the window nearest to the rack.

In order to increase the FGGA sample flow rate, a dry scroll pump (Edward's nXDS 20i, later referred to as nXDS) was installed on the neighbouring rack in parallel to already existing KNF Neuberger N920APDCB pump (KNF). As shown in Figure 2.3 both external pumps were connected to the instrument's exhaust. The nXDS allows approx 32 SLPM flow, while the lower capacity KNF pump maintained approx. 3 SLPM during instrument calibrations, as the standard gases are delivered at maximum of 5 SLPM by the calibration deck. In order to ensure that the CC2 pump is kept conditioned, eV10 (MKS Instruments CV25-K2K2-ECNVV-24DC) normally closed valve was fitted to the pump's inlet. The data acquisition rate was set to 10 Hz,

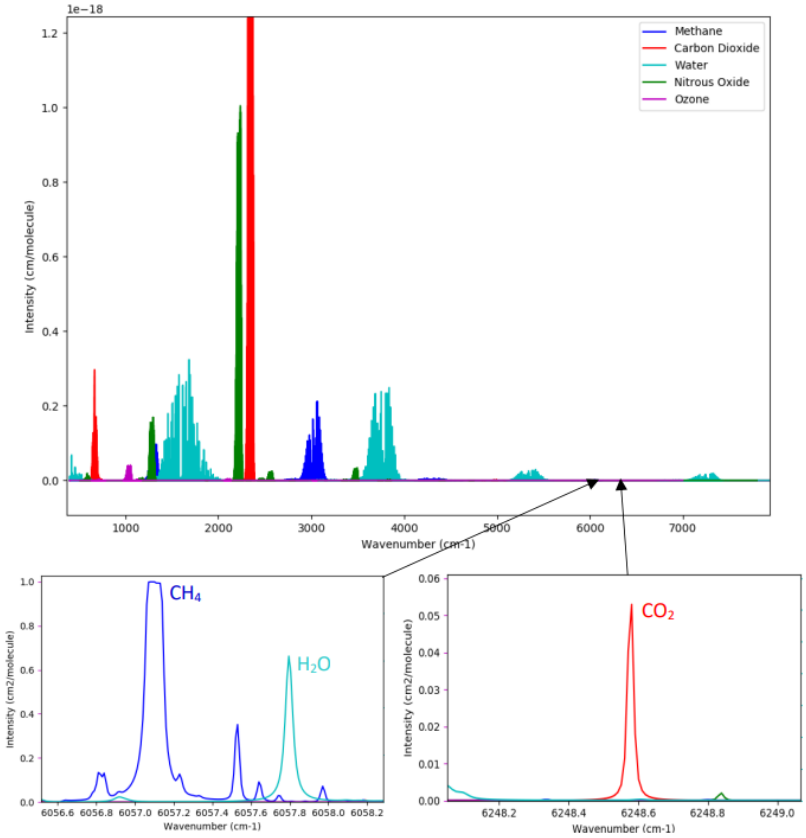

Figure 2.2: Absorption features of CH_4, water and CO_2 targeted by FGGA in comparison with other common atmospheric species absorbing in IR. Source: Barker [64].

however the actual flushing speed was 6 Hz in the 'fast' mode and 1 Hz in the 'slow' mode.

The upgrade affected also the pressure regulation system. The nXDS pump operated with its own bypass to avoid manual adjustment of the manual throttle valve every time the pump was changed. This was intended to allow shorter stabilisation time and remote operation. Each bypass was equipped with an automated solenoid valve (Norgren-KIP Series 3, #351118) and manual throttle valve (Swagelok, SS-1RS6) that could be adjusted in-flight. The system proved to show issues with pressure stability and very narrow altitude range.

Every 45 minutes a high and then low concentration standard gases are injected to the system to capture drift. For each set of high and low calib-

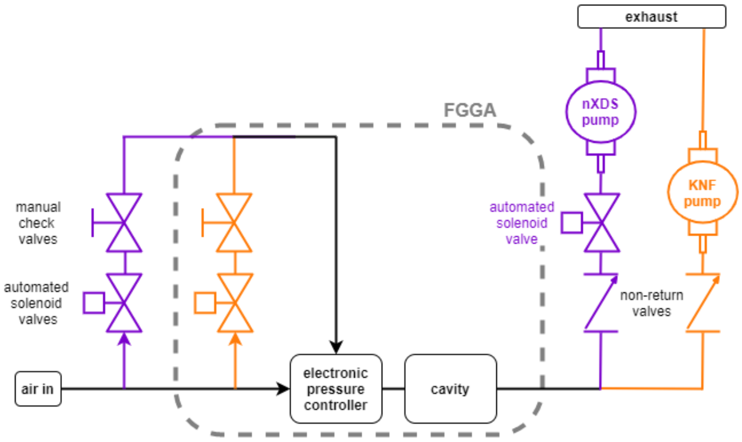

Figure 2.3: Plumbing diagram for FGGA modification for the MOYA and ZWAMPS campaigns. Source: Shaw et al. [59].

rations slope and intercept values are calculated and linearly interpolated across the flight to account for slope and offset. Between each set of high and low calibrations a target concentration standard gas is injected to calculate accuracy for a period of flying (e.g. a campaign). All of the calibration gases are traceable to the World Meteorological Organisation (WMO) greenhouse gases scales and the standard concentrations are certified by EMPA.

However, during ACRUISE-1 greenhouse gas measurements on board FAAM BAe-146 aircraft were considerably limited by a software fault which made operating with FGGA model 907-0011 (from 2017)[64] ‘dual mode’ setup impossible. The fault occurred when operating the FGGA in fast mode with SO_2 analyser rather than O_3 analyser, which normally should be interchangeable in the Core Chemistry rack. The issue was not discovered early enough, because the SO_2 configuration was not tested at the software development stage. Hence, the rack was reverted to the pre-2019 state featuring FGGA model 907-0010 (from 2009) [58]. The cavity pressure was 50 Torr and measurement rate was 1 Hz. The difference between old and new FGGA was not only the speed but also qualities like signal to noise ratio (1.5 ppm noise for ACRUISE-1 CO_2 vs 0.75 ppm for ACRUISE-2 CO_2) hence the first campaign suffered substantially from the reduction of quality in

CO_2 data. Moreover, wrong pressure broadening coefficients accounting for molecular collisions interfering with characteristic emission were applied during summer 2019. This lead to an unknown error estimated to approx. 5-10% in the CO_2 data. The correct coefficients cannot be reapplied because spectral data is not saved due to storage constraints.

During ACRUISE-2 and -3 the new FGGA was operated in fast mode, with an improved pressure control system compared to the original 2019 'dual mode' setup. A pressure building McLaughlin inlet with 1/4" OD Teflon tubing replaced the simple rearward facing stainless steel tube. FGGA's internal pressure control system with two external pumps was also simplified and only the stronger Edward's nXDS 20i pump was kept. This allowed for 10 Hz measurements.

Thermo Scientific model 43i Trace Level Enhanced Pulsed Fluorescence SO_2 Analyser (TEi43i or TECO)[54, 65] was used to measure SO_2 during all three campaigns. TEi43i is a commercially available analyser utilising an absorption band between 190 – 230 nm. It was modified in 2016 to improve its airborne measurement capacity. The critical orifice was replaced with a mass flow controller to increase the flow rate and an extra hydrocarbon kicker (Thermo Scientific patented membrane) was added to reduce interference from highly fluorescent hydrocarbons. The inlet is a rearward facing stainless steel tube housing 3/8" OD Teflon tube separate to the FGGA, but shared with CO and O_3 analysers. It is also equipped with a Nafion dryer (MD-series, Perma Pure) to remove water vapour from sampled air. This allowed an in-flight response time of 4 ± 1 s, 3σ LOD of 1.5 ppb and ± 6% uncertainty for 1 Hz acquisition rate.

During ACRUISE-3, there were two more SO_2 measurements available on board: SO_2-LIF and SO_2-CIMS. LIF is a custom built at the University of York laser-induced fluorescence instrument using tunable narrow-linewidth laser to provide fast high precision SO_2 data. The instrument is based on 2016 Rollins design [56]. This technique is highly sensitive and selective and it allowed for 3σ LoD of 300 ppt at 1 Hz during ACRUISE, which was the instruments first campaign.

Time-of-Flight (ToF) Chemical Ionization Mass Spectrometer (CIMS) manufactured by Tofwerk. The instrument provided continuous measurement of a range of VOCs and SO_2 using reduced pressure ion molecule reaction coupled to a high resolution ToF-MS [57]. Unfortunately, CIMS proved unsuitable for this study due to low signal to noise ratios.

NO_x [60, 66] was measured during ACRUISE-1 using a custom built NO chemiluminescence two channel analyser measuring NO_2 by photolytic conversion at 385 nm and NO on a second channel. There was no NO_x measurement taken during following campaigns.

2.1.3 Whole air sampling

Whole Air Sampler (WAS) is a NCAS and University of York developed sampling grab system compatible with the FAAM aircraft and designed to capture whole air for off-line analysis, e.g. for VOCs. The setup was described in detail by Andrews et al. [67] and pictured in plot Figure 2.4.

WAS wa located in the rear hold of the aircraft and samples air from a forward-facing inlet using a metal bellows pump (Senior Aerospace PWSC 28823-7). A full WAS set contained of 6 cases with total of 64 3 L SilcoCan bottles (Restek), which are kept under vacuum. Each bottle was sealed by pneumatic bellows valves (Swagelok, P/N SSBNVVCR4-C) after it was filled to approx. 40 psig for a user adjustable time, which varies with altitude and sample type. Despite being successfully deployed on numerous campaigns all over the world, WAS was retired from airborne use in late 2021 and repurposed for ground measurements. During ACRUISE campaign the bottle fill time was set to 30 s at task area.

During ACRUISE-1 a new system - Son of Whole Air Sampler (SWAS), was trialed along with the original WAS, to completely take over during the following campaign. SWAS consists of a cabin mounted rack and drawer cases with sample bottles inside. The rack is fitted with with a Metal Bellows Compressor pump (model 28823-7), compressed air cylinder actuating bottle valves and has 6 drawer slots for the cases. At the time of writing, there are 14 identical size cases, 8 of which contain 16 1.4 L to-vacuum bottles and 6 which contain 8 2 L flow-through bottles. All bottles are stainless steel fitted with pneumatically actuated bellows-sealed valves (Swagelok, SS-BNVS4-C). To-vacuum bottles contain only one valve and are can be filled only once, similar to the WAS system. The flow-through bottles contain two valves, one at each end, allowing the air to flow through bottle and upon user command closing one valve, topping bottle up to 40 psig and closing the other valve. If need be they can be flushed and filled again. They can also be used as to-vacuum bottles. The fill timeout during ACRUISE-2 and -3 was set to 15 s, but the bottles generally took 6 to 9 s to fill to 40 psi at task area. The values varied with atmospheric pressure.

SWAS was created by Steve Andrews as an improvement for the existing WAS. The first, most apparent difference is size. SWAS can fit up to 96 bottles in one rack and second set can be easily transported in the hold in 3 easy to handle cube cases. Meanwhile WAS needed the entire rear hold for just one set with 64 bottles. Having the system in the cabin rather than in hold means that any minor issues can be fixed in-flight. An important aspect was also safety of handling. There was a number of minor injuries acquired by staff loading and unloading WAS from its hold, due to weight of the cases, number of sharp edges, securing pins being bent and poorly fitted and a number of hoses hanging of the ceiling. Another improvement are the transport cases, which can be plugged in to the GC or other analysis instruments without having to remove the bottle drawers. Software for SWAS operation was incomparably better then for WAS and the in-flight operation much easier. Finally, the lag time and the fill time decreased, allowing targeting narrower structures. The flow-through bottles, which can be flushed in case of unsuccessful attempt, increased the filling efficiency.

All the samples were analysed for VOCs using GC-FID-QMS. The experiment setup consisted a case containing two SWAS 'drawers' connected to a thermal desorption unit (custom) which delivered the samples to Agilent 7890A gas chromatograph (GC). The detection system was a flame ionisation detector (FID) and an Agilent 5977A quadrupole mass spectrometer (QMS). Sampling of the air from the SWAS bottles was automated with custom software actuating appropriate valves in cooperation with the thermal desorption unit. Logging of the sampling times and bottles was also automated. Regular calibrations and blanks were included in the analysis routine to ensure that any change in instrument performance is accounted for. Usually three calibrations and at least 5 blanks were performed after each sample set (16 to 32 bottles). The calibration gas is a mix of thirty non-methane VOCs in nitrogen (from the National Physical Laboratory).

The analysis process is described in detail by Warburton et al. [68]. 500 mL sample is taken from a canister and passed to the thermal desorption unit. There the sample is dried in a -40°C water trap and once dry it is pre-concentrated in an adsorbent packed tube kept below -120°C. Then the tube is heated to 80°C to desorb carbon dioxide which would interfere with the measurement and purged with helium. Once no CO_2 is left in the sample the tube is heated to 190°C to desorb the rest of the compounds and flushed with helium as carrier gas. This mixture is transferred to the focus trap, which is also packed with adsorbent material and kept below -120°C. Once the entire sample is in the trap it gets rapidly heated to 200°C and purged with helium again. Then it is ready to analyse. All three traps are heated and purged between runs to ensure they are clean when next sample is introduced.

In the GC oven, the sample enters a 60 m long, 150 μm internal diameter (ID) VF-WAX column flowing at 1.6 mL s^{-1}. This column combined with a Deans switch, allows separation of smaller VOCs (C2 – C8; up to 8.5 min) which otherwise would not be resolved from larger ones which otherwise take forever to elute. The first fraction is transferred from WAX column to a porous-layer open tubular (PLOT) column (50 m x 320 µm ID) straight away to be separated further and analysed with FID. Then Deans switch is actuated diverting rest of the sample to a 2 m x 150 µm ID fused silica length to give the first fraction time to be analysed. Finally, the second fraction is split between FID and QMS and analysed. FID peak integration was used to quantify all the VOCs.

CO_2 and CH_4 in the SWAS samples were analysed using FGGA's 'little sibling' UGGA (Ultraportable Greenhouse Gas Analyser). This was done in order to quantify the extent to which the plume was captured by comparison with the continuous measurements from the flight and background SWAS samples. A simple setup with an overflow was used. If the reading remained unstable the sample was rejected, otherwise the stabilised data was averaged. It is important to note that in case of ACRUISE-2 the samples were waiting 4 months to be analysed, but since both CO_2 and CH_4 are stable that should not have affected them. In case of ACRUISE-3 the UGGA analysis was coupled with the VOCs measurement.

For ACRUISE-1 WAS samples no CO_2 or CH_4 measurements in the sample were done and the GC setup did not include QMS. This work focuses mainly on chosen case studies from ACRUISE-2 SWAS dataset.

2.1.4 Marine Traffic

Marine Traffic (www.marinetraffic.com) [70] is a provider of ship tracking and maritime intelligence. It tracks over 550 thousands ships at minutes to days resolution (depending on ship location), indicating their positions, speed, heading and load. Each ship has also characteristics such as size, weight, age or ownership structure. The level of insights depends on the subscription tier or purchased data product. Marine Traffic utilises a net-

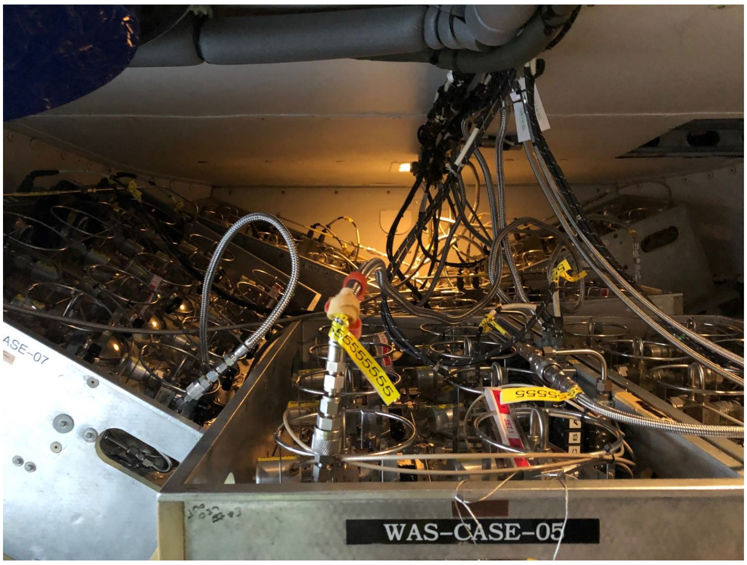

Figure 2.4: Whole air sampler.

work of coastal automatic identification systems (AIS) as well as a satellite tracking system. AIS works using very high frequency (VHF) transmitters and receivers to broadcast and receive parameters such as ship position or heading from nearby vessels. It is used to avoid collisions and to monitor ship traffic [71].

An exceptionally useful feature of Marine Traffic is their live map. The map offers a wide range of features and custom views. An example is shown in Figure 2.6. Options that were most useful to the ACRUISE project were:

- **Vessel filtering:** the map can display general (e.g. cargo) or specific (e.g. bulk container) type of ships, different capacities or years of construction. This feature is extremely useful to narrow down the targeted group of ships which were large enough and eliminate e.g. fishing boats, which due to high bird density were not suitable for safe measurements.

- **My fleets:** Marine Traffic allows saving custom lists of vessels and displaying them highlighted on the map. This way it was easier for the ground team to direct the BAe-146 crew to ships that are meant to be

Figure 2.5: Son of whole air sampler in an aircraft. Source: SWAS TSSE [69].

revisited in or out of SECA or to save particularly interesting ships.

- **Layers:** enable inputting custom areas e.g. areas with flying permissions or SECAs as well as adding ship names and 30 min track forecast. These features helped both ground and flying teams to match encountered ships with their names and plan the next target.
- **Density maps:** show ship traffic for given year, either including bulk of the ships ships or general types (e.g. tankers). For ACRUISE mainly the bulk ship density was used to identify position of the busy shipping lanes for background measurements. It is also a great visulalisation tool.
- **Playback:** The playback option was used sometimes to identify ships on the ground based on their relative positions to known ships that were sampled.

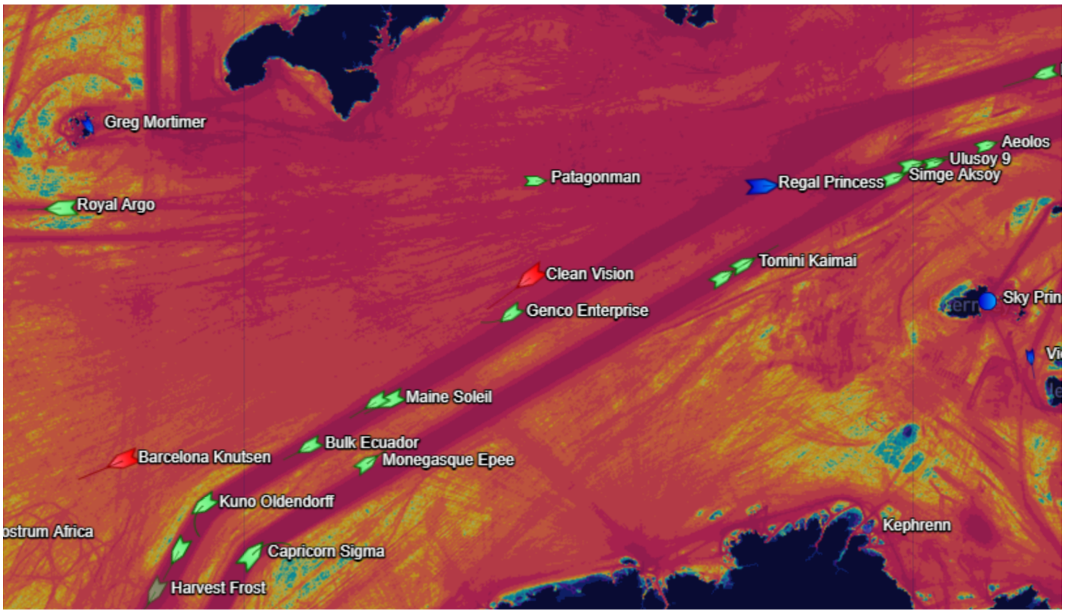

Figure 2.6: Marine Traffic map function. In this example the background is ship traffic density map for 2021. Ships displayed are LNG tankers, bulk carriers and passenger ships with their 30 min course forecast.

2.2 ACRUISE campaigns

2.2.1 Flights overview

There were 30 dedicated ACRUISE flights: 13 in the 2019 campaign, 13 in the 2021 campaign and 4 in the 2022 campaign. Additionally, there was an LNG tanker encountered during ACSIS-7 campaign following ACRUISE-3 (flight C292). They are summarised in Table 2.2 and the task areas are indicated on a ship density map in Figure 2.7. These areas were chosen to cover busy shipping lanes (coast of Portugal, Bay of Biscay, English Channel), Sulphur Emission Control Area (SECA; English Channel) and coastal area adjacent to SECA (SW Approaches). During ACRUISE-2 ships were targeted in and out of SECA to observe any differences in SO_2 emissions.

Four main strategies were used throughout all three campaigns: plume transecting, plume following, shipping line following, shipping line transecting.

Plume transecting was the standard approach to first contact with a target ship. As shown in Figure 2.8b, the plume is transected perpendicularly as close to the ship as possible (i.e. 500 m). Based on the first impression of the plume, further steps were decided. In ACRUISE-1 the typical next step was to study plume aging using NO_x as plume marker, in some cases even all the way to the cloud deck. However, since NO_x was not available for the remaining two campaigns and the SO_2 enhancement was generally lower and the instrument less sensitive, it was frequently difficult to detect aged plumes. In such cases multiple close passes were performed to build up better statistics. If the plume was distinct enough, passes further downwind were attempted. **Plume following** is also shown in Figure 2.8b. After transecting the plume perpendicularly, the plume was followed from ship down as long as possible. Combination of the pilots visual assessment and feedback from fast measurements such as NO_x (only ACRUISE-1), SO_2-LIF (ACRUISE-3) and fast mode FGGA CO_2 (except ACRUISE-1). It is designed to study plum aging and allow taking more whole air samples.

Shipping lane transecting was used in order to measure the change in pollution between high ship density areas, known as shipping lanes [70] and low ship density areas. See Figure 2.8a, C187 (blue). It was done predominantly in ACRUISE-1 because Portuguese coast lanes were much busier than Bay of Biscay ones and likelihood of seeing any effect was higher. **Shipping lane following** meant flying along the shipping lanes, down- and upwind to asses the difference in pollution. For both task areas it required easterly (i.e. oceanic) wind approximately perpendicular to the lanes, to prevent mixing of plumes with land emissions. Both these types of 'background' measurements were performed mainly during ACRUISE-1.

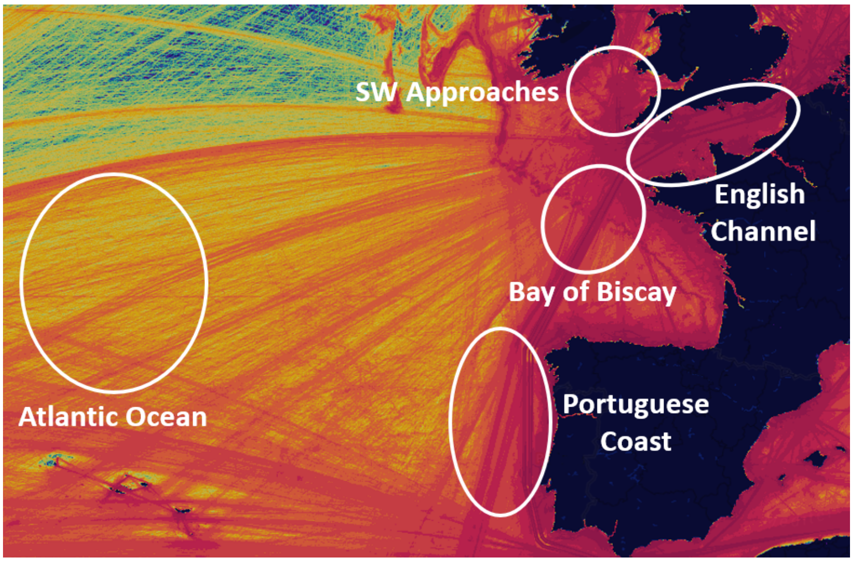

Figure 2.7: ACRUISE task areas against a ship density map. All three campaigns included flights in English Channel and SW Approaches. ACRUISE-1 focused on Portuguese Coast and following two campaigns on Bay of Biscay. Additionally, there was one LNG tanker captured accidentally in the middle of Atlantic Ocean during campaign following ACRUISE-3. Map source: Marine Traffic [70].

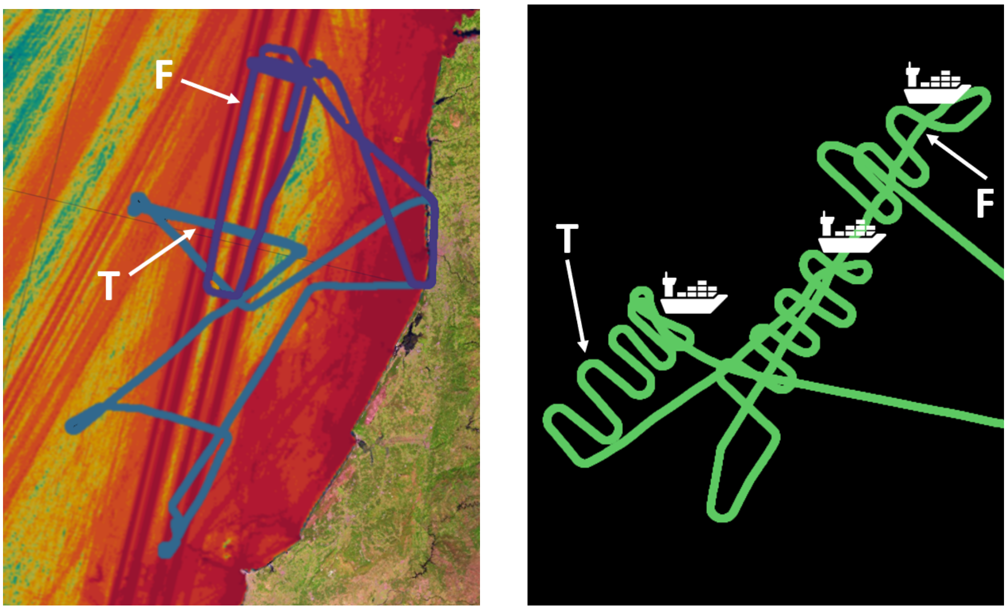

(a) Flights C187 (blue, westerly wind) and C189 (purple, southwesterly wind) against ship density map. Arrows point at shipping lane (marked in dark red) transecting (T) and flying up and down wind of them (F). Map source: Marine Traffic [70].

(b) Flight C182, arrows point to plume transecting (T) and plume following (F). Map source: GLAD Landsat MOSAIC 2021 [72].

Figure 2.8: Four types of ACRUISE flight patterns - background and bulk studies shown on the left and single ship studies shown on the right.

Campaign	Flight	Date	task area	Main target	Comment
1	C178	10/07/2019	English Channel	random ships	along the channel
1	C179	11/07/2019	SW Approaches	plume ageing	MSC Poh Lin, Stena Horizon and Eagle Brisbane focus
1	C180	11/07/2019	SW Approaches	plume ageing	Marianna VV focus
1	C181	12/07/2019	Portuguese Coast	plume aging	WE runs, Sti Beryl focus
1	C182	12/07/2019	Portuguese Coast	plume aging	Bow Chain, Max Jacob and Trammo Laoura focus
1	C183	13/07/2019	Portuguese Coast	shipping lane background	NS runs
1	C184	15/07/2019	Portuguese Coast	plume aging	WE runs, KT Birdie focus
1	C185	15/07/2019	Portuguese Coast	clouds	WE runs
1	C186	16/07/2019	Portuguese Coast	plume ageing	Hirado focus
1	C187	16/07/2019	Portuguese Coast	clouds	WE runs
1	C188	17/07/2019	Portuguese Coast	plume aging	BTG Eiger and Lake Superior focus
1	C189	17/07/2019	Portuguese Coast	shipping lane background	NS runs (pint flight)
1	C190	18/07/2019	English Channel	same ships in SECA	MSC Mirja focus
2	C253	27/09/2021	English Channel	random ships	ship sailed with wind so little plume
2	C254	28/09/2021	Bay of Biscay	same ships out of SECA	plumes sank quickly
2	C255	29/09/2021	English Channel	same ships in SECA	catching ships from C254
2	C256	01/10/2021	SW Approaches	random ships	
2	C257	03/10/2021	Bay of Biscay	random ships	starting from S and moving N
2	C258	04/10/2021	Bay of Biscay	random ships	NE corner
2	C259	05/10/2021	Bay of Biscay	shipping lane background	stronng wind, invisible plumes
2	C260	06/10/2021	Bay of Biscay	clouds	not very good cloud
2	C261	07/10/2021	SW Approaches	clouds	aged LNG plume
2	C262	08/10/2021	Bay of Biscay	same ships in SECA	
2	C263	09/10/2021	English Channel	same ships out of SECA	catching ships from C262, high background
2	C264	11/10/2021	Bay of Biscay	random ships	
2	C265	12/10/2021	SW Approaches	clouds	whale watching
3	C284	29/04/2022	SW Approaches	LNG terminal and tankers	slack wind, sampled 3 other LNG tankers
3	C285	30/04/2022	SW Approaches	LNG terminal and tankers	more wind
3	C286	01/05/2022	Bay of Biscay	shipping lane background	not much ship traffic, some cloud
3	C287	02/05/2022	Bay of Biscay	shipping lane background	sampled some cloud and ships

Table 2.2: Details of all flights during which ships studied in this work were encountered.

During ACRUISE-2 and -3 precise direction of the plume was derived in flight as follows [73]. First north- and east-bound velocities (vN_x and vE_x) were calculated for both ship ($_s$) and wind ($_w$) base on their speed (s_x, in knots) and direction (d_x, in degrees):

$$vN_s = s_s \times cos(d_s) \quad vN_w = -s_w \times cos(d_w) \quad vE_s = s_s \times cos(d_s) \quad vE_w = -s_w \times cos(d_w) \tag{2.1}$$

Subsequently relative wind velocities are calculated (vN_r and vE_r):

$$vN_r = vN_s - vN_w \qquad\qquad vE_r = vE_s - vE_w \tag{2.2}$$

Then final plume direction (d_p) is calculated:

$$d_p = \begin{cases} 630 - \text{atan2}(vE_r, vN_r) & \text{if } 270 - \text{atan2}(vE_r, vN_r) < 0 \\ 270 - \text{atan2}(vE_r, vN_r) & \text{if } 270 - \text{atan2}(vE_r, vN_r) > 0 \end{cases} \tag{2.3}$$

See Figure 2.9 for visual explanation. This approach was used to increase success rate of transecting plumes, which previously relied on visual assessment and NO_x. The former is not very reliable for weaker and paler plumes, as well as in strong wind, the latter was not available for ACRUISE-2 and -3.

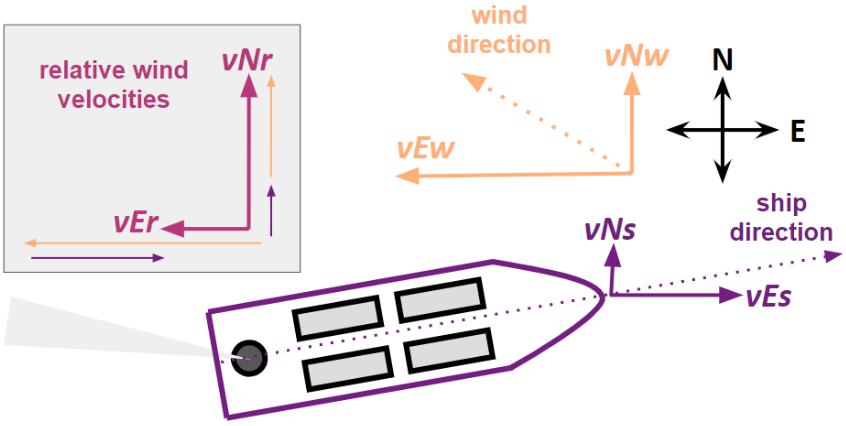

Figure 2.9: Plume direction calculation, where vN is north-bound speed vE is east bound speed and s indicates ship, while w indicates wind.

2.2.2 Mission science

On the operations side, it is important to mention the role of mission scientists and pilots in this campaign. This kind of flying requires fast situation assessment and decision making, as well as great agility in meeting the plumes with a large research aircraft like BAe-146. Communications with the ground are essential when targeting ships, since they are not easy to find. Plume direction had to be calculated on board.

All of this meant that having at least two mission scientists on board was necessary. The mission scientist in the cockpit having a better outlook on the situation would make strategic decisions regarding ship choice and number of passes collecting feedback from the scientists at the back and consulting decisions with pilots. The second mission scientist would be responsible for communication with the team on the ground, requesting Marine Traffic images or ship details and consulting the 'Mission 1'. Additionally, the 'Mission 2' would be responsible for keeping timestamped log of ship encounters and whenever possible feeding the encountered ships to the ground team. This role was sometimes combined with SWAS operation.

The main objective of flight sometimes changed completely based on meteorological conditions or ship abundance on the day. ACRUISE-1 showed also that keeping good record of ships is crucial for data analysis. Hence the ground team was necessary to successfully target the ships and choose operation areas with right meteorology.

The data collected for this work would not be there without hours of tracking the ship and finding patterns in their behaviour to optimise the flight planning. A lot of the improvements from ACRUISE-1 to the following two campaigns are part of this PhD. Finally, the decision making while on the task area and efficient communication were a crucial for obtaining the results presented below.

2.3 Apparent Sulphur Fuel Content (SFC)

2.3.1 Observed SFC

In this work the apparent sulphur fuel content (SFC) was calculated using Equation (1.1) [35, 37, 74].

$$\mathrm{SFC}[\%] = \frac{\mathrm{S[kg]}}{\mathrm{fuel[kg]}} = \frac{\mathrm{SO_2[ppb]}}{\mathrm{CO_2[ppm]}} \times 0.232[\%] \tag{1.1 revisited}$$

where SO_2 and CO_2 are peak areas for each species expressed in ppb and ppm, respectively. 0.232 is mass conversion factor for fuel content derived by Kattner et al. [35] with assumption that 87% of ship fuel by mass is carbon. This method was successfully applied to ground measurements of over 1400 ship plumes in the harbour of Hamburg.

Equation (1.1) relies on assumption that all sulphur is emitted as SO_2 and all carbon is emitted as CO_2. This is not entirely the case. Little to no CO was measured during the three campaigns, hence 100% CO_2 conversion is a fair assumption, especially that a complete combustion leads to most efficient (and cost effective) usage of fuel. However, it is known that not all sulphur is emitted as SO_2.

Yu et al. [75] show that directly emitted SO_4^- increases with increasing SFC. The conversion to sulphate also increases with plumes ageing. Since a precise position of the ship at the time of interception of its plume is not known, the age of the plume has to be assumed. Yu et al. [75] estimates the age of most of the plumes suitable for integration to be max. 15 min old for all the ACRUISE campaigns and the sulphate percentage for this age of plume is 6% of the ship emitted sulphur. According to Corbett et al. [76] 95% of the overall sulphur emission is in the form of SO_2. Since most plumes included in this work are very fresh they are not corrected for sulphates but the possible 6% is included in the uncertainty calculations.

2.3.2 STEAM

Ship Traffic Emission Assessment Model (currently third version - STEAM3) developed by the Finnish Meteorological Institute uses Automatic Identification System (AIS) data to evaluate exhaust emissions of individual ships [77]. The model estimates emissions of gaseous species such as SO_2, NO_x or CO_2, but also aerosols and particulate matter. The input for the model, apart from AIS data (e.g. speed, heading, load), includes ship parameters (especially engine specifications, such as model, fuel type, rpm) and meteorological data (to estimate impact of waves). Engine-specific fuel consumption is especially important in determining SO_2 and CO_2 emissions [78].

The model setup used in this study provides estimate of the annual emission of SO_2, CO_2 and NO_x. The values obtained from model are expressed in kilograms of each compound. Equation (2.4), which is a modification of Equation (1.1), was used to calculate average yearly SFCs. Moreover, NO_x to CO_2 ratios were calculated.

$$\mathrm{SFC}[\%] = \frac{\mathrm{SO_2[kg]}}{\mathrm{CO_2[kg]}} \times 1.60[\%] \tag{2.4}$$

For NO_x/ CO_2 (ppm / ppm) ratios a conversion was needed too. Assumption was made that NO_x can be treated like NO_2 to convert mass ratio to mixing ratio. Modelled mixing ratios were calculated as follows (Equation (2.5)):

$$\frac{\mathrm{NO_x}}{\mathrm{CO_2}} = \frac{\mathrm{NO_x[kg]}}{\mathrm{CO_2[kg]}} \times 1.05 \tag{2.5}$$

2.4 Peak integration

2.4.1 Code description

The peak integration code was initially developed by Stuart Lacy, Steph Batten and Dave Sproson. Deriving the emission rations happens in five steps: background identification, plume identification, background refitting, peak integration and peak matching with QA/QC. The `acruiseR` package, which contains all the code described below is available on GitHub [79].

To define plumes the concentration time series is assumed to consist of background, characterised by normal distribution and constant variance, and irregular peaks distinguished by different variance and higher mean*. Firstly, a Generalised Additive Model (GAM, R function `mgcv::gam`) with an adjustable smoothing parameter k is fitted for the entire time series. GAM is similar to Linear Regression:

$$Z = A_0 x_0 + A_1 x_1 + ... \tag{2.6}$$

where A_n is weight of the variable x_n. Except, in GAM, A_n weights are replaced with non-linear smooth functions or splines, S_n:

$$Z = S_0 x_0 + S_1 x_1 + ... \tag{2.7}$$

Splines, can be simplistically defined as polynomial functions covering a relatively small range. A simple polynomial could also be used for the baseline fitting, however, it would easily be driven by peaks not capturing the actual background well. Therefore a more sophisticated method was used. Another alternative approach that could be used is rolling average. It was used in the early development stage, but proved to be challenging to apply to a noisy and variable background (e.g. for CO_2 data), see Section 2.4.2.

---

*Except for ozone, which is typically titrated in fresh plume and so characterised by lower mean. However it is not discussed in detail in this work.

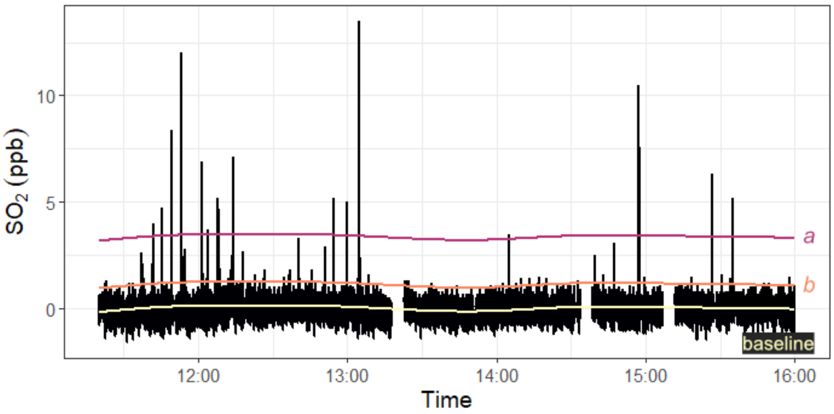

Figure 2.10: Initial baseline fitting for ACRUISE flights, where baseline is the initial GAM fit, *a* is standard deviation multiple describing edge of noise, *b* is standard deviation multiple describing peak threshold.

Once the first step of **background identification** is finished, two thresholds based on standard deviation are chosen (see Figure 2.10). Threshold *a* is used for **plume identification** to select data spikes which are large enough to be quantifiable plumes and separates them from background changes or noise. The value depends on the background variability, as well as height and number of peaks in the flight. The lower threshold - *b* ideally sits on the 'top edge' of the noise. Plumes identified by threshold *a* get extended all the way to threshold *b*. All the parameters used are showed in Table A.4, as they are adjusted for each flight based on the background variability, number and height of peaks.

The reason for threshold *b* is to avoid including the noise in the peak integral or creating additional data points[†], which would happen if the mean was used. The former would obviously affect the area, the latter is known to be a bad practice and would cause risk of biasing the data. It is important to emphasise that the main idea behind this algorithm is the reduction of human input, and hence bias, to a minimum. Using the baseline would also require embarking on a philosophical quest of defining where the

---

[†] Since it is not given that there will be a point right at the baseline, there would have to be a point added where lines between data points transect the baseline.

plume starts and ends for each species, which in case of a very non-trivial ACRUISE dataset is beyond scope of the project. This approach might seem controversial, since there is possibility of losing part of the peak between threshold *b* and baseline, but it simplifies the algorithm significantly and helps to tackle low signal to noise data. This method was used previously by Barker et al. [80].

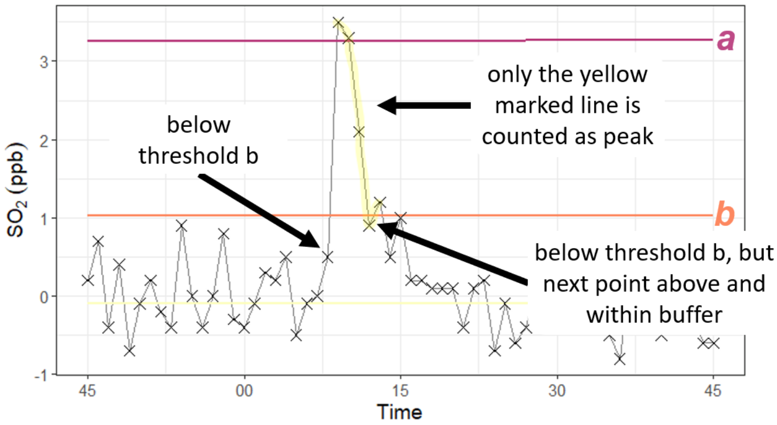

Figure 2.11: Peak detection caveat - peaks might seem ‘incomplete’. Peak from flight C256 is marked in orange and the remaining data is grey.

Everything comes with a price, which in this case is the treatment of the very small peaks as illustrated in Figure 2.11. Such peaks might seem ‘fragmented’ because they consist of very few points (5 in the example) and one data point being below the threshold actually makes a visible difference. Hence small peaks bear additional, unquantifiable error. Moreover, an exception to integrating an entire flight in one go with minimal human intervention is made in rare cases when during ACRUISE-2 and -3 an SO_2 peak is detected but CO_2 peak is not due to a high background variability. In such cases a smaller chunk of the time series including the CO_2 peak is integrated separately.

Once the peaks are identified and extended, the baseline gets refitted using only the data classified as background. This means it no longer is biased by peak clusters. More details on **background refitting** can be found in Section 2.4.2. The refitted baseline is then subtracted from the data.

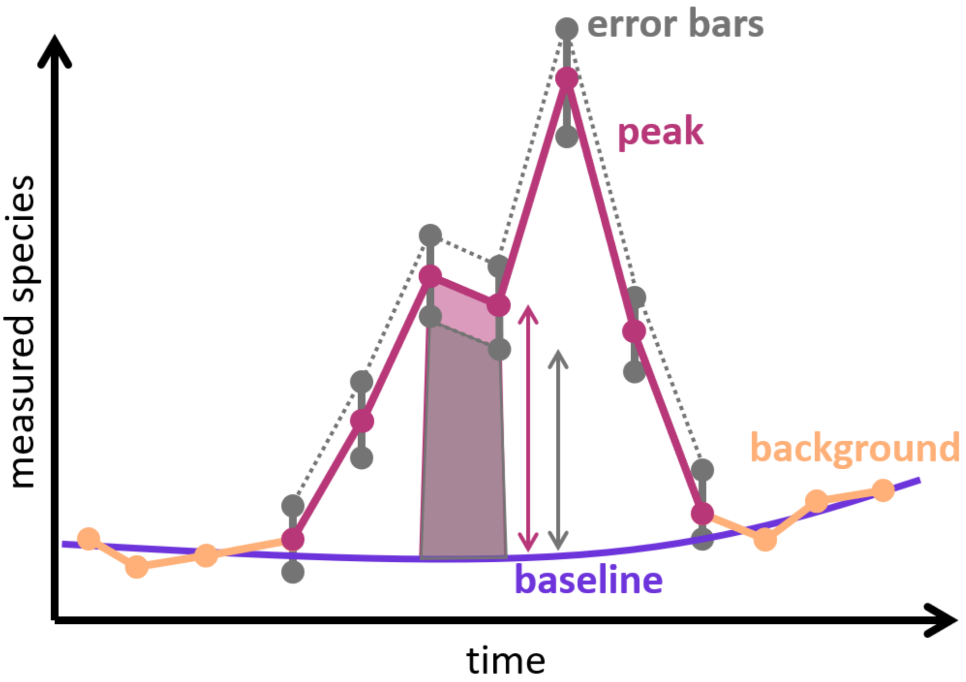

Figure 2.12: Trapezoidal approximation shown on a hypothetical peak (pink line with data points marked) with its uncertainty (grey bars). Baseline (purple line) is fitted to the background (orange line with data points marked) and serves as one side of the trapezoid. Grey dotted line connects the maximal values within uncertainty.

The following step is **peak integration** using trapezoidal approximation, as shown in Figure 2.12. Each two points of the peak can be connected to the baseline with a straight vertical line giving a trapezoid, which area can be calculated. Sum of trapezoids formed using all pairs of the neighbouring points in a peak gives an approximate peak area.

In case of more ‘structured’ peaks there is a user adjustable time buffer within which adjacent peaks are counted as one plume. In this work the buffer is always 15 s. An example of technically two peaks, which however fall within 15 s of each other and are counted as one is shown in Figure 2.11. At the same time the instrument uncertainty is propagated, as described in detail in Section 2.4.5.

The final stage is **peak matching and QA/QC**. Each of the colour coded peak, as shown in Figure 2.13, is individually inspected for any abnormalities, e.g. being a sudden background change rather than a plume, omission of a part of a plume or inclusion of background in the peak area, data glitch. These are the basis for peak rejection, but are not corrected manually in order to reduce human bias. Furthermore, any peaks that might have their origin on land are deleted (two cases). The integrated areas of peaks in different species are then matched based on timestamps. When SFCs are calculated any outliers or suspicious values are checked manually.

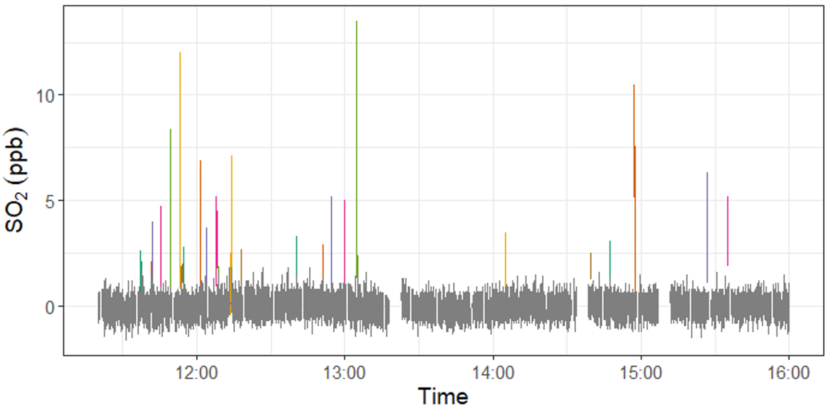

Figure 2.13: Peak detection with refitted baseline. Each peak is marked in different colour and the remaining data is grey.

2.4.2 Comparison of baselines

In this work a refitted GAM baseline with parameter k dependent on flight characteristics was chosen as the best option available at the time.

The initial choice was between a rolling average and GAM. The latter is described in detail in Section 2.4.1. A simple rolling average, otherwise known as moving average is a series of averages of small subsets of the entire dataset (see Equation (2.8)). Hence each point in baseline derived this way would be in fact an average of given width of data surrounding the point of interest.

$$A_k = \frac{p_{a-k} + \ldots + p_a + \ldots + p_{a+k}}{2k+1} = \frac{1}{2k+1}\sum_{i=a-k}^{a-k} p_i \qquad a \in [k+1, n-k-1] \quad (2.8)$$

where n is number of points in data set, A_k is rolling average at point a, $2k+1$ is width of the subset of the time series with a being its middle point.

The method was implemented in `acruiseR` package [79] with three adjustable parameters: background standard deviation window, background standard deviation threshold and background mean window. Background mean window corresponds simply to $2k+1$. The standard deviation parameters refer to the further step of peak recognition: for the given window standard deviation is calculated and if it falls under the given threshold this data point is considered background [81].

GAM baseline was chosen over the rolling average since it was easier to implement across a diverse range of measurements. Having said that it can yield equally good results, it just requires more human intervention in case of this rather diverse data set. A comparison is shown in Figure 2.14.

As mentioned in Section 2.4.1 after finding and separating the peaks data the baseline gets refitted just to the remaining background data. The importance of this step is illustrated in Figure 2.15. Where there are no peaks (10:30-10:35) both baselines overlap, but as soon as peaks start appearing the non-refitted baseline is driven up, while the refitted baseline follows the background reasonably closely. For small, sharp peaks the difference is negligible, but especially for wider peaks and peak clusters the difference increases.

2.4.3 Comparison with other methods

Another popular approach to peak integration is using a interactive data analysis program such as Origin Pro. This method was tested for the ACRUISE-1 dataset but eventually abandoned, as it relied too much on human judgement and due to the commercial nature of the program there was no insight

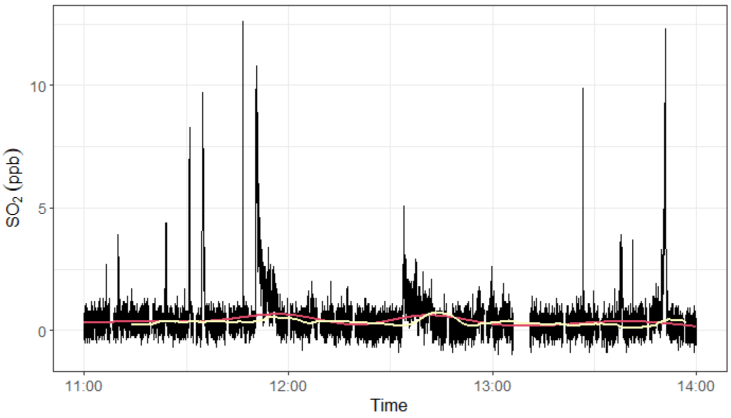

Figure 2.14: Comparison of GAM (pink) and rolling (yellow) baseline, both refitted. GAM: k=10, a=3, b=0.5. Rolling: standard deviation window = 180, standard deviation threshold = 0.5 (same as in case of GAM), background mean window = 660 (as suggested by Batten [81]). The data comes from flight C264.

in the exact algorithms used to identify the background and peak areas. Additionally, no error calculation was available. Figure 2.16 shows SO_2 and CO_2 areas obtained using both methods where the peaks could be matched and both species were integrated. The data sets were constrained by the above assumptions because the QA/QC criteria have became stricter since the previous work was done and more peaks were rejected.

There is a reasonable fit between the SO_2 data as shown in Figure 2.16a with Origin Pro derived values tending to be larger than their R derived equivalents. This is likely due to a different way of defining the baseline and peak start/end, however since the peaks are integrated for ratios rather than absolute values these differences should mostly cancel out. Main outcome is however to always apply same method for both species. In case of CO_2 the fit is worse and shows the opposite tendency - Origin Pro assuming smaller areas than R, as shown in Figure 2.16b.

Difference between the SFCs calculated with peaks integrated in each software is shown in Figure 2.17. Although looking for multiple trend lines in such a small population would not be statistically robust and would provide not much further insight, it is worth pointing out that for SFCs below 2.5%

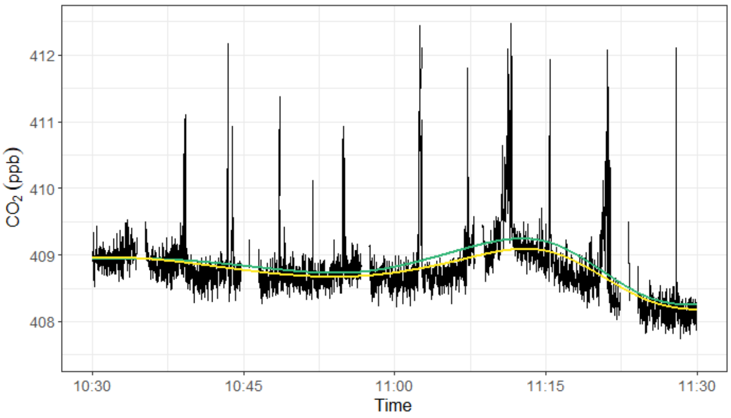

Figure 2.15: Comparison of refitted (yellow, bottom) and not refitted (green, top) GAM baseline in relatively stable CO_2 background with both perpendicular passes and plume following. The data comes from flight C257.

all Origin derived values are bigger than R derived ones, however above 2.5% some Origin values become smaller. Since these values do not originate out of particularly high or low SO_2 peak areas (see Figure 2.16a, green points), so this is most likely driven by CO_2. The same points were coloured green in Figure 2.16b and this time they stand out a bit more, since all of them are below the linear fit between Origin and R data. These areas are smaller than their R counterparts, while the opposite is usually the case. Hence either Origin underestimates these areas or R overestimates them. All these peaks pass the QA/QC process so either method could be wrong. Since the `acruiseR` package has little user interaction it seems likely that some of the not obvious CO_2 peaks were perhaps not fully captured.

Alternatively, Yu et al. [75] used a different Matlab based algorithm for the ACRUISE-1 data set, however it was designed primarily for aerosol data and it is not available in public domain, so it was not used here.

Finally, there exists a completely different approach to deriving the SO_2 to CO_2 ratio for SFCs which was used by Wilde et al. [82] to quantify SFCs of ships entering the port in Valencia. The background is defined as 1^{st} percentile measurement in a rolling 5-minute, centred window and

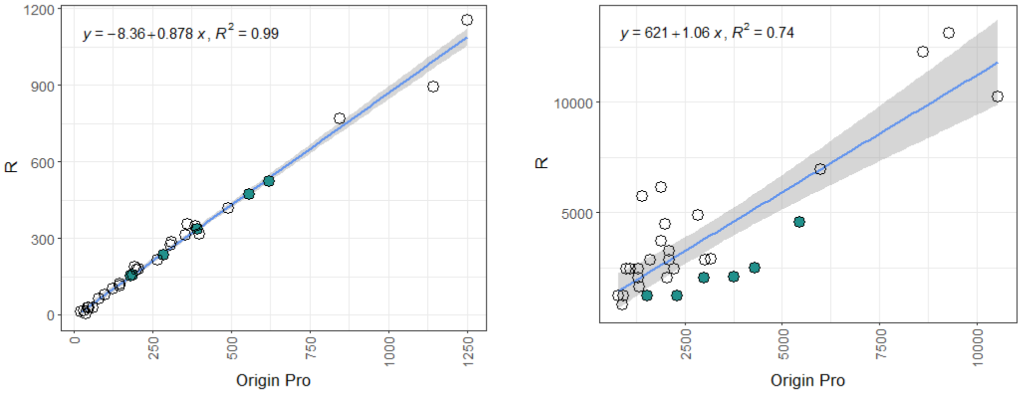

(a) SO_2 comparison.

(b) CO_2 comparison.

Figure 2.16: Comparison of Origin Pro and R integration [79] for all peaks where both SO_2 and CO_2 were detected by both methods. The points filled in green indicate areas which yielded positive difference of SFC_{Origin} - SFC_R.

subtracted. Then a cross correlation is used to correct for the lag between instruments and the ratios are derived using ordinary least squares (OLS) regression for each plume. This approach is also found to be sensitive to differences in the data resolution.

Regression and integration methods have a good potential to compliment each other. The regression method works well for wide plumes which increase the population on which the regression is performed. However is not viable for short sharp plumes due to too low number of data points qualifying for regression (sometimes even just one). On the other hand, integration handles the sharp plumes well, while being inconsistent with wider plumes. Combining those methods is beyond the scope of this study, however it should be taken into consideration in future works.

2.4.4 NO_x integration in Origin

Origin Pro was used for NO_x integration due to the complexity and structure of the signal which could not be handled and matched with other species without human intervention. The CO_2 signal was also processed in Origin Pro to match the methods. Since no uncertainties could be obtained using

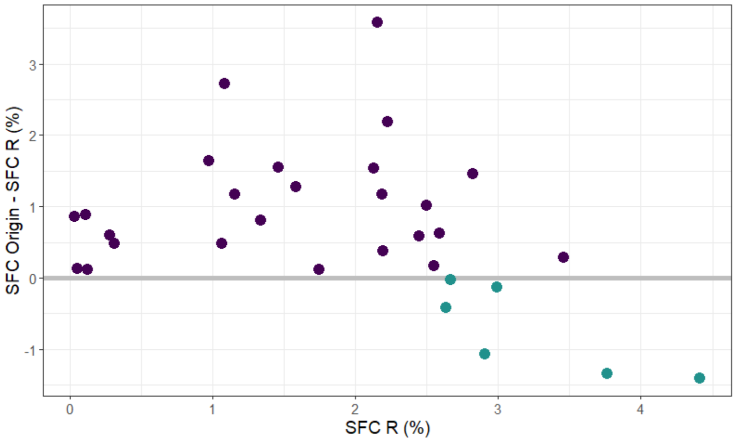

Figure 2.17: Difference between SFCs calculated using Origin Pro and R depending on size of SFC. Green points fall below zero and correspond to green points in Figure 2.16.

this software a conservative assumption of 11% relative error was made (mean relative error for SFCs from ACRUISE-1 is 10.24% and it is largely driven by CO_2).

In the Origin Pro analysis there were three steps of post-processing needed before the CO_2 and NO_x data could be integrated. Both the post-processing and integration were done in Origin Pro 2020. First, to remove at least part of the noise in the CO_2 data a low pass filter (0.14 Hz) was applied. This allowed clear identification of the beginning and end of the peak. The frequency was chosen to maximise the noise reduction without distorting the peaks significantly. It was not necessary for NO_x.

Then background was removed. For CO_2 Asymmetric Least Squares Smoothing (ALS) baseline was used and for NO_x it was assumed to be zero. Origin 2020 allows adjustment of 4 parameters, which were set as follows:

- Asymmetric factor (0-1) = 0.001 (weight of points above baseline; closest possible to zero since only positive peaks are of interest)
- Threshold (0-1) = 0.1 (ratio of peak-baseline to background-baseline critical distance, which determines the percentage of the points above the baseline; established visually)

- Smoothing factor (2-9) = 5 (the larger the smoother the baseline; compromise well fitted baseline and bias introduced by wider peaks on case to case basis)
- Number of iterations = 30 (maximised to ensure best fit for longer data frames)

Origin's algorithm tended to include the negative 'dip' in front of the peak, which is often additionally amplified by the low pass filter. The origin of this 'dip' was impossible to establish, since Origin Pro does not disclose the full algorithm. Hence, negative values were zeroed to improve the consistency of peak detection.

Peak height threshold used to determine peaks which can be reliably integrated, was 1.2 ppm for CO_2 (processed), which is 3 times the uncertainty of the instrument. Since NO_x had by far the best peak to noise ratio and other instruments are the limitation, no threshold was used.

To account for different response of each of the instruments, the integrated area under the peak was used instead of peak height. Additionally, NO_x integration had to be adjusted to account for the poor resolution of other species, *i.e.* if two peak were overlapping in CO_2 but not in NO_x they were still integrated together for NO_x. For CO_2, the peak detection was consistent, however poor peak to noise ratios and high limit of detection meant that CO_2 could not be integrated for over half of the identified plumes in this method as well.

2.4.5 Quality and uncertainty

Once peaks are matched, SFCs are calculated (Section 2.3) and the quality control process starts. Any suspicious SFCs are inspected. In the case of ACRUISE-1, the frequent cause of too high SFCs is a situation when the algorithm integrates an SO_2 peak with its entire 'tail', while for CO_2 the tail is either below the integration threshold or below the limit of detection all together. The tail usually comes from a non perpendicular pass through a plume. In that case the peak is deleted, because it's clearly a problem of inadequately low quality of CO_2 data. Similarly, in a few cases, two CO_2 peaks had to be summed to reflect one wider SO_2 peak, which applied for more plume following type of transects. An example of difference between plume transecting and plume following peaks is shown in Figure 2.18.

The improvement of data quality in the second campaign, meant there were very few cases of this kind. However, if a CO_2 peak had no equivalent in SO_2 or the SO_2 peak was too small to integrate, the SFC was assumed to be zero (as per Kattner et al. [35]). This is because the lowest SFC calculated was 0.0042% which rounds up to 0.00% hence this is assumed to be the lowest measurable SFC. The opposite situation, i.e. when there was no CO_2 peak, but there was an SO_2 one, was the only case when CO_2 peak gets reintegrated in order to quantify the SFC. This exception was made because such rare situation usually results from highly variable CO_2 background, which can be better captured when taking a smaller part of the data series. There were however cases of rejecting outliers if it was clear that the come from plume following peaks that were not correctly captured by integration, like in case of Mindoro plume in flight C265. See Figure 2.19.

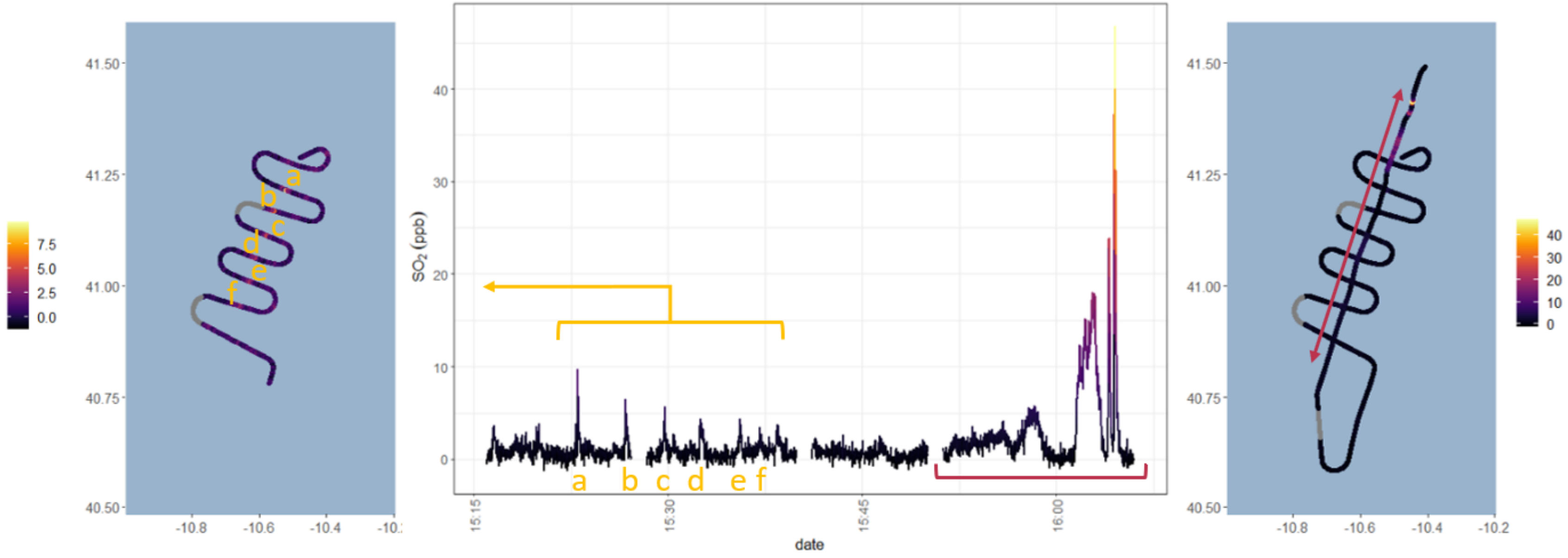

Figure 2.18: Comparison of peaks originating from plume transecting (yellow) and plume following (pink) on example of SO$_2$ emissions of Max Jacob, C182.

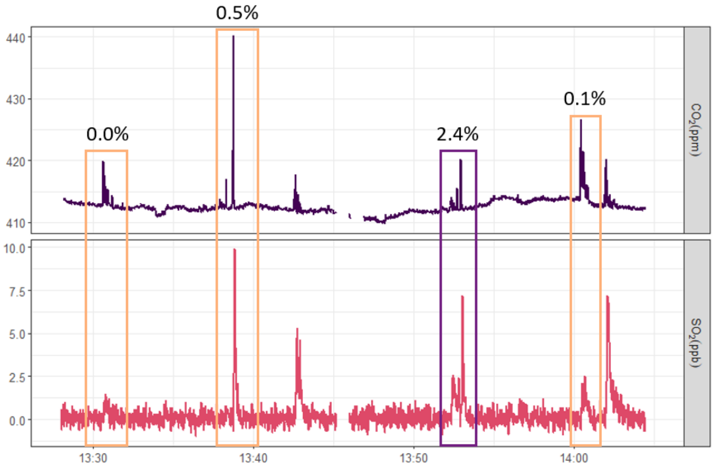

Figure 2.19: Plume outlier rejection on example of crude oil tanker Mindoro, C265. Even though the peak marked in purple passed initial QA/QC it was inspected in detail when it showed SFC value very different to other passes through Mindoro's plume. It was concluded that the integration of a plume following peak was incorrect in this case, since other peaks (in orange) yielded consistent values.

Sources of uncertainty for SFCs are:

- **Plume choice bias**, i.e. not being able to measure smaller ships and not being able to quantify smaller plumes. This is further described in Section 3.5.3.
- **Measurement uncertainty**, origination from instrument and calibration standard uncertainty.
- **Integration uncertainty**, in this case related mainly to how well the peak was identified.
- **SFC calculation uncertainty**, originating from assumptions made in Section 2.3.
- Unknown random and systematic error contributions that have not been captured by any of the above.

Measurement uncertainty is characteristic for each instrument and propagated in the trapezoidal integration step of the algorithm, as described by Batten [81] and implemented by Lacy [79] in `acruiseR` package.

All instrument uncertainties were summarised in Table 2.1. Visual explanation of the instrument uncertainty propagation through trapezoidal approximation is shown in Figure 2.12. Since every point of the peak has its uncertainty it could well be shorter or taller by that uncertainty affecting the area of the trapezoid underneath. Hence, for each trapezoid in a peak the extreme areas are calculated - smallest for both points being in the bottom of the uncertainty bracket and biggest for both points being in the top of the uncertainty bracket. The difference between the smallest and largest possible peak is the uncertainty bracket. In this case it is symmetrical since the individual uncertainties are symmetrical. Asymmetry in the quoted SFCs is introduced by possible underestimation due to sulphate conversion.

Integration uncertainty depends on the threshold b and how well really the beginning and end of peak was defined. This is difficult to quantify due to lack of a better method available for the project. In Section 2.4.3 results for one flight were compared with results obtained using Origin Pro, however it is debatable if Origin Pro is a better, more objective method.

SFC calculation uncertainty assumes all sulphur is emitted as SO_2, however up to 6% [75] might be converted to SO_4 hence there is a positive uncertainty of 6% applied to all values.

No validation experiment, such as a controlled release or intercomparison with direct exhaust measurement was performed for the ACRUISE project. Even though such validation is not essential it would help a lot in establishing the overall uncertainty and ensuring no systematic error went unnoticed. There is no established methodology for this kind of measurements and it is likely the only data set of this kind, hence it is a shame such experiment was not conducted.

Additionally, in each campaign there are ships for which **multiple passes** were suitable for quantification. As already discussed in Section 2.3, there is certain level of SO_2 conversion to SO_4, but it can be assumed to be constant [34] since only fresh plumes are integrated, as shown by Yu et al.[75] in previous work on ACRUISE-1 dataset. Hence, it could be assumed that all the calculated SFCs should be the same for each ship during one flight. However, this is not always the case, either because of the method or because of wrong assumptions. So, if multiple passes are available for a ships within a given flight the range of values is quoted.

2.4.6 Peak height dependence

Initial data analysis showed a trend of higher peaks (not necessarily greater) are yielding higher SFCs. This kind of dependence is not trivial to capture due to varying conditions during each flight and and possible differences between ships. Hence, multiple passes through the same plume were analysed. In cases of more than 10 SFCs York regression was used to exam the relation between peak height and SFC value. 10 SFCs is an arbitrary number that is certainly not ideal for any statistical analysis, however the dataset is limited and an attempt with a caveat is better than no attempt at all. Only Anthem of the Seas had more than 10 SFCs.

Regression aims to estimate statistically the relationship between dependent (y) and independent (x) variable. Ordinary least squares regression (OLS) is a popular linear regression model. It aims to minimise the sum of squares of the differences between the measured and modelled linear function. York regression, which was originally developed by Derek York [83], is also a linear model. The main difference is that York regression accounts for both x and y errors (see Equation (2.9) [84]) while OLS assumes x bears no error. In case of the SFCs and peak heights both bear an uncertainty hence York regression is more suitable.

$$S = \sum_{i=1}^{N} \left[\omega(X_i)(x_i - X_i)^2 - 2r_i\sqrt{\omega(X_i)\omega(Y_i)}(x_i - X_i)(y_i - Y_i) + \omega(Y_i)(y_i - Y_i)^2 \right] \frac{1}{1 - r_i^2} \tag{2.9}$$

where S is the regression, X_i and Y_i are observed dependent and independent variables, x_i and y_i are their regressed equivalents, $\omega(X_i)$ and $\omega(Y_i)$ are inverse standard deviations of the measurement errors of each variable, and r_i is correlation coefficient between measurement errors in both variables.

2.5 Influence of data quality on peak integration

At this point there arises a question - does instrument resolution and signal to noise ratio affect the SFC calculation? Comparing the quality of CO_2 measurements between ACRUISE-1 and ACRUISE-2 it seems unlikely that they would yield comparable results. Below are shown two case studies in which multiple measurements of the same species with different resolutions are available.

2.5.1 Methane-To-Go-Poland

Methane-To-Go-Poland is a project completely unrelated to ACRUISE and focusing on methane emissions from Polish coal mines using a HELiPOD helicopter towed probe shown in Figure 2.20. It was used in this work to demonstrate that the peak integration software can be applied to airborne data set acquired in completely different way and check if, and to what extend, the universal instrument quality influences the peak integration. The setup was deployed in the Upper Silesian Coal Basin, which is among Europe's most active areas for coal mining. Mine ventilation shafts were targeted for methane emissions with up- and downwind runs from 0.5 to 5 km away from source. The flights took place at different times of day and shafts were revisited to account for diurnal activity patterns and meteorological conditions.

Figure 2.20: DLR's helicopter towed probe HELiPOD during take off.

HELiPOD is a helicopter probe developed by the Technical University of Brunswick and ran during the campaign with DLR Institute of Atmospheric Physics. The probe is flown as a sling load on a rope below the helicopter with no electric connection to the helicopter, hence it does not need to be certified, making it a very flexible and adjustable measurement platform. It was equipped with a range of sensors, however, for interest of this work the most important instruments are Picarro and Li-7700, both measuring methane. Comparison between the peak shape and quality, both in 1 Hz, is shown in Figure 2.21.

Only downsampled to 1 Hz Li-7700 data was available at the time of writing this work due to data handling issues. However, it still was used to demonstrate difference between noisier and smoother data. Peaks were integrated and matched exactly the same way as described in Section 2.4.

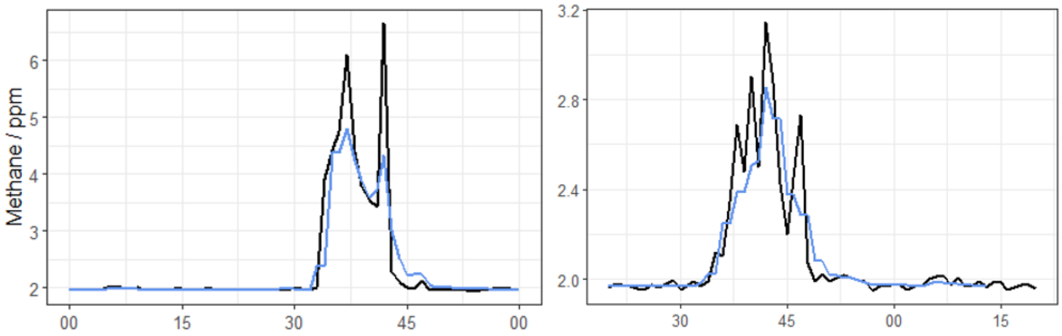

Figure 2.21: Methane-To-Go-Poland Li7700 (black) and Picarro (blue) CH_4 peak comparison at 1 Hz (Li-7700 downsampled from 40 Hz).

2.5.2 SO_2 comparison for ACRUISE-3

During ACRUISE-3, three SO_2 measurements were available: FAAM's core Thermo 43i SO_2 (1Hz, struggling), custom built SO_2-LIF (5 Hz) and CIMS SO_2 (4 Hz). Detailed description of each of these instruments can be found in Section 2.1.2. SO_2-LIF is still an instrument in development stage and the data used here is preliminary, with no zeros applied. The flight chosen for the comparison is C286. All three SO_2 measurements were treated the same way, as described in Section 2.4. Same baseline parameters and peak thresholds were used as well, see Table A.4.

Chapter 3

Results: Gaseous emissions from ships

3.1 ACRUISE outcomes summary

3.1.1 Data summary

ACRUISE SO_2, CO_2 and CH_4 data is summarised in Appendix A.1 as time series for each flight. CO_2 and SO_2 are also shown in terms of their longitudinal distribution in Figures 3.1 to 3.3. Only data under 500 m of radar height was included to focus on actual ship environment rather than transits, profiles or in-cloud runs.

ACRUISE-1 can be divided into four distinct areas longitude wise: South West approaches (SW), Portuguese coast shipping lane (PTL), Portuguese coast open waters (PTO), English Channel (EC). The majority of the flights took place off the Portuguese coast. The one flight in EC (C191) was very short with westerly wind dominating, while on the two flights in SW (C179-80) there was mixture of westerly and southerly wind. This meant reasonably low land influence. For the Portuguese coast flights, days without easterly wind were mostly chosen to avoid high background from the land. Even though easterly wind could not have been entirely avoided, northerly wind was prevalent. The majority of the peaks in CO_2 is in PTO and PTL as shown in Figure 3.1a and the background varies, but is lower than in SW (influence of air from Ireland). The SO_2 baseline is more stable as expected (see Figure 3.1b, however there is a slight elevation in EC. This however might be disproportionately driven by targeting MSC Mirja during the short time at the task area.

ACRUISE-2 can be divided in two areas in terms of longitudinal distribution: EC and SW with Bay of Biscay (BB) which overlap. A variety of wind directions were observed due to less predictable weather patterns in September/October in South England compared to July in Portugal. Easterly winds came from the land (French side) and in EC northerly wind also came from land, but this time British side. As demonstrated in Figure 3.2a, it is quite clear across the ranges that CO_2 background is higher for N and E winds than for W winds, which especially in BB bring clean oceanic air. Flight C263 (marked in orange) really stands out due to its very high background caused by slack NE wind and buildup of a mixture of shipping and land pollution. On the day the buildup was visible to human eye as a faint fog-like layer over the channel, with visibility sufficient for low level flying yet affected the aerosol. Interestingly, the pollution buildup can also be seen in SO_2 (Figure 3.2b), which is really the only representative case of elevated SO_2 background (C191 is a small sample) observed during all 3 campaigns. In general, SO_2 distribution shows that most of the higher concentration SO_2 peaks were observed outside of the EC SECA zone.

Finally, ACRUISE-3, the campaign with only four flights, all in BB or SW, brought no surprise. N and S winds dominated, SO_2 background remained low and stable (see Figure 3.3b), while CO_2 background varied more (see Figure 3.2a).

To summarise all 3 campaigns, the background SO_2 concentration is rather stable and averages at 0 ppb as expected. The situation of CO_2 is more complicated due to the background being more variable and influenced by emissions from land, especially in coastal areas.

3.1.2 Ships statistics

Across the three campaigns over 270 ships were measured: over 100 during ACRUISE-1, 143 during ACRUISE-2 and 30 during ACRUISE-3. The first campaign should be treated separately since only 48 ships were identified and the overall number is estimated to over 100 based on the number of peaks that came from unknown, randomly encountered ships. Unfortunately significant part of the peaks (mostly the unidentified ones) were not suitable for integration due to poor quality of CO_2 data. The recognised ships might have a bias to vehicle carriers due to their very characteristic appearance and memorability (compare Figure 3.4d and Figure 3.5d). The distribution of age (Figure 3.4a) is unlikely to be affected by identification bias, but the gross tonnage (Figure 3.4b) might have been impacted (albeit not obviously), since it easier to recognise big ships. The main comparison drawn between ACRUISE-1 and ACRUISE-2/-3 is the percentage of ships with scrubbers - 4% for the former and 22% for the latter. There is no readily available data on fuel type used by a ship at specific time, especially that ships can alternate between different fuels. Hence scrubbers are just one of the paths that can be taken to reduce emitting sulphur yet the increase in their popularity in the sampled ships from pre- to post- regulation campaigns is clear.

The ACRUISE-2/-3 data set reflects well the sample of ships present near British and French coasts. According to the Review of Maritime Transport 2021[85], the majority of ships sailing all over the world are bulk carriers (43%), oil tankers (29%) and container ships (13%). Currently oil tankers are the fastest growing fleet. In case of ACRUISE-2/-3 (see Figure 3.5d) the dominant type were container ships (34%), followed by crude oil and chemical tankers (24% together) and bulk carriers (10%). Hence the data set

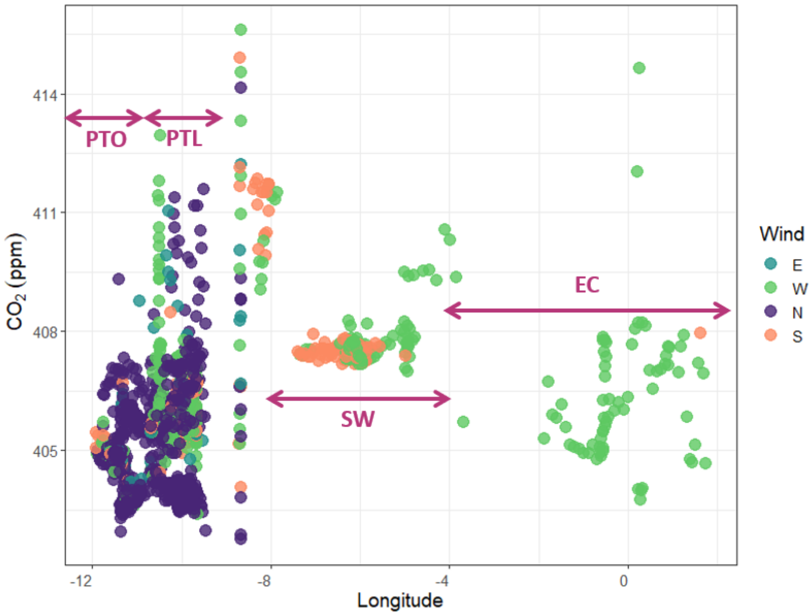

(a) ACRUISE-1 CO$_2$ distribution

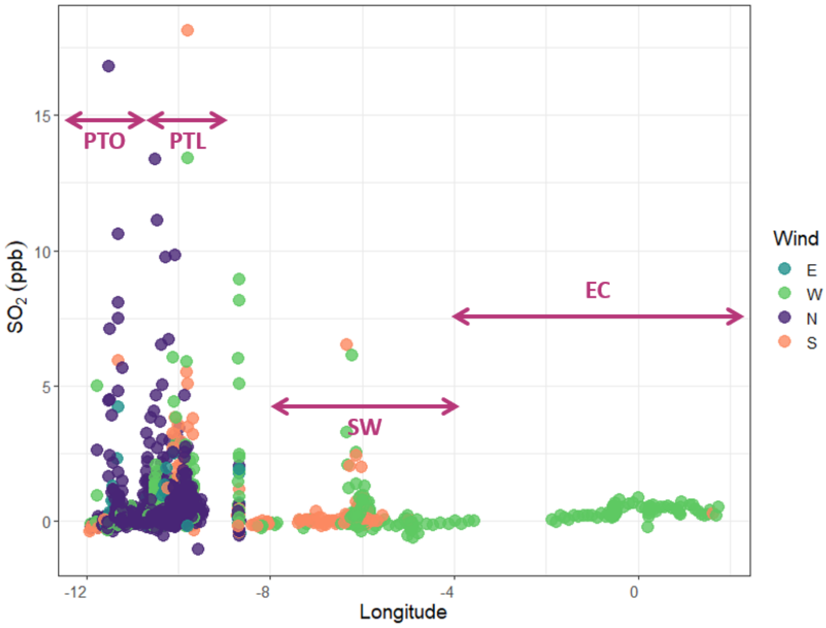

(b) ACRUISE-1 SO$_2$ distribution

Figure 3.1: ACRUISE-1 longitude distribution of 1 min averages of all flights time series coloured by wind direction, where SW - South West approaches, PTL - Portuguese coast shipping lane, PTO - Portuguese coast open waters, EC - English Channel.

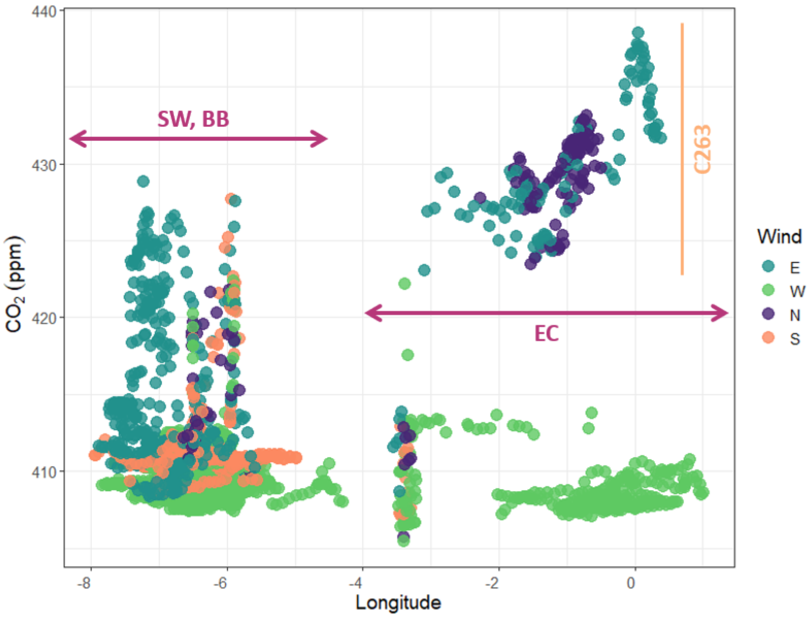

(a) ACRUISE-2 CO_2 distribution

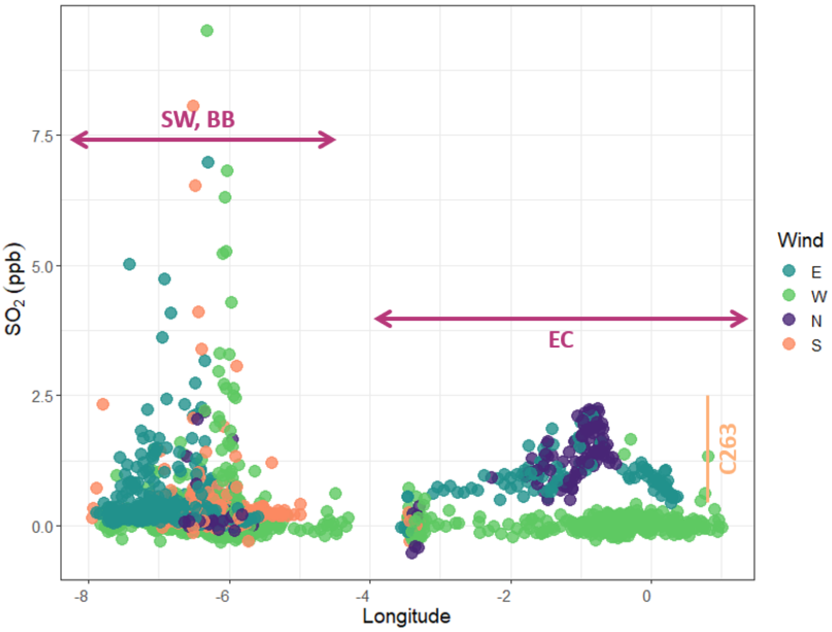

(b) ACRUISE-2 SO_2 distribution

Figure 3.2: ACRUISE-2 longitude distribution of 1 min averages of all flights time series coloured by wind direction, where SW - South West approaches, BB - Bay of Biscay, EC - English Channel. Flight C263 stands out due to slack wind on the day leading to increased background.

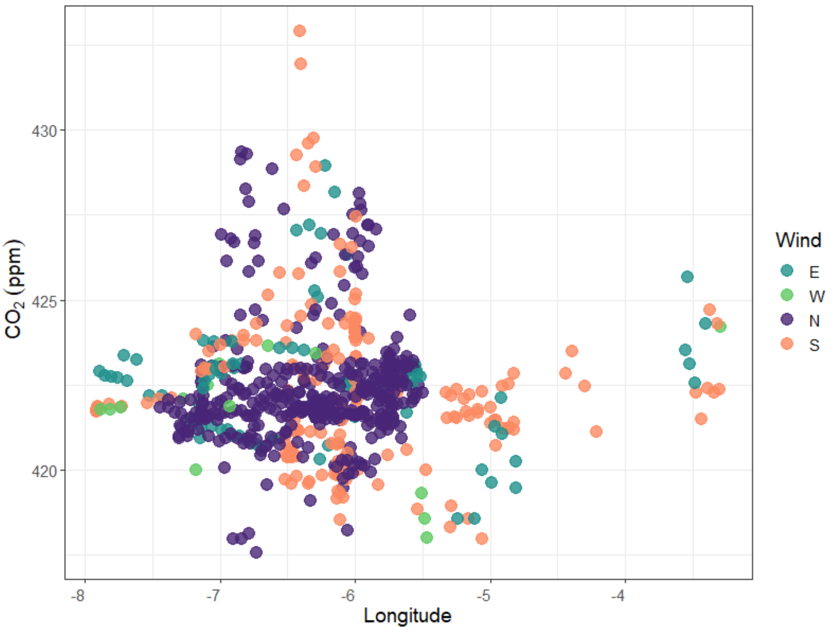

(a) ACRUISE-3 CO_2 distribution

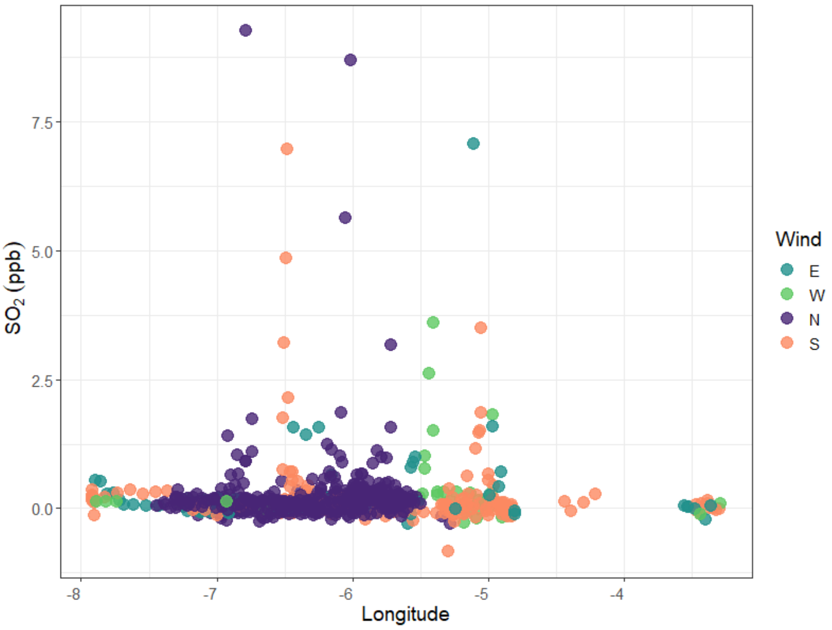

(b) ACRUISE-3 SO_2 distribution

Figure 3.3: ACRUISE-3 longitude distribution of 1 min averages of all flights time series coloured by wind direction, most of data falls in South West approaches and Bay of Biscay.

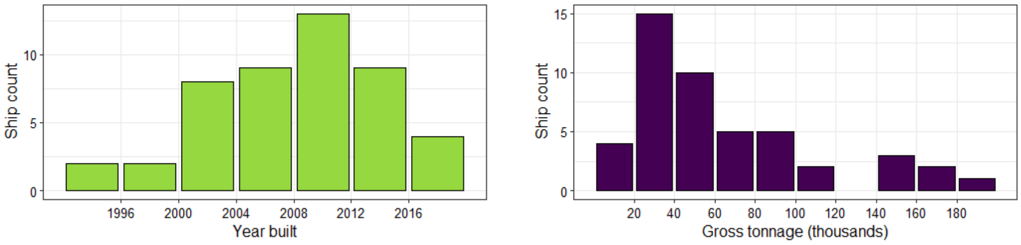

(a) ACRUISE-1 ship year of building distribution.

(b) ACRUISE-1 ship gross tonnage distribution.

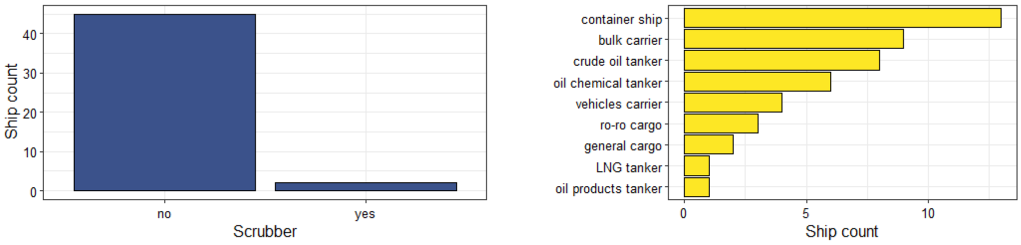

(c) ACRUISE-1 scrubbing technology presence.

(d) ACRUISE-1 ship type distribution.

Figure 3.4: ACRUISE-1 ship statistics

is comparable yet noticeably different from the global averages, even bearing in mind the ships were not chosen at random. The dominance of container ships comes from their large size and tall stacks that make them excellent target to sample. Meanwhile, fishing vessels were avoided all together due to high numbers of sea birds following them.

Ship population is also aging continuously [85], with the global average ship age being 22 years! This number however needs to be put into context. For bulk carriers the average age is 11 years, for oil tankers 20 years and for container ships 13 years. For so-called ‘developed economies’ the average ship age is 21 years, while for so-called ‘least developed economies’ 29 years. If the average is taken for dead-weight tonnage rather than number the age decreases in all cases, because ‘normal’ ships become bigger and more mega-vessels are being built. So the average age by weight is 12 years for all ships globally, 10 years for bulk carriers and container ships, 11 years for oil tankers.

The average age by number of the ships sampled during ACRUISE-2/-3 is 10 years, so considerably younger than global average, which possibly relates to the relatively large size of ships sampled (2500 t minimum, 57 300 t median)[*] and regional characteristics. The distribution of age and weight (Figures 3.5a and 3.5b) is however reasonably wide, bearing in mind size constraint and non-random sampling.

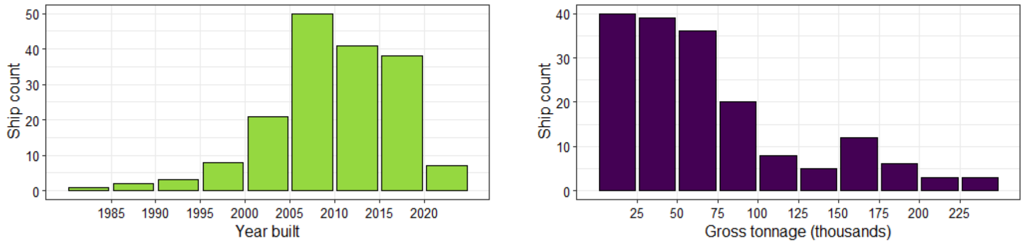

(a) ACRUISE-2/-3 ship year of building distribution.

(b) ACRUISE-2/-3 ship gross tonnage distribution.

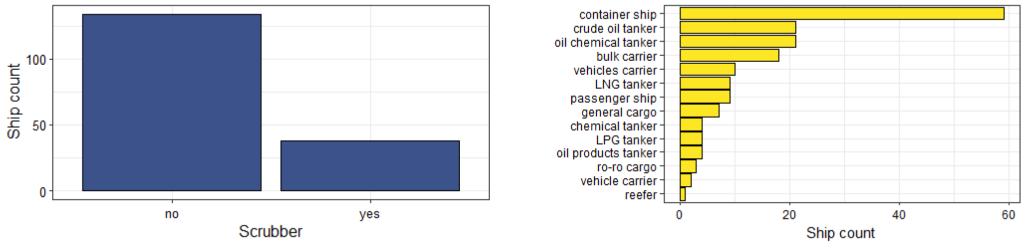

(c) ACRUISE-2/-3 scrubbing technology presence.

(d) ACRUISE-2/-3 ship type distribution.

Figure 3.5: ACRUISE-2/-3 ship statistics

3.2 ACRUISE-1

3.2.1 Data quality

Differences in data treatment between campaigns are present due to changes in data quality. For ACRUISE-1 there are barely any CO_2 peaks with no matching SO_2 peak and these are kept (SFC being equal to 0%). However

---

[*] As the technology progresses ships are getting larger, hence most of the big ships sampled tend to be built in the last 10-15 years. Ship size, or more precisely stack height is a limitation due to the minimal altitude BAe-146 can fly on and sensitivity of the instruments. A small weak plume is impossible to quantify. Drawing a statistically significant comparison between the >20 year old ships and younger ones was be impossible due to too few old ships sampled.

there are several SO_2 peaks with no match in CO_2 (see Figure 3.6). For ACRUISE-2 and -3 these would be kept and CO_2 data would be re-analysed with different parameters (successful with one exception). The poor quality CO_2 data in 2019 makes reanalysis impossible and using an estimate of minimal integratable CO_2 peak in case of this bad signal to noise ratio would introduce bias to the data, hence these peaks are rejected. Moreover the reduced quality of CO_2 data might lead in some cases to overestimation of the SFC values. All flight tracks are showed in Figure 3.7.

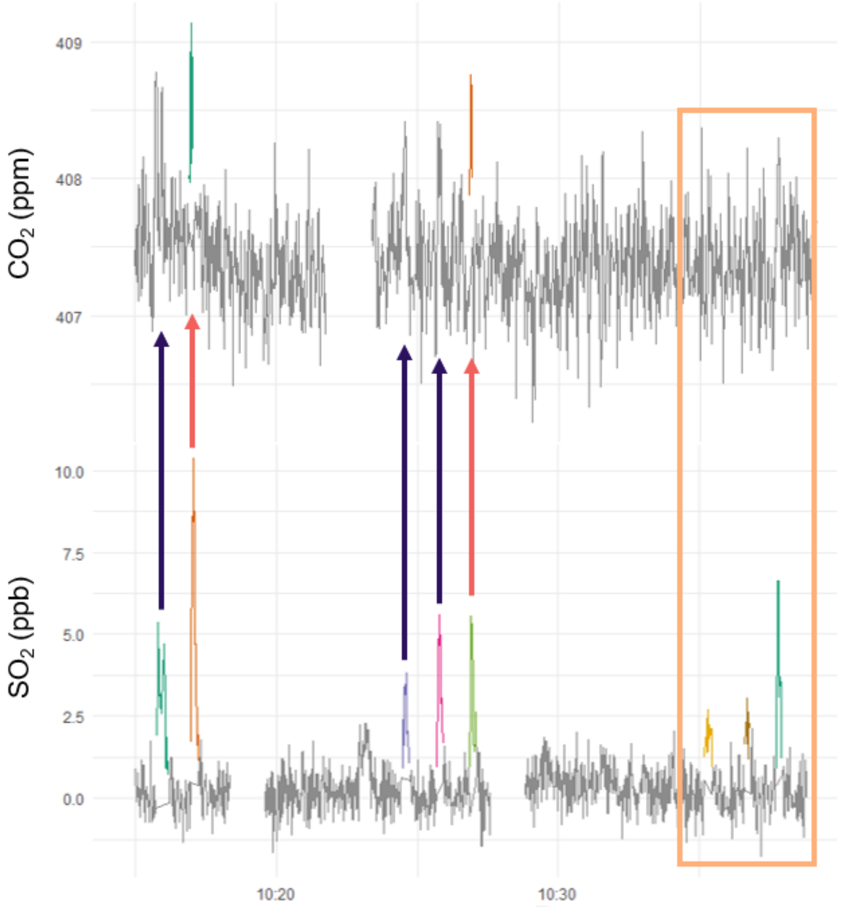

Figure 3.6: ACRUISE-1 example of critical difference in LOD between SO_2 and CO_2. Red arrows indicate where SO_2 has integratable equivalent in CO_2, purple where there is visible peak but it does not pass the integration threshold. Orange box shows SO_2 peaks that are reasonably well resolved , but their equivalents in CO_2 are not even visible in the noise.

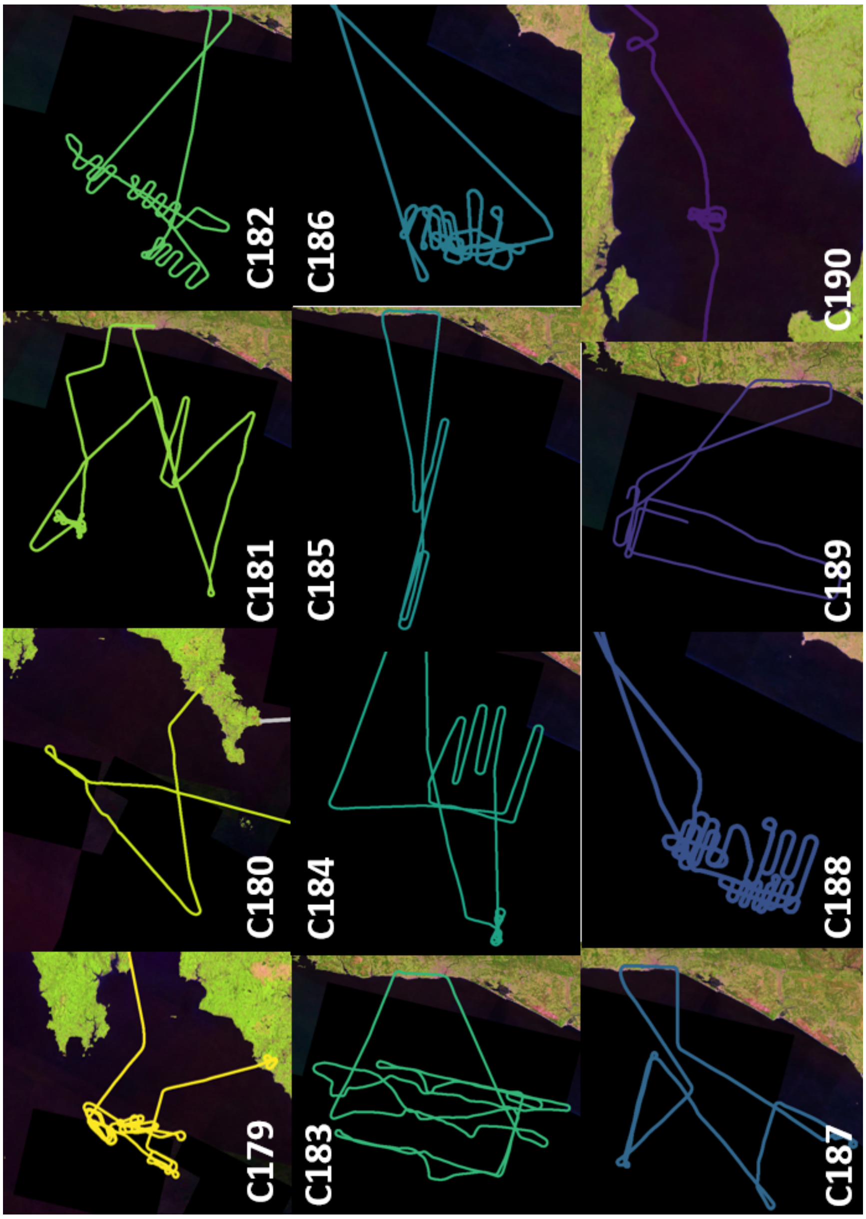

Figure 3.7: ACRUISE-1 individual flight tracks.

3.2.2 SFCs overview

Overall 48 SFCs from 21 ships were successfully derived from ACRUISE-1 data set, as shown in Figure 3.8. All peaks suitable for integration were successfully assigned to specific ships, however due to low quality of CO_2 data there were a relatively high number of plume transects that were not suitable for integration. The only ship which was encountered during multiple flights was the container ship MSC Mirja. It was measured in Portuguese coast shipping lane (PTL) and English Channel (EC) showing SFC reduction from 2.51% - 3.45% to 0.00% - 0.13% (all uncertainties can be found in Appendix A.4). Since at the time the ship was not fitted with a scrubber it is safe to assume, that it changed to cleaner fuel upon entering SECA. Most ships adhere to the limits, only 4 SFCs exceed the non-SECA limit of 3.5%. As discussed in Section 3.5.2, poor data quality might impact the value, hence this data cannot be used to make a case against these ships.

Overall, ships outside of SECA averaged on 1.82% ± 0.20% SFC and the only ship in SECA - MSC Mirja, showed average of 0.08% ± 0.03%. The average for Portuguese waters was 2.33% ± 0.21% and for SW 0.92% ± 0.28%. These values are however affected by poor detectability of CO_2 plumes due to low quality data. This leads to underrepresentation of weaker plumes, which often yield in lower SFCs. Moreover most of the CO_2 peaks from ships emitting little to no SO_2 were below the threshold which disqualified them from further analysis. For this reason, the mean SFCs are likely overestimated.

Eagle Brisbane encountered in South West approaches of Wales (SW) during flight C179 and shown in Figure 3.9, is an interesting case. There were 3 peak sets in space of 15 min suitable for SFC calculation, in other cases CO_2 was insufficient quality. The two weaker plumes yielded 1.45% and 0.98%, while the stronger plume resulted in SFC of 4.41%. The snippet of data containing these peaks was reintegrated, but the values agreed within uncertainty, so it was not an error in peak picking. See Section 3.5.2 for

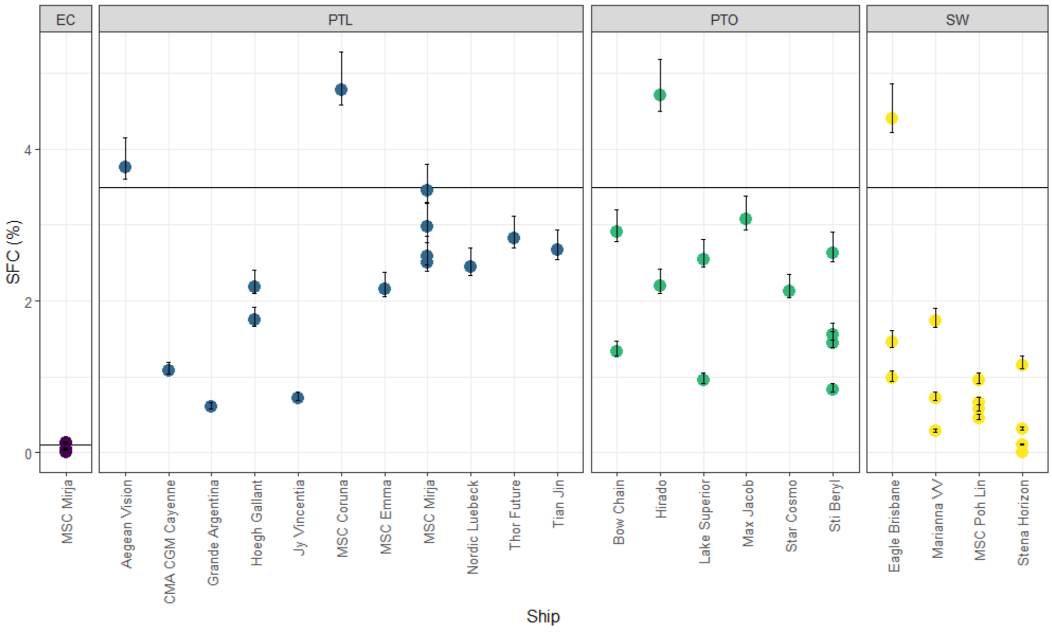

Figure 3.8: ACRUISE-1 SFCs, sea and ship, where SW - South West approaches, PTL - Portuguese coast shipping lane, PTO - Portuguese coast open waters, EC - English Channel. Black line shows IMO sulphur limits: 3.5% for non-SECA and 0.1% for SECA.

more detailed explanation. Another ship was Hirado, targeted in open ocean (PTO) during flight C186. Only two SFCs could be calculated and the were 2.20% and 4.71%. Again the higher concentration peak yielded higher SFC. In the case of the two ships encountered in Portuguese coast shipping lane (PTL), namely MSC Coruna (C187, 4.79%) and Aegan Vision (C183, 3.77%), only one plume pass was available.

In 2019 scrubbers were already implemented in some ships, however sadly only 2 SFCs from one ship represent the scrubber population, so no statistically sound comparison can be drawn here. Figure 3.10 shows SFCs distribution against year of production of ship with presence of scrubber indicated by colour. Ships identified during ACRUISE-1 show quite a good representation of older and younger ships (see also Figure 3.4a), hence here some comparison could be drawn. A first guess would be that older ships would emit more sulphur, however in reality there is nothing stopping the owner from using cleaner fuel or retrofitting a scrubber. In fact it turns out

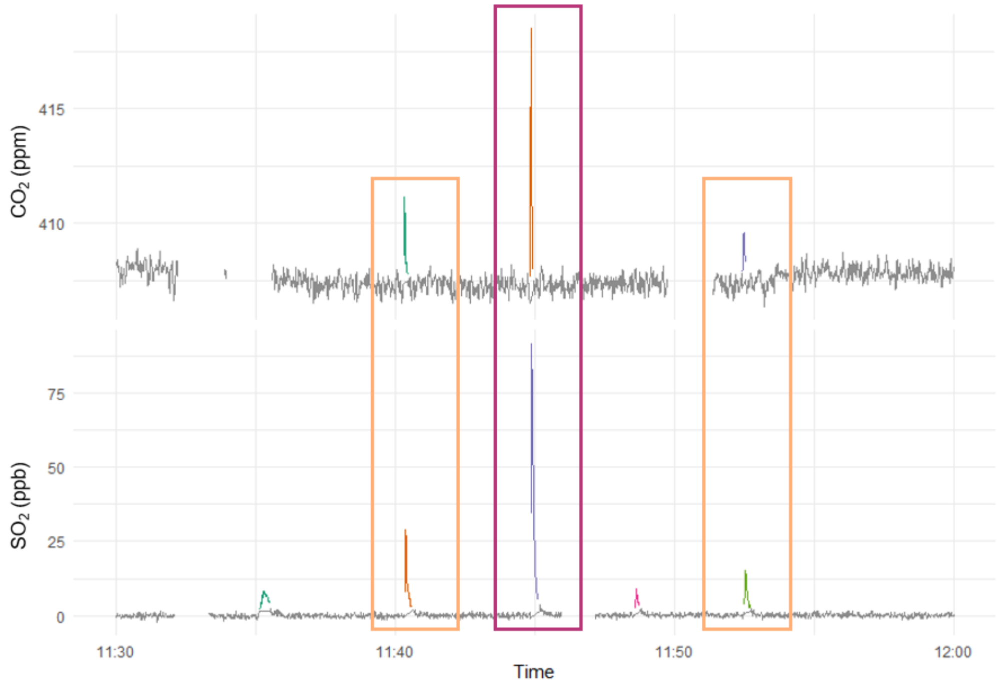

Figure 3.9: Eagle Brisbane three encounters suitable for SFC calculation (in rectangles), flight C179 (South West approaches). The highest peak is the one that exceeds the 3.5% non-SECA norm (in purple).

that it is the younger ships that exceed the 3.5% threshold. However, it is fair to make an assumption that ships built after 2016 when Marine Environment Protection Committee (MEPC 70) decided to implement IMO 2020 0.5% limit from 1st January 2020 [86], would be cleaner. This was not observed in 2019, which means they left all the upgrades for the last minute. Two targeted ships that showed no SO_2 (and sadly not enough CO_2 to quantify it) were BTG Eiger and Lake Superior. The former is a bulk carrier built in 2016, the latter is a vehicle carrier built in 2007, so showing no obvious trend.

Ship type and gross tonnage are also a potential factor in the sulphur fuel content, although SFC depends on fuel and scrubbing, not on type and size in itself. However, ship operators could possibly take these factors into account when making decisions on fuel and scrubber use. For example, cruise ships operators could invest more readily in cleaner fuels and scrubbers since they

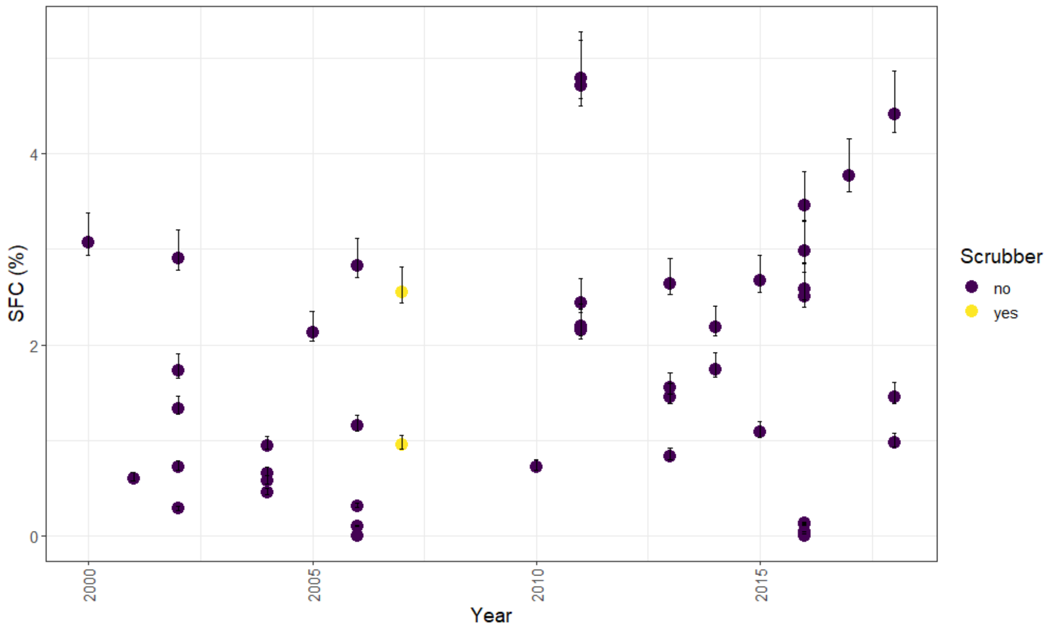

Figure 3.10: ACRUISE-1 SFCs, scrubbers and production year.

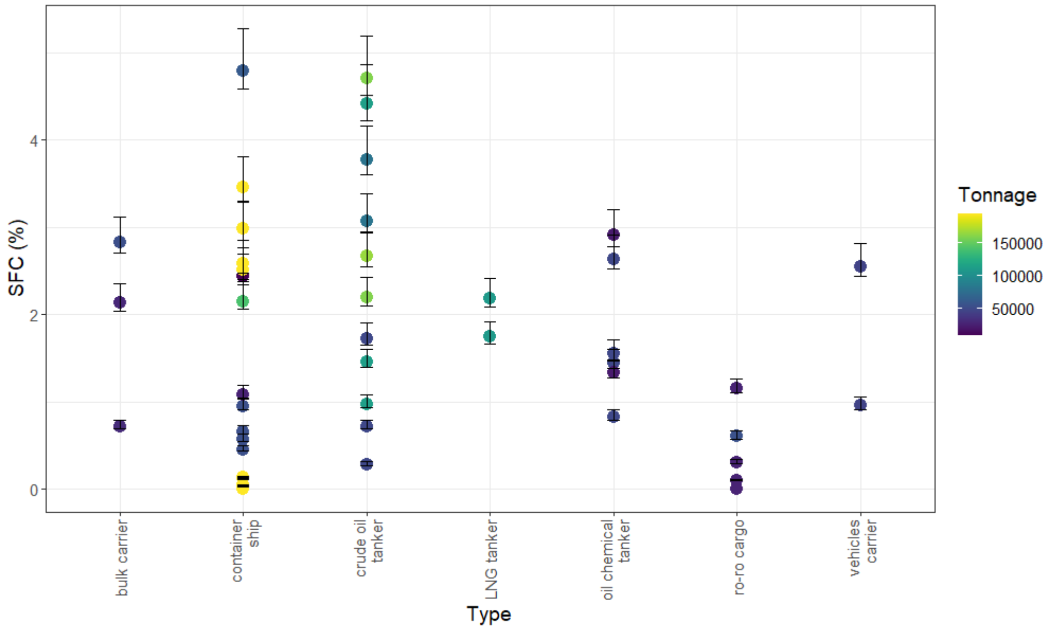

Figure 3.11: ACRUISE-1 SFCs, type and tonnage.

sail more along coastlines. However, as shown in Figure 3.11, there is no particular trend. Hence it can be concluded, that factors like age, tonnage or type are irrelevant for SFCs, but could play a role for a more detailed study of plume chemistry. Although, even then things like engine type, speed and actual load at the time (information not available for ACRUISE-1) are suspected to be more important, at least when it comes to general plume content.

To summarise ACRUISE-1 SFCs, they show that back in 2019 most of ships stuck to the rules and there is not much dependence on any of the analysed factors. More importantly though, this data set is an excellent case showing how speed of measurements can hinder such studies. It was not all bad and there was a large volume of background data collected that was very useful to the modelling part of ACRUISE project. It was also an opportunity to work on operational strategies and establish requirements for such fieldwork, so that the following campaign results in more useful data.

3.3 ACRUISE-2

3.3.1 SFCs overview

ACRUISE-2 data set showed a massive improvement in the quality of CO_2, which led to a much higher success rate in calculating SFCs. However, the lack of improvement in the SO_2 measurement means that the data quality difference problem remains, but this time SO_2 is the poorer quality species. From practical perspective, higher quality CO_2 is more important because it can be used as a plume indicator, especially when SO_2 is not present or very low. So, basically, at least it is possible to undoubtedly tell where the plume is. All flight tracks are shown in Figure 3.12.

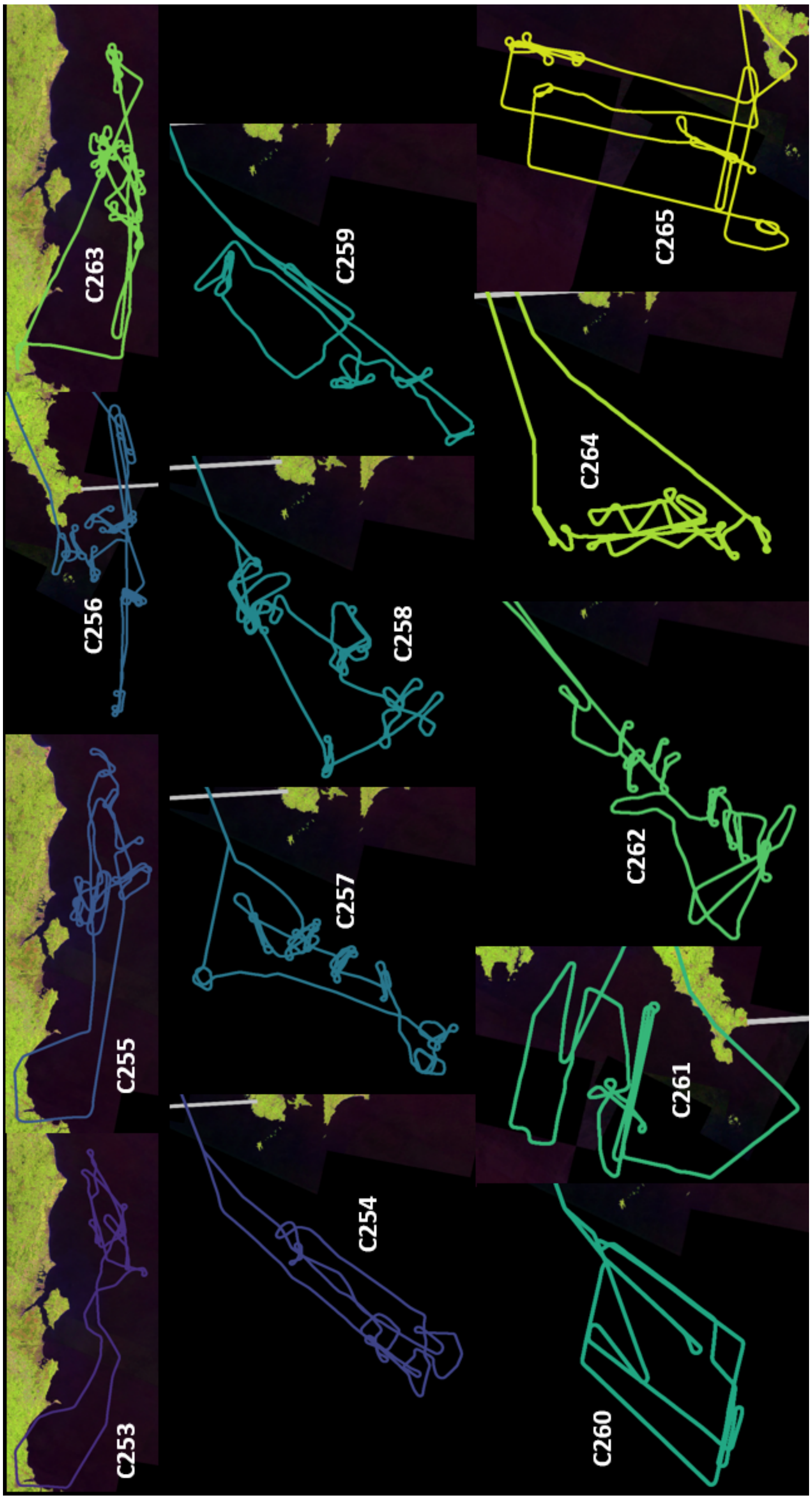

Figure 3.12: ACRUISE-2 individual flight tracks.

As in case of ACRUISE-1 (Figures 3.10 and 3.11) for ACRUISE-2 there are no particular trends relating to the year of manufacturing, scrubber presence, type or tonnage (Figures 3.13 and 3.14). However, comparing to ACRUISE-1 there were considerably more ships with scrubbers so at least the comparison between scrubber and presumably cleaner fuel can be made. Precisely 25 out of 82 identified ships had a scrubber fitted at the time of the 2021 campaign, compared to 1 in 22 during the 2019 campaign. It is fair to conclude that the method of lowering sulphur emissions does not matter in terms of adherence to the sulphur emissions limits. Further description of ships fitted with scrubbers can be found in Section 3.3.4. The age of the ships also does not seem to play a significant role, although it is worth mentioning that in ACRUISE-2 the oldest ships observed had actually low SFCs. When it comes to type, similarly to ACRUISE-1, ACRUISE-2 shows no particular correlation even though more types were observed. Tonnage was also not an important factor.

An overview of all the calculated SFCs from ACRUISE-2 matched with ships is showed in Figure 3.15. They are divided into three distinct areas: South West approaches, near Welsh coast (SW), Bay of Biscay shipping lanes and open water (BB) and English Channel SECA (EC). The reason why BB is not split into lane and open water is that BB lanes are nowhere as busy as PTL, so that division would be made on purely operational and not scientific ground. Most of plumes (precisely 180 out of 191) were attributed to specific ships, but there were some plumes that could not be matched to ship with sufficient certainty either because identification of the ship name in flight was impossible or because there were multiple ships the plume could have come from.

In the SECA the average SFC was 0.08% ± 0.03%, whereas out of the SECA 0.29 ± 0.04. Specifically 0.34% ± 0.06% in SW and 0.27% ± 0.05% in BB. The SFC reduction in the SECA is what was expected, however a more surprising observation is that SW (more coastal area) show slightly higher average

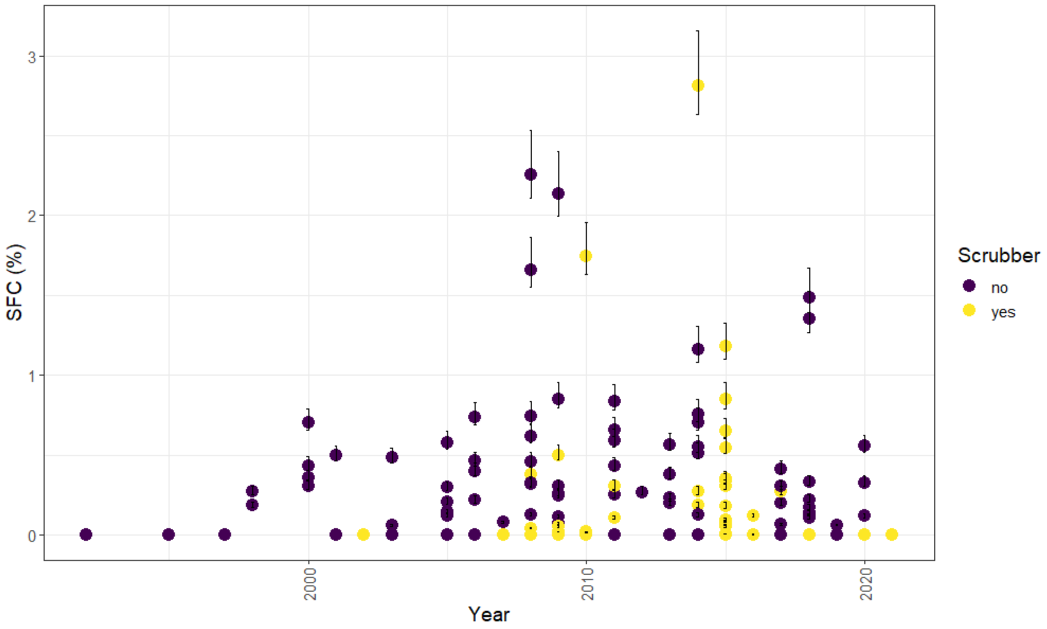

Figure 3.13: ACRUISE-2 SFCs, scrubbers and production year.

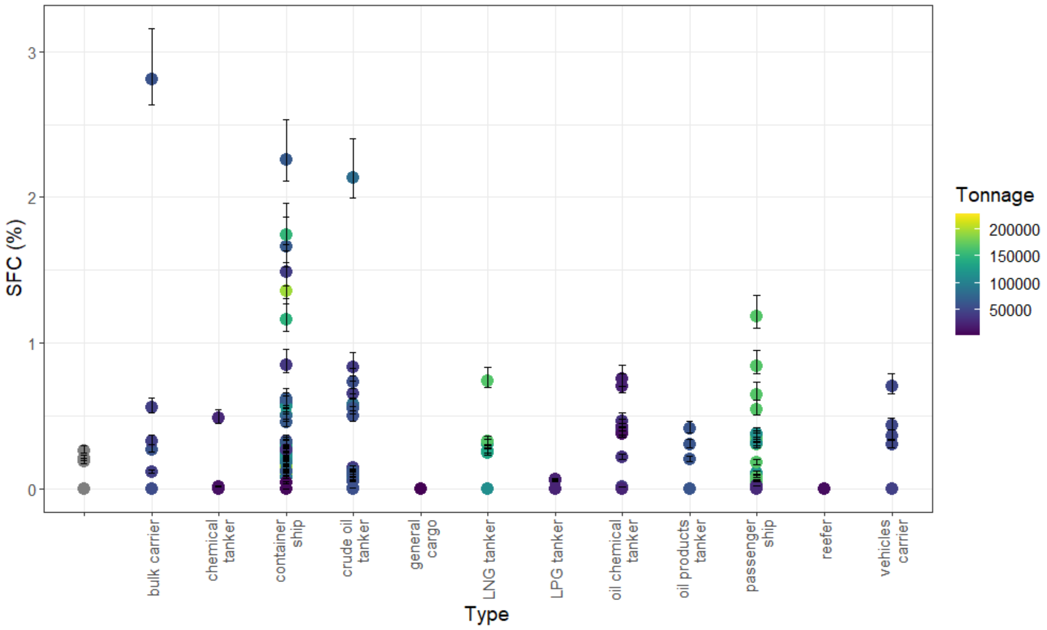

Figure 3.14: ACRUISE-2 SFCs, type and gross tonnage.

SFC than BB (open sea). However, it is not a large difference and it could be caused by not entirely representative sample, since during ACRUISE-2 specific ships were targeted mostly, rather than randomly encountered ones like during a number of flights in ACRUISE-1.

There were 34 SFC that exceeded the limits for their areas, i.e. 0.5% for SW and BB and 0.1% for EC. This is 18% of all SFCs calculated. These SFCs belong to 23 out of 82 ships that were quantified, i.e. 28%. This might seem like a high value, but an important disclaimer is that some ships presented a range of values and only some of them exceeded the norm, which is described in more detail below.

Another aspect worth mentioning is that ships in EC mostly adhere to the very strict 0.1% limit, but in SW at best stick to the 0.5% as shown in Figure 3.15. This clearly shows that introducing SECA does not necessary have positive impact on its wider surroundings, i.e. ship operators do not decide to expand the low emission policy to all neighbouring coastlines. That lack of effect was seen also during the 2019 campaign (see Figure 3.8). The conclusion is, that introduction of SECAs was a necessary mean to reduce the sulphur emissions and their expansion to other coastal areas could be the only way of reducing sulphur pollution (other than lowering the non-SECA to current SECA limit). The financial barriers mean that ship operators will rather switch between fuels or scrubbers to reduce cost than adopt SECA standards where it is not necessary. This is an understandable approach in the sad capitalistic world around us.

On the other hand, IMO 2020 made a noticeable difference in sulphur emissions. Less than 2 years in, there was no SFC above the previous norm. This cannot be said about 2019 dataset, where 4 out of 21 measured ships exceeded the 3.5% limit. So even if the ships do not always stick to the new regulations, they at least ceased to exceed the previous ones.

3.3.2 Multiple passes and encounters of the same ship

During ACRUISE-2 the ship targeting strategy changed and focused more on multiple passes through one plume then sampling as many ships as possible. That not only provided multiple SFC values for exactly half of the identified ships (42 out of 82), but also made the identification process considerably easier. In case of the ships that have only one SFC value calculated from their plume, the main reason was usually unsuitability of other plume transects. It is hard to comment on how accurate the SFC value is in their case since there is no comparison, hence let's leave them aside for now. Figure 3.16 shows all the ships that had more than one SFC calculated. The ships that show more than 0.5% range of SFC values are: Al Ghuwairiya, Anthem of the Seas, Cosco Shipping Scorpio, Maran Progress, MSC Madrid, MSC Oriane, Mindoro, Polar Argentina, Thalassa Elpida and W Kithira.

All together there were 10 cases of SFCs derived successfully for ships encountered during more than one flight or, in case of Anthem of the Seas (C256), in two different areas within one flight. In 7 of them it was part of the in and out of SECA study, when ships were targeted in BB or EC specifically so the next day they can be measured in the other area. The ships were: Eagle Le Havre, GWN 2, MSC Soraya, Straum, Tanja Star and Troodos Oak between C262 (BB) and C263 (EC) as well as MSC Branka during C254 (BB) and C255 (EC). APL Merlion was also encountered in and out of SECA, albeit accidentally, first time during C253 (EC) and second during C262 (BB). Final ship encountered twice was LNG Gaslog Georgetown both times in BB (C257 and C262). Anthem of the Seas (C256) has its own section (Section 3.3.3).

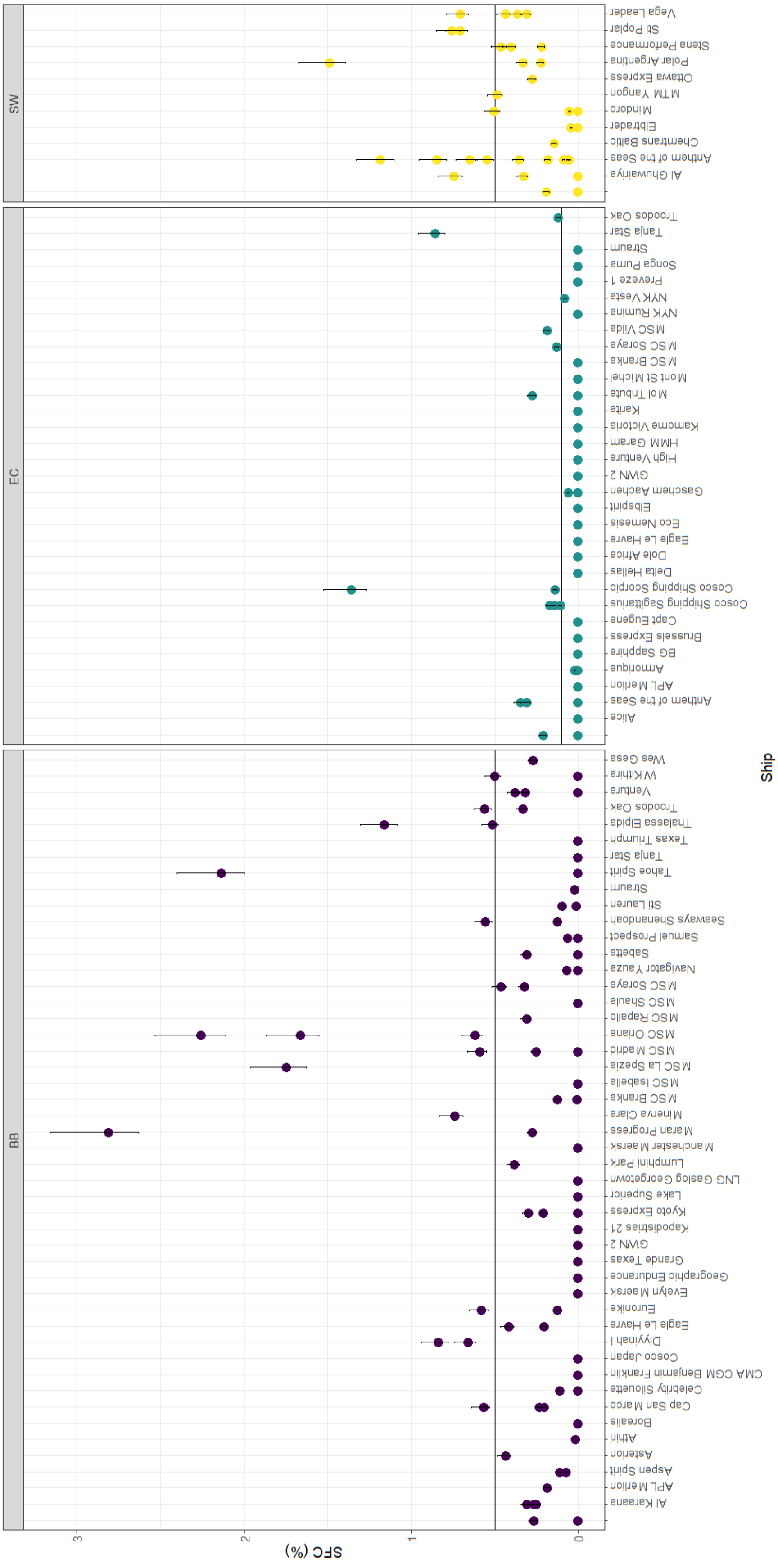

Figure 3.15: ACRUISE-2 SFCs, sea and ship, where SW - South West approaches, BB - Bay of Biscay, EC - English Channel. Black lines shows IMO sulphur limits: 0.5% for non-SECA and 0.1% for SECA.

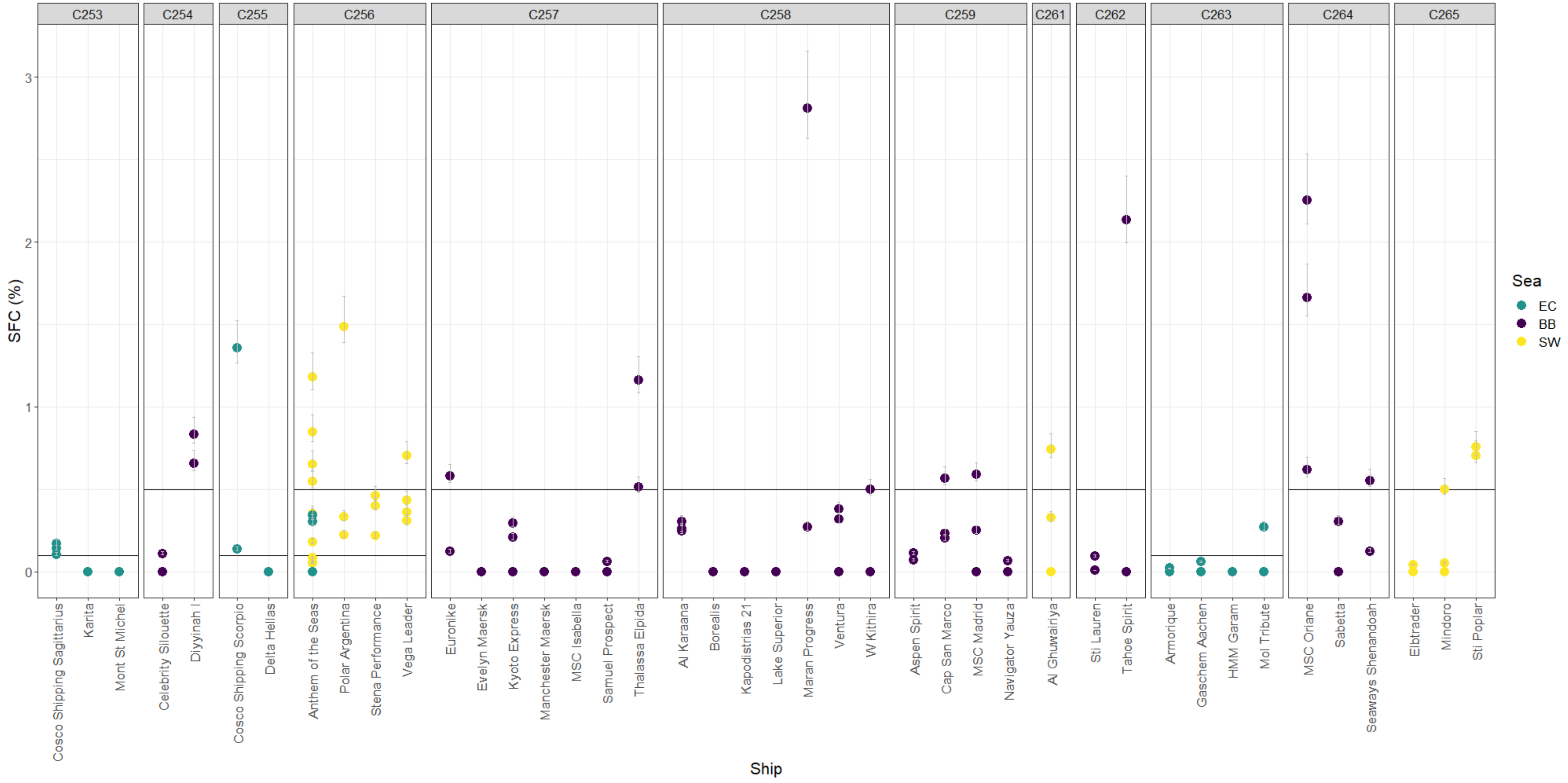

Figure 3.16: ACRUISE-2 multiple passes through the same plume, where SW - South West approaches, BB - Bay of Biscay, EC - English Channel. Black lines shows IMO sulphur limits: 0.5% for non-SECA and 0.1% for SECA.

In 5 out of 7 cases the SFCs out of SECA are higher than in SECA, in 2 the same (both 0% or nearly 0%) and in 1 case the SFC in SECA is higher then out. That case is Tanja Star and it is likely due to previously observed discrepancy between multiple SFCs derived during single encounter of a ship (see Section 3.5.2 for details). The only other possible justification for that would have been a failure of a scrubber, however Tanja Star has no scrubber fitted. On average revisited ships SFC was 0.13% ± 0.6% in SECA and 0.28% ± 0.06%.

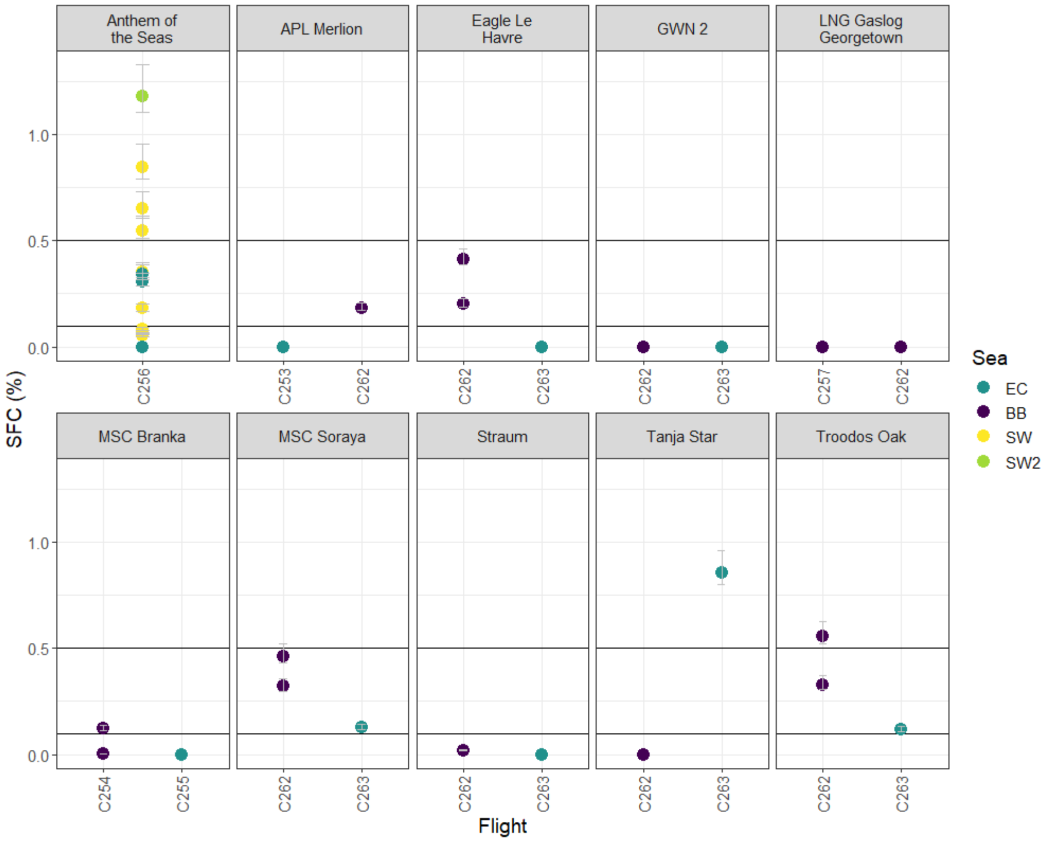

Figure 3.17: ACRUISE-2 multiple of the same ship during different flights, where SW - South West approaches, BB - Bay of Biscay, EC - English Channel. Black lines shows IMO sulphur limits: 0.5% for non-SECA and 0.1% for SECA.

3.3.3 Anthem of the Seas case study

As already mentioned passenger ship Anthem of the Seas was met 3 times during flight C256 and total of 13 SFC were calculated for it. The locations of the encounters are shown in Figure 3.18 with three distinct areas of encounter marked. The westmost encounter between Isles of Scilly and Cornwall yielded 8 out of the 12 SFCs. The ship was targeted multiple times due to good plume visibility, clear SO_2 peak and crew's enthusiasm. Second encounter was a coincidence after targeting Stena Performance right outside of SECA border. At that time it was decided to return to Anthem once it enters EC. Last encounter was in SECA and yielded 3 SFCs.

SFCs values span between 0.00% and 1.18%: 0.05% - 0.85% during first encounter, 1.18% in the random encounter and 0.00% - 0.34% in EC. This results possibly arise from issues wider described in Section 3.5.2. However, putting that aspect aside, following observations can be made. Since Anthem was fitted with a scrubber at the time of the encounter, it possibly uses relatively sulphur rich fuel and switch the scrubber on when entering emission control areas. The high 'transition' SFC value could hence be due to switching the scrubber on or changing its settings before entering EC. The average emission out of SECA is 0.44% ± 0.13% and in SECA 0.22% ± 0.11%. Even though the averages overlap within standard error, the maximal value was over twice lower for outside SECA. With current algorithm used for peak detection being the limiting factor it is hard to draw any robust conclusions from this case study.

3.3.4 Ships with scrubbers

Only ACRUISE-2 has sufficient number of ships fitted with scrubbers to analyse them, precisely 25 out of 82. Average SFC for ships with scrubbers was 0.16% ± 0.05% (0.00 - 2.81%) and for ships without scrubbers 0.29% ± 0.04% (0.00 - 2.25%). Hence both methods on average bring the SFC below

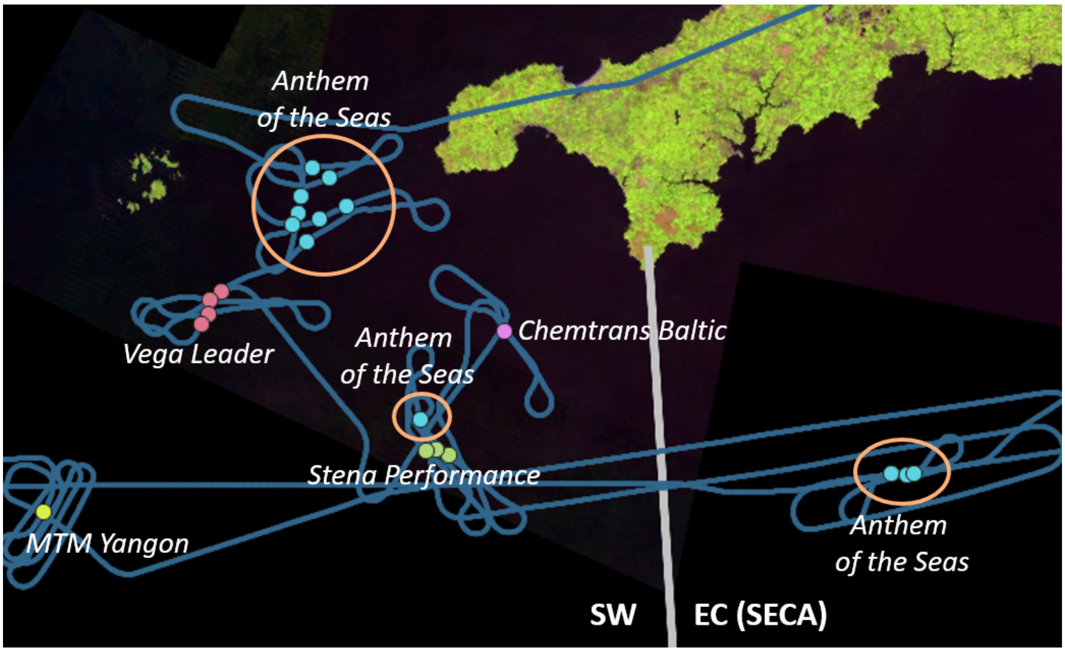

Figure 3.18: Anthem of the Seas (C256) SFCs positions indicated by blue dots with three distinct encounter locations circled in orange.

the 0.5% limit. However, taking a closer look at the ships with scrubbers might show if they change the scrubber settings in and out of SECA which they likely do for financial reasons. Figure 3.19a shows all the ships with scrubbers encountered during ACRUISE-2, including Anthem of the Seas which was encountered both in and out of SECA, as described above (Section 3.3.3). In EC the SFCs ranged from 0.00% to 0.34% averaging on 0.04% ± 0.02%, in BB from 0.00% to 2.81% averaging on 0.18% ± 0.09% and in SW from 0.00% to 1.18% averaging on 0.28% ± 0.09%. Overall SFCs calculated for ships out of SECA average on 0.21% ± 0.07%. Hence there is a 5-fold reduction of observed SFC in SECA compared to outside, which confirms assumption that scrubber setting are altered depending on regulations. It is worth mentioning that in all three areas there are both plumes exceeding the regulations and ones without quantifiable SO_2 peak. Figure 3.19b shows spatial distribution of plumes in three limit bands, i.e. below SECA limit of 0.1% between SECA and general limit of 0.5% and above 0.5%. There does not seem to be a clear dependence on area, however the sample might be too small to fully asses where and when the scrubber setting change happens.

3.4 ACRUISE-3

3.4.1 SFCs overview

ACRUISE-3 was the final airborne campaign of the project using hours leftover from ACRUISE-1 and hoping to find some LNG tankers and measure them offloading. all flight tracks are shown in Figure 3.20.

SFCs from each ship divided by the area of encounter are shown in Figure 3.21. Notably all the plumes yielding an SFC could be attributed to a specific ship, which shows the progress made in on board ship identification and logging. In BB as well as Atlantic Ocean (AO) the ships mainly stick to the sulphur limits, however in SW it again is less of the case, with three out of 7 ships exceeding the 0.5% limit. The average SFC for ships outside of SECA was 0.53% ± 0.15% - 0.12% ± 0.05% in BB and 1.00% ± 0.29% in SW. This shows again that the SFCs in SW are higher than in BB, with a caveat that mainly LNG tankers were targeted in SW during ACRUISE-3 which could affect the objectivity of the data. Unlike ACRUISE-2, where no ship exceeded the old limit of 3.5%, in ACRUISE-3 MSC Pilar reached the 3.5% within the uncertainty. Other ships remained below.

There were no flights in the SECA in this campaign, so no in/out of SECA comparison is possible, however most of the ships (12 out of 15) yielded more than 1 SFC. For most of the ships all the values fit within 0.5% range, which is assumed to be 'close enough' for the 1 Hz data. The only ship that resulted in wider range of SFCs is the unfortunate MSC Pilar encountered during C285 (0.79 - 3.43%). Multiple encounters of ships (see Figure 3.22) show the same inconsistency observed for ACRUISE-2 and described in Section 3.5.2.

Most of the ships encountered during ACRUISE-3 were rather young by

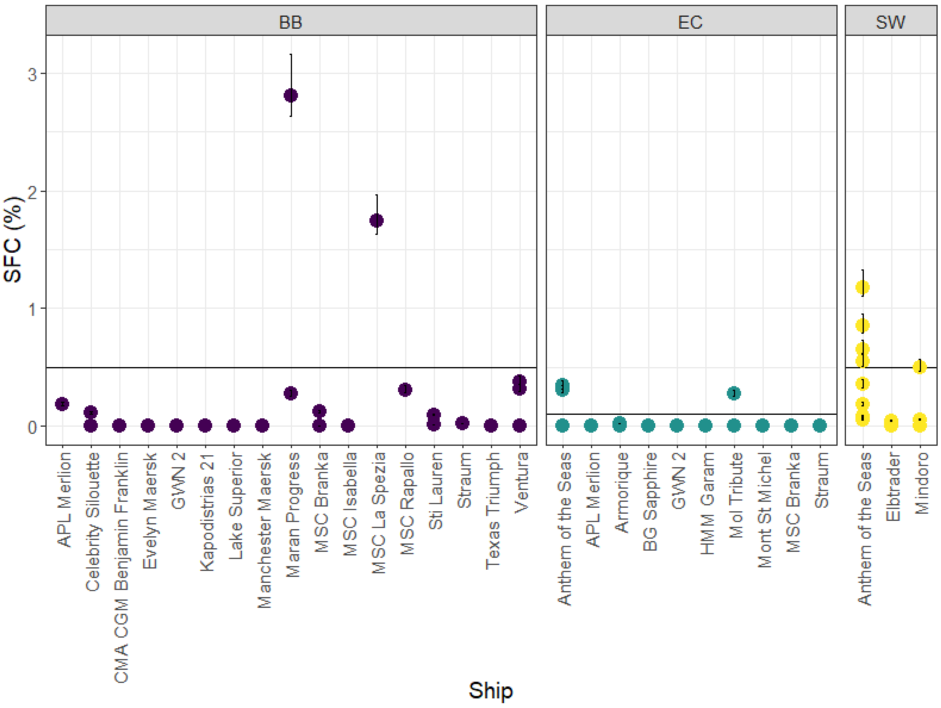

(a) ACRUISE-2 SFCs from ships with fitted scrubbers, where SW - South West approaches, BB - Bay of Biscay, EC - English Channel.

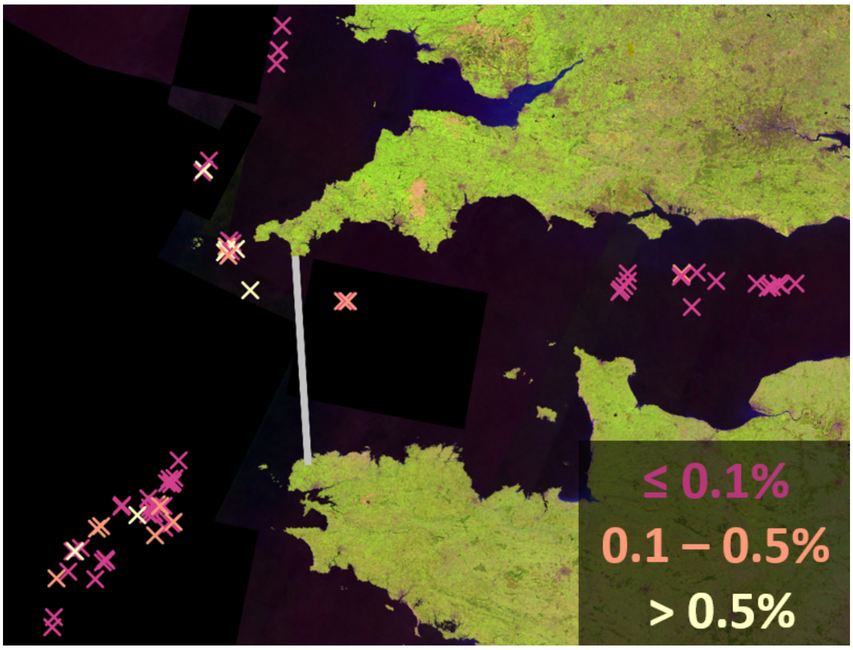

(b) ACRUISE-2 SFCs grouped by SECA and non-SECA limits.

Figure 3.19: Overview of ACRUISE-2 ships fitted with scrubbers at the time of the campaign. Map source: GLAD Landsat MOSAIC 2019 map [72].

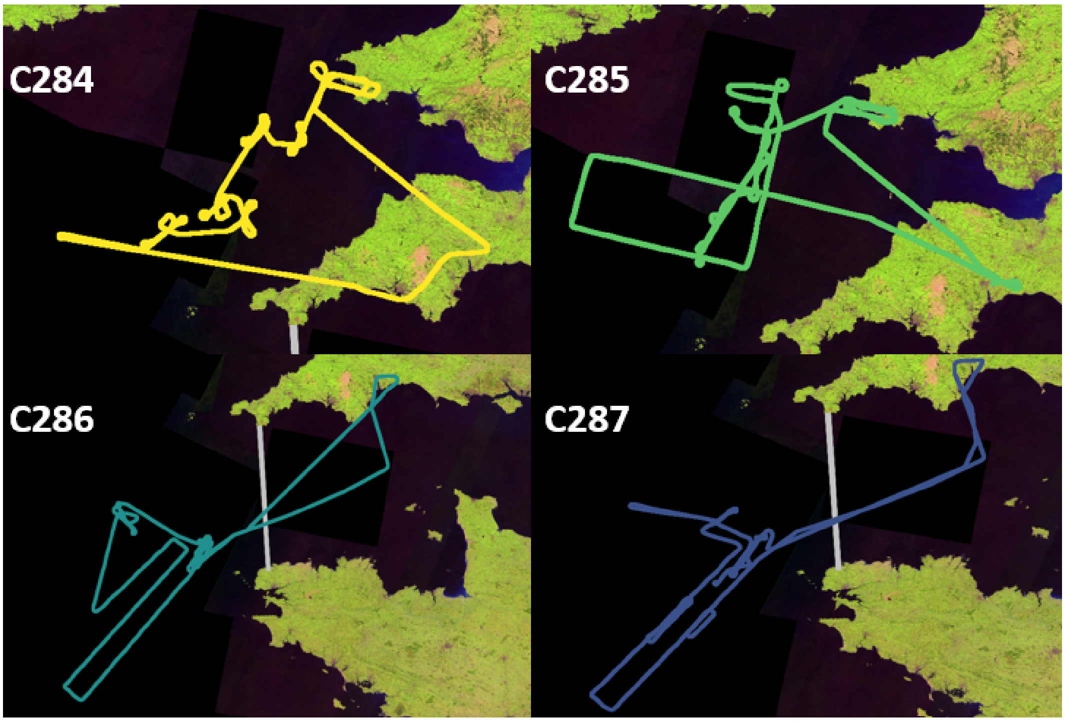

Figure 3.20: ACRUISE-3 individual flight tracks.

ship standards, as summarised in Figure 3.23. All but MSC Pilar, which also happened to be highest SFC ship of the campaign, were built past 2005. It is possible that the ship owner decided not to invest in converting an old ship to current SO_2 emission standards, although this is not always the case. In previous campaigns there were also few ships from 1990s, however plenty from 2000-2005. The number of encountered ships was lower in the third campaign, so such differences come as no surprise. There were three ships with scrubbers (out of total of 15 ships): APL Fullerton, Ever Act and Marchen Maersk and all of them were container ships encountered in BB. They did not stand out from the group in any way.

Figure 3.24 shows the ACRUISE-3 fleet divided by ship type and gross tonnage. The dominant ship type of the campaign were container ships followed by LNG tankers, which obviously does not reflect the global fleet at all, but is a result of an attempt to study the latter in more detail. In terms of tonnage the data set is dominated by rather large ships (over 100 000 t).

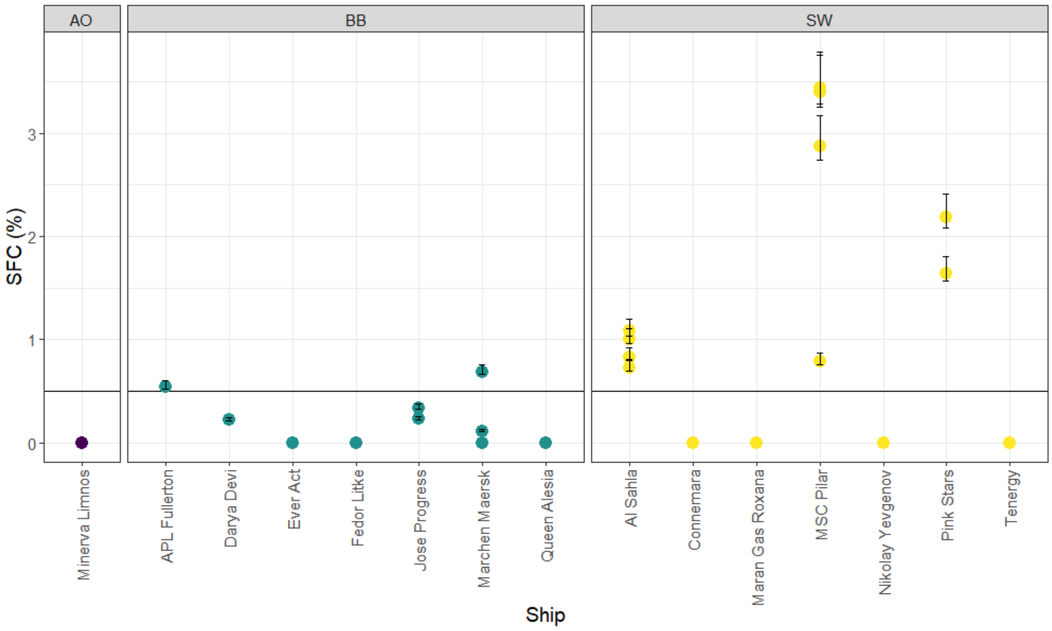

Figure 3.21: ACRUISE-3 SFCs, sea and ship, where SW - South West approaches, BB - Bay of Biscay, AO - Atlantic Ocean. Black lines shows IMO sulphur limits: 0.5% for non-SECA.

3.5 SFCs limitations

3.5.1 Influence of data quality on peak integration

ACRUISE-3 allowed a direct data quality comparison since there were three sub 1 Hz measurements: 10 Hz FGGA CO_2, 5 Hz LIF SO_2 and 4 Hz CIMS SO_2, which however were not of sufficient quality for peak integration.

First a frequency sensitivity test was carried out. In case of CO_2 only one measurement was available so the data got averaged down to 5 Hz and 1 Hz for comparison as shown in Figure 3.25. There is a noticeable difference between each of the three frequencies, which likely is driven by highly variable background. Background variability makes picking peaks much more difficult. As shown in plot Figure 3.26, the differences vary by flight but in all but three cases show that 10 Hz data yields higher area, possibly because the plume is better resolved and its entire structure is detected and integrated. For C284 - C285 (SW) and C292 (AO) the differences are

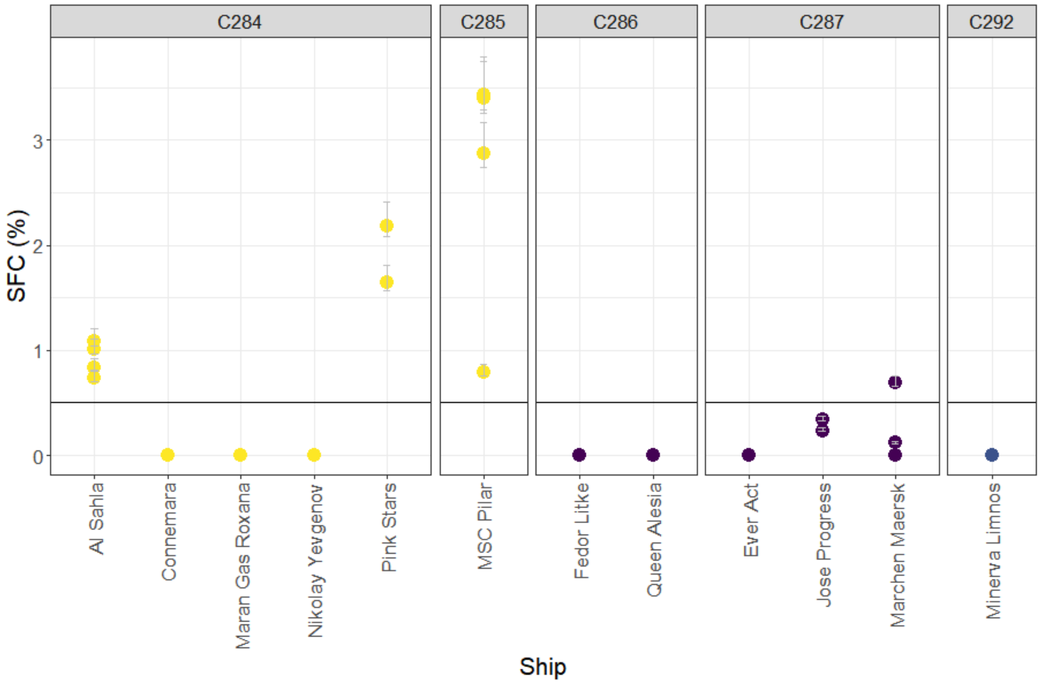

Figure 3.22: ACRUISE-3 multiple passes through the same plume, where SW - South West approaches, BB - Bay of Biscay, AO - Atlantic Ocean. Black lines shows IMO sulphur limits: 0.5% for non-SECA.

smaller than for C286 - C287 (BB), which can be attributed to more variable background and larger peaks in BB.

5 Hz areas are closer to 10 Hz, suggesting that 5 Hz might be just about enough for ship plume measurements. 1 Hz is certainly not enough, especially for species with fluctuating background like CO_2. This is of course specific to speed of the measurement platform and source of plume, hence if the method is applied in a different project the data resolution requirements might change.

SO_2 on the other hand shows greater consistency in the integrated peak area, as shown in Figure 3.27. In most cases the values that stand out are from 5 Hz data, but not with a consistent bias. This is likely due to very stable background across all flights and less ambiguous peaks. Hence it is fair to assume that it is the variable background that drives the frequency dependency.

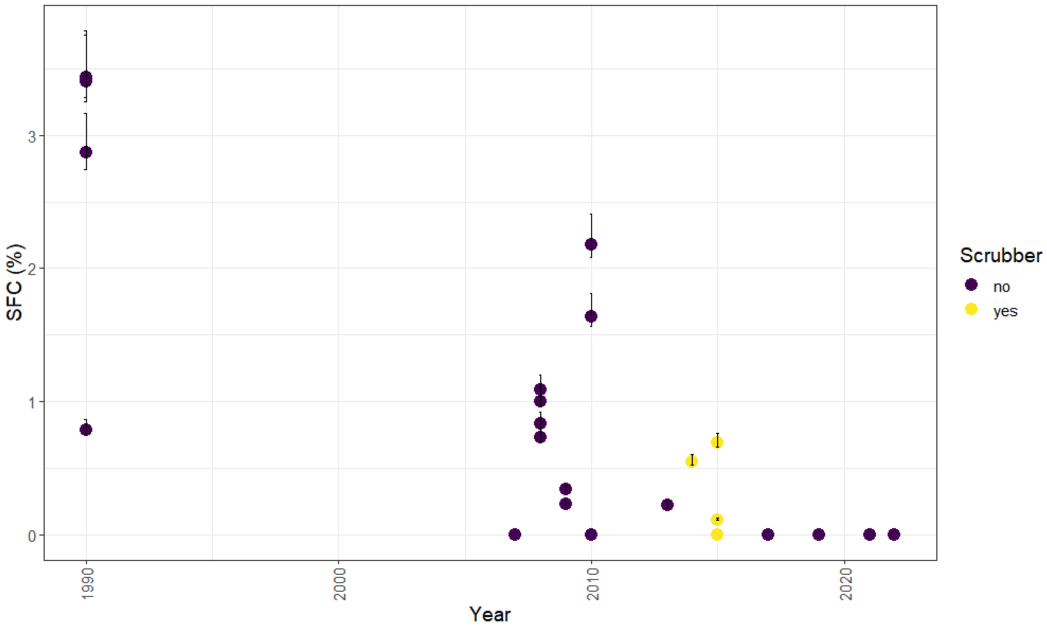

Figure 3.23: ACRUISE-3 SFCs, scrubbers and production year.

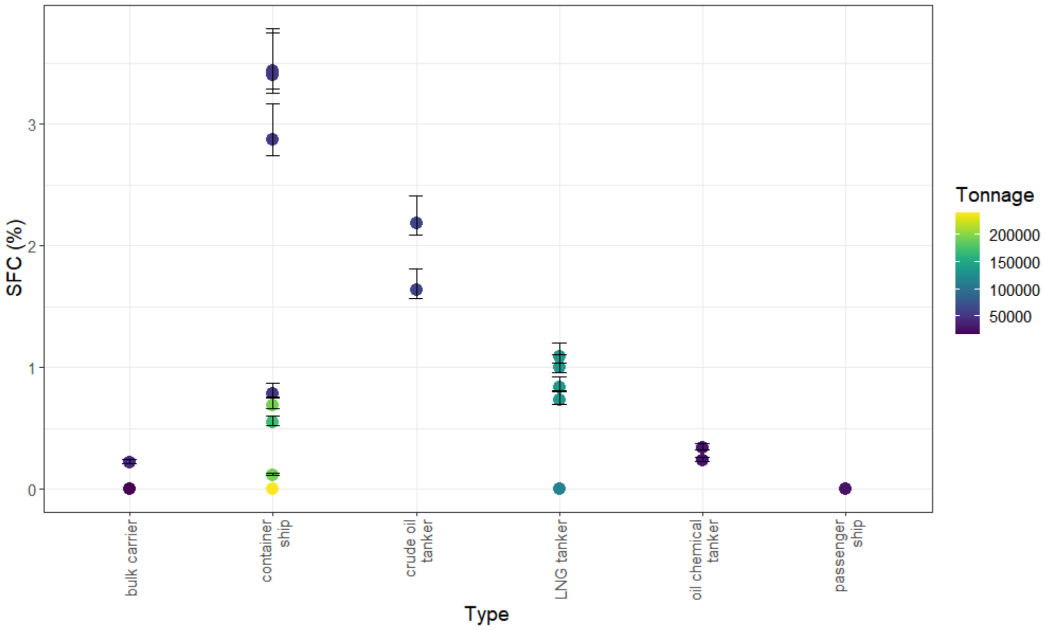

Figure 3.24: ACRUISE-3 SFCs, type and gross tonnage.

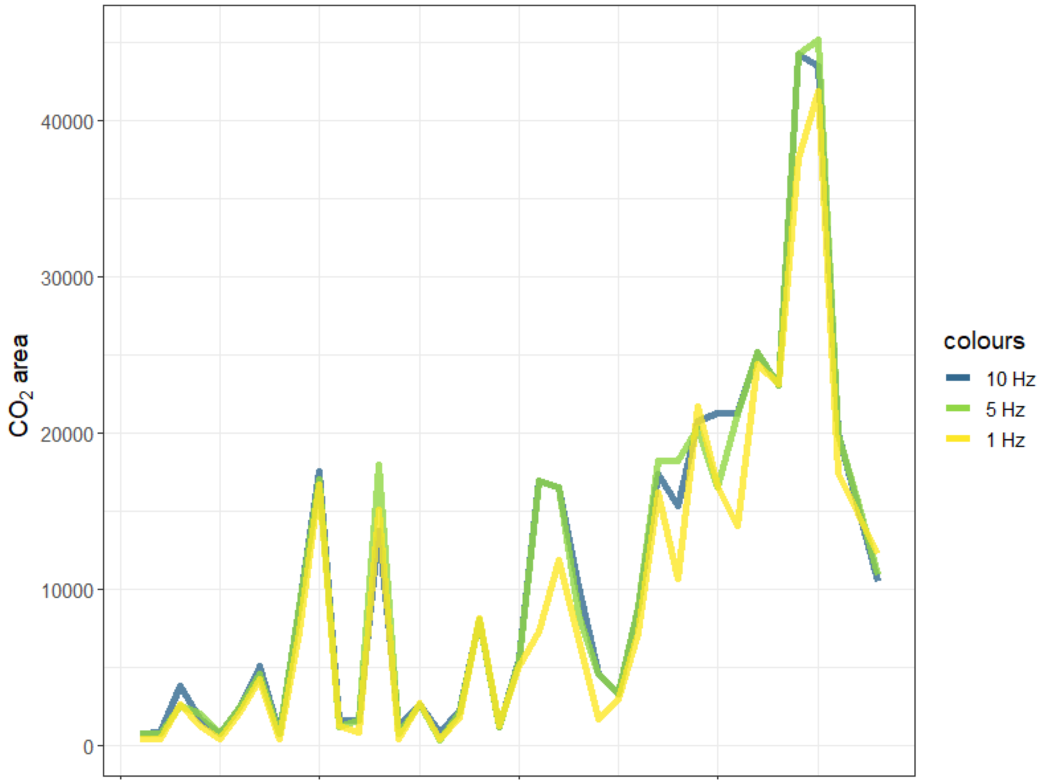

Figure 3.25: ACRUISE-3 CO_2 peak area comparison.

Comparing between two instruments, i.e. FAAM core SO_2 (TECO) and LIF SO_2 it is only fair to compare 1 Hz data with 1 Hz data. Hence the LIF data was also averaged down to 1 Hz. As shown in Figure 3.28 York regression was used to account for the error in area of each instruments and yielded very close to 1 slope, which suggests that it is the frequency rather than instrument that have a dominant influence on the area. It is important to note, that York regression provides considerably more reliable fit than OLS regression, since the latter ignores the uncertainties and in this case gives slope of 0.44 with R^2 of 0.67. This could be very misleading if not verified by York regression. However, York regression (blue line), which takes into account errors of both variables gives $y = 0.95x - 0.06$ with slope error of 0.02, which is nearly ideal, but indicates that LIF gives slightly higher values than TECO. This comes as no surprise, since TECO peaks “drown" in noise unlike LIF peaks.

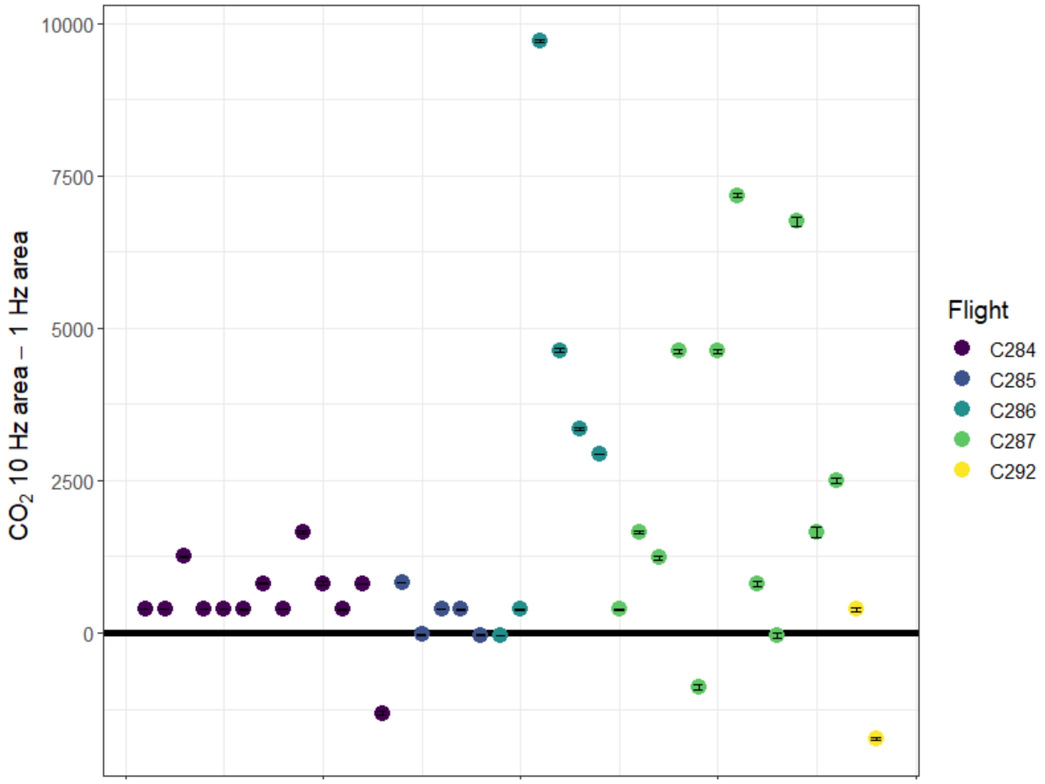

Figure 3.26: ACRUISE-3 CO$_2$ peak area comparison between 10 and 1 Hz data by flight.

Hence, it can be concluded that for ACRUISE-3 the instrument has little influence, but frequency can bias the bulk SFC statistics, in this case leading mostly to overestimation (since in 1 Hz data CO$_2$ area is mostly underestimated due to poorer peak resolution). The impact on the individual SFCs varies depending on the background stability. With that caveat, ACRUISE-3 and ACRUISE-2 can be safely compared directly when 1 Hz data is used for ACRUISE-3. Whether ACRUISE-1 can also be compared directly is another question, since the the CO$_2$ data quality is very low and might possibly have a greater effect than what is described here.

This can be further validated by a different airborne study where `acruiseR` package peak integration can also be applied: Methane-To-Go-Poland. The work used a helicopter towed probe equipped with, among others, two methane measuring instruments - low noise and low speed (1 Hz) Picarro and high speed (40 Hz) high noise experimental Licor open path setup. Unfortunately

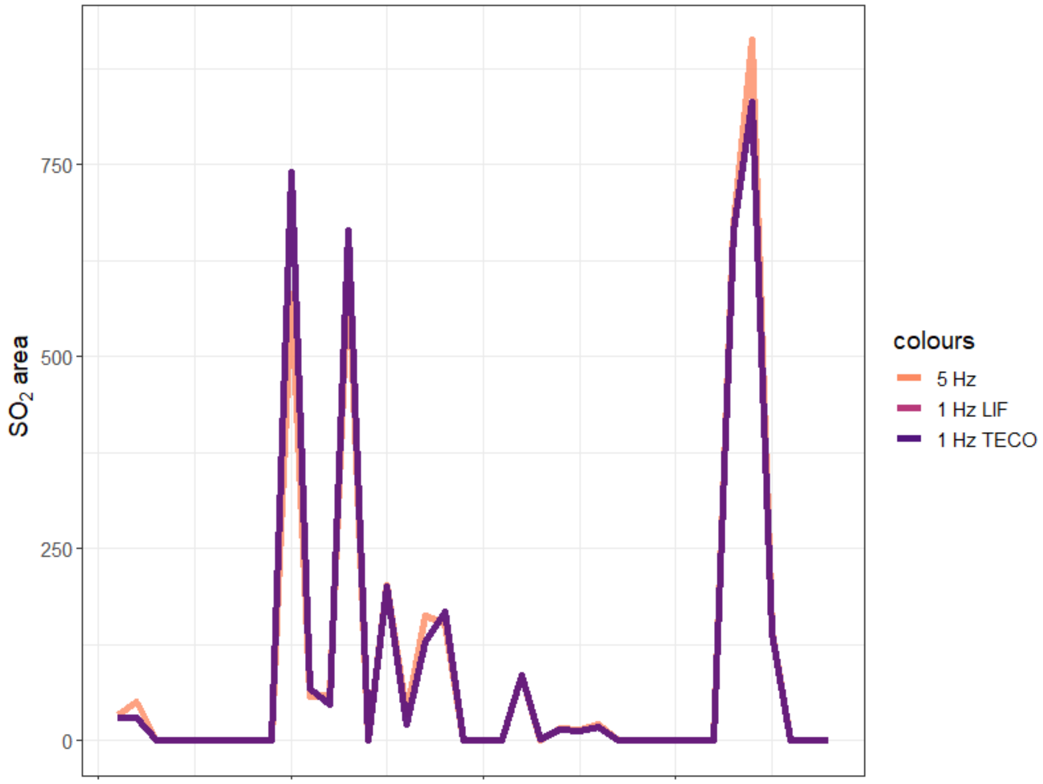

Figure 3.27: ACRUISE-3 SO_2 peak area comparison.

only 1 Hz quick look data with no uncertainty calculated was available for this work, but it still can be used to illustrate difference between 'smooth' and 'noisy' data. Figure 3.29 shows how the difference between peaks translates to calculated areas even though both data sets are technically 1 Hz and measure the same, large (often over 1 ppm difference), clearly defined plumes. Areas calculated with Picarro data are higher than areas calculated with Licor data: despite Licor being the faster instrument it is much noisier and the signal is downsampled to 1 Hz by picking every 40th data point. This way it captures all the noise without the benefit of higher measurement speed. If Licor data was averaged to 1 Hz from the 40 Hz data it would likely be similar to Picarro. This is also observed in ACRUISE data - the algorithm struggles more to pick more structured and noisy peaks. This additional example shows that the quality difference in data can influence the area even for very large and well defined peak.

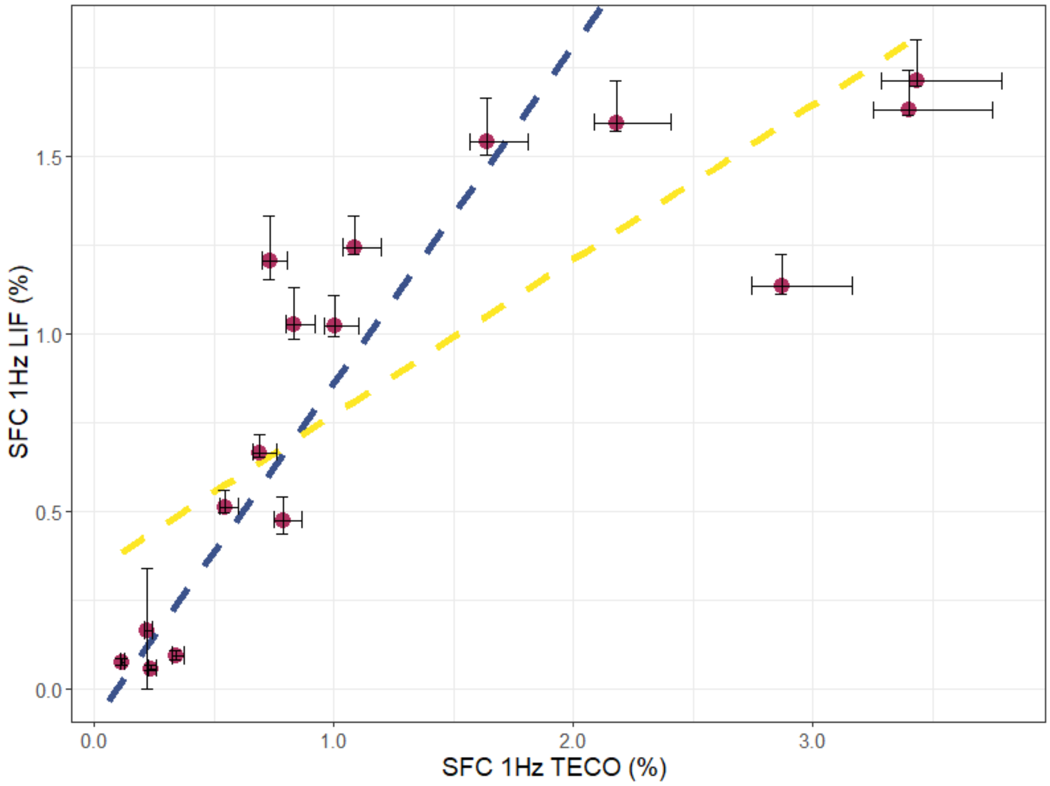

Figure 3.28: ACRUISE-3 SO_2 peak area from LIF and TECO instruments comparison. The yellow line is ordinary least square (OLS) regression: $y = 0.44x + 0.34$, $R^2 = 0.67$. The blue line is York regression[83]: $y = 0.95x - 0.06$ with slope error of 0.02.

3.5.2 Differences in SFCs for one ship

The data resolution dependence is a factor when comparing data between campaigns or experiments, but it might also affect values within the same data setup. This is because as shown in Figure 3.26 the difference between high resolution areas assumed to be true and low resolution areas is not constant. Some plumes were targeted multiple times in row which often resulted in more than one SFC derived during the same encounter. As explained in Section 3.5.1 the value would be expected to be the same within uncertainty. The data however shows it is rarely the case and the resolution sensitivity is likely one of the factors, but there is a number of other issues that might also play a part.

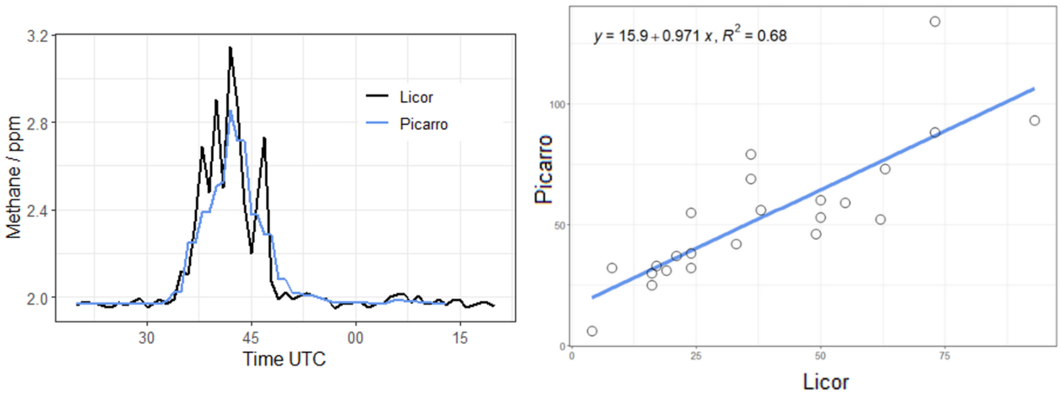

Figure 3.29: Methane-To-Go-Poland coal mine venting CH_4 peak area and peak shape from Li-7700 and Picarro instruments comparison.

First, most obvious, would be that the peak extents are not chosen correctly. That however was proven not to be the case, when data was reintegrated with specific focus on these peaks, which shows the method and QA/QC work well. Another reason could be that the change is driven by different performance of CO_2 and SO_2 analysers e.g. varying with peak width or maximal concentration. This likely has some influence on the values. BAe-146 flies at task area at approx. 100 ms^{-1}, so it could also be that the measurements are in general too slow for narrow ship plumes, especially in case of ACRUISE-1. That could cause each instrument capturing the plume to different extend and hence affecting the SFC. It could also be that the assumption that SFC should stay the same in relatively fresh plume is wrong. This possibility cannot be outright excluded, especially that sulphates and other sulphur compounds were not used in this work, however a number of studies (see Section 3.5.1) suggests that is not the case. The ratio could also vary depending if plume was transected in the ‘middle’ or on the ’edge’, but it is unlikely to have noticeable impact. Finally, there is one more explanation, which is the most plausible explanation for the exceptionally high values. Ships usually have more than one engine and can run additional generators on board. It is possible that in fact different plumes from the same ship are captured, e.g. from auxiliary engine, from generator and from main engine. And since e.g. generators are a grey area in terms of sulphur emissions regulations they could be the source of the high values.

This study is unlikely to provide a definitive answer to the question of differing SFCs, as it is likely driven by a range of factors. However, the main contributions are likely different emission sources and the difference in data resolution.

In case of both ACRUISE-1 and ACRUISE-2 it appears that higher concentrations i.e. fresher, better captured plumes yield higher SFCs. This is a very plausible consequence of insufficient measurement speed and poor quality of signal, i.e. high noise, which means tall peaks that "stand out" from the noise are captured by the algorithm more precisely than small ones for which it is very difficult to tell start and end even visually. The nature of the algorithm used to detect and integrate peaks also means that smaller peaks are more susceptible to incorrect baseline fitting, especially if they are in close proximity (seconds or minutes) from larger peaks. York regression was used to show this dependence for ACRUISE-1, as shown in Figure 3.30. Indeed it turns out that the SFC value changes more with the poorer quality species, i.e. CO_2 than the better quality species, i.e. SO_2 (even with the same sampling rate - 1 Hz). Ideally data of as poor quality as ACRUISE-1 would not be used for this kind of work. Improved quality of the data would allow stricter filtering criteria, which would possibly eliminate the issue (like in case of ACRUISE-3). Another approach would be algorithm redevelopment, so that each peak is treated separately with its adjacent background. This would eliminate the influence of other peaks and improve baseline fitting, but could be limiting for peak clusters and considerably more complicated to implement.

Another aspect, that is beyond the scope of this work, however is worth investigating in the future is the influence of peak shape as mentioned in Section 3.4.1. Since the peak integration method in its current state seems

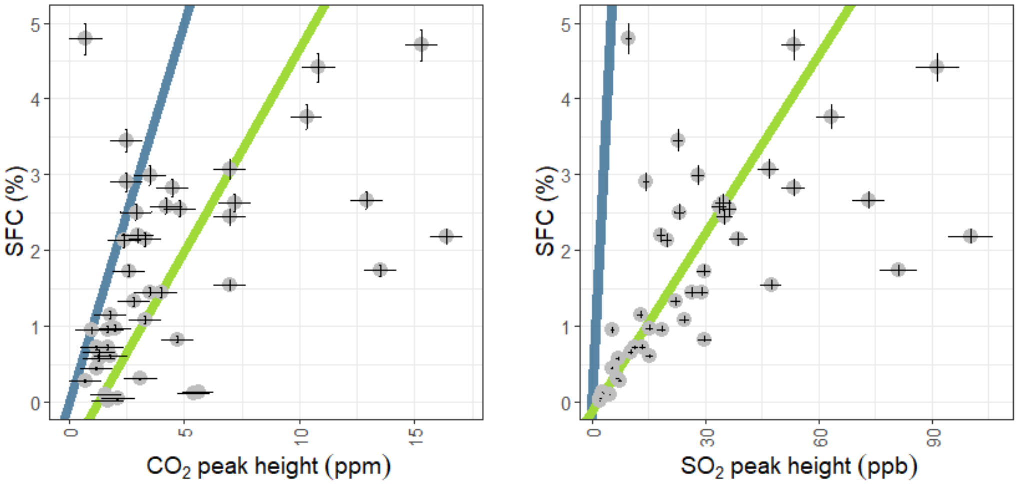

(a) ACRUISE-1 York regression of SFCs against CO_2 peak height: $y = 0.53x - 0.67$, with slope error of 0.03 (5%)

(b) ACRUISE-1 York regression of SFCs against SO_2 peak height: $y = 0.08x - 0.13$, with slope error of 0.01 (2%)

Figure 3.30: ACRUISE-1 York regression of SFCs against peak height (44 observations). Blue line shows $y = x$.

to perform better at sharper, less structured peaks, it could be combined with the cross correlation method described in Section 2.4.3, which in turn favours wider peaks regardless of their structure. That however would require finding strict criteria of dividing peaks into ‘sharp’ and ‘wide’, which is a non-trivial task. Moreover, this approach would resolve only part of the problem - data quality mismatch and insufficient sampling frequency would still affect the data.

3.5.3 Representativeness of the dataset

Plume choice bias is an inherent part of working with a large aircraft. Small ships with low stacks are simply impossible to measure. The smallest ship for which SFC was calculated was Karita, a 4100 ton general cargo ship built in 2013 encountered during ACRUISE-2 campaign. Hence there is a size of ship bias. There is also bias in which plumes actually pass the QA/QC - ‘weaker’ plumes likely will fail to be used for SFC calculation, hence ships which ‘emit less’ might be underrepresented[†]. It is important to acknowledge this bias, but there is not much that can be done to counteract it without further fieldwork using smaller aircraft.

3.6 Comparison of SFCs

3.6.1 ACRUISE campaigns

Figure 3.31 shows a summary of individual SFCs in all three campaigns by in three distinct areas: shipping lanes (SL), understood as so any area where ships are just en route; English Channel SECA (EC) and South West Approaches (SW). SW is treated differently because it is a coastal area bordering with SECA and so any activity concerning scrubber or fuel switching would be expected there. In 2019 mean SW SFC was 0.92% ± 1.09% 1σ and in 2021 0.34% ± 0.35% 1σ (meanwhile in 2022 1.00% ± 1.22% 1σ).

SW aside, SFCs in the EC are much lower than outside in both 2019 (0.08% ± 0.05% 1σ) and 2021 (0.08% ± 0.22% 1σ), as expected. In SL a large drop is seen from 2019 (2.34% ± 1.09% 1σ) to 2021 (0.27% ± 0.50% 1σ), hence before after the introduction of 0.5% limit. There is however a further decrease from 2021 to 2022 (0.12% ± 0.21% 1σ).

To summarise, the expected decrease from 2019 to 2021 was clearly observed in non-SECA waters. A further decrease was seen in 2022. IN EC constant, low level of SFC was maintained in 2019 and 2021 (no data from 2022). However, it is important to bear in mind that not all ships took on board the new regulations like, for example, some LNG tankers in SW.

[†] Of course weak signal can also be related to ship being further away or not crossing the plume at its widest.

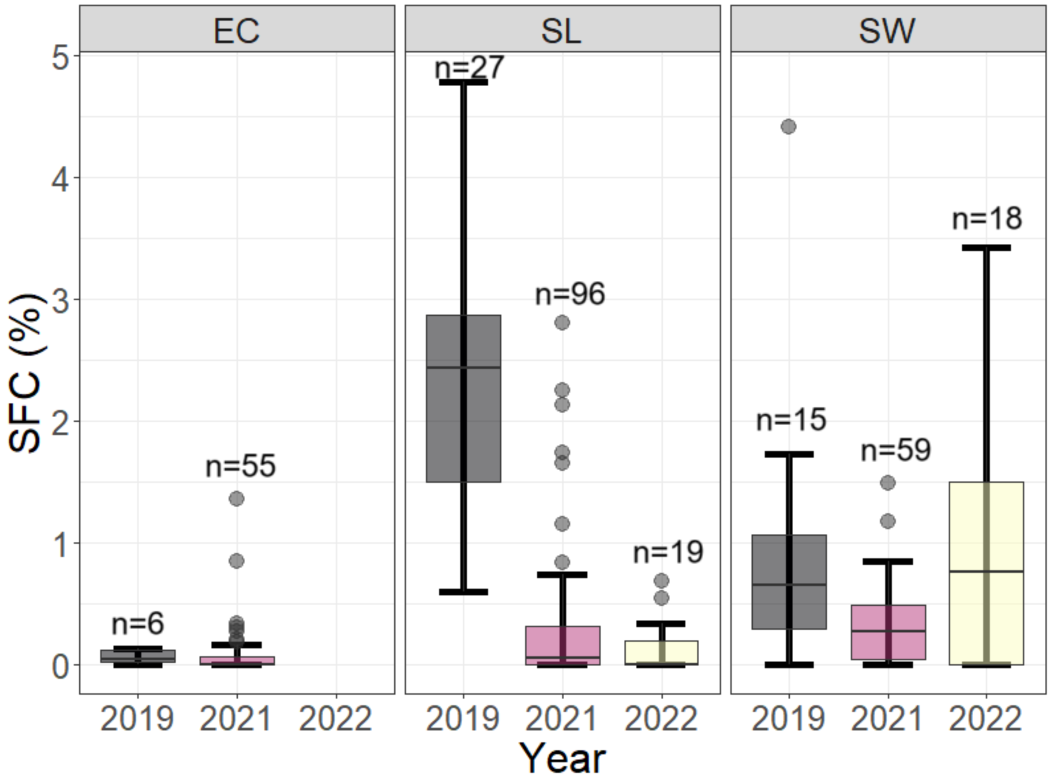

Figure 3.31: SFCs from all ACRUISE campaigns grouped by area: EC - English Channel (SECA), SL - shipping lanes (here including PTO) and SW - South West Approaches. Boxes extend from 1^{st} to 3^{rd} quantile, whiskers show range of values without outliers and the points show outliers (i.e. points falling either below 1^{st} quantile - 1.5 interquantile range or above 3^{rd} quantile + 1.5 interquantile range.)

3.6.2 SFC comparison with STEAM

The STEAM3 model data for ships encountered during ACRUISE-1 and ACRUISE-2 was provided by Jukka-Pekka Jalkanen from Finnish Meteorological Institute. It is important to note that the model concerns a bulk yearly emission rather than emission at the point of encounter, hence some variation is to be expected. However, it is still a great opportunity to validate modelled and observed data against each other. In both cases SFC represents apparent sulphur fuel content, since the model takes into account sulphur removal.

Comparison between modelled and observed SFCs for each ACRUISE-

1 ship is shown in Figure 3.32. The model places most of ships about 2.0 - 2.5% SFC with two notable exceptions: a 2014 built Norwegian LNG tanker Hoegh Gallant (0.03%) and a 2006 built Italian ro-ro cargo ship Stena Horizon (0.92%). Neither of the ships was fitted with a scrubber. In the case of Hoegh Gallant its modelled SO_2 emissions are lower than other ships with CO_2 emissions typical for the fleet. Stena Horizon on the other hand does not stand out in therms of absolute emissions of neither SO_2 nor CO_2. For Hoegh Gallant the measured value is more in line with the typical model output range for other ships (1.97%), while for Stena Horizon the measured value (0.31%) is in line with the modelled one.

Ships that yielded over 1% higher measured values compared to the modelled ones are: MSC Coruna (4.79%), Aegan Vision (3.77%), Hirado (3.46%) and Max Jacob (3.07%). Only Hirado was passed multiple times, precisely twice (yielding different values), hence it is possible that in case of these ships the model is closer to the truth. As described in Section 3.5.2, this could be driven by reduced quality CO_2 measurement. Ships that yielded over 1% lower measured values were CMA CGM Cayenne (1.08%), Marianna VV (0.91%), Jy Vincentia (0.72%), MSC Poh Lin (0.66%) and Grande Argentina (0.60%). Since values for ACRUISE-1 are overestimated if anything, it is likely that the values are indeed lower than predicted by the model.

Comparing averages of modelled (1.94% ± 0.54% 1σ) and observed (2.02% ± 1.18% 1σ) values for ACRUISE-1 it becomes obvious that the model captures mean well, but misses the scatter represented in measured data. That makes perfect sense since the measurements are derived based on maximum 5 passes within a space of minutes or hours, and the model concerns a year average. Hence it can be concluded that before the change of regulation the model reflected reasonably well average emissions.

The ACRUISE-2 data set is much larger with more multiple SFCs calculated for individual ship, and so presents a better point of comparison

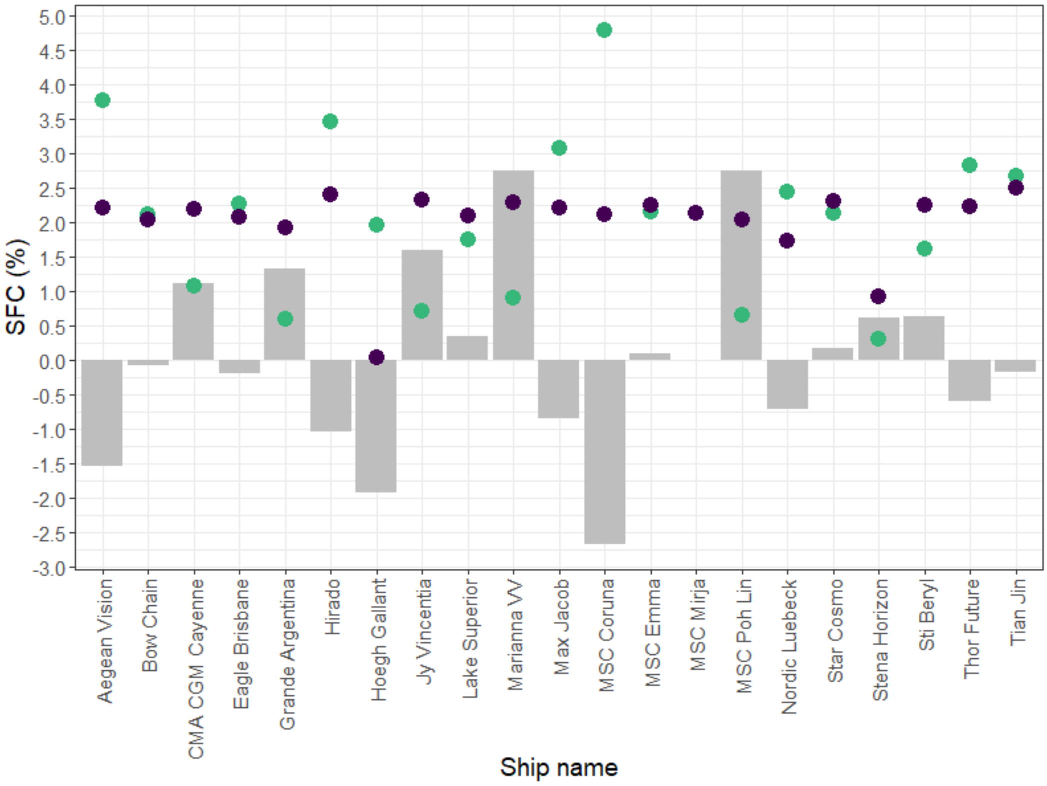

Figure 3.32: ACRUISE-1 comparison of SFCs derived from observed data (green) and model (purple). Difference between modeled and observed values is shown in grey. Model data credit: Jukka-Pekka Jalkanen.

with the modelled values. On average the modelled SFC for ACRUISE-2 was 0.31% ± 0.16% 1σ and observed SFC was 0.23% ± 0.34% 1σ. Both values come close again, although this time the observed values are slightly lower. The 1σ is higher for observed values as expected. Modelled dataset shows over a 6-fold decrease in SFC and the observed dataset shows nearly 9-fold decrease for all ships and 7-fold decrease for non-SECA (0.29% ± 0.46% 1σ; model output does not separate English Channel).

A detailed breakdown of measured and modelled values per ship is shown in Figure 3.33. Cases where ships exceed modelled values by over 1% are: MSC La Spezia (1.74%), Maran Progress (1.54%) and MSC Oriane (1.51%). These ships have also highest averages in ACRUISE-2 dataset in general. It can be assumed that these ships simply did not follow the IMO regulations at the time of the encounter and so the model does not estimate their emissions correctly. On the side, there were no ships that yielded values lower by over 1% than modelled since the model assumed that the ships adhere to the limit of 0.5%.

Overall, for ACRUISE-2 11 out of 87 (13%) ships exceed the modelled values by over 0.1%. Meanwhile, in the ACRUISE-1 dataset that is the case for 9 out of 24 (38%) ships, which could however be influenced by the slight positive bias of the dataset. More importantly though, only 13% of the sampled ships have exceeded the modelled values in 2021 and most ships showed similar or lower values suggesting that the 2020 IMO legislation was implemented successfully.

Finally, there is the question of when the model and observed values diverge the most. Figure 3.34 shows the differences between modelled and observed values against the observed values for ACRUISE-1 and -2. Both show that the difference inversely proportional to the observed SFC, which is no surprise, since the model assumes full compliance with legislation, i.e. if the limit is 0.5% the model usually assumes 0.5% emission, while in reality the values are either considerably lower or higher. The outlier from the ACRUISE-2 'linear' trend is Hoegh Gallant, which was assumed to have very low emissions by the model, yet presented average values when encountered. It is possible that the ship was assumed to be LNG powered and hence having no SO_2 emissions, but in reality it was running a diesel generator or powering some of the engines with conventional fuel.

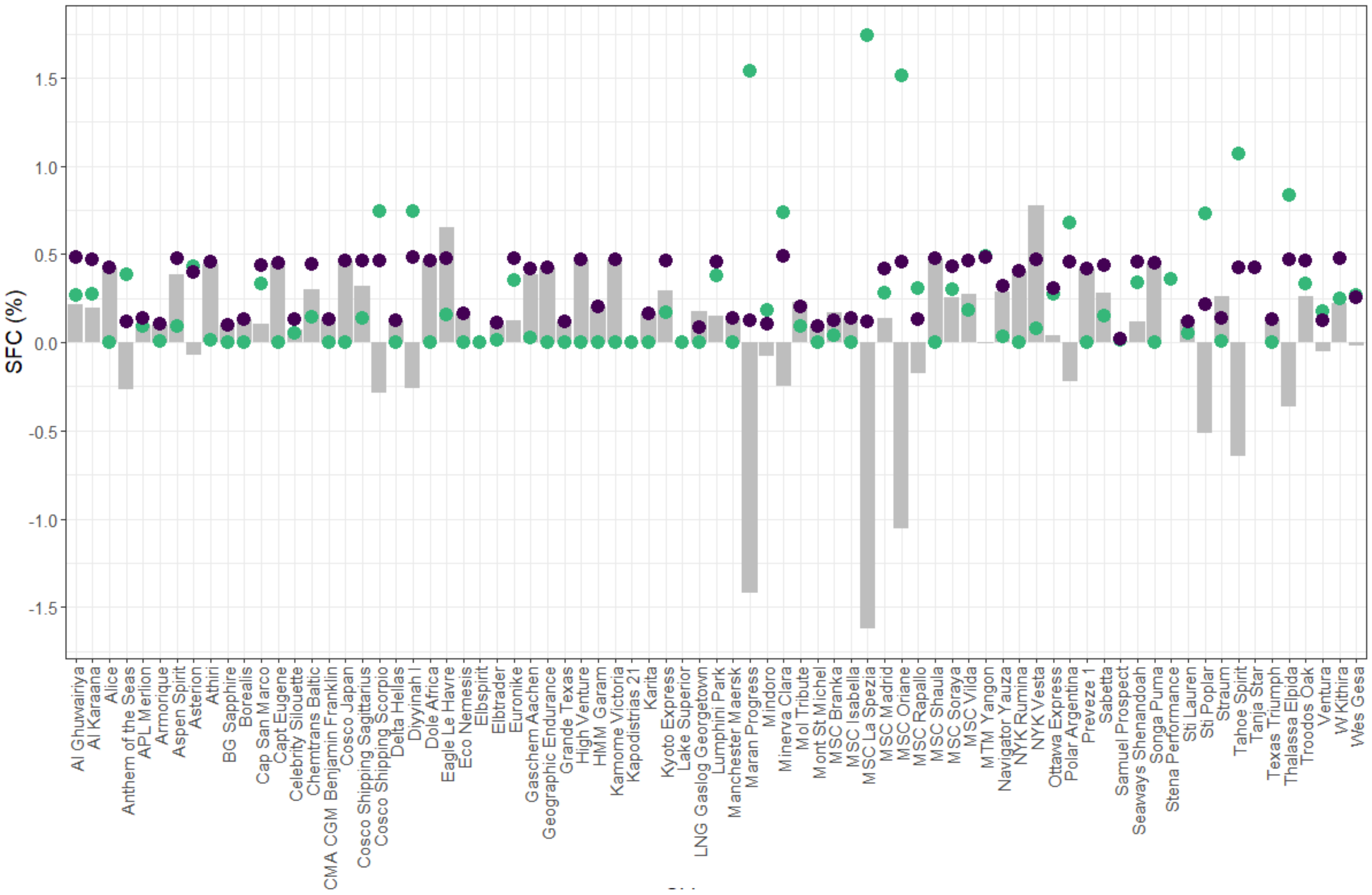

Figure 3.33: ACRUISE-2 comparison of SFCs derived from observed data (green) and model (purple). Difference between modeled and observed values is shown in grey. Model data credit: Jukka-Pekka Jalkanen.

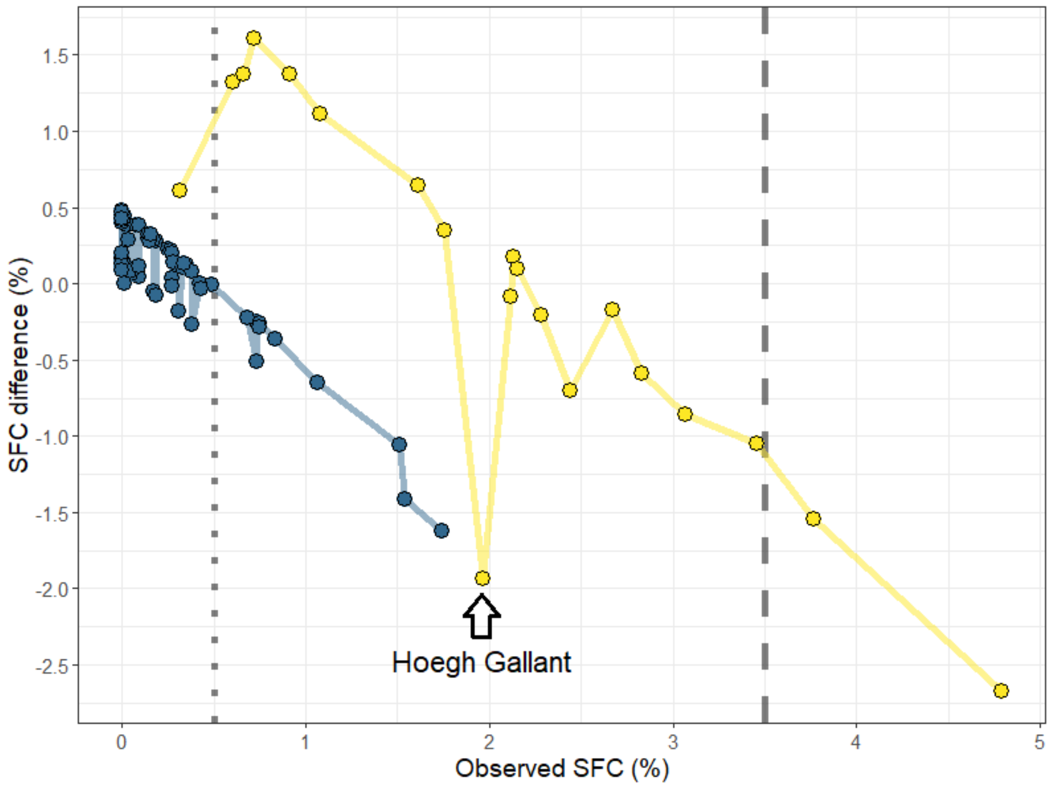

Figure 3.34: Comparison of differences between modelled and observed SFCs against observed SFC. The difference is defined as SFC_{model} - $SFC_{observed}$. ACRUISE-1 in marked in yellow, ACRUISE-2 in blue and the grey lines show the 2019 (3.5%, dashed) and 2021 (0.5%, dotted) limits. The point that stands out among the ACRUISE-1 value is Hoegh Gallant. Model data credit: Jukka-Pekka Jalkanen.

3.7 Liquefied Natural Gas tankers

LNG tankers encountered during ACRUISE campaigns are summarised in Table 3.1. They can be divided into two groups by age: young (built after 2015) and old (built before 2010) and two groups by LNG storage capacity: large (170 - 175 thousands m^3) and huge (210 - 260 thousands m^3). The same three tankers fall in the old and huge categories: Al Karaana, Al Ghuwairiya and Al Sahla. Another characteristic that sets them apart is being owned by Qatargas (see Table 3.2). Al Karaana and Al Sahla are part of Q-Flex fleet of above average size tankers built to distribute Qatari gas. Al Ghuwairiya is a Q-Max fleet tanker, designed at the same time as a part of a fleet of the largest LNG tankers in the world. All three are loaded predominantly in Ras Laffan (Qatar). The other tankers are of similar size and age but each of them is run by a different owner. Two more tankers were measured, but not included here. Yiannis (C283) was omitted due to IT issues during flight that affected the data, Hoegh Gallant (C183) because it was observed before change of the regulations and the FGGA data was lower quality.

Name	Flight	IMO	Year	Gross tonage	Size (m)	Capacity (m^3)
Gaslog Georgetown	C257, C262	9864916	2020	114000	293 x 46	174 000
Al Karaana	C258	9431123	2009	137000	315 x 50	210 000
Al Ghuwairiya	C261	9372743	2008	168200	345 x 55	258 000
Yiannis	C283	9879674	2021	115500	295 x 46	170 800
Al Sahla	C284, C285	9360855	2008	136400	315 x 50	211 800
Maran Gas Roxana	C284, C285	9701229	2017	113000	295 x 46	173 400
Nikolay Yevgenov	C284	9750725	2019	129000	299 x 50	172 000
Tenergy	C284, C285	9892456	2022	116500	299 x 46	174 000
Minerva Limnos	C292	9854375	2021	113700	295 x 46	173 400

Table 3.1: ACRUISE LNG tankers information.

Figure 3.35 shows two examples of LNG tankers time-series with multiple peaks. The rest can be found in Appendix A.5. For Al Sahla (2008) over 30 ppb SO_2 enhancement was measured in its largest peak, meanwhile Nikolay Yevgenov (2019) encountered during the same flight showed no detectable enhancement in SO_2, despite similar level of CO_2 in its biggest peak. This example illustrates very well the overall trend of old tankers emitting SO_2 and new tankers being below the level of detection of the Thermo SO_2. This translates to SFCs being non-zero only for the older tankers. The enhancements and SFCs are showed in Table 3.3. They belong to Q-Max and Q-Flex fleets which at the time were a breakthrough especially in terms of size, but nowadays they seem to fall behind in terms of sulphur emissions.‘

A CH_4 to CO_2 ratio is used to compare the emissions from the tankers. CO_2 and CH_4 are both measured with FGGA so the peak ratios can be

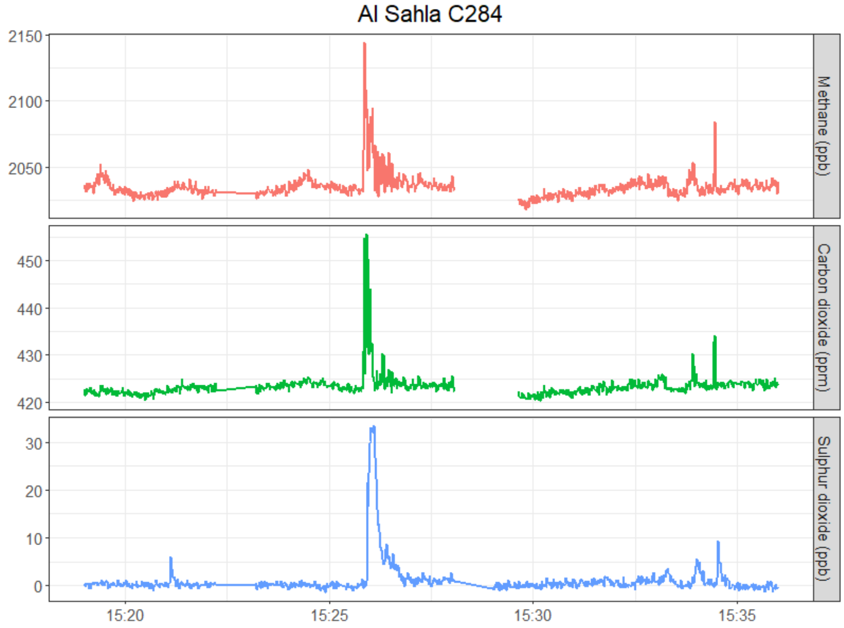

(a) Al Sahla, tanker showing large SO_2 enhancement.

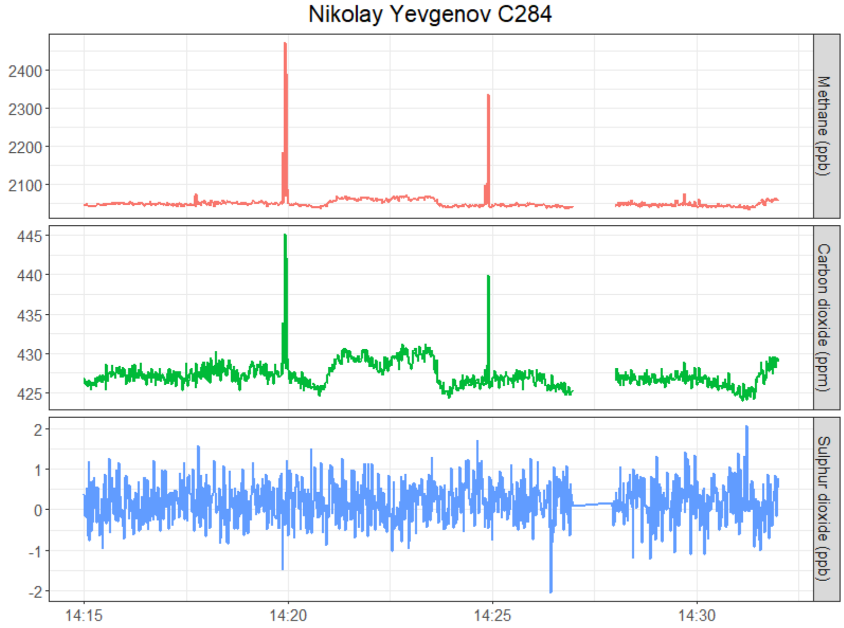

(b) Nikoly Yevgenov, tanker showing no SO_2 enhancement in plume.

Figure 3.35: Time series of CH_4, CO_2 and SO_2 for LNG tankers.

compared. The Qatari tankers measured might emit more SO_2 than the younger fleet, but their CH_4 to CO_2 ratios are lower. This could mean two things. Either they emit less methane overall or the methane plume does not coincide with the engine plume. All three ships have conventional diesel engines. The later possibility cannot be completely excluded, however based on Balcombe et al. [51] detailed empirical study of Gaslog Galvestone's methane emissions venting and fugitives is relatively small compared to engine slip in modern tankers using LNG also as fuel. The ratio is also low (0.03) for Nikolay Yevgenov and medium for Maran Gas Roxana (0.13). The other ships show values between 0.23 and 0.50 suggesting higher methane emissions. Hence it could be concluded that for LNG tankers using LNG as fuel is on one hand far cleaner, on the other hand increases the methane emissions. Further investigation is required to back up this conclusion.

The methane emissions of the tankers were meant to be quantified using ADMS 3 (Atmospheric Dispersion Modelling System) using tanker as a point source and varying the emission rate to match the aircraft observation. For this purpose, each pass though the tanker plume was treated separately and the tanker was assumed as a still point of reference. Unfortunately, the crucial obstacle turned out to be the lack precise distance between the aircraft and the tanker. The currently available Marine Traffic data is significantly too low resolution and too imprecise to even place the tanker upwind of the aircraft in some cases. Alternatively, the assumption that for the closest passes the plume was always crossed at approx. 500 ft from the ship in straight line (minimal allowed distance) gave better results. However, the emission rate is highly dependant on the exact distance and such approximations are also insufficient to achieve plausible results. Efforts to find more precise ship position are being made, but the potential results are far beyond the time span of this work. For this reason, only an overview of the methane peaks is presented.

Name	Builder	Owner	Manager	Flag	Classification
Al Karaana	Daewoo	Qatargas	Stasco	Marshall Islands	Lloyds Register of Shipping
Al Ghuwairiya	Daewoo	Qatargas	Nakilat	Marshall Islands	Lloyds Register of Shipping
Al Sahla	Hyundai	Qatargas	NYK	Marshall Islands	Det Norske Veritas Germanischer Lloyd
Gaslog Georgetown	Samsung	Gaslog	Cheniere	Bermuda	American Bureau of Shipping
Maran Gas Roxana	Daewoo	Maran	Shell	Greece	American Bureau of Shipping
Nikolay Yevgenov	Daewoo	Teekay	China LNG	Bahamas	Russian Maritime Register of Shipping
Tenergy	Hyundai	CMB	NA	Greece	Det Norske Veritas Germanischer Lloyd
Minerva Limnos	Daewoo	Minerva Gas	Minerva Gas	Malta	Det Norske Veritas Germanischer Lloyd

Table 3.2: LNG tankers ownership.

Flight	Tanker	Year	CH_4 (ppm)	CO_2 (ppm)	Ratio	SO_2 (ppb)	SFC (%)
C257	LNG Gaslog Georgetown	2020	1.0	3	0.33	< LOD	0
C258	Al Karaana	2009	0.7	15	0.05	15	0.27
C261	Al Ghuwairiya	2008	0.2	30	0.01	15	0.27
C262	LNG Gaslog Georgetown	2020	3.0	6.0	0.50	0.5	0
C284	Nikolay Yevgenov	2019	0.4	15	0.03	< LOD	0
C284	Maran Gas Roxana	2017	4.5	35	0.13	< LOD	0
C284	Al Sahla	2008	0.1	30	0.00	35	0.91
C285	Tenergy	2022	3.5	15	0.23	< LOD	0
C286	Fedor Litke	2017	5.0	15	0.33	< LOD	0
C292	Minerva Limnos	2021	0.6	2.0	0.30	< LOD	0

Table 3.3: LNG tankers data summary including only tankers measured with fast FGGA. SFCs are averages for the ships and in number of cases SO_2 was below the limit of detection (LOD). CH_4 to CO_2 ratio is used as a proxy to relative methane emissions.

3.8 Volatile Organic Compounds

3.8.1 ACRUISE-1

VOCs were measured in whole air samples taken using WAS during ACRUISE-1 and SWAS during ACRUISE-2 and -3. WAS samples have the disadvantage of being very slow (30 s fill time) and having long lag time. Additionally, they were taken during first campaign which focused more on transecting the plumes perpendicularly and measurements of random ships. There was no log of which sample was taken in which ship's plume either. All samples with their plume or background classification are shown in Figure 3.36. Flight C187 shows enhanced background compared to all the other flights which have similar overall concentration of VOCs. For this reason it is treated separately. It was a cloud flight at Portuguese coast after the C186 flight.

Despite the slow fill time and relatively small enhancement, Figure 3.37 shows a clear difference in composition of the samples considered to be in and out of plume with the high background C187 flight treated separately. The WAS samples for ACRUISE-1 were assigned as plume showed enhancement in absolute volume of VOCs compared to the closest sample which was intentionally taken in the background and enhancements in species other than ethane. Only 3 samples, all of them from Hirado, could be confidently assigned to a specific ship. Assigning samples to individual ships proved nontrivial for the dataset due to scarce record and uncertain lag.

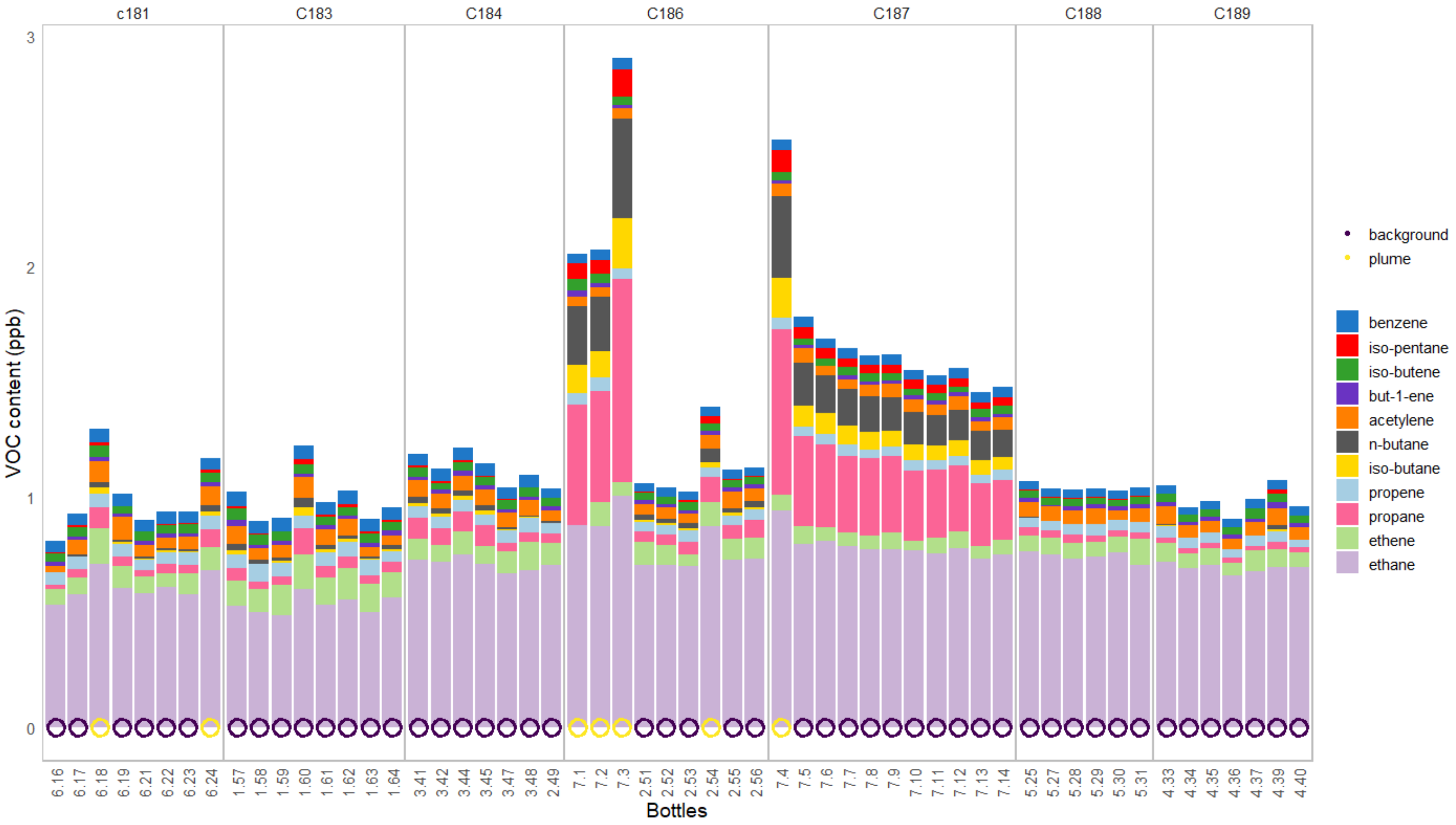

Figure 3.36: ACRUISE-1 all WAS samples VOCs compositions. In plume bottles marked with yellow circles.

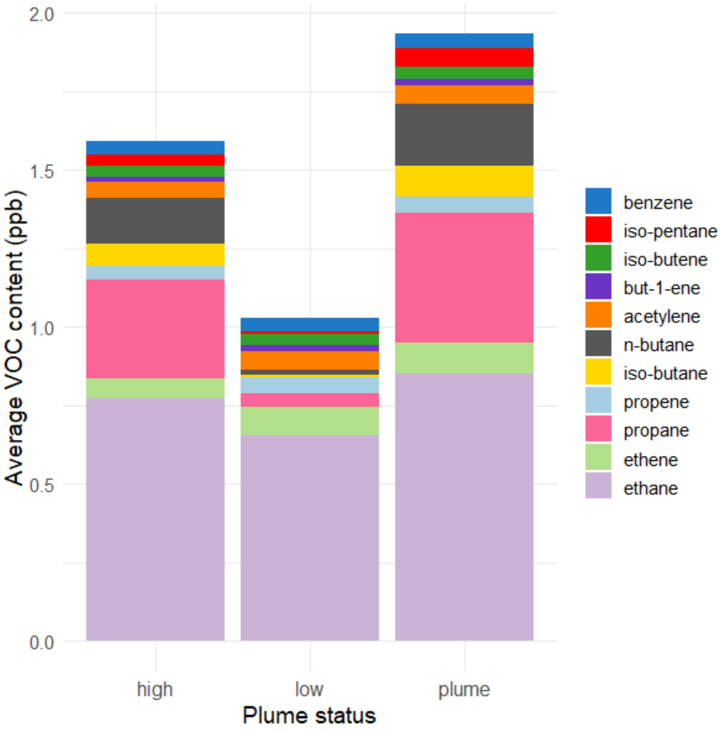

Figure 3.37: ACRUISE-1 total average VOCs in plume vs in low or high background. Not all the species could be quantified in every single sample.

Comparing average VOCs in and out of a plume as visualised in Figure 3.37 shows, the added up concentration of the plume samples is higher than the background ones. However, comparing individual species differences as visualised in Figure 3.38, shows some species are pretty much identical, while others can potentially serve as markers of a plume. For benzene, iso-butene, but-1-ene, acetylene, propene and ethane all 3 types of sample are quite similar. Propane, iso-butane, n-butane and iso-pentane show the biggest differences both for the plumes and high background, suggesting that the high background has ship origin. In all four cases the ratios between high background, low background and plume are similar. In case of the high background the concentrations of individual VOCs are often comparable to plume concentrations, although in all cases lower. No CO_2 ratios were derived since it was not measured in the WAS samples.

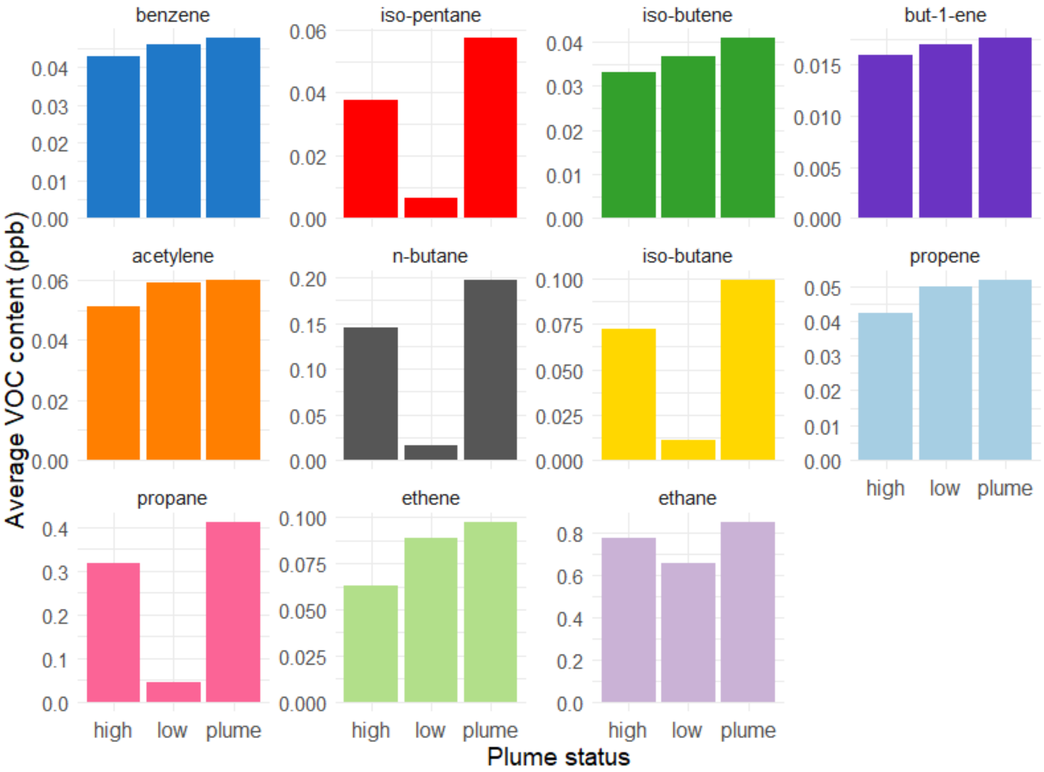

Figure 3.38: ACRUISE-1 average VOCs in plume vs out of plume species by species.

3.8.2 ACRUISE-2

During ACRUISE-2 SWAS was used to capture air and background samples allowing shorter fill time and lag time. Moreover more samples were taken and more species were quantified. However, capturing ship plumes remained tricky and there is no obvious marker of whether a sample is in the plume or not. Perhaps, the shorter fill time of SWAS bottles is simultaneously a blessing and a curse. On one hand it allows catching the plume without 'diluting' it with too much background, on the other hand more variability in the background samples shows, making it more difficult to tell a plume from background, especially when the plume is not very strong. Meanwhile, in ACRUISE-1 more plumes were missed, but the enhancement is more obvious even without a log.

It is important to note that there is a high confidence in the GC analysis of the samples and a long history of SWAS proving to be a reliable sample grab system. SWAS might have a number of operational improvements but in principle it uses the same methods and any bottles that were subject to any doubt were discarded from the data set. Both systems functioned well throughout the campaigns. Thus, it is highly unlikely that any of issues with plume recognition lay on the post-sampling side. The major contribution to the unreliability of plume detection is likely the operators uncertainty of the lag time and relatively low concentrations of the VOCs in the plume.

During mission flights in ACRUISE-2 a detailed log was taken by the SWAS operator listing what ship was the sample intended to be from. Often followed by comments on whether it is likely missed or captured and whether the plume seems strong. This was the first step of separating background from plume samples. The background samples are certain, since they were taken when the aircraft was well clear of any plumes. With plume samples, it is often not obvious whether they were successful or not. In such cases they are left out of comparisons.

Due to the reasons described above this work does not focus on individual plumes, except for the Al Ghuwairiya case study. Figure 3.39 shows the average of plume and background, with distinction for the high background event in English Channel during flight C263, so it does not obscure the difference between background in more typical conditions. The mean measured VOCs sum in plume is completely overshadowed by the high background during C263 (5.77 ppb), but it is distinctly higher than the low background. The total of measured VOCs in plume averages at 2.63 ppb, while the low background averages at 1.92 ppb. The total VOCs concentrations should not be compared to ACRUISE-1 since different VOCs were analysed.

Comparing these three distinct types of sample on a species by species basis, as shown in Figure 3.40, gives similar impression: low background has the lowest concentration and high background has the highest with plume samples being somewhere in between. Ethane is the dominant VOC in in

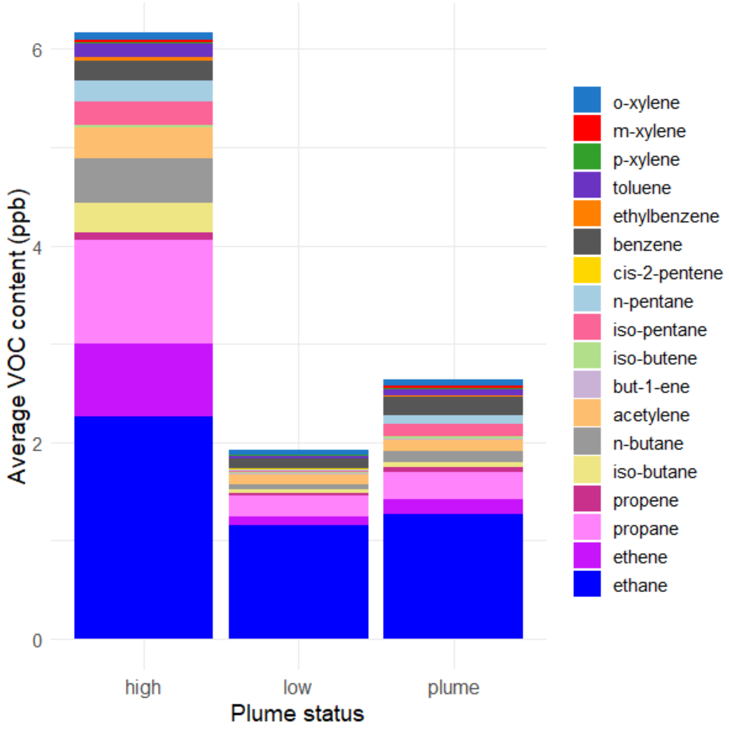

Figure 3.39: ACRUISE-2 total average VOCs in plume vs the low and high (only C263) background. Not all the species could be quantified in every single sample. The samples which were logged as in plume but showed little to no enhancement or composition change were excluded from the comparison or in rare cases classified as background.

all three cases. Interestingly the average concentration is very similar for low background (1.61 ppb) and plume (1.27 ppb). The second highest concentration VOC is propane, which again is similar between low background (0.21 ppb) and plume (0.27 ppb) and much higher for C263 (1.01 ppb). Following species is ethene which again is much higher for C263 samples (0.62 ppb), but this time shows more difference between plume (0.15 ppb) and low background (0.09 ppb). For iso-butane, n-butane and to lesser extent acetylene there is a big contrast between high background and low background / plume. The two first species show clear difference between low background and plume, while acetylene is similar for both. For iso-pentane, n-pentane and toluene the difference between high background and plume is less pronounced but still clear and low background is considerably lower.

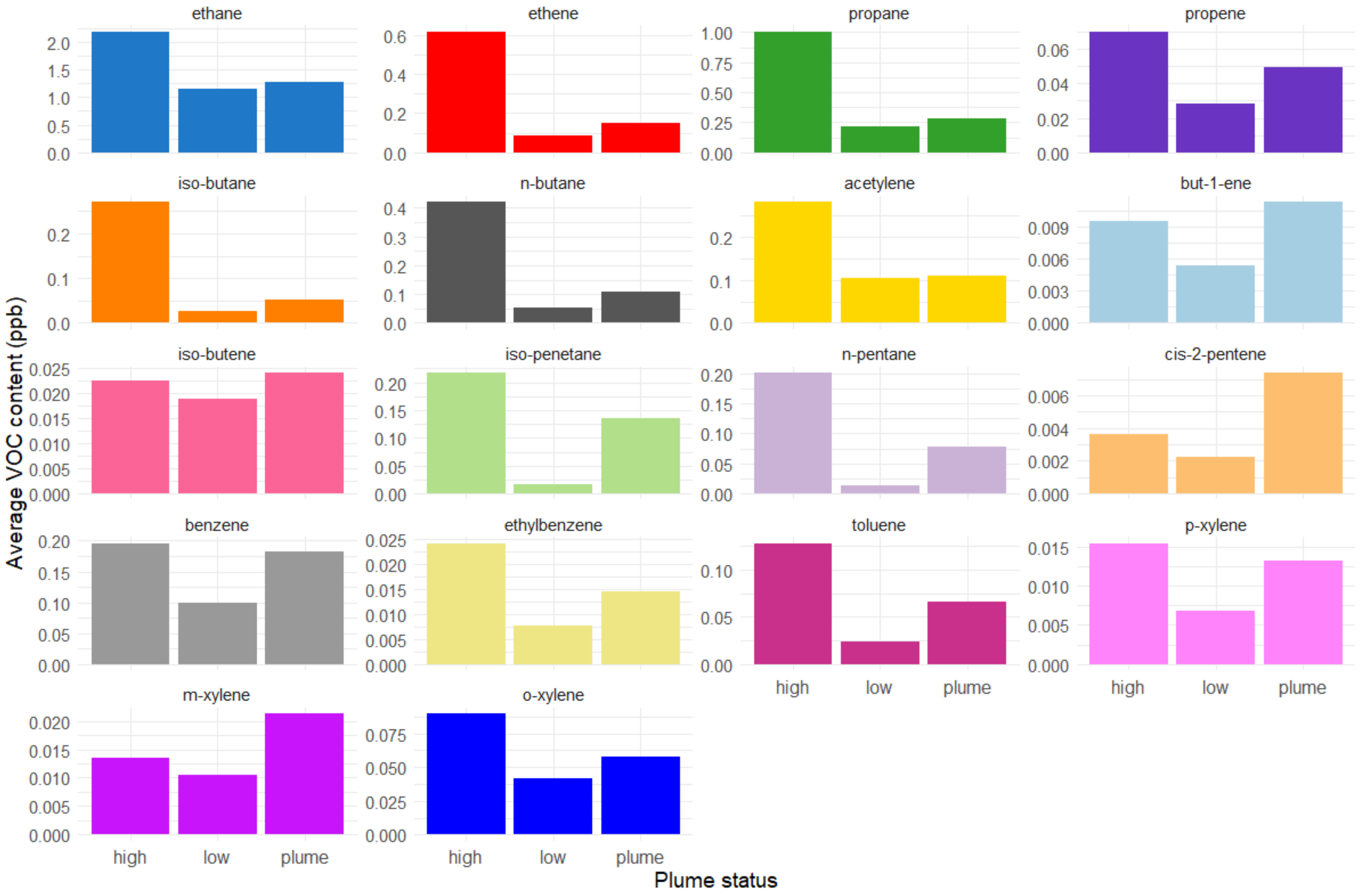

Figure 3.40: ACRUISE-2 average VOCs in plume, in low background and in high background species by species.

For benzene the plume and C263 concentrations are very similar (0.18 ppb and 0.20 ppb, respectively) and the low background is nearly half lower. The remaining VOCs are at sub 0.1 ppb levels.

Taking a closer look at the identified plumes it is clear that they don't have a particular pattern in common. No characteristic VOCs ratios were found either. Figure 3.41 shows VOC ratios with CO_2 measured in bottles thought to be taken in plumes. Some of the bottles, have interesting features, for example 101.3 and 101.4, both attributed to a 2020 built oil/chemical tanker Gwn 2 show large enhancement, especially in iso-pentane and n-pentane (to lesser extend n-butane). Such enhancement is not seen in any other sample, so it could be related to Gwn 2's cargo.

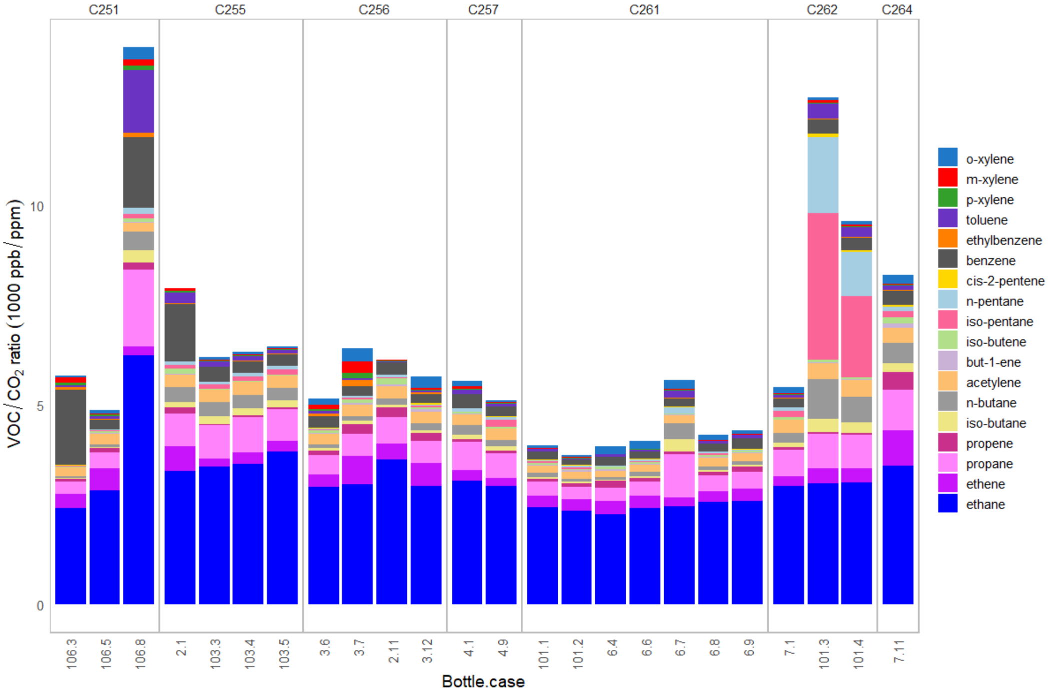

Figure 3.41: ACRUISE-2 VOCs to CO_2 ratios in plume.

Finally, among the individual background samples during ACRUISE-2 shown in Figure 3.42 the background levels are quite different in terms of composition, bulk concentration and different species concentrations. This is a combination of shipping and land air influence.

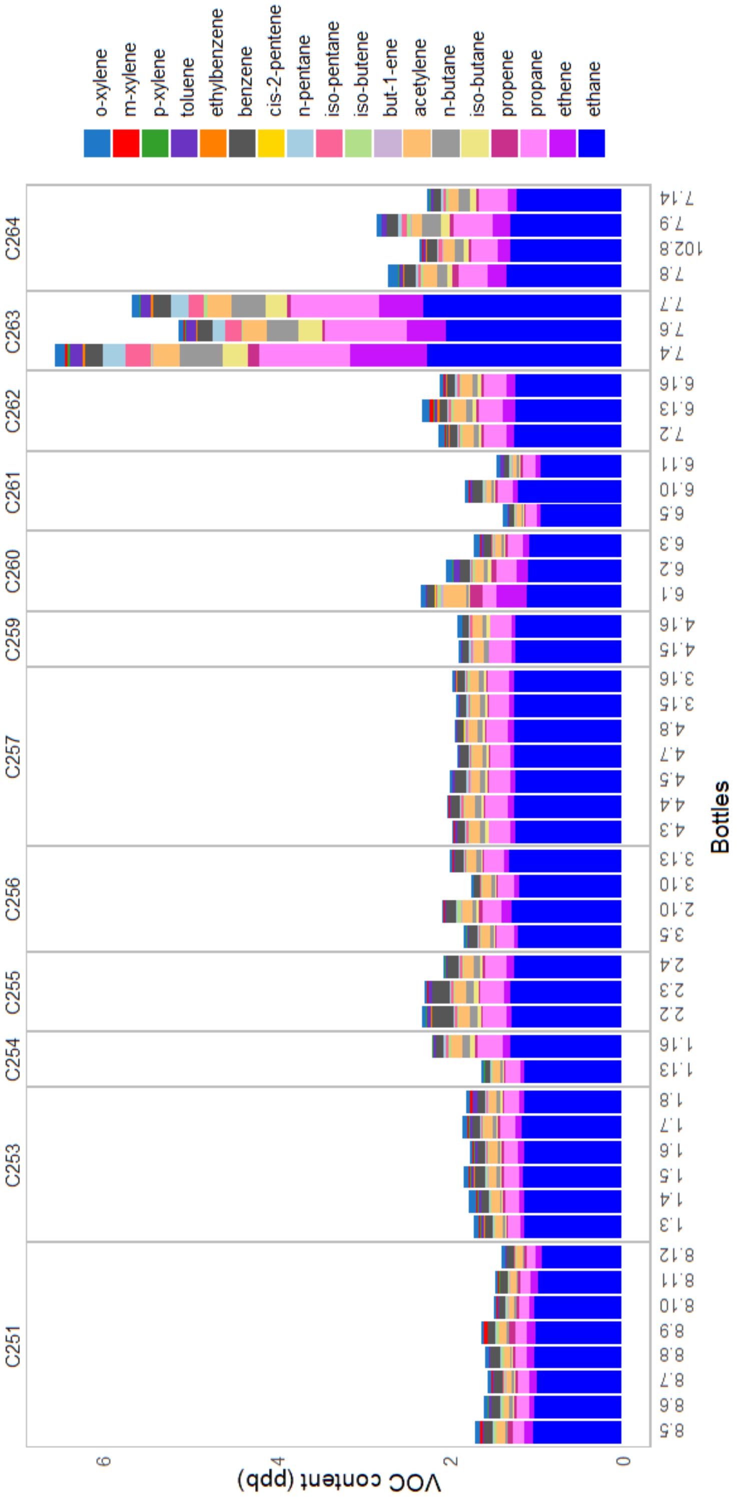

Figure 3.42: ACRUISE-2 all background VOCs samples

3.8.3 Case study: Al Ghuwairiya

During ACRUISE-2 7 SWAS samples were taken to capture the aging plume of Al Ghuwairiya. Despite the best effort, it is unclear which samples actually were taken in the plume. There is high confidence in the VOCs quantification, but telling a diluted plume sample from background is non trivial. An aspect that could additionally influence the VOC composition and make their attribution to specific ship or even to a plume at all is that different engines and generators on the ships likely have different signatures (similarly to SFCs), which might be the very case of Al Ghuwairiya.

Figure 3.43 shows the flight track map for the Al Ghuwairiya encounter with SFC suitable peaks and and SWAS samples marked. Bottle 6.4 was taken at the first plume targeting, but likely missed and bottle 6.5 was taken as background. Upon the first attempt of plume following one flow through bottle (101.1) was taken and on the second attempt another flow through bottle was used (101.2). In both cases the log indicates high certainty of capturing the plume. Since following the plume was highly successful 4 single fill bottles were taken, however they targeted an aged, diluted plume.

Figure 3.44 and Figure 3.45 show the measured VOCs as absolute values and enhancements compared to the average of two background samples. Enhancements show which species in the plume differ from well mixed background being an average of two samples from the area. Of course some local variability of the background is possible, but since the same values were subtracted from each bottle any offset will not affect the relative comparison between the bottles. The uncertainty is combined from both the sample and background. The absolute concentrations say less about the ships contribution to the VOC mix, but show the relation of each species to the uncertainty, removing ambiguity of whether there simply is no enhancement or whether both the background and sample contain too low concentration of a given species to quantify it. For example in case of iso-butane the enhancement is

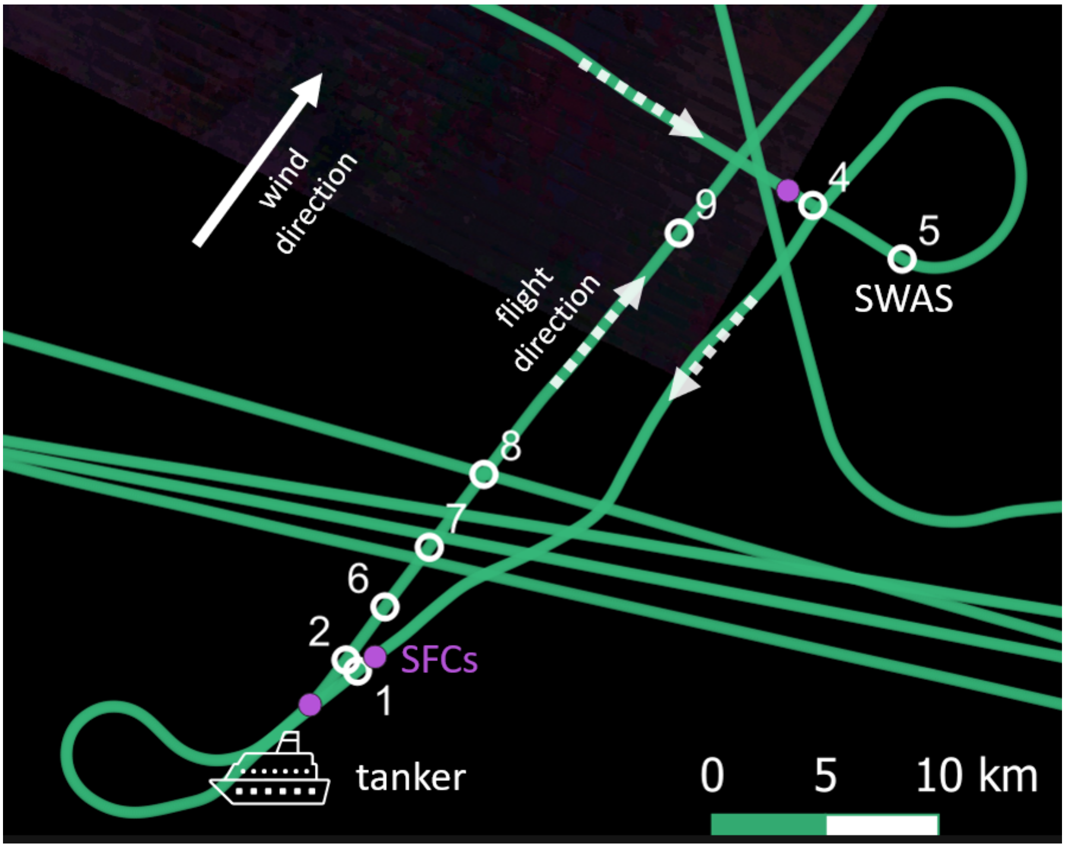

Figure 3.43: Al Ghuwairiya SWAS sample location with bottle number indicated. Plume fragments used for SFCs are marked in purple.

lower than uncertainty but the absolute values are substantially higher than uncertainty, but for o-xylene both the enhancements and absolute values are within the uncertainty bars, which means the concentrations are simply to low to quantify and no conclusion can be drawn.

Looking at the enhancements in Figure 3.45 the observation that stands out the most is that the CO_2 enhancement is very low for bottles 101.1 and 101.2 (sub 5 ppm) and below uncertainty for the remaining bottles. Similarly for methane - first two bottles show enhancement below 20 ppb. The time series for Al Ghuwairiya is showed in Appendix A.5. Compared to concentrations measured by FGGA and taking into account that the plumes might have been caught partially, these enhancements seem reasonable. This in turn implies that using whole air samples to analyse plume aging might not be an optimal method due to the level of plume dilution. It was nevertheless worthwhile attempting such a study for the benefit of future fieldwork. One species that is clearly enhanced in all of the bottles is ethene and one bottle that stands out is 6.7 showing far larger enhancements of propane, iso-butane, n-butane, n-pentane and m-xylene. With low methane it could be speculated that this sample was influenced by a different engine or generator to the dominant plume.

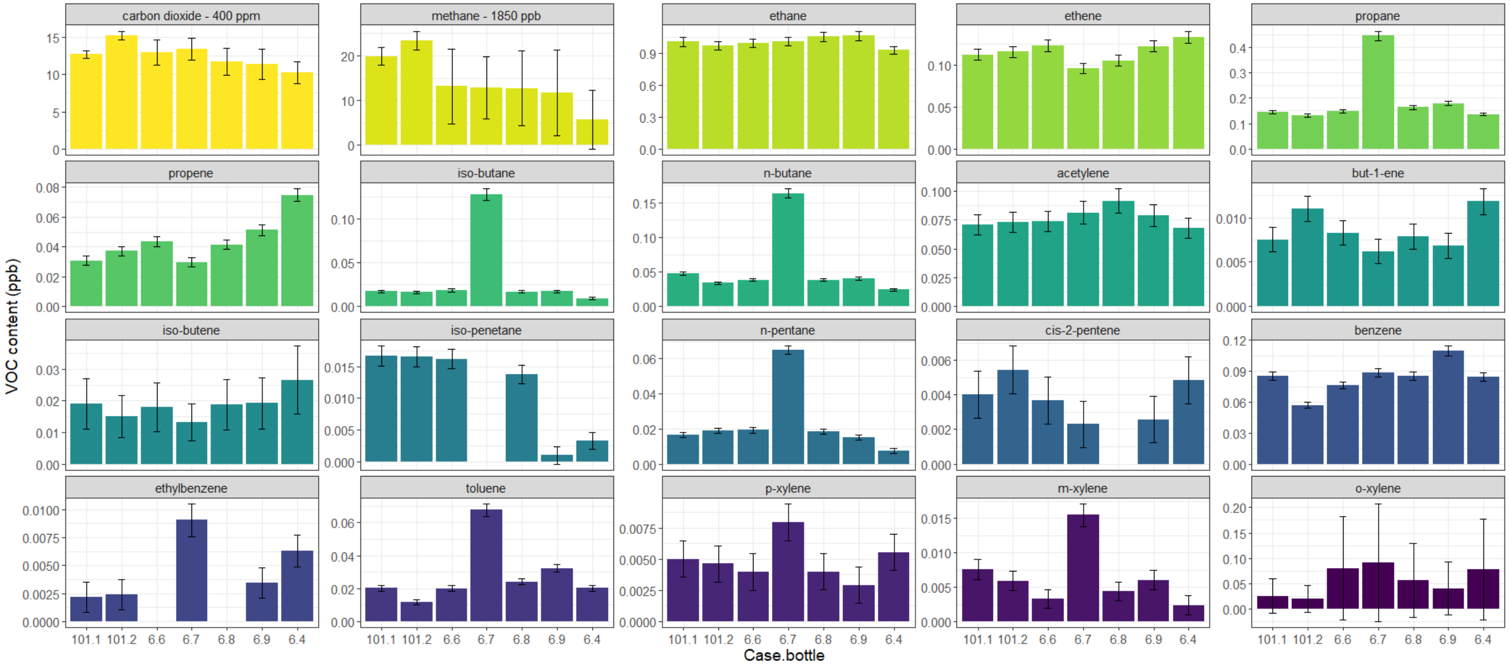

Figure 3.44: Al Ghuwairiya VOCs profile along the plume. Bottles ordered by distance from ship (leftmost is closest). Absolute concentrations are shown with methane and carbon dioxide having a baseline of 1850 ppm and 400 ppm, respectively, subtracted to show the differences better.

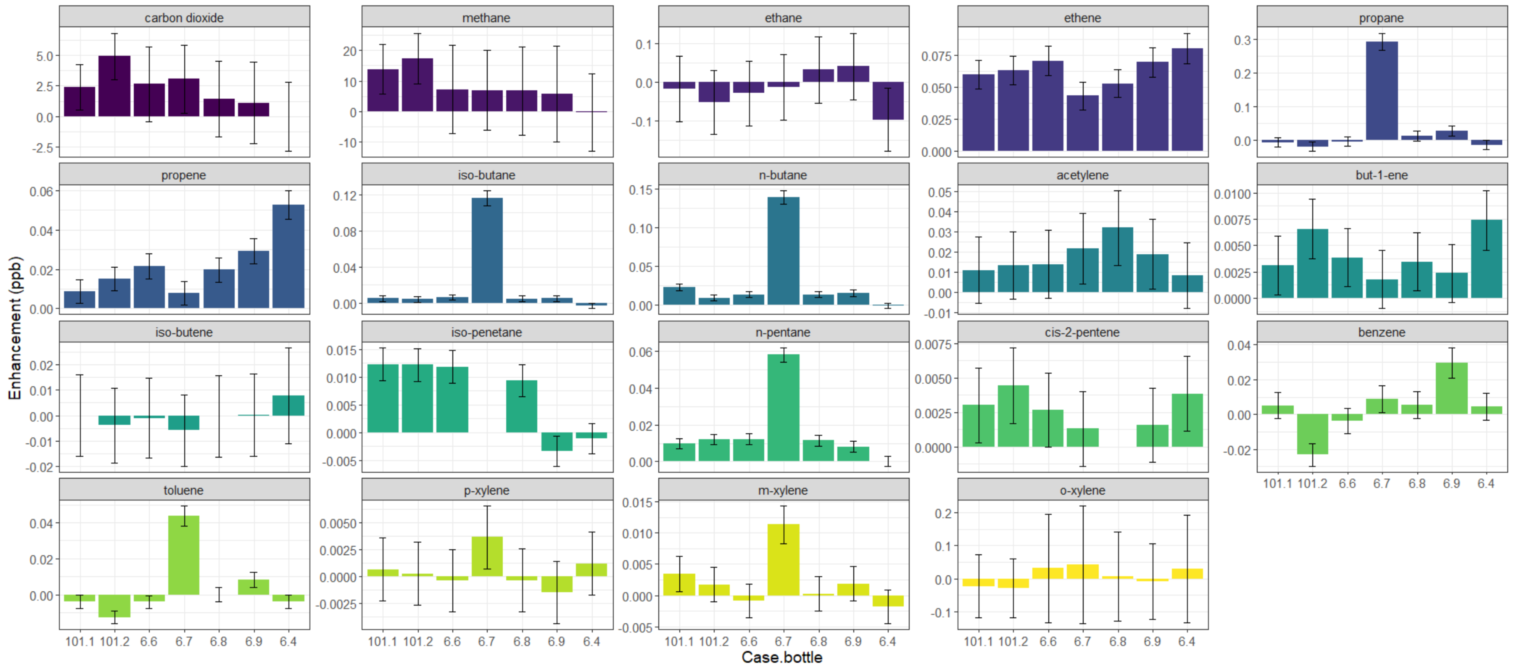

Figure 3.45: Al Ghuwairiya VOCs profile along the plume. Bottles ordered by distance from ship (leftmost is closest). The background was removed based on the average of the two closest bottles: 6.5 and 6.11. No ethylbenzene is shown because it could not be quantified in the background samples, so the enhancement could be calculated.

3.9 NO_x to CO_2 ratios

3.9.1 ACRUISE-1 measurements

During ACRUISE-1 NO_x was measured hence NO_x to CO_2 ratios can be derived for the dataset. The data was integrated in Origin rather than with `acruiseR` package, since there is a significant difference is peak resolution.

Average NO_x to CO_2 ratio for MSC Mirja in EC is 0.020 ± 0.006 and outside of SECA it is 0.020 ± 0.002. All NO_x to CO_2 ratios are in ppm ppm^{-1}. Hence despite a large change in emitted sulphur (0.08% ± 0.03% in SECA vs 2.88% ± 0.22% out of SECA), there is no change in NO_x to CO_2 ratio. Sadly, this is the only ship for which NO_x was measured in and out of SECA. No other ships could be sampled in SECA either.

For the ships outside of SECA the average NO_x to CO_2 ratio was 0.021 ± 0.002, hence higher than for MSC Mirja. The individual values ranged from 0.002 to 0.050, while average values for identified ships from 0.009 to 0.041. Similarly to SFCs values for one ship can vary slightly, although mostly agree within uncertainty.

3.9.2 Comparison with STEAM and road vehicles

Like in case of Section 3.6.2 the STEAM3 model data for ships encountered during ACRUISE-1 provided by Jukka-Pekka Jalkanen from Finnish Meteorological Institute was used as a comparison with the measured NO_x to CO_2 ratios. Figure 3.47 compares modelled and observed ratios, showing a reasonable agreement. The ships that stand out are CMA GCM Cayenne with the highest ratio observed, Hoegh Gallant (again), Jy Vincentia and Hirado (which actually has lower ratio than predicted). Figure 3.48 shows the differences as a function of the observed ratios. Similarly to SFCs comparison (see Figure 3.34), the higher the observed value the more negative the difference, which is reasonable when comparing instantaneous values

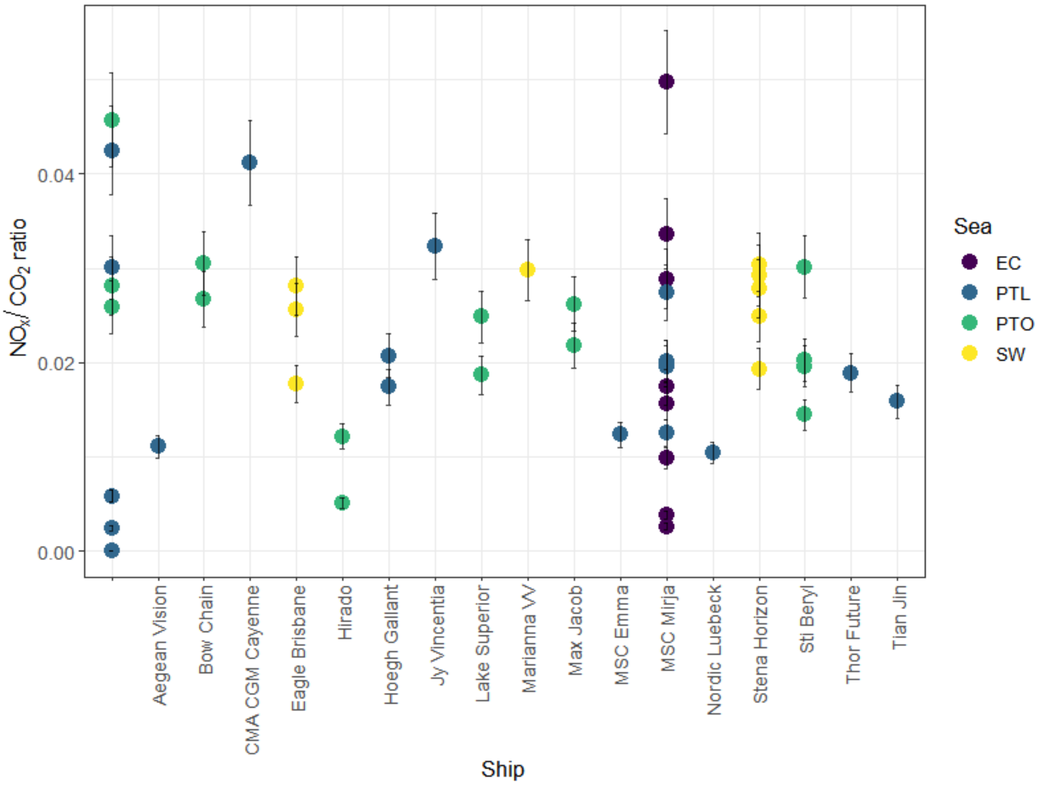

Figure 3.46: ACRUISE-1 NO_x to CO_2 ratios coloured by area of encounter, where SW - South West approaches, PTL - Portuguese coast shipping lane, PTO - Portuguese coast open waters, EC - English Channel.

with average yearly values.

Wilde et al. [87] conducted very recently a study of NO_x to CO_2 ratio from vehicles in London. The ratios measured using a mobile van laboratory as well as remote sensing ranged from 0.000 to 0.015 in the most extreme cases. Meanwhile, all the observed ship ratios averaged on 0.022 ± 0.002, with average values for individual ships ranging from 0.009 to 0.041. Hence the highest road vehicle ratios are comparable to the lowest ship ratios, meaning that they can have a significant influence on the local NO_x budget in coastal areas.

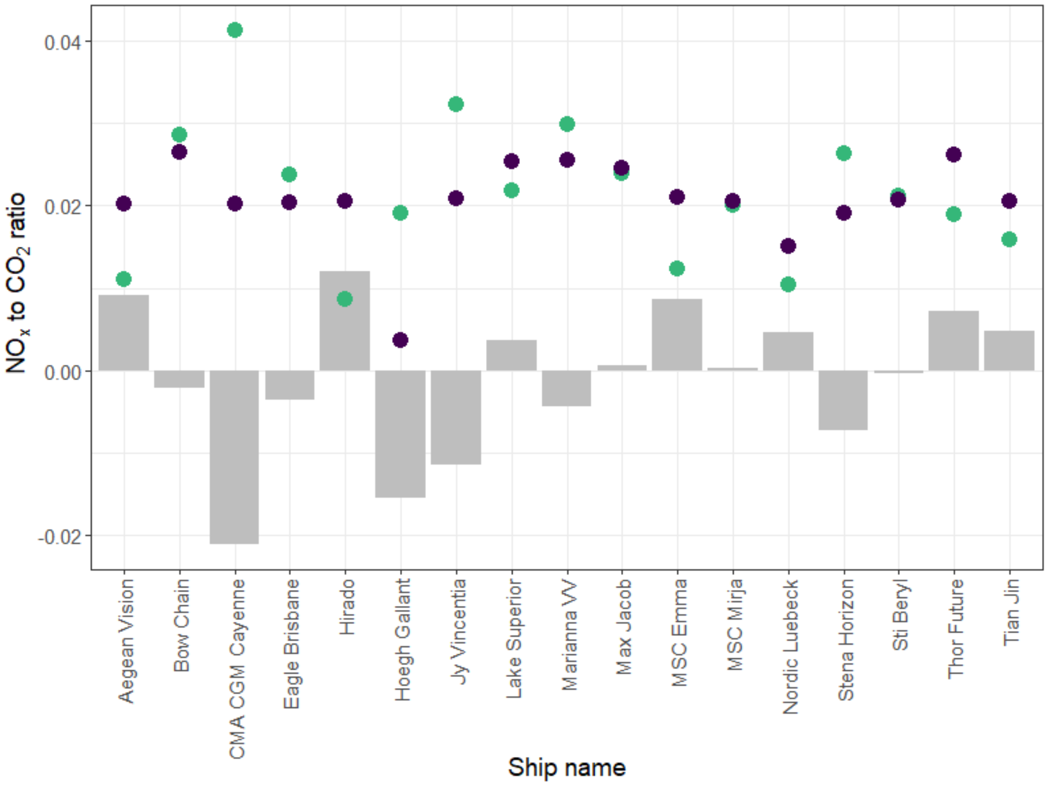

Figure 3.47: ACRUISE-1 comparison of NO$_x$ to CO$_2$ ratios from observed data (green) and model (purple). Difference between modeled and observed values is shown in grey. Model data credit: Jukka-Pekka Jalkanen.

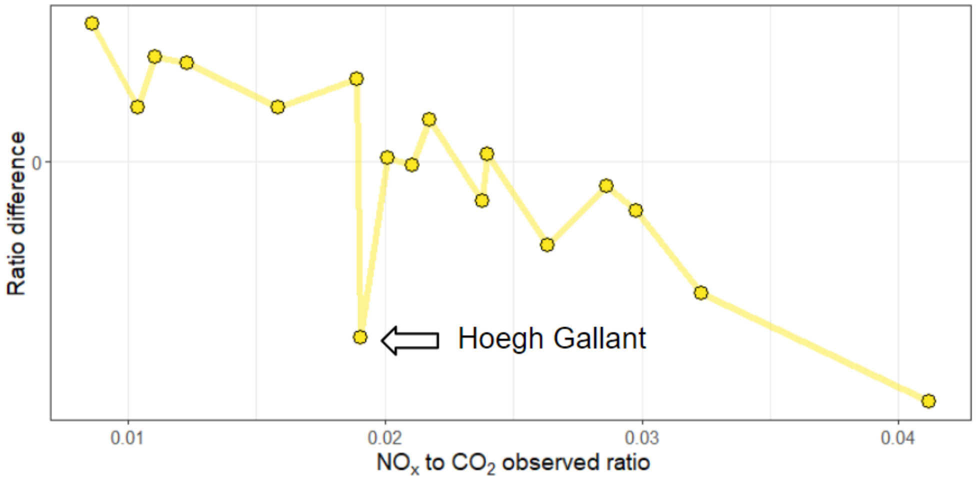

Figure 3.48: Comparison of differences between modelled and observed NO$_x$ to CO$_2$ ratios against observed NO$_x$ to CO$_2$ ratios. The difference is defined as ratio$_{model}$ - ratio$_{observed}$. The ship standing out of the trend is Hoegh Gallant. Model data credit: Jukka-Pekka Jalkanen.

Chapter 4

Conclusions: Gaseous emissions from ships

4.1 Lessons learned

The first ACRUISE campaign took place in July 2019 from Stansted and Porto. The weather conditions during that time of the year were favourable for the cloud flights, as expected. NO_x instrument worked well for detecting the plume in the cloud and a good aerosol and cloud focused dataset was collected. There was also a lot of successful shipping lane surveys for modelling purposes, i.e. not purposefully deviating flight pattern to transect ship plume. Most of days double flights were flown.

However, the campaign had some serious setbacks too. The gas phase chemistry payload (Core Chemistry) was seriously affected by lack of a in-house IT specialist and had to be reverted back to pre-2019 configuration, which meant using the old FGGA in below 1 Hz mode, which was insufficient for the type of plumes measured. The CO_2 measurement was a limiting factor and meant that a lot of plumes could not be quantified. The dominant strategy for intercepting plumes was crossing them perpendicularly, which was challenging for filling the WAS samples. Finally, the identification of the ships took place 3 months after the campaign, with hope of somehow backtracking the ships and matching them with aircraft track. At that point, most of the data was not available within the Marine Traffic licence and the resolution of saved data proved insufficient for busy shipping lanes. Luckily all the ships with CO_2 signal strong enough to be integrated were identified, based mainly on the flight chat logs and screenshots of Marine Traffic maps sent to the aircraft during the flight. During ACRUISE-1 more flights in English Channel and SW Approaches were planned, however they did not take place due to an aircraft fault. Overall, the first campaign could be considered unlucky with the technical faults, but it provided an excellent learning opportunity for the future fieldwork and a unique dataset which was also used for modelling purposes.

The next ACRUISE campaign was originally planned sometime in May-July 2020 based in Porto, but it was delayed by the pandemic until September 2021 and moved to Exeter. A number of important improvements was made. Mostly long single flights were flown, to maximise on task time compared to the transit. The Core Chemistry suite had its IT problems resolved which allowed operating all instruments in the fastest modes additionally improved by a new, fast inlet (see Section 2.1.2). WAS was upgraded to SWAS allowing shorter lag and filling times. The ships were identified and logged live on board. The ground communications played bigger role in this campaign, which improved use of the on task time. There were also successful flights designed specifically to target ships in and out of SECA on consecutive days. More individual ships picked ahead of the flight were targeted and studied in more detail, including flying along the plume to help taking SWAS samples. Plume directions were determined in flight.

A lot of improvements were made thanks to hard work of the ACRUISE team and most of the drawbacks were caused by factors out of our control. The delay and relocation caused by the pandemic meant that the cloud conditions were far from ideal. The location was also not optimal for the shipping lane surveys and for modelling purposes - in Bay of Biscay the ships were too sparse, whereas English channel is under significant influence of the continental air. Plume aging and cloud interaction work, which relies on NO_x as a tracer was impossible due to the NO_x rack not being serviceable at the time. Moreover, there was a 10 month delay in receiving calibrated CO_2 and SO_2 data, which further delayed the work. The campaign was a success at the end, despite the shift of focus.

The final campaign took place in May 2022 (in dashed hopes of the NO_x rack being resurrected). The main focus of the campaign were LNG tankers and sampling each plume multiple times, staying in it as long as possible. There were also 3 SO_2 instruments, including fast and sensitive SO_2-LIF. The main operational improvement was logging the speed of the ships during encounters and their load status by the ground team. The cloud conditions were again far from ideal.

ACRUISE fieldwork demonstrates how planning and testing proposed solutions are crucial to the optimal use of the flying hours. If this work could be redone, first there should have been a full test flight e.g. in English Channel and South West Approaches at least 6 month before the first campaign. This would allow training ground communication and testing the capacity of Marine Traffic. And second, the complete data analysis including peak integration for emission factors and VOCs content analysis of WAS should have been performed in order to verify if the proposed strategy delivers optimal data for this purpose. This would allow making the improvements seen from ACRUISE-1 to -2 before the main campaigns would have started.

4.2 Sulphur fuel content

The main objective of this work was developing methodology for measuring apparent sulphur fuel content in ship plumes of board of large research aircraft and to check the level of compliance to the new IMO legislation.

Both objectives were fulfilled.

The study has shown that most of the ships comply to the new legislation and to the SECA limits. It also became apparent that for future work fast (5 Hz or faster) measurements are needed and that using a whole air sampler to study VOC composition in ship plumes is inadequate.

Since previous studies included mostly ground measurements of ships passing coastal areas or measurements in ports, the methodology developed here is very much novel. The basis for it were measurements of offshore oil and gas rigs using FAAM aircraft, however the first campaign verified a lot of assumptions originally made. Ship plumes are far more difficult to capture due to lower stack height, constant movement of the ship and smaller size of the plume. However, during the two next campaigns the methods were improved offering an established framework for the future measurements. The key throughout the campaigns was ground communications and decision making on board, as well as meticulous note keeping. This also made FAAM BAe-146 particularly suitable for the ship measurements. On one hand it is big enough to take up to three mission scientists on the other hand, thanks to four engine setups it can maintain minimum of 100 ft over water. Even though most of the research aircraft shifts to high automation and fewer people on board, projects like ACRUISE show that more staff on board can be advantageous. In future using smaller aircraft or unmanned aerial vehicle could reduce costs of such measurements.

In terms of compliance to the legislation, the campaigns showed that the ships mostly stay under the SECA limits. In 2019 MSC Mirja, the only ship measured in English Channel showed average of 0.08% ± 0.05% 1σ. In 2021 the ships measured in SECA also averaged on 0.08% ± 0.22% 1σ. In the shipping lanes and open ocean the average SFC dropped from 2.34% ± 1.09% 1σ in 2019 to 0.27% ± 0.50% 1σ in 2021 and 0.12% ± 0.21% 1σ in 2022. It is important to note that, even though 23 out of 82 ships in 2021 and 4 out of 20 ships in 2022 showed at least one SFC above the new limit of

0.5% none of them exceeded the previous limit of 3.5%. Meanwhile, in 2019 4 out of 21 ships encountered out of SECA gave an SFC above the 3.5% limit.

In short, the levels of compliance to the new legislation is good despite higher cost of clean fuel or scrubber installation. It is also worth noting that no correlation with age was found, hence even the old ships are retrofitted with cleaner systems. This finding might not be the most exciting case, but it certainly confirms successful marine law enforcement. The comparison with the models is also a success story - for 2019 data the agreement is good with the caveat of comparing instantaneous to yearly average emissions and for 2021 ships are often overestimated, also suggesting the success of the new sulphur limits introduction.

4.3 Other species

Methane, NO_x and VOCs are also briefly presented in this work. In each of the cases the measurements did not hold up to the expected results for different reasons, but that should be expected when developing a novel sampling strategy. Hopefully in future more precise ship positions are available and the methane data can be successfully used for dispersion modelling. Estimating the emission rates from LNG tankers would help to fill in a huge gap in understanding of the exact impact of LNG transport. So far, the CH_4 to CO_2 ratios seem to agree with the only empirical LNG tanker study by Balcombe et al. [51] which is very promising. Also the difference between older and younger tankers is worth further investigation. Establishing whether waterborne LNG transport and usage as fuel does not offset the air quality gains by deteriorating the climate is crucial for future policy making. Further work on the NO_x data is possible as a part of plume chemistry project however it is rather limited by absence of NO_x in ACRUISE-2 and -3 when the quality of other chemistry measurements was better. VOCs work will be continued as a part of a different PhD project with emphasises on background composition, since plume sampling proves to be rather unreliable. Moreover, the methane, NO_x and VOCs work presented here can be used as a guideline for the future studies.

Chapter 5

Introduction: Methane fluxes from tropical wetlands

> *In reality, it is very difficult to find out the cause of a bad or disturbed eddy correlation measurement*
>
> Foken & Wichura, 1996 [88]

5.1 Global methane budget

For thousands of years, human activity has altered the environment. Air pollution was recognised as an issue as early as the Greeks and Romans, with the first known air quality regulation issued in England in 1306 [89]. However, since the Industrial Revolution a rapid increase in concentration of greenhouse gases (GHG) such as methane and carbon dioxide has been observed. At the end of the 19th century Arrhenius made a theoretical prediction of human-induced global warming [89]. Even though his theory was deemed too controversial at the time, his estimations have since been proven accurate. The changes observed from the 1950s have been unprecedented and exceed any possible natural climate cycle variability [90].

GHG are capable of absorbing and re-emitting IR radiation, increasing surface temperature on our planet. Without GHG the global average would be about -15° C, but with GHG it is approx. 20° C. The two most significant GHG are carbon dioxide and methane. CO_2 is a long lived species, which equilibrates between atmosphere and ocean in $1:4$ ratio on the course of millennia. It is believed to cause irreversible climate change [91]. CH_4 is shorter lived (approx. 12 years), but a more potent compared to CO_2 [90]. It was identified by Volta in the late 18th century and initially deemed as an interesting phenomenon of flammable gas bubbling from wetlands [92]. Even when climate change became an internationally recognised problem, it was CO_2 that attracted most of the attention. Currently methane constitutes 18% of anthropogenic GHG emissions in terms of CO_2 equivalents [93].

In 2015, the Paris Agreement provided a breakthrough in combating the climate change. It was agreed that [94]:

- substantially reduce global greenhouse gas emissions to hold global temperature increase to well below 2°C above pre-industrial levels and pursue efforts to limit it to 1.5°C above pre-industrial levels, recognizing that this would significantly reduce the risks and impacts of climate change
- periodically assess the collective progress towards achieving the purpose of this agreement and its long-term goals
- provide financing to developing countries to mitigate climate change, strengthen resilience and enhance abilities to adapt to climate impacts.

To achieve these goals, the Agreement encourages all parties to preserve sinks and reservoirs of GHG, maintain international cooperation, recognise efforts of developing countries and mitigate effects of the climate change (e.g. extreme weather events). However, according to Climate Action Tracker (climateactiontracker.org), at the time of writing this work only two countries, namely Gambia and Morocco, complied with the 1.5 degrees target, while further 6 (Bhutan, Costa Rica, Ethiopia, India, Kenya and Philippines) met the 2 degrees targets. All other countries and organisations failed to meet the target significantly. Nisbet et al. [95] warn that the fast and poorly understood growth of atmospheric methane since 2014 can jeopardise Paris Agreement targets. This means that there is an urgent need of reducing anthropogenic methane emissions.

Global methane emissions are estimated to be between 550 and 740 Tg yr^{-1}, out of which 50-60% is attributed to human activity [96]. Overall a quarter of anthropogenic radiative forcing is related to methane [96]. Overview of all climate forcers is shown in Figure 5.1, while more detailed description of all methane sources and sinks is below.

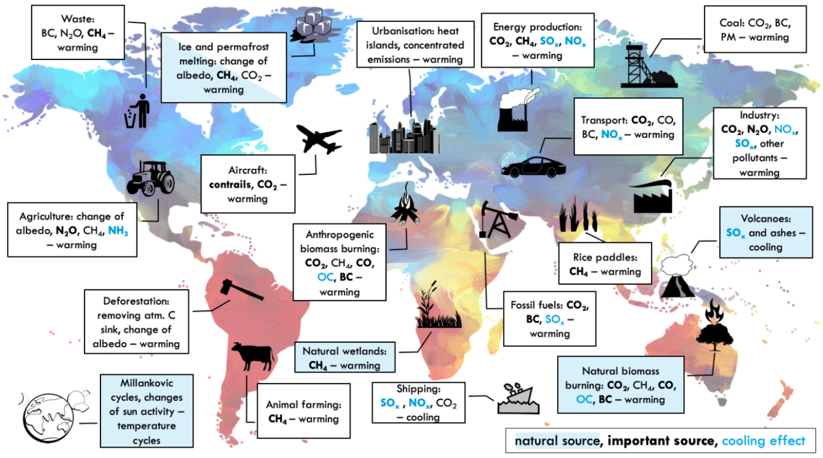

Figure 5.1: Overview of major natural and anthropogenic climate forcers by source (BC = black carbon, OC = organic carbon). Based on: IPCC AR5 [90].

Current research suggests that the major sources of atmospheric methane are natural wetlands, described further in Section 5.3. The next major natural methane source is geological emissions. The increasing temperature of ocean water facilitates the release of methane present in the ocean floor sediments; this, is however compensated by carbon dioxide uptake [97]. Microseepages are the effect of buoyancy of methane (and other light alkanes) located underneath sedimentary rocks. The gas often leaks around the edges of geological basins [98].

Over 700 mud volcanoes are known to exist around the world. Each contains a number of gas vents that also lead to microseepage in surrounding area. The emitted gas contains over 90% CH_4. One volcano is estimated to release up to 10^3 t CH_4 y^{-1} (i.e. 10^{-3} Tg) just from the main venting [99].

Freshwater bodies, here understood as natural lakes, rivers and floodplains, release methane through ebullition, diffusion and plant transport, lessening the terrestrial methane sink [100]. Ebullition is particularly difficult to study due to its irregular occurrences. However, methane bubbles trapped in frozen water help to map 'hotspots' and quantify the overall flux. A study of North Siberian thaw lakes formed on carbon-rich yedoma permafrost showed that the average flux for such lakes (43.7 ±3.2 g CH_4 m^{-2} yr^{-1}) is higher than originally assumed. 90% of the flux comes from ebullition. Moreover, about 15% growth of lakes area since 1970s resulted in about 60% increase in methane emissions. Overall, it is estimated that lakes emit 8-48 Tg CH_4 yr^{-1}, which is more than oceans [101].

One of the minor methane sources according to The Intergovernmental Panel on Climate Change (IPCC) [90] is permafrost. However, its importance is growing with climate change. For example, in the Interior Alaska 2014 and 2016 were relatively wet and the rainfall facilitated an increase of deep soil temperatures. The methane emissions at the edges of wetland having direct contact with permafrost doubled compared to drier years [102].

Biomass burning can be associated both with human activity, e.g. crop-related biomass burning clearance in post-harvest season [103, 104], and with naturally occurring fires. The intensity of natural fires is related to local climate variability. For instance, in 2010 during a drought in the South Amazon, methane emissions from biomass burning were approx. 6 times higher than in the subsequent 'wet' year, making the overall methane flux estimate in the region 22% higher than in 2011 [105, 106]. Deforestation activities in dry season also can lead to biomass burning outbreaks [106].

Considering purely anthropogenic sources of methane, the use of fossil fuels is the major contributor. Methane from fossil fuels can be distinguished from, e.g. wetland CH_4 by relatively higher, although still negative $\delta^{13}CH_4$ (i.e. ratio of the heavier stable isotope of carbon). The resumed increase of methane, after the relatively flat period of 1998-2007, is claimed to be driven by increase in microbial activity for unknown reason (approx. 36 Tg y^{-1}) and fossil fuel use (approx. 15 Tg y^{-1}). Both values, however bear high uncertainty (30% and 50% respectively) [107, 108]. This claim is based on the analysis of isotopic signature of carbon. Different biological and chemical processes can yield methane with characteristic ratio of the two stable isotopes of carbon: ^{12}C and ^{13}C. These ratios can be used to identify source of methane. Schwietzke et al. [109] suggest that there are great underestimations in methane emissions from fossil fuels (both from usage and geological seepages) in the first place. Nisbet et al. [110], however, attribute the change specifically to increased methanogenic activity of tropical wetlands and agricultural land, since fossil fuels cannot explain the ^{13}C depletion.

Livestock especially ruminants, emit significant amount of methane. A number of small scale studies show that on average about 6.5% of cattle's energy intake is used up on methane production, with the worst results (8%) for grazing animals and best (3%) for animals fed high-concentrate diet [111]. Another aspect of livestock's methane fluxes can be illustrated by a study of cattle's excrements in rangeland dominated by C3[*] or C4[†] plants [112]. It shows that even though the uptake of methane for C3 pastures is about one-third greater than for C4 pasture, the emission is over twice as large. In both cases, the presence of cow excrement reduces methane

---

[*] Most plants are C3, e.g. wheat, sunflower

[†] Minority of plants including e.g. maize, sugarcane

uptake by the soil, with C3 pastures leading to considerably greater flux. The majority of plants is C3 - they capture carbon in Calvin cycle simply using rubisco enzyme and producing 3-carbon phosphoglyceric acid. C4 plants, in turn, developed a photo-dependant carbon-capture stage before Calvin cycle involving 4-carbon oxaloacetic acid to reduce photorespiration in hot climate. The difference in isotopic signatures between these is caused by enzyme preference for ^{12}C compounds and slower diffusion of ^{13}C compounds in plants tissues, which is more pronounced in case of C4 plants.

Most of the landfills across the world have no control over their methane emissions and only a small fraction attempts to produce biogas for heat and electricity generation. It is estimated that 50 m^3 of methane can be produced for every tonne of typical landfill waste assumed to contain 60% of dry biomass [113]. Using landfill covers, i.e. layers of compressed soil covering waste, can oxidise part of the emitted methane; however the efficiency of this process is limited by amount of methanotrophs in the soil. This is a serious drawback as landfills typically contain methane 'hotspots' [114].

The substantial impact of rice paddies on the global methane budget was first noticed in early 80s [115]. Approximately 9 to 19% of global emissions come from rice cultivation. Additionally, methane release from rice fields is forecasted to grow with increasing temperature and levels of CO_2 [116]. However, there is potential for limiting methane emissions through introduction of high-yield cultivar, characterised by highly porous roots facilitating oxygen transport to the soil and resulting CH_4 oxidation [117]. Another way is applying water saving regimes [118–120].

The major sink of methane is the oxidation by the hydroxyl radical:

$$\begin{gathered}
CH_4 + OH \longrightarrow CH_3 + H_2O \\
CH_3 + O_2 + M \longrightarrow CH_3O_2 + M \\
CH_3O_2 + NO \longrightarrow CH_3O + NO_2 \\
CH_3O + O_2 \longrightarrow HCHO + HO_2
\end{gathered}$$

Some authors hypothesise that the resumed increase in global methane after 2007 can be attributed to a drop in OH concentration [121, 122]. In the stratosphere, an additional sink is $O(^1D)$ [123]. In the marine boundary layer CH_4 can be removed by chlorine radicals [124]:

$$CH_4 + Cl + O_2 \longrightarrow CH_3O_2 + HCl$$

This fact was noticed thanks to studies of the kinetic isotope effect (KIE) on methane removal by OH based on $\delta\ ^{13}CH_4$. Anomalous results were explained by a competing reaction with chlorine radicals having a much larger KIE [125, 126].

Soils [127] are, overall, considered sinks for methane, nevertheless their role in methane budget is more complex. In anaerobic conditions, the methanogens living in soil produce methane, however they are sensitive to oxygen presence - in aerobic conditions, methanotrophs dominate. It is thought, that both types of microorganisms co-exist and the external conditions - humidity, temperature, pH etc. determine which of them dominates. The use of agrochemicals also has an effect on methane production, e.g. nitrogenous fertilisers are known to inhibit methane oxidation and so lead to its increased emissions.

Looking at all the sinks and sources in the methane budget, it becomes clear that high uncertainty is a common problem and the scale of methane's influence on climate remains only an estimate. Relatively poor understanding of natural processes governing methane cycle, especially for wetlands, permafrost or soils, and insufficient regulation and monitoring of anthropogenic activity (e.g. landfills, fossil fuels) provide an imprecise and likely biased bottom-up picture. Measuring methane and verifying its isotopic signatures helps to refine such models, but also provides greater data density for top-down estimates.

5.2 Methane measurements in Africa

Most of methane is present in the troposphere, though in mid-high latitudes up to 25% of the vertical column resides in the stratosphere compared to 5% near the equator [128]. Otherwise, methane is relatively well mixed with annual average mixing ratio of 1879 ppb (2020) [129], which is approx. 730 ppb increase since pre-industrial times. Seasonal and latitudinal methane variability is well described thanks to programs such as NOAA Global Greenhouse Gas Reference Network, however there are huge gaps in ground measurement coverage (see Figure 5.2) - methane in parts of Siberia, inland Africa and inland South America is measured only remotely [96].

Even though the global methane estimates are deemed fairly accurate, such gaps in measurement network introduce biases and increase uncertainty. Unfortunately, making the coverage more even proves to be difficult due to political and logistic reasons [96, 130].

Abandoning the 'Western-centred' approach to GHG research can be motivated not only on ethical ground, but also on not to introduce bias. For instance, Turetsky et al. [131] conducted a meta-analysis of methane emissions from 71 wetlands only from Europe and North America. Based on the data collated it seems that subarctic wetlands are characterised by considerably higher flux (per area unit) then subtropical ones, yet that is purely result of the bias. The study is certainly useful as a characterisation of boreal and temperate wetlands in Europe and Northern America, but it fails to paint the full picture of global methane emissions from wetlands.

Filling the gaps in the measurement network is crucial, since Africa is currently the most dynamically developing and growing continent [132]. According to the International Monetary Fund [133], the top 5 countries with the highest real gross domestic product growth rate before the COVID-19 pandemic were: Libya, Rwanda, Ethiopia, Bangladesh and Uganda. The significant population increase as well as socio-economical changes will

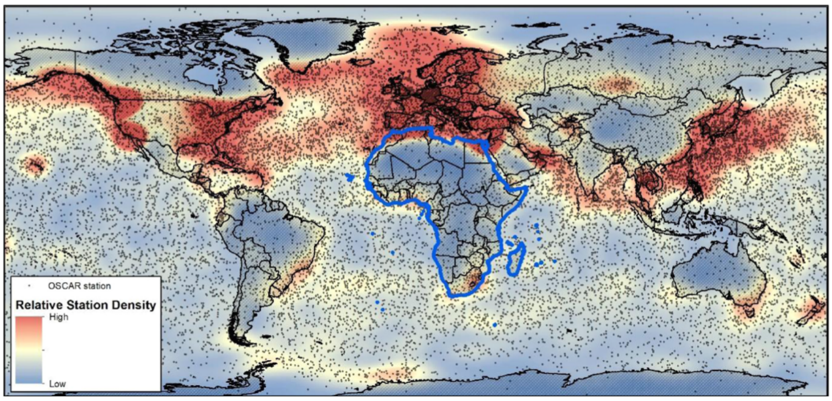

Figure 5.2: Global distribution of measurement stations listed by WMO's Observing Systems Capability Analysis and Review (OSCAR). Source: López-Ballesteros et al. [132].

impact the emissions of GHG, hence filling the gaps in the site network should be prioritised in order to introduce efficient mitigation policies [132].

Another example illustrating the Western centred bias of the environment monitoring is the quality and GHG flux of inland waters. Africa has approx. 2 water quality measurement stations for every 1 mln km^2, which orders of magnitude less than Europe [134]. For instance, in global inland waters CO_2 data review by Raymond et al. [135] less than 20 out of nearly 7000 data points represent Africa (excluding South Africa, which is better researched). Methane data coverage is no better [136] and studies frequently use Amazonian data as a proxy, both in terms of inland waters content and emissions [134, 136]. Borges et al. [136] point out that the ratio of CO_2 to CH_4 flux is considerably lower in Sub-Saharan Africa than in most of studied temperate climate rivers. They show that the water content of methane correlates positively to the fraction of catchment area covered by wetlands. Moreover, riverine fluxes often assume only diffusive emissions, yet ebullition accounts for approximately a fifth of the overall emissions in case of Congo and Zambezi [136, 137]. The issue is well summarised by Kim et al.:

> there are huge research gaps. Africa is a vast continent, with a multitude of land uses, climates, soils, and ecosystems. Field-

> based data on soil GHG emissions from many areas, soil types, and environments are extremely sparse, and as a result our understanding of Africa's contribution to global GHG emissions remains incomplete and highly uncertain. There is an urgent need to develop and agree on a strategy for addressing this data gap. The strategy needs to involve identifying priorities for data acquisition, utilizing appropriate technologies, and establishing networks and collaboration.... ([94])

The last (and possibly only) attempt to quantify African methane budget dates back to 1992 [138] and is now outdated, especially in light of recent methane emission developments [95]. Despite the technological advances made since the early 90s, nowadays scientists researching GHG emissions in Africa struggle with the same issues as Delmas et al. - wetland seasonality, insufficient data coverage and high uncertainty of the wetland area.

5.3 Wetland methane emissions

Wetlands can be defined as follows for purposes of methane emissions studies:

> ecosystems with inundated or saturated soils or peats where anaerobic conditions lead to methane production. ([139])

They are the biggest source in the IPCC global methane budget [90] contributing 20-40% of global emissions, yet they are subject to 50% uncertainty [140], due to high uncertainty over their exact extend, seasonality and complex response to changes in meteorological conditions [139]. Boreal and tropical wetlands show strong positive feedback to increasing mean surface temperatures, meaning that by the end of 21st century they might dominate anthropogenic emissions by even 55% [110, 141].

The two main routes in which methane is emitted is plant transport, especially in temperate climate, and ebullition, dominant in tropical climate or for plants with undeveloped aerenchyma (i.e plant tissue creating air spaces or channels to enable exchange of gases between the emergent and submerged parts of the plant). Intensity of ebullition depends strongly on a balance between methanogens, i.e. archaea producing methane and methanothrops, i.e. mainly aerobic bacteria that oxidise methane. Since aerobic conditions dominate in this environment, methane flux from wetlands is positive in most cases. Methanogenesis takes one of the two following routes:

$$\mathrm{CO_2 + 4\,H_2 \longrightarrow CH_4 + 2\,H_2O} \quad \text{or} \quad \mathrm{CH_3COO^- + H^+ \longrightarrow CO_2 + CH_4}$$

Diffusion through soil is also possible, albeit extremely slow and hence insignificant on the scale of a wetland [141].

The major factors affecting the methane flux are anoxia (i.e. oxygen depletion in water), temperature and organic carbon availability [139, 141]. Additionally, factors like pH, rate of decomposition, inundation or macrophytes, i.e. aquatic plants either emergent, submerged or floating [141]. Tropical freshwater wetlands are especially poorly studied compared to their arctic, boreal and temperate friends [142].

Wetlands might emit methane, but they are also one of the major terrestrial carbon reservoirs, containing between 20 and 30% of global soil carbon, despite covering only 5-8% of Earth's surface. In fact, most wetlands are net carbon sinks [143–145]. Unfortunately, it is estimated that in Europe half of the original peatlands were lost to human activity, mainly agriculture [141]. Compared to 300 years ago, over 75% of worldwide natural wetland area was destroyed or gravely affected by human activity [146]. Currently it is believed that wetland restoration is an excellent way of mitigating GHG emissions and increasing biodiversity [144, 147]. Indeed, more and more local governments try to preserve the wetlands that still exist and restore the lost ones benefiting additionally from improvements in water management.

5.4 Zambian wetlands overview

5.4.1 Kafue Flats

Kafue Flats are wetlands in Central Zambia along the Kafue River, covering approx. 6500 km^2 (15° 18' to 16° 05' S, 27° 48' to 26° 44' E) at 914 – 1218 m above MSL between Itezhi-tezhi and Kafue Gorge dams. The land coverage map is shown in Figure 5.3. Since 1991 they are included on Wetlands of International Importance (Ramsar) list designated by the Convention on Wetlands of International Importance especially as Waterfowl Habitat from 1971 [148]. Out of all the African wetlands discussed in this work, Kafue Flats are likely the most researched sites [149], albeit not in terms of methane emissions.

Apart from wetlands and swamps, Kafue Flats contain large lagoons and geothermal sites as well as grassland and woodland. The area is characterised by periodic inundation supporting a great diversity of wetland fauna, including the endemic Kafue lechwe (*Kobus leche*). The wetland's climate is strongly influenced by the Inter-Tropical Convergence Zone with rain season falling between November and March (see Figure 5.4). The daily mean temperatures range from 13-20 ° C in July to 21-30 ° C in November. Thanks to the heavy and poorly draining soils of the flats, the average annual rainfall of about 850 mm leads to the flooding of an area between 300 and 5000 km^2 up to the depth of 1-3 meters at the end of the season [151–153].

At the beginning of the rain season, rapid growth of the marsh vegetation is observed. Overall, the flora of the Flats can be divided into five water proximity dependant zones according to the Ramsar information sheet [151]:

1. Levees and lagoon shores are covered with numerous grasses and sparsely distributed trees, such as African fan palm (*Borassus aethiopum*) or apple-ring acacia (*Faidherbia albida*).

2. Floodplain grassland, being the predominant zone, consists mainly of

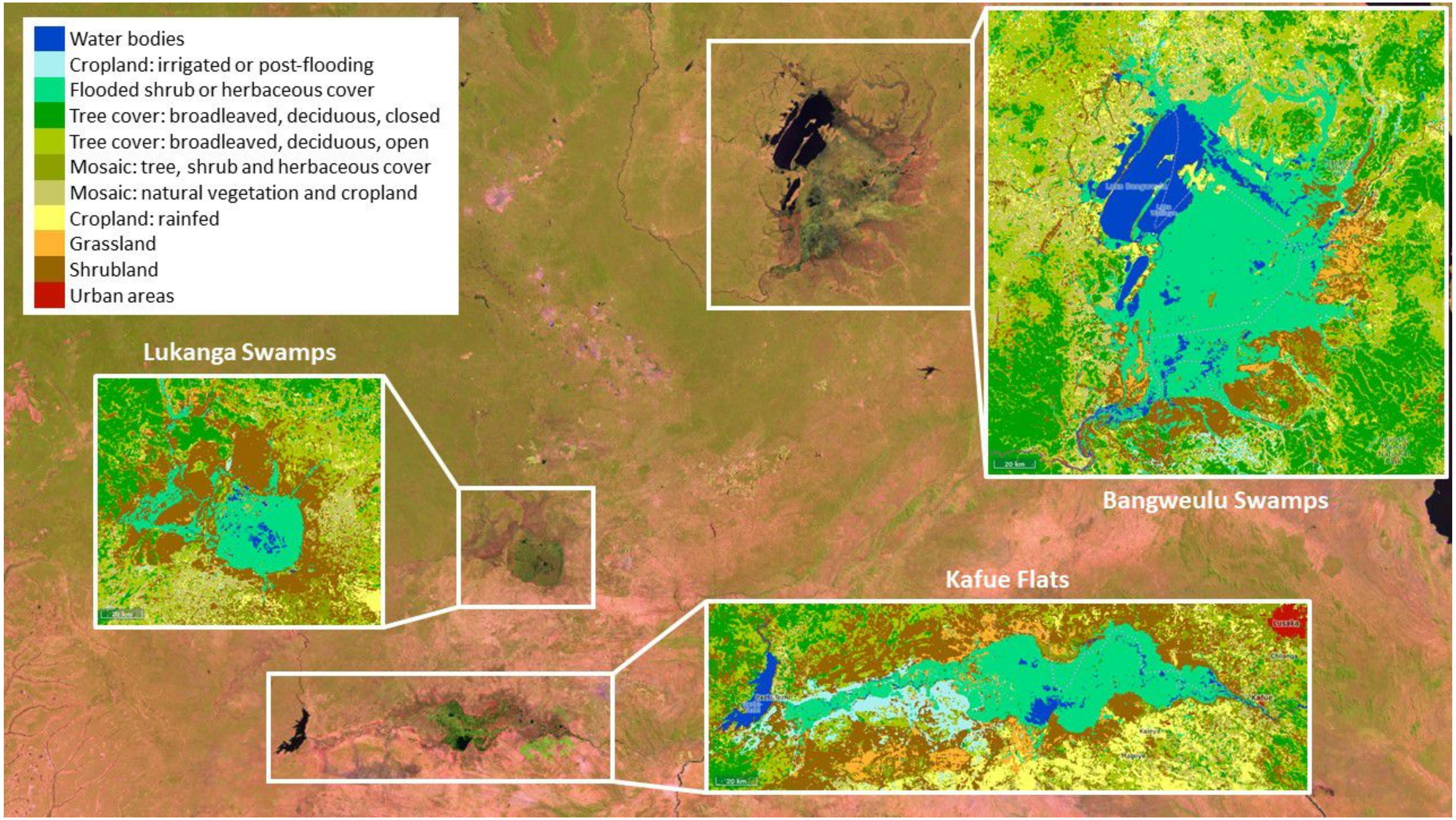

Figure 5.3: Kafue Flats, Lukanga Swamps and Bangweulu Swamps Climate Change Initiative (CCI) Land Cover map (2019). The size of CCI Land Cover maps reflects the relative size of the wetlands. Map sources: European Space Agency CCI Land Cover map [150] and GLAD Landsat MOSAIC 2019 map [72].

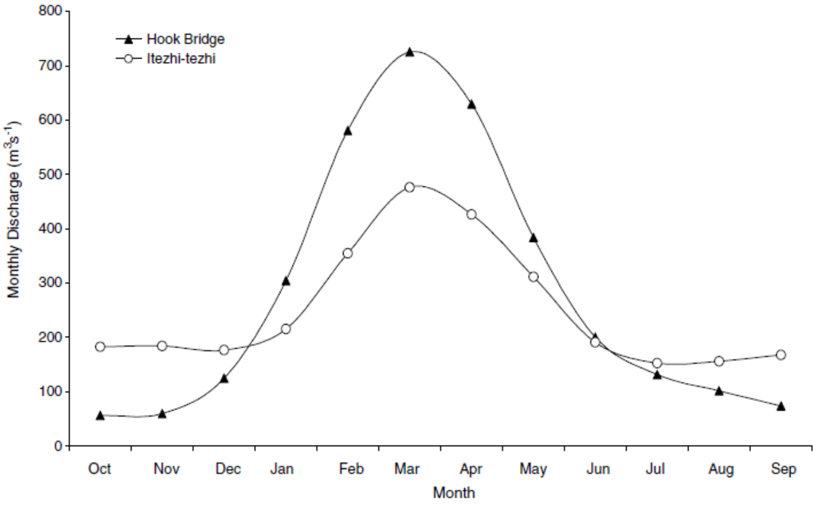

Figure 5.4: Kafue River monthly mean discharge for years 1978-2000 from two sites neighbouring Kafue Flats. Hook Bridge is located on M9 road from Lusaka to Mongu, on the unregulated part of the river. The second site is 60 km downstream at the Itezhi-tezhi Dam. Source: Mumba and Thompson [149].

hippo grass (*Vossia cuspidata*) and tall grasses from *Oryza* genus.

3. Water meadows, found at the edges of the floodplain are characterised by shorter grasses, e.g. torpedograss (*Panicum repens*) or Nile grass (*Acroceras macrum*).

4. Termitaria grassland lies above the flood line, albeit it can be flooded on exceptionally wet years. As the name suggests, it is commonly inhabited by termites, being a globally significant source of methane [154]. The vegetation includes tall grasses like African bristlegrass (*Setaria sphacelata*) or Guinea grass (*Panicum maximum*) as well as species of *Acacia*, Bell mimosa (*Dichrostachys cinerea*) or giant sensitive tree (*Mimosa pigra*).

5. Woodland is the furthermost from the water zone, where predominant species are White Thorn (*Senegalia polyacantha*) and *Albizia harveyi*.

However, the area is also a home to over a million people, mainly from the Tonga and Ila tribes native to the Flats. They use the grasslands as a grazing area for their cattle and small-scale farming. However, large-scale agriculture (mainly sugar production) is also slowly emerging in the region [149].

The major anthropogenic impact on the Flats is the construction of two hydropower dams - downstream Kafue Gorge (completed in 1971) and upstream Itezhi-tezhi (commissioned in 1978). The upstream dam altered the natural flow, replacing the seasonal variation with rapid releases of large volumes of water throughout the year, including the dry season. This means, that currently the flooding area is smaller compared to pre-1978. But due to the constant flow, some parts of the wetland became permanently inundated. Additionally, the downstream dam created a substantial reservoir. The change is illustrated in Figure 5.4, which shows the difference between Kafue River's discharges up- and downstream of the Itezhi-tezhi dam. Unfortunately, there are insufficient hydrological records within the Flats themselves to quantify how the dam has affected water levels of the wetland itself [149].

Another aspect of dam building is the alteration of the transport of nutrients and the biogeochemical processes naturally occurring in rivers and wetlands. It is estimated that globally 12% of river total phosphorus mass was retained by man-made reservoirs in 2000, nearly twice more than 30 years before [155]. It is estimated, that the widespread dam construction decreased the sediment transport by rivers into the oceans by half [156]. The research on greenhouse gas emissions from hydroelectric reservoirs is very limited, both in terms of the number of studies and their extend. Based on published data from 85 of such water bodies Barros et al. [157] estimate the global methane emissions from hydroelectric reservoirs to be 4 Tg of CH_4 yr^{-1} with the highest emissions observed in Amazon. However, there were no reservoirs included, which are located in the tropical zone of Africa. Even though these emissions are not crucial on the global scale, they are still significant.

The only publication presenting measurements of methane emissions from Kafue Flats, Teodoru et al. [137], shows that rivers in the Zambezi basin are a net source of methane due to oversaturation of water. The authors note that the spacial heterogeneity of the methane flux is greater than temporal. However, during wet season the emissions are dominated by diffusion and in dry season by ebulliative processes (similarly to Amazonian rivers). Analysing methane data for the Kafue River in Kafue Flats area and Itezhi-tezhi reservoir (see Table 5.1), the following observations can be made: in wet season both flux and water content are considerably higher for the Kafue Flats than the reservoir, however in dry season there is no obvious trend.

A closer look at the ebullitive methane emissions was taken by DelSontro et al. [158] who studied Lake Kariba (a reservoir on the border of Zambia and Zimbabwe) using surface chambers as well as echosounder. They estimate the Lake's flux to be about 40 mg CH_4 m^{-2} h^{-1} in river deltas and below 40 mg CH_4 m^{-2} h^{-1} in bays. This shows spatial heterogeneity of such lakes and the importance of river deltas. The implication of these findings reveals that chamber flux studies of such areas might not have sufficient extent to capture the full image of the methane flux.

A comparison study between Barotse Plains (a floodplain in Western Zambia) and Lake Kariba [134] shows the complexity of the changes introduced by building a dam on greenhouse gas emissions. On one hand, creating a reservoir can facilitate carbon dioxide uptake, on the other hand, its extent might be insignificant, since during the transition from the wet to the dry season, when the saturated deep water reaches the surface it can release the stored CO_2, making the net uptake negligible. In addition, the sediments at the bottom of the reservoir usually have methanogenic tendencies. Having said that, there are not enough studies comparing net greenhouse gases flux change over the creation of a reservoir in the place of a wetland.

	wet season		dry season	
	flux[1]	water content[2]	flux[1]	water content[2]
upstream the reservoir	0.13	196	0.25	656
Itezhi-tezhi reservoir	0.02	22	5.4	71
downstream the reservoir	0.04	100	1.1	92
Kafue Flats 1	4.26	524	3.18	539
Kafue Flats 2	1.05	550	0.82	898

[1] mg CH_4 m^{-2} h^{-1}, [2] nmol CH_4 L^{-1}

Table 5.1: Mean methane flux and water content in 2013 in Itezhi-tezhi reservoir and Kafue River up- and downstream of the reservoir and within Kafue Flats (two sited). Source: Teodoru et al. (supplement) [137].

5.4.2 Lukanga Swamps

Similarly to the Kafue Flats, the Lukanga Swamps belong to the Kafue River basin and is located in Central Zambia. It covers approx. 2600 km^2 (14° 08' to 14° 40' S, 27° 10' to 28° 05' E) in a local depression between the town of Kabwe and east bank of the Kafue River at the altitude of 1100 m above MSL [159]. The land coverage map is shown in Figure 5.3. The Lukanga Swamps are a Ramsar site since 2005, causing tensions between local communities, immigrant fishermen and the government. People inhabiting the wetlands are one of the poorest communities in Zambia [160].

The Swamps are relatively flat and shallowly inundated, which allows photosynthetic activity right down to the bottom and supports phytoplankton [159]. One of the early European explorers of the Lukanga Swamp describes it as:

> an unpleasant country covered with tall grass and inundated with water that varied from ankle deep to waist deep [in April, but] [...] the flats were dry and I was able to bicycle [...] only having to wade when crossing the larger channels [...] [in July].... ([161])

Nearly 90 years later, the seasonality of Lukanga's climate remains with the main seasons being: wet (600 - 1400 mm rain, 20 - 22.5° C), cool dry

(15° C) and hot dry (22.5 - 27.5° C). The majority of rainfall occurs between October and March. The main sources of water in the Swamp are the Kafue River flooding, rainfall and water flow from the higher grounds [159].

The Swamp consists mainly of palustrine wetland (including lacustrine and riverine). Its acidic soils support a number of vegetation zones: open water, permanent swamp, dambos, savannah, termitaria grassland, reed marshes and *Brachystegia* woodland. The area is dominated by *Phragmites* and *Typha* genera, however *Nymphaea* is predominate in shallow lake water, while hippo grass (*Vossia cuspidata*) typically occupies river banks and lagoons. Interestingly, the above species have displaced papyrus (*Cyperus papyrus*) [159].

5.4.3 Bangweulu Swamps

Bangweulu Swamps are another Ramsar site (since 1991 [162]) and the least studied area included in this work. The wetland is located at the border of Luapula and Northern provinces, covering approx. 11000 km^2 (10° 33' to 12° 17' S, 29° 15' to 30° 43' E) at the altitude of 900 - 1200 m above MSL. The land coverage map is shown in Figure 5.3.

It consists of a number of lakes and smaller water bodies connected with a network of channels and surrounded with swamps and seasonally inundated grasslands with some islands covered with termitaria. The main river connected with the Swamps is Luapula. The wetland water level changes seasonally by 1-2 m with the highest levels observed in April and lowest in November and December. Similarly to the Lukanga Swamps, Bangweulu experiences wet (December - March), cool dry and hot dry seasons. The mean annual temperature is 20.6° C [163].

According to Ramsar information sheet [163] the following vegetation zones can be distinguished in Bangweulu Swamps:

1. Swamps which are covered primarily with papyrus (*Cyperus papyrus*),

Phragmites mauritianus, southern cattail (*Typha domingensis*) and blue lotus (*Nymphaea nouchali* var. *caerulea*).

2. Grasslands with patches of termitaria which are seasonally flooded and host a variety of grasses, inluding genera such as *Acroceras* or *Leersia*. Islands are mostly covered in grassland as a result of fires and agriculture.
3. The slope of the wetland with its characteristic catena is covered with *Brachystegia* woods, including species such as miombo (*Brachystegia boehmii*) being scattered across the entire Swamp as well.

Mismanaged agriculture and fishing threaten the unique ecosystem of the Bangweulu Swamps [163].

5.5 Ugandan wetlands overview

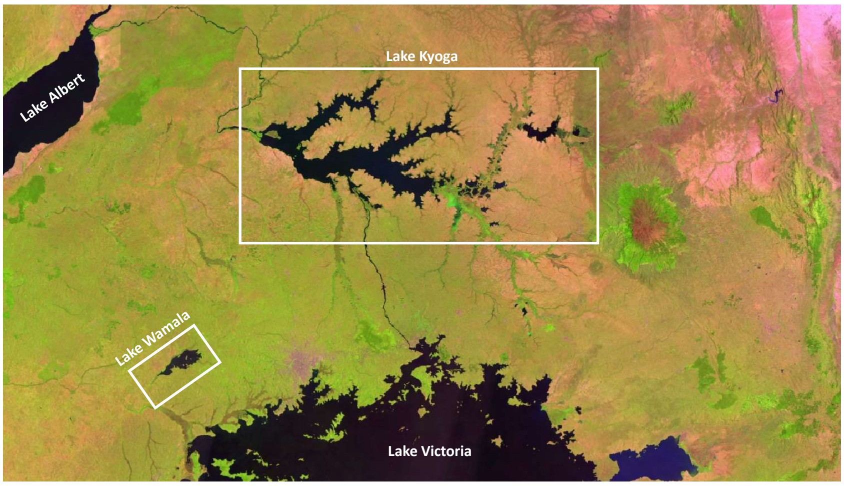

Figure 5.5: Lake Wamala and Lake Kyoga satellite map. Map sources: GLAD Landsat MOSAIC 2019 map [72].

5.5.1 Lake Wamala

Lake Wamala is located in Central Uganda, between Kassanda and Mityana districts (see Figure 5.5). The Lake's are and depth have been a subject of violent changes over last 50 years. Mean depth of the Lake decreased from 4.5 m in the 1970s to 1.5 m 20 years later. The surface of approx. 250 km^2 in the 1980s, halved in following decade (see Figure 5.6). Neither mean depth nor surface have fully recovered by the 2010s [164, 165]. This change is related to the shift in temperature, wind speed and rainfall. Even though since the 1970s, Lake Wamala sees an increase in rainfall, which is offset by an evaporation increase caused by temperature and wind speed rise. Similar trends have been observed in other shallow lakes. For the years 2011-2013, the balance for Lake Wamala was -5 mm month^{-1}, which is alarming [166].

Since the 1950s the Lake was one of the major fisheries in the region, however in the 1970s overfishing led to collapse of the industry [164]. Additionally, climate change has resulted in considerable worsening of the local fishermen situation. Some have moved to high-value livestock and crops, but due to limited access to credits, education and modern agricultural resources, fishing remained the main source of income for the local communities [165].

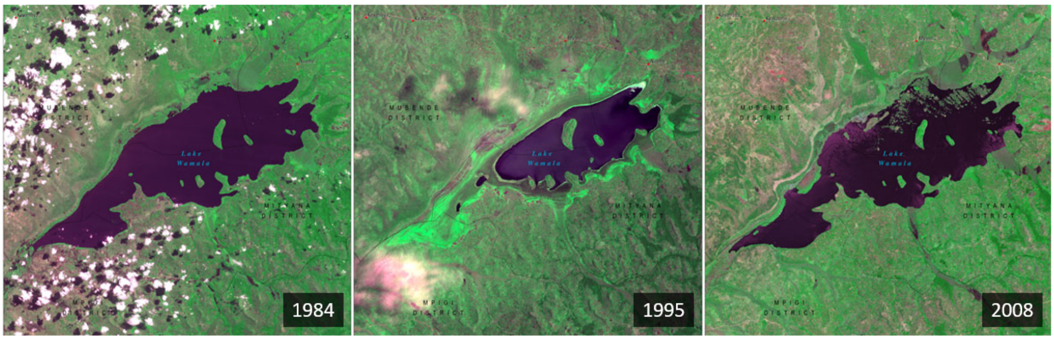

Figure 5.6: Satellite images showing area change of Lake Wamala. Source: UNEP [164].

5.5.2 Lake Kyoga

Lake Kyoga is a large (approx. 4 000 km^{-2}) shallow (avg. 3.5-4.5 m) lake on the River Nile located partially in East Uganda and partially between Central and North Uganda, stretching through 10 districts. It is rich in sudds - large patches of floating vegetation (mainly papyrus), which after the 1997-8 El Niño clogged the River Nile outlet causing disastrous flooding in the area. These events led to the construction of two channels and extensive dredging of the outlet [167, 168]. On the other hand, some parts of the lake show an increasing risk of dry spells, which can be detrimental to rainfall dependent agriculture [169].

Were et al. [170] conducted a methane and carbon dioxide chamber study of natural Naigombwa wetland in Lake Kyoga basin in February-April (dry season) and August-October (wet season) 2019, hence pretty much at the same time as MOYA-2 campaign. The work focuses on the influence of vegetation on GHG emissions, however it is also the first published study of GHG emissions from Ugandan wetlands. The work looks atnative Ugandan wetland species popular across the entire country: Papyrus growing mainly in the downstream part of the wetland both in emergent and floating form and upstream emergent growing Typha (reedmace) and Phragmites (perennial reed grasses). The study found that only Phragmites stand out showing higher CO_2 and lower CH_4 emissions during dry season. In wet season there is no significant difference. Papyrus emits most methane and least carbon dioxide among the described vegetation, while Phragmites emit least carbon dioxide and most methane.

However, what is more interesting from the perspective of this work is the average flux. For carbon dioxide flux across all three habitats was 2890 ± 192 mg CO_2 m^{-2} h^{-1} and 2475 ± 193 mg CO_2 m^{-2} h^{-1} for dry and wet seasons respectively. Hence, the flux during dry season is slightly higher thane for the wet season. For methane the opposite is true - the average for dry season, i.e. 16.1 ± 1.1 mg CH_4 m^{-2} h^{-1}, is lower than the average for wet season, i.e. 21.8 ± 1.8 mg CH_4 m^{-2} h^{-1}. These difference are statistically significant, even though the wetland was submerged in water throughout the study with average seasonal difference of 22 ± 7 cm in water level. Comparing the emissions it becomes rather apparent that carbon dioxide plays considerably greater role in carbon budget than methane with carbon mass ratio of 49:1.

5.6 Sápmi wetlands overview

Sápmi is a region stretching across northern Fennoscandia (see Figure 5.7), which takes its name from Sámi people, who are its native inhabitants. Large parts of this region are covered in mire (i.e. peatland). The predominant mire region in Sápmi is Aapa mire. It is characterised by large fen complexes with high relative humidity and a short growth period [171]. For Finland, it is estimated that 14% of the entire country is covered in protected mire, yet originally it was over 30%. The decline is historically related to agriculture and forestry expansion. Since 1743 over 3000 Finnish lakes have been either drained or reduced and nearly 70 thousand km^2 of mire have been trenched. This has a detrimental effect not only on biodiversity but also on reindeer herding and currently the Finnish government works with Ramsar to restore the wetlands [172].

The region is affected not only by land use changes but also by climate change. Temperatures in sub-polar and polar regions increases twice faster than the global average putting in danger GHG permafrost reservoir [173]. The lowland area of Sápmi is frequently studied for its permafrost levels and GHG emissions.

Lagomasino et al. [174] have studied GHG emissions dependence on vegetation in Finnish Sápmi. They found that wetland mire emits by far the most methane (1.45 mg m^{-2} h^{-1}), while all other habitats except for palsa mire (0.25 mg m^{-2} h^{-1}) are characterised by slight uptake (-0.04 mg m^{-2} h^{-1}

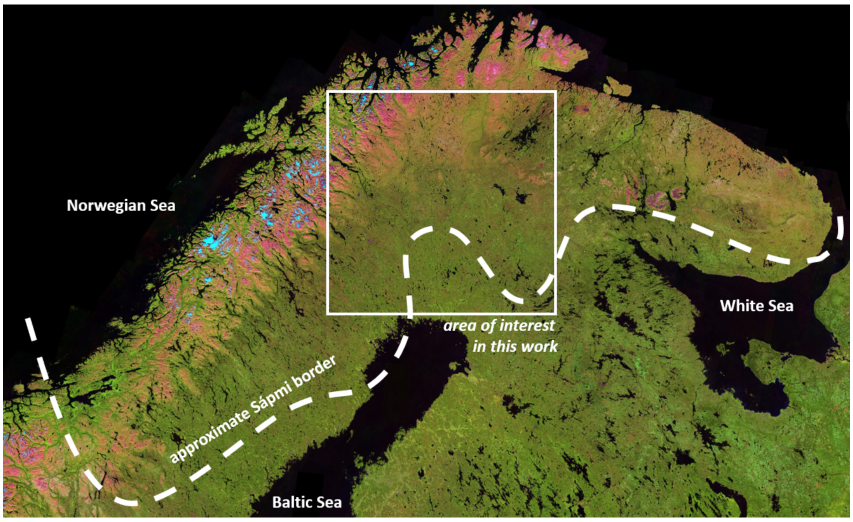

Figure 5.7: Sápmi satellite map with marked approximate border and area of interest for this work. Map sources: GLAD Landsat MOSAIC 2019 map [72].

range). The differences in methane emissions are striking, but carbon dioxide flux is much more even between different vegetation groups. Birch, mixed and open birch forests show major emissions (up to 270 mg CO_2 m^{-2} h^{-1} for birch forest), while alpine palsa and non-mire wetlands show the smallest emissions (down to 20 mg CO_2 m^{-2} h^{-1} for the latter).

O'Shea et al. [173] have studied the area on board of FAAM aircraft in July 2012, finding that the regional-scale methane flux is 1.2 ± 0.5 mg m^{-2} h^{-1} and carbon dioxide flux is -350 ± 143 mg m^{-2} h^{-1}. These values were in agreement with chamber studies and EC tower. The EC study at Sodankylä also shows that the summer diurnal flux variation is negligible for methane, but for carbon dioxide the difference between night and the daytime dip is approx. 600 mg m^{-2} h^{-1}. Another EC tower study of methane emissions from Aapa mire near Kaamanen conducted in years 1995-1998 shows mean flux of 0.63 ± 0.05 mg CH_4 m^{-2} h^{-1}. No dependence on water table level was found, but the thaw emissions happening over 20-30 days in spring had 11% contribution to the yearly average [175].

Chapter 6

Methods: Airborne eddy covariance

6.1 Instrumentation

All measurements were conducted on board of FAAM aircraft. The position, heading and roll angle were measured with Applanix POS AV 410 GPS-aided Inertial Navigation System, while height above the ground was measured with Thales AHV16 Radar Altimeter. Temperature and three-dimensional wind components were measured from the aircraft's nose using, respectively, Rosemount 102 Total Air Temperature probe and nose-mounted five-port turbulence probe. The true airspeed (dry-air) was derived based on data from the turbulence probe, the on-board Air Data Computer and the Total Air Temperature probe. Static pressure from the the on-board Air Data Computer was also used.

The instrument crucial to this work was the Fast Greenhouse Gas Analyser (FGGA) measuring methane, carbon dioxide and water. It is a Near-IR Off-Axis Integrated Cavity Output Spectroscopy (near-IR OA-ICOS) Model 907-0011, Los Gatos Research Inc purchased in 2017 to replace its predecessor - FGGA Model 907-0010 from 2009. It is described in Section 2.1.2.

6.2 Flights overview

Methane Observations and Yearly Assessments (MOYA) project was funded by Natural Environment Research Council (NERC) between 2016 and 2020. Its main aim is ”closing the global methane budget through undertaking new observations and further analysis of existing data” [176]. MOYA-1 focused on fires in Senegal, whereas MOYA-2 and ZWAMPS (Zambian Swamps) have targeted wetlands in Uganda and Zambia. ZWAMPS is a particularly important campaign, since it allowed studying Upper Congo and Zambezi rivers’ basins. The Congo River and wetlands surrounding it are deemed a key to fill the gaps in global methane budget. At this point it is impossible to conduct studies in Democratic Republic of Congo, being home to most of the Congo River basin. Zambia on the other hand is much more accessible and provides a very promising proxy for the Congese wetlands.

MOYA campaign had multiple objectives, for example the biomass burning in North Uganda was studied during the MOYA-2 campaign [80]. Hence not all of the flights provided data suitable for AEC. A map summarising all the MOYA-2 and MOYA-Arctic flights having AEC potential is shown in Figure 6.1 and more details are provided in Table 6.1.

Flight	Date	Location
C128	25/01/2019	Lake Wamala
C129	26/01/2019	Lake Wamala
C132	28/01/2019	Lake Kyoga
C136	01/02/2019	Bangweulu Swamps
C137	02/02/2019	Kafue Flats
C138	03/02/2019	Lukanga Swamps
C195	31/07/2019	Sapmi
C196	01/08/2019	Sapmi

Table 6.1: Summary of all the MOYA-2 and MOYA-Arctic flights having AEC potential.

With AEC on board of the FAAM aircraft being in a very early trial stage, the flight plans were not specifically designed for AEC. This means, there were no stack legs on altitude suitable for AEC and that many of the legs were not perpendicular to the wind. The flights were not repeated, hence this work does not comment on the temporal variability of the fluxes. Moreover due to restrictive flying permissions there was little flexibility with regard to the weather conditions and a lot of the flights were affected by disadvantageous meteorology.

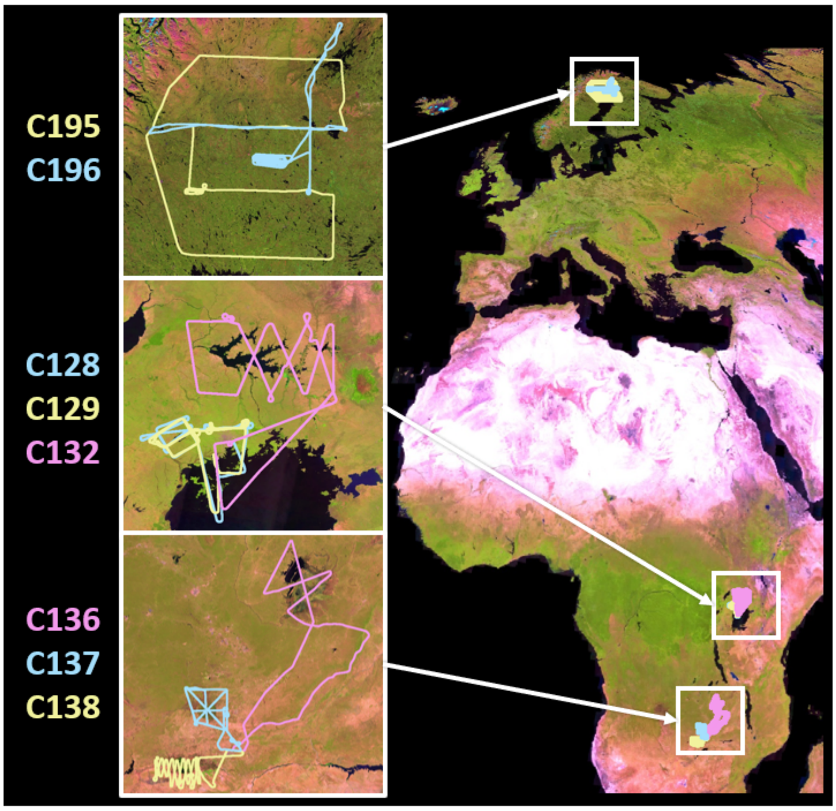

Figure 6.1: Map of all the AEC flights during MOYA-2, ZWAMPS and MOYA-Arctic campaigns. Map source: GLAD Landsat MOSAIC 2019 map [72].

6.3 Airborne eddy covariance

6.3.1 Flux and mass balance overview

Flux is a measure of how much of the species of interest moves through a unit of area over unit of time. A popular approach to flux quantification over large area using aircraft data is mass balance. The general idea is to compare upwind and downwind legs to derive bulk flux, however there are different approaches to the boundary layer treatment. In case of the Lake Bangweulu the flux was calculated directly from Equation (6.1) [59], because the wind was very slack (below 2 ms^{-1}) and its horizontal direction was very changeable:

$$f = BLH\frac{d\,c_{BL}}{d\,t} - (c_{BL^{+}} - c_{BL})\left(\frac{d\,BLH}{d\,t} - w\right) \tag{6.1}$$

where f is scalar flux density, BLH is PBL height, t is time, c_{BL} is concentration in PBL, $c_{BL^{+}}$ is concentration above PBL, w is vertical wind speed. BLH used for the correction comes from Numerical Atmospheric dispersion Modelling Environment (NAME), which was driven by data from a Numerical Weather Prediction model (the Unified Model; UM) [59].

This kind of mass balance is based on the net mass flux into a column of air advected vertically and constrained by the surface and BLH. Estimating the area from which emissions originate is far from trivial since wetlands are dynamic and non-discrete formations. Here, the official Ramsar estimate of the wetland area was used to obtain the bulk flux.

Since in case of the Lukanga Swamps the wind was faster and less changeable, a more popular and more sophisticated approach was used:

$$E = BL^{d}\int_{a}^{b}(c_{BL^{+}} - c_{BL})u_{p}\,dx \tag{6.2}$$

where BL^{d} is PBL of the downwind leg, E is total emission factor (in g s^{-1}), a and b are wetland plume edges, u_{p} is speed of wind perpendicular to the leg and x is the length of the downwind leg. The Equation (6.2) is derived from Equation (6.1) on assumption of a constant wind speed and direction across the wetland and a constant methane concentration above PBL (criteria which the Bangweulu flight did not fulfill) [59].

Another frequently used method is eddy covariance, which is described in more details below.

6.3.2 Principles of eddy covariance

Eddy covariance flux is based on the covariance between measured species and vertical wind speed in eddies, which are swirly components of turbulence with a varying range of turnover timescales. This requires very fast and sensitive measurements to capture changes of concentration and meteorology. Eddy covariance can be described by the following equation:

$$f \approx \overline{\rho_a w' c'} \tag{6.3}$$

where f is the vertical flux, ρ_a is air density, w' is instantaneous change in vertical wind and c' instantaneous change in concentration [177].

6.3.3 Continuous wavelet transform

Recently, thanks to technological advances it became possible to use airborne data for eddy covariance. The most popular method of recovering time- and frequency-resolved information from the signal is continuous wavelet transform (CWT) [178].

As described by Metzger et al. [179], to account for heterogenity of the terrain, wavelet transform was used to study the covariance in frequency, rather than time domain. Wavelets are structures localised in time as well as frequency. Following is a brief description of the core equations used by the NEON eddy4R AEC algorithm (see Section 6.3.4). The wavelet used by eddy4R is Morlet wavelet shown in Figure 6.2 and described by Equation 6.4:

$$\psi(q) = \pi^{-0.25}\, e^{i\omega_0 q}\, e^{-0.5q^2} \tag{6.4}$$

where ω_0 is a dimensionless frequency parameter and $q = \frac{t-b}{a}$, with a and b being, respectively, are scale (in frequency domain) and location (in time domain) parameters and t being time. Daughter wavelets refer to wavelets of the same shape but in different localisation:

$$\psi_{a,b}(t) = \frac{1}{\sqrt{|a|}}\, \psi(q) \tag{6.5}$$

A daughter wavelet can be convoluted with signal (x) to obtain a wavelet coefficient (W):

$$W_x(a,b) = \int x(t)\, \psi_{a,b}(t)\, dt \tag{6.6}$$

In case of AEC there are two signals: x being vertical wind and y being instantaneous concentration. A global covariance of these is described as:

$$cov_{a,b} = \frac{\delta_j \delta_t}{C_\delta N} \sum_{j=0}^{J} \sum_{n=0}^{N} \frac{W_x(a_j,b_n)\, W_y(a_j,b_n)^*}{a_j} \tag{6.7}$$

where $W_x(a_j,b_n)W_y(a_j,b_n)^*$ is the wavelet cross-scalogram (the star denotes complex conjugate), $j = 0,...,J$ with J being the number of increments and $n = 0,...,N-1$ with N being the length of the data set. a_j exists in frequency domain and is spaced exponentially, while b_n exists in time domain and is spaced linearly:

$$a_j = a_0 2^{j\delta j} \quad \text{and} \quad b_n = n\delta t \tag{6.8}$$

where a_0 is the initial scale parameter, which is chosen to match the period of the folding frequency. δ_j, δ_t are the levels of increment and C_δ is reconstruction factor specific to the mother wavelet (in this work 0.776 for Morlet wavelet). However, CWT would result in a loss of large scale (low frequency) contributions, so j and n can be divided into subintervals to retain them. This in turn results in edge artifacts above so called cone of influence (COI). The less reliable values can be either included (requiring correction) or excluded (decreasing uncertainty but also excluding part of the scale).

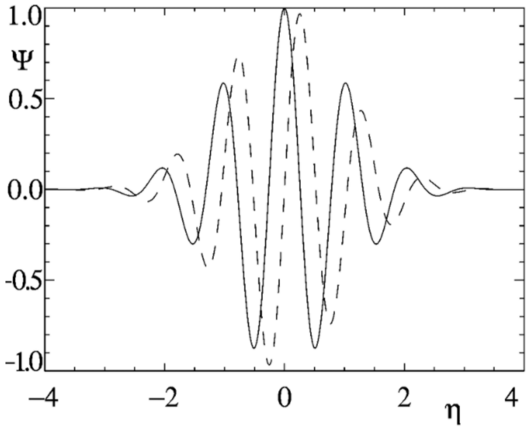

Figure 6.2: Morlet wavelet where x-axis is in time and y-axis in frequency domain. Source: Metzger et al. [180].

6.3.4 NEON eddy4R AEC algorithm

The first step is de-spiking the wind, temperature and methane data using median filter following Starkenburg et al. [181]. Then, since measurements come from different instruments the temperature, water and concentration data is lag corrected against the wind. The correction is based on the highest cross correlation between the quantities of interest as shown in Equation (6.9) [182]:

$$\left| \frac{\overline{w'(t)\,c'(t+l)}}{\overline{w'}\,\overline{c'}} \right| \rightarrow \max \tag{6.9}$$

where t is time, l is lag, w' is instantaneous change in vertical wind speed and c' is instantaneous change in quantity. To improve lag detection, a high pass filter is applied and the cross-correlation search window, which typically is an order of magnitude greater than the input frequency. In previous studies Hartmann et al. [183] have successfully applied this method for lag of 0.66 -

0.72 s, so it seems reasonable to apply this method to 0.4 - 0.5 s lags in this work. After lag correction the data is resampled to desired frequency [184].

The first step in calculating the AEC is using the classical time-domain only approach (mean de-trended), that yields a single flux number per leg (see Section 6.3.2). Then, integral turbulence characteristics (ITC) are calculated along with uncertainties, limit of detection (LOD), signal to noise ratio (SN), stationarity tests and high frequency loses (NK12). ITC are described by Thomas at al. [185] as "statistical measures describing atmospheric turbulence in the surface layer" which in practice quantify the connectivity to the surface. The flagging threshold used is 100%.

The flux uncertainty is defined in terms of random and systematic error. Random error originates from too short averaging window [186], while systematic error originates from insufficient sampling of the large scale atmospheric events responsible for turbulent flux [184]. LOD and SN were calculated using Billesbach's 'random shuffle' approach [187]. The covariance for each variable is recalculated for randomly shuffled data giving the coincidental correlation contributions. The main assumptions are that the covariance with randomly shuffled data set is zero, that the averaging period is long enough to capture lowest frequency contributions that are significant and that the instrument does not bear a significant systematic error which is not calibrated out. The main advantage of this approach is that as a statistical method it does not require additional measurements and yields parameters for each leg rather than an entire campaign or flight.

High and low frequency losses are intrinsic to AEC, the former originating from instrumental limitations (e.g. air mixing in tubes of a closed path setup) and the latter happening due to insufficient sampling window. Currently only high frequency loses are considered by the NEON AEC algorithm using simplified Nordbo and Katul method (NK12) [188]. The method accounts for environmental variability by correcting each averaging window separately, is species independent, does not rely on gas co-spectrum and is fully automatable.

The next step is calculating wavelet time-frequency domain AEC (see Section 6.3.3), which yields flux numbers for every 500 or 1000 meters of a leg (with the same averaging window). ITC, NK12 and uncertainty is then calculated for each flux (as described above). Finally, a footprint model calculates "a spatial representative weighting matrix for each measurement along the flight track" [184].

6.4 Input data

Section 6.1 provides details of the instrumentation used to acquire data necessary for AEC. The planetary boundary layer (PBL) data was sourced from NAME model (Numerical Atmospheric dispersion Modelling Environment), rather than from empirical data. This is because the NAME model provides a continuous simulation of the PBL, which develops over the course of a measurement, whereas empirical data is only available for when profiles were performed (i.e. 2-4 times per flight). Where available empirical and modelled data agreed well.

The data required for AEC was acquired at different frequencies, namely:

- 10 Hz calibrated FGGA methane
- 10 Hz uncalibrated FGGA water
- 16 Hz Thermistor temperature
- 32 Hz core data: latitude and longitude, static pressure (RVSM), roll angle and heading, wind (u, v, w) , true airspeed (turbulence probe)
- 1 Hz core radar altitude (due to problems with 32 Hz file)
- 1 min NAME model BLH

All variables are interpolated to 32 Hz to be subsequently resampled by the AEC algorithm to 6 Hz (true FGGA measurement speed). The data was filtered by two criteria - altitude and roll angle. The former was decided to be 610 m of radar altitude, i.e. above the ground, to eliminate any data above the entrainment layer. The latter was chosen to be greater than ± 20 ° to eliminate sharp aircraft turns, in which the wind data is not reliable. The remaining data was divided into 'legs' whenever there was a gap of 5 s or more in the time series. 5 s was chosen because it is an equivalent of approximately 500 m of flight track (assuming no turns / ascents / descents) and the desired AEC resolution was 500 m.

Each of the legs is tested against three criteria: no gaps longer than 500 m, actual travelled distance equal or longer than 15 km, no altitude difference over 10% from the mean. Legs which pass all three tests are checked manually and fed to AEC algorithm.

6.5 Post-processing

Each of the legs for which AEC was calculated was checked against a range of diagnostics to ensure sufficient quality of the output. Some of the criteria were treated as absolute keep or reject and some were treated more as an indicator of potential problem that needs further investigation.

First the calculated lag times (quoted always in seconds) of methane, water and temperature compared to the wind data were controlled. Since methane and water are measured by the FGGA with inlet localised in the middle of the plane there is a lag of about 0.4-0.5 s compared to the wind measured at the nose of the aircraft. Temperature is measured at the nose as well, so there should be little or no lag. If more than one lag time was deviating from these values the leg was rejected. The cross-correlation plots were checked for remaining legs - if they presented strong positive correlation (see Figure 6.3a) small inaccuracies in lag time calculations were ignored. Otherwise the leg was rejected (see Figures 6.3b to 6.3f).

The second check was comparing the mean of each leg with the LOD. If the mean was lower than the LOD the leg was rejected, since the EC was not

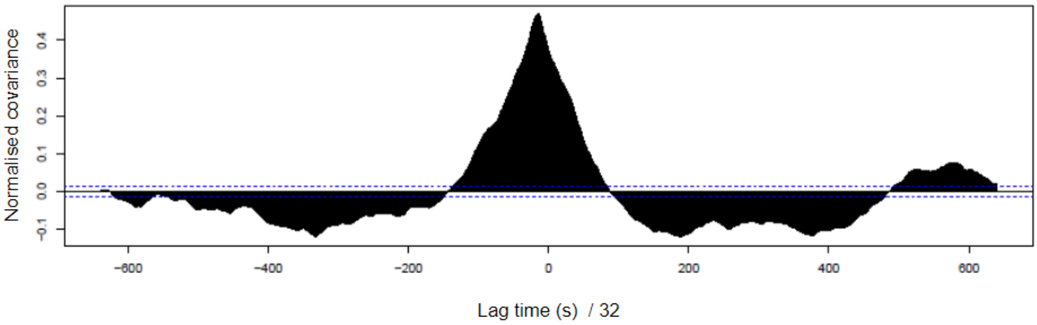

(a) Strong positive methane correlation showing a clear peak at approx. -0.4 s in leg 8 of flight C138.

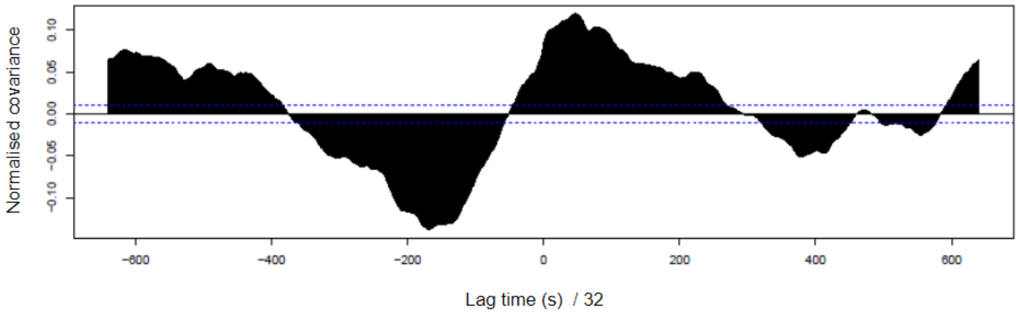

(b) No clear temperature peak can be found in leg 4 of flight C136.

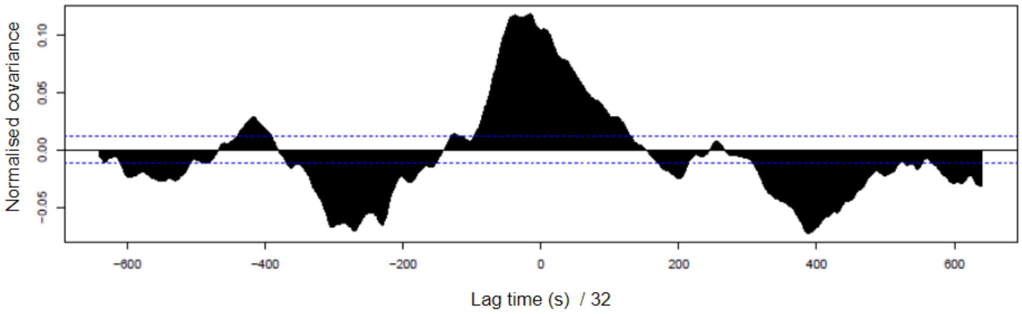

(c) Unclear flattened ‘double’ methane peak in leg 8 of flight C136.

Figure 6.3: Example of cross-correlation plots and common issues with finding the correct lag time. The dark blue lines indicate LOD, the x axis is the frequency of input data multiplied by factor of 10-20 (depending on the flight) and the y axis is the strength of the correlation. In case of all the flights a strong positive (emission) peak would be expected.

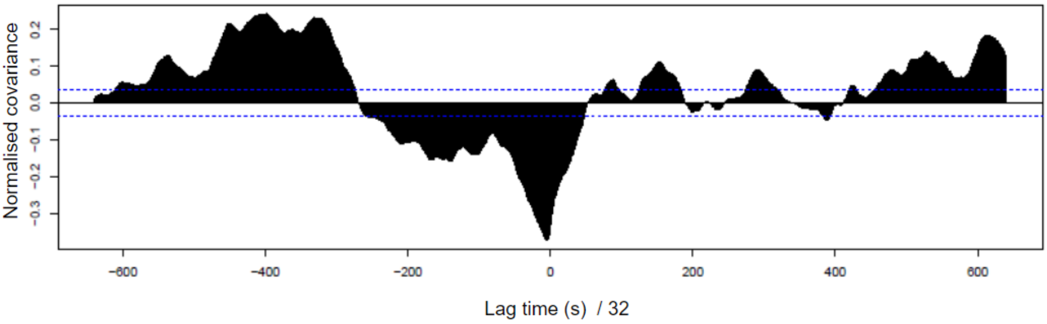

(d) A strong and clear, but negative temperature peak in leg 7 of flight C129.

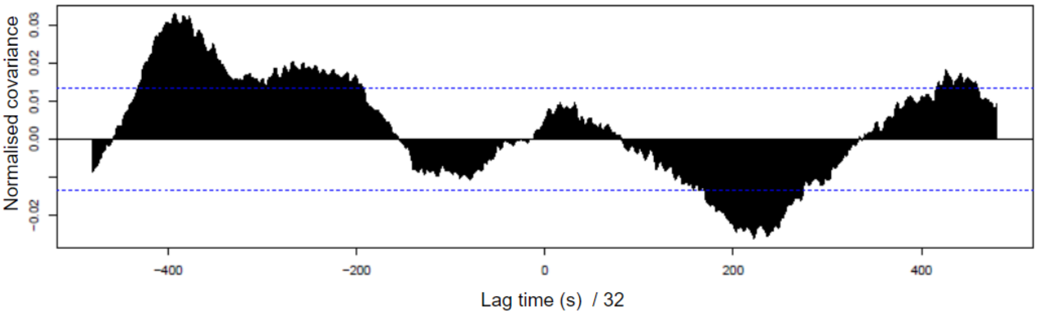

(e) The weak signal leaves methane correlation in the area of interest below the LOD in leg 2 of flight C195.

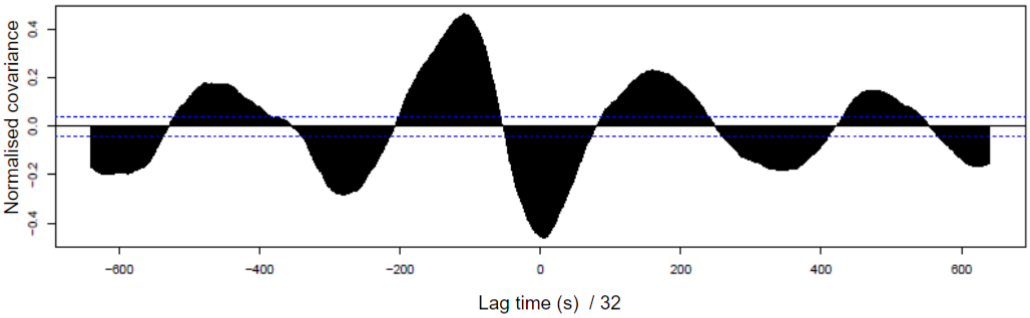

(f) The sinusoidal pattern in methane in leg 3 of flight C129 is also a sign of the algorithm struggling to pick up the correlation correctly.

Figure 6.3: Example of cross-correlation plots and common issues with finding the correct lag time. The dark blue lines indicate LOD, the x axis is the frequency of input data multiplied by factor of 10-20 (depending on the flight) and the y axis is the strength of the correlation. In case of all the flights a strong positive (emission) peak would be expected.

strong enough to give a meaningful result. For the African wetlands, mean sensible and latent heat flux were expected to be positive, since the flight took place during the day in very warm weather. If the mean heat flux for the leg was negative then the leg was rejected. Similarly, an uptake of methane would be highly unlikely in a tropical wetland scenario, so the legs showing a strong average negative methane flux were rejected too (individual negative points were kept). In all cases that coincided wit other parameters being out of desired range, so the negative mean methane flux served as a confirmation. The stationarity flag generated by the AEC algorithm was also used since one of the EC assumptions is that statistical properties of the flow do not change with time.

After rejecting all the legs failing to fulfill the conditions described above, other parameters were analysed to ensure the further use of correct data only. Legs with relatively high errors or relatively low signal to noise ratio were removed if their mean flux was not considerably lower than in other legs. The NK12 parameter (based on Nordbo and Katul [188]) accounts for under/over estimation of flux due to the low frequency of measurements [180] and should ideally be approx. 0.9-1.1. Even though its main use is in tower studies, it was used as an additional check and particularly low values were flagged.

Moreover, individual flux values were filtered using ITC threshold of 100% [189]. In some legs there are particularly large hotspots usually covering 1-2 km worth of data. These were not removed since there was no basis to do so, however, in plots the scales were moderated not to include them for visual clarity purposes.

The calculated AEC flux is not an exact representation of the surface emissions since there is a gradient of flux in the PBL as described by Metzger et al. [189]. The flight altitudes were limited by local regulations and safety reasons to approx. 0.5 PBL, hence significant losses can be observed and need correcting for [190]. A simple, linear correction was applied, assuming complete flux decay at the bottom of the entrainment zone (or top of convective part of boundary layer) and 100% of flux at the surface, see Equation (6.10) [189]:

$$f_{\text{cor}} = \frac{f_{\text{raw}}}{1 - \frac{alt}{0.8BLH}} \tag{6.10}$$

where f is flux (raw and corrected), alt is flight altitude, BLH is PBL height. BLH used for the correction comes from NAME model. The entrainment zone, ie. PBL region in which the mean temperature, moisture and aerosol show strong gradients [191], is defined here to start at 0.8 BLH following Metzger et al. [189].

Chapter 7

Results: Airborne eddy covariance

7.1 Methane AEC flux

Out of all the 8 flights that had AEC potential, i.e. included long (>15 km), level (within 10% from mean) and low (ideally below 0.5 BLH) legs, only two gave satisfying results. All the other flights failed to meet every criterion for a good quality AEC (specific reasons are described below). Probably, the best flight was C138 (Lukanga Swamps), but C137 (Kafue Flats) also provided flux of good quality. Flights C128 and C132 contained three additional legs which resulted in acceptable AEC when 10% from mean altitude rule is neglected. Even in case of C137 and C138, it is important to bear in mind that all the measurements were performed as a trial and it was not a designated AEC campaign, which means there were no stacked legs and a lot of them were not perpendicular to the wind, which is not ideal from the footprint perspective. Moreover, FAAM aircraft is a large passenger jet, which restricts the minimal flight altitude, meaning PBL dept correction becomes necessary.

The filtering by integral turbulence characteristics (ITC) 100% threshold has proven not to have significant effect on the fluxes, in fact for both C137 and C138 it caused no change in the average flux for the area. The filtered out values tend to coincide with low to medium flux values, but there is no apparent correlation (see Figure B.3 in Appendix B). All the diagnostic parameters as well as mean values for each leg, both for the successfully and insufficient quality flights, are presented in Tables B.1 to B.2 in Appendix B.

Flight C137 (as well as the legs salvaged from C128 and C132) shows a number of negative values. They originate from the measurement uncertainty (see Figure B.4) - no measurement is negative within its error bars. This can be confirmed by ITC filtering - none of the particularly low values got rejected on this basis, suggesting it was not a meteorological issue. The median error for a single flux value at 500 m averaging window is 222% for C137 and 130% for C138. This might initially seem like a significant value but in fact, C138 has remarkably low error for individual flux, considering that there was no leg stacking and relatively low depth in BLH [192]. LOD was intentionally omitted as a filtering category not to bias the average towards higher values.

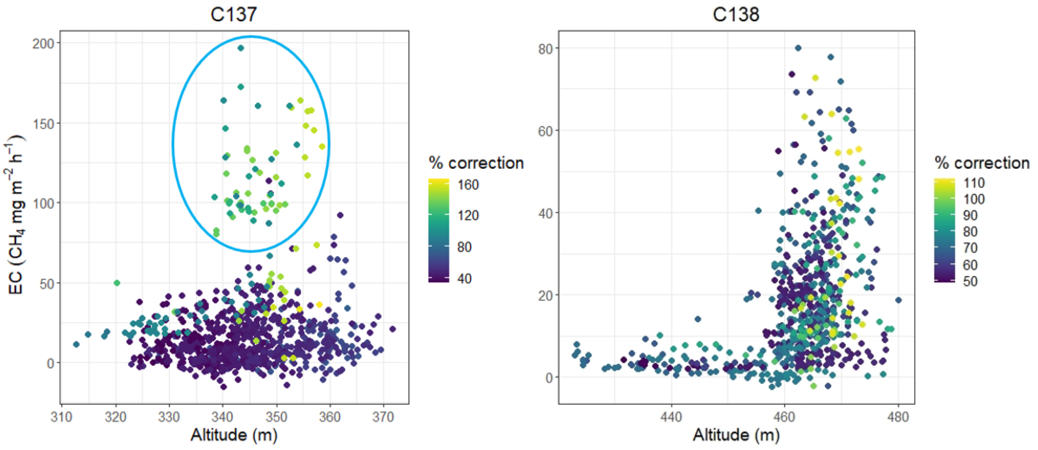

Figure 7.1: Distribution of AEC flux values depending on flight altitude and % correction for PBL depth. The blue circle indicates the area suspected to display suspicious dependence on the PBL depth correction that can be explained by PBL expansion over the course of the flight.

A correction for PBL depth was necessary for all the flights due to the relatively high altitude of measurements. It had a dramatic effect on individual flux values and the averages. To ensure there was no suspicious dependence in the corrected data, all the fluxes were plotted against flight altitude and coloured by percentage correction (see Figure 7.1). There was no trend in case of C138, but in case of C137 a suspicious area was identified (marked by the blue oval in Figure 7.1). It corresponds mainly to leg 5, which stands out also in Figure 7.3 with its 150 mg CH_4 m^{-2} h^{-1} enhancement. The flight altitude and BLH data was investigated. Leg 5 was the first leg flown out of the ones that passed AEC QA/QC process and it happened relatively early in the morning (7:36-7:45) with the next leg to follow being an hour later (leg 19, 8:33-8:39). Over that hour the PBL was expanding substantially and settled only about 8:45 for the rest of the flight as shown in Figure 7.2. Nota bene, leg ID numbers for C137 and C138 are shown in Figure B.1 in Appendix B.

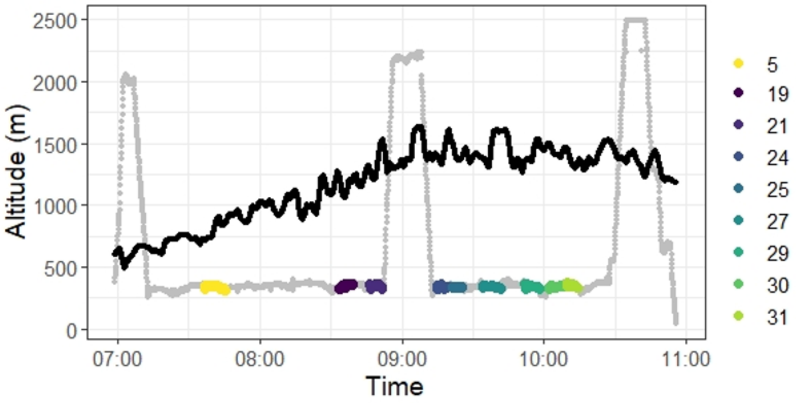

Figure 7.2: BLH (black) and altitude (gray) throughout C137 flight with colour marked legs.

Leg 5 is considered correct - PBL behaviour explains the higher correction and hence higher values, its diagnostics are all correct with the only abnormality being the water cross correlation plot which however, is corrected by adjusting the search window from 10 to 15 times the raw frequency. This still leaves the question of why leg 5 is higher in flux than the other legs. It is possible that the time of the day played a role and leg 5 reflects the overnight buildup, which disappears by the time leg 19 happens. The enhancement coincides with the wetland, hence it might be just the natural diurnal variability so the enhancement cannot be seen on the way back. Finally it can be just a coincidence, since the legs were not stacked it is impossible to confirm how stable this flux was. It is important to bear in mind that footprints of the legs were not the same, in fact some were substantially different. E.g. legs 19 - 24 have over 5 km wide footprints, whereas legs 5 or 31 have footprints barely reaching 4 km in width.

In case of C138, leg 14 is perpendicular to the wind direction, which is an ideal situation for AEC, as the flight track cuts the atmosphere like a cake [192]. The wind direction is also reflected in the footprints - leg 14 has by far the largest one, while leg 17 (parallel to the wind) has by far the smallest one. This flight is pretty much a textbook example of AEC, with exceptionally low error and nearly ideal diagnostics. Regrettably, the legs have not been repeated at similar altitude. Nevertheless, it is apparent that the major emissions come from the wetland.

Comparing both flights, it is noticeable that except for leg 5-C137, the flux is rather similar. The average is 23.0 (± 1.57) mg CH_4 m^{-2} h^{-1} for Kafue (all AEC fluxes), and 27.9 (± 1.67) mg CH_4 m^{-2} h^{-1} for Lukanga (precisely, area between 14.24 and 14.60° S and 27.61 and 27.95° E) where the error is mean of the sum of systematic and random error divided by square root of the number of observations. Figure B.2 shows both flights on scale limited by C138 flux range. The interesting observation is that in case of the Lukanga Swamps the flux visibly coincides with the wetland, yet this corelation is less obvious for the Kafue flats. This might be due to the length of flight and the temporal changes in methane flux throughout the flight.

Another aspect of there two flights worth discussing here is the error of these fluxes. The uncertainty quoted in this work consists of random and systematic error (see Section 6.3.4). No propagation of the instrumental errors was performed, since they are negligible compared to the overall AEC error [192, 193]. Especially that the study is more of a demonstration of

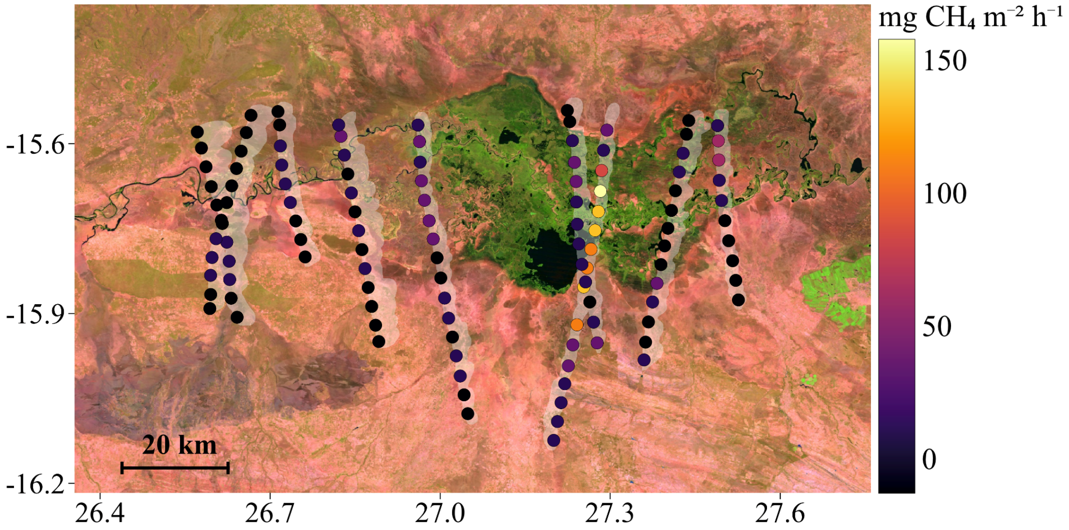

Figure 7.3: Airborne eddy-covariance fluxes (at 3 km intervals) for the Kafue Flats wetlands (C137). White highlighted areas indicate calculated emission footprints (90%). Map source: GLAD Landsat MOSAIC 2019 map [72].

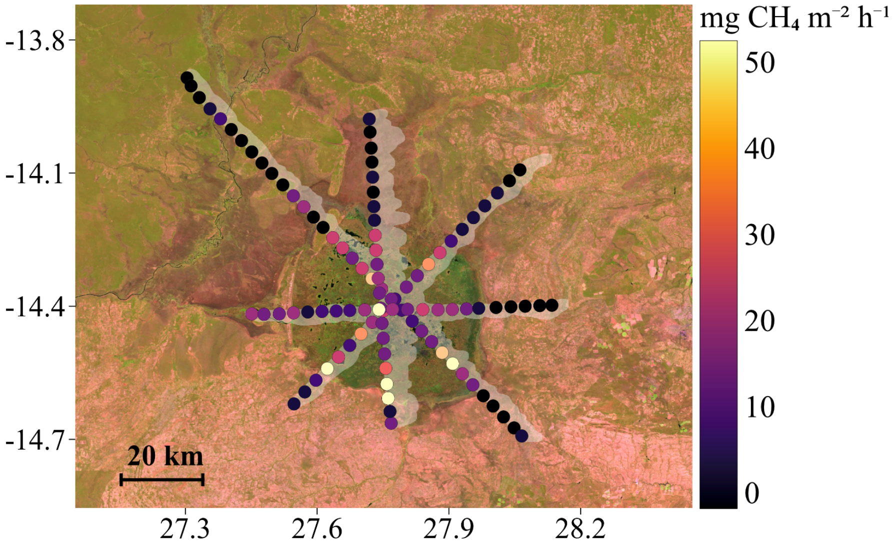

Figure 7.4: Airborne eddy-covariance fluxes (at 3 km intervals) for the Lukanga Swamp wetlands (C138). White highlighted areas indicate calculated emission footprints (90%). Map source: GLAD Landsat MOSAIC 2019 map [72].

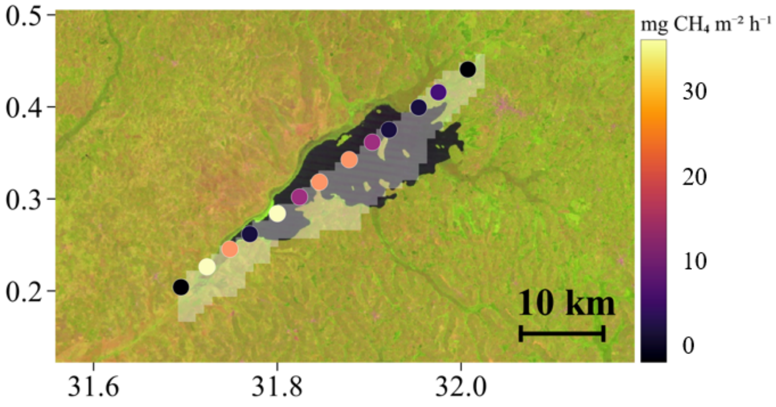

(a) Flight C128 flown over Lake Wamala in the afternoon.

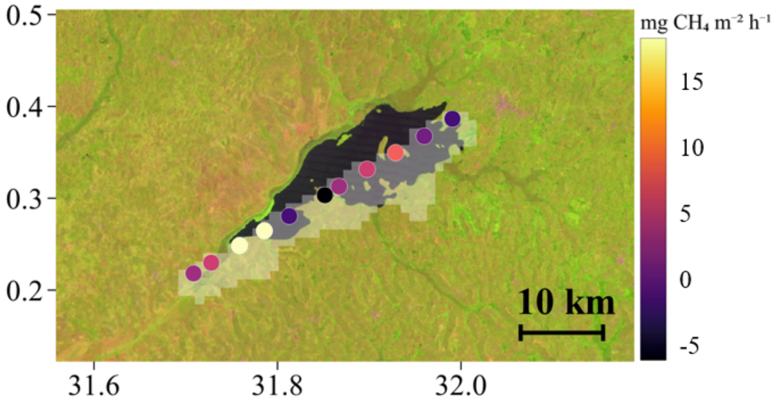

(b) Flight C129 flown over Lake Wamala in the morning.

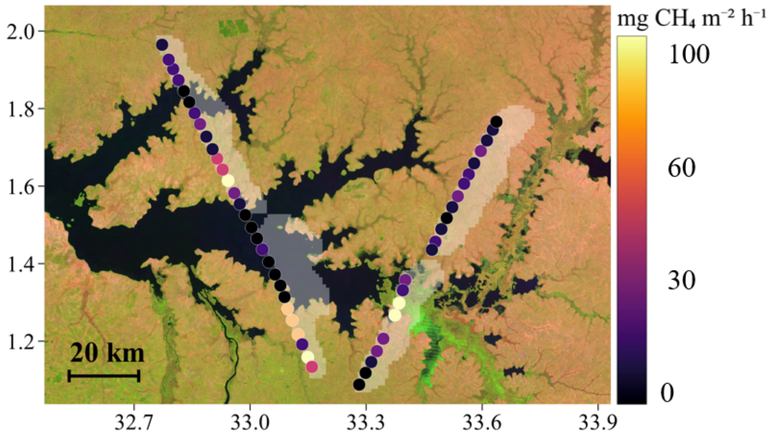

(c) Flight C132 flown over Lake Kyoga.

Figure 7.5: Airborne eddy-covariance fluxes (at 3 km intervals) for Lakes Wamala and Kyoga. White highlighted areas indicate calculated emission footprints (90%). Map source: GLAD Landsat MOSAIC 2019 map [72].

FAAM aircraft's capacity to deliver this kind of product and a pilot study for wetlands which were not previously studied at this scale. An alternative measure of uncertainty for AEC flux averaged over the wetland's area is standard deviation, which was used by Shaw et al. ([59]). The standard deviations for both flights are very high especially at 500 m resolution and only illustrate how heterogeneous the flux is. For Kafue the standard deviation was 31.6 mg CH_4 m^{-2} h^{-1} and for Lukanga 14.3 mg CH_4 m^{-2} h^{-1} hence 137% and 57%, respectively.

There is, however, a significant source of uncertainty that, at this point, is impossible to quantify, namely the PBL depth correction. There are two aspects to this problem. Firstly, there are only a few profiles allowing empirical BLH qualification. Correcting an entire flight by a gradient between 2-3 points, which additionally are spaced geographically would be an extremely crude. Hence, a NAME model was used [59]. The modelled values are validated by the empirical data from profiles, however the modelled BLH is by no means a precise and reliable value. Secondly, the correction (discussed in Section 6.5) relies on assumption that PBL over tropical wetland behaves in similar way as over temperate sites studied previously [189]. It also treats the BLH as a single well defined value, whereas in reality PBL does not end so sharply. This aspect is very important, since the correction is rather extreme and dominates any averaged values. For Kafue the average correction was 76% (13.1 ± 0.79 vs 23.0 ± 1.57 mg CH_4 m^{-2} h^{-1}), while for Lukanga it was 70% (16.4 ± 0.69 vs 27.9 ± 1.61 mg CH_4 m^{-2} h^{-1}). Nevertheless, this correction is necessary to account for loss of flux and the uncertainty introduced by its application has to be accepted until a better method is developed.

Apart from the two successful Zambian flights, four legs could be 'saved' from the Ugandan flight: two from C132, one from C129 and one from C128 (see Figure 7.5). Both C132 legs and C129 leg were flown in the morning, whereas C128 leg was flown in the afternoon. The flights were corrected by single value empirical BLH and the 10% from mean altitude rule was relaxed to 15%. Moreover, the QA/QC process was eased allowing more diagnostics outside of the 'desirable' range - otherwise only leg 21-C128 and leg 12-C132 would be acceptable. Especially leg 21-C129 is of very poor quality, but it would be a shame not to present it as a comparison for C128, even though caution in drawing any conclusion is needed. More details can be found in Appendix B in Table B.1.

The legs over Lake Wamala (Figures 7.5a to 7.5b) both suggest enhancement over the west end of the Lake, but the lake area seems to be active as well. It is likely because Wamala is a very shallow lake, so unlike in case of the bigger deeper lakes methane emitted from the bottom ebulliates from the surface rather instead of getting oxidised by water organisms. Moreover, the emissions in the afternoon are considerably larger than in the morning. Flight C132 covers much larger surface than the other flights and shows quite clearly enhancements over the wetlands (much larger than in case of Lake Wamala) and no flux over open water.

Finally, Sápmi wetlands flights (C195 and C196) suffered from insufficient depth in PBL for the subtle methane enhancements observed. Heat flux was not used as a QA/QC criterion since it cannot be assumed to be positive even in case of a summer day in the Arctic. Also, the 10% from mean altitude rule was neglected, since the fluxes failed at a very early stage. The eddy4R algorithm fundamentally struggled to find correlation for instrument lag and rejected most of the legs. From ones that passed the basic criteria, none gave satisfying quality AEC flux, starting with little to no cross correlation between wind and methane and ending with very low signal to noise ratios. Perhaps using a smaller aircraft, flying lower and slower would help to derive AEC, but in case of FAAM aircraft this is not possible.

7.2 Carbon dioxide AEC

Before discussing carbon dioxide fluxes from Zambian and Ugandan wetlands it is important to emphasise, that since this data is not being published the QA/QC process was relaxed. Table B.3 shows all the legs that provided satisfying AEC, with the legs 21-C128, 21-C129, 24-C137 and 27-C137 accepted conditionally. Moreover, CO_2 fluxes are far more complex, especially in terms of plant and fire dynamics, than CH_4 fluxes and a single instantaneous measurement flight is not a good basis for drawing meaningful conclusions. As shown by Hannun et al [194] carbon dioxide can vary day to day significantly and are heavily dependent on land coverage. Hence, in this work they are more of a showcase of instrument capacity to provide data suitable for CO_2 fluxes.

Carbon dioxide fluxes measured in Uganda (C128, C129 and C132) are shown in Figure 7.6 and these measured in Zambia are shown in Figure 7.7 (NB the colour scales are different for each country). Except for Lake Kyoga, all other lakes and swamps average to negative values, which should be expected due to carbon dioxide uptake by vegetation. The diurnal cycle means that during daytime uptake will dominate, while at night CO_2 will be emitted (see Figure 7.8). This variation applies also to methane, albeit its extend is less dramatic [194] and it remains unclear what is its main driver - soil temperature, radiation, photosynthesis or root exudation [145]? Or, most likely, combination of all.

According to Kim et al.'s meta-analysis of African GHG emissions wetlands [94], vegetable gardens and rivers emit most CO_2 per unit of area - over twice more than woodland or cropland and over 5 times more than savanna. Contrary, Hannun et al.'s AEC study of Mid-Atlantic region in the USA [194] show that open water emissions are minor but frequently positive, while wetlands and croplands show largely negative flux. Overall, there is not much consensus as to what should the flux be for each land coverage type - as mentioned above, it is complicated.

In this study it is apparent, that wetland areas emit more than savanna, which is characterised by uptake. This seems to be in line with what Kim et al. [94] suggest, but goes contrary to what could be deduced from the diurnal profile described by Saunders et al. [195] (see Figure 7.8). According to the profile, during mid-day photosynthetic uptake of CO_2 should dominate and the flux should be negative. One possible explanation could be fires. That was ruled out by inspection of condensation particle count (CPC) and CO concentrations measured during the flight as shown in Appendix B Figures B.5 to B.6. The precise reasons for this flux distribution will likely remain a question, since the data set is very limited and only further measurements could confirm or disprove this observation. It is crucial to remember however that the literature presents a broad range of values when it comes to wetland CO_2 flux and there is a scarce amount of large scale research on tropical wetlands, not to mention lack of AEC studies of similar environments.

7.3 Comparison of AEC with other methods and studies

Another method used to quantify methane emissions from Lukanga Swamps and Lake Bangweulu was mass balance. Different approaches used are described in Section 6.3.1 and the data analysis was done by Jacob Shaw (University of Manchester) [59]. In case of Lukanga Swamp the mass balance flux was 11.2 ± 2.0 kg CH_4 s^{-1} for the entire wetland and, assuming Ramsar estimate of the area (2600 km^{-2} [159]), 15.5 ± 2.7 mg CH_4 h^{-1} for square meter of wetland. The quoted uncertainty includes uncertainties originating from wind and methane measurements, boundary layer mixing processes and background variability.

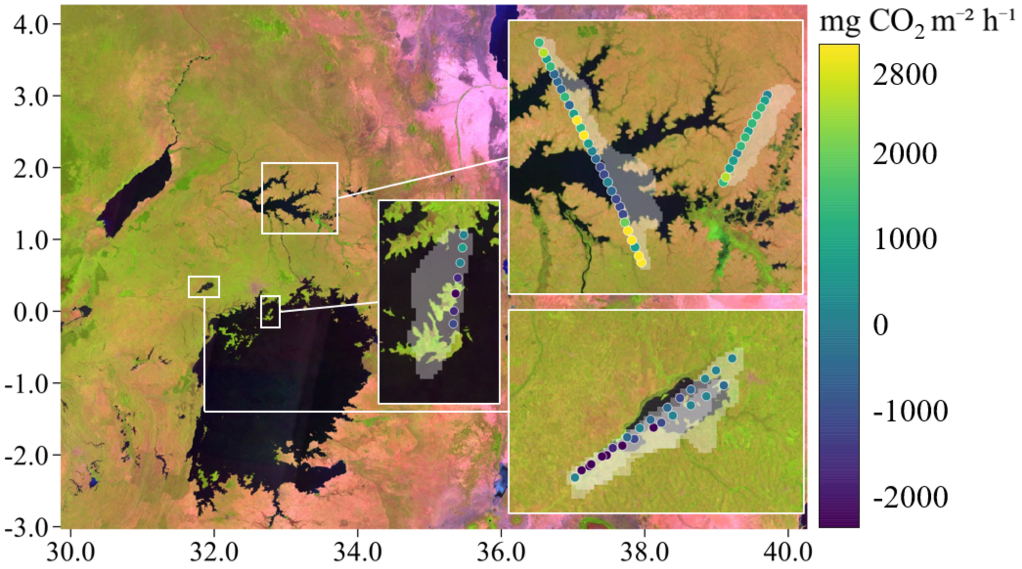

Figure 7.6: All CO$_2$ AEC fluxes in Uganda.

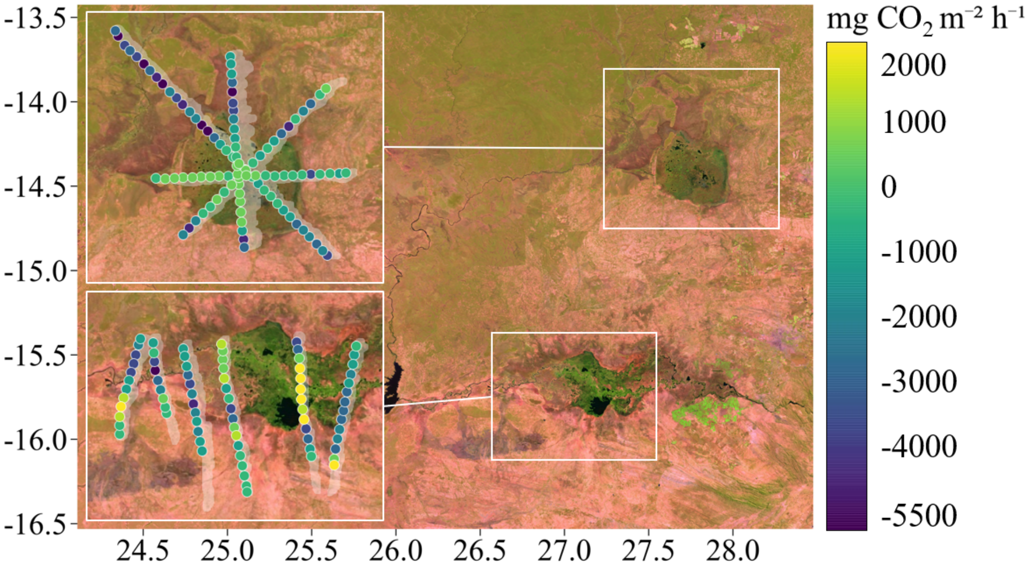

Figure 7.7: All CO$_2$ AEC fluxes in Zambia.

A direct comparison with AEC is possible, however, the two methods represent a diametrically different approach to quantification of the methane emissions. Mass balance quantifies the bulk flux of the entire wetland while AEC effectively quantifies flux of just a fraction of the wetland showing spacial resolution but being potentially less representative. In this study the the average of mass balance and AEC should not be directly compared, since AEC is derived based on relatively few legs and showing just a snapshot of time. This could obviously be improved in future with more AEC oriented flights, which would make the results a bit more universally representative. Interestingly enough, the mass balance results for Lukanga Swamp agree within uncertainty with uncorrected AEC - respectively, 15.5 ± 2.7 vs 13.1 ± 0.79 mg CH_4 m^{-2} h^{-1} (no mass balance for Kafue Flats is available). Bangweulu Swamps, which failed attempts of deriving AEC due to challenging meteorology, resulted in 21.1 ± 6.1 mg CH_4 m^{-2} h^{-1}, which results in 46.9 ± 13.6 kg CH_4 s^{-1} bulk flux (scaled by its Ramsar surface, i.e. 11000 km^2, see Section 6.3.1).

All three Zambian wetlands were also modelled using NAME, which is a Lagrangian atmospheric dispersion model, in conjunction with an inverse method. Scaled *a priori* methane emissions gave mean *posterior* fluxes from the Bangweulu, Kafue, and Lukanga wetlands of 9.0 ± 3.4, 5.0 ± 0.7, and 14.6 ± 2.5 mg CH_4 m^{-2} h^{-1} respectively. Bulk fluxes based on there values are shown in Table 7.1. The values cannot be compared as “like to like" in this study.

Taking all the measured values and comparing them to modelled ones it becomes apparent that the models significantly underestimate the emissions. Global Carbon Project (GCP) and WetCHARTs are wetland model ensembles that were deployed to simulate methane fluxes from all the Zambian wetlands, based on model climatology from years 2000-2017. WetCHARTs model ensemble turns out to suggest mean values for methane emissions that are 15 time smaller than the measured values for Lukanga Swamp. This

	Per-unit-area flux (mg CH_4 m^{-2} h^{-1})			Bulk flux (kg CH_4 s^{-1})		
	Bangweulu	Kafue	Lukanga	Bangweulu	Kafue	Lukanga
Mass balance	21.1 ± 6.1	NA	15.5 ± 2.7	46.9 ± 13.6	NA	11.2 ± 2.0
AEC	NA	23.0 ± 1.57	27.9 ± 1.61	NA	42.2 ± 58.0	20.2 ± 10.3
NAME	9.0 ± 3.4	5.0 ± 0.7	14.6 ± 2.5	20.0 ± 7.6	9.2 ± 1.3	10.5 ± 1.8
GCP[1]	1.7 ± 2.0	1.2 ± 1.6	3.9 ± 5.0	3.9 ± 4.3	2.3 ± 3.0	2.8 ± 3.6
WetCHARTs[2]	2.7 ± 2.1	0.6 ± 0.6	1.6 ± 2.3	6.0 ± 4.7	1.2 ± 1.1	1.1 ± 1.7

[1] Mean of 13 models for 2000-2017.

[2] Mean of 9 models in 324 different ensemble members for 2009-2010.

Table 7.1: Comparison of all fluxes. Source: Shaw et al. [59].

proves how important is to conduct *in situ* large scale measurements. The usefulness of AEC spatial resolution shows when looking at the WetCHARTs terrestrial biosphere models (e.g. BIOME-BGC). Some of them simulate methane enhancements mainly over open water bodies, which show clearly lower flux in AEC measurements. This likely comes from a 1980s study of Australian lakes indeed showing high methane flux from the open water, however this has never proven to be a worldwide case [196].

Moreover, a comparison with other published studies on tropical research GHG emissions is shown in Appendix B in Table B.5. Especially Were at al. [170] provides an useful reference, not only because they studied a wetland from Lake Kyoga basin, but also because the study was performed right after the MOYA-2 campaign. More information about this study can be found in Section 5.5.2. Comparing carbon dioxide fluxes to literature is slightly less obvious, since the flux is heavily influenced by the plant dynamics and the diurnal cycle needs to be taken into account (see Figure 7.8).

All these comparisons above have one fundamental flaw - scaling the 10 h of available data to entire year is a far fetched extrapolation, which are not captured. Moreover the methods are very different and direct comparison is not necessarily possible. Diurnal cycle of carbon dioxide and methane are worth bearing in mind when comparing this work to other studies, especially these utilising chambers or EC towers. They refer not only to considerably smaller area but also provide averages over considerably longer periods of time than this study. The latter means that the diurnal cycle is averaged out, whereas this study falls on the greatest uptake period. Hence, for carbon dioxide AEC fluxes no absolute values comparison is relevant (also because this study was not designed for AEC).

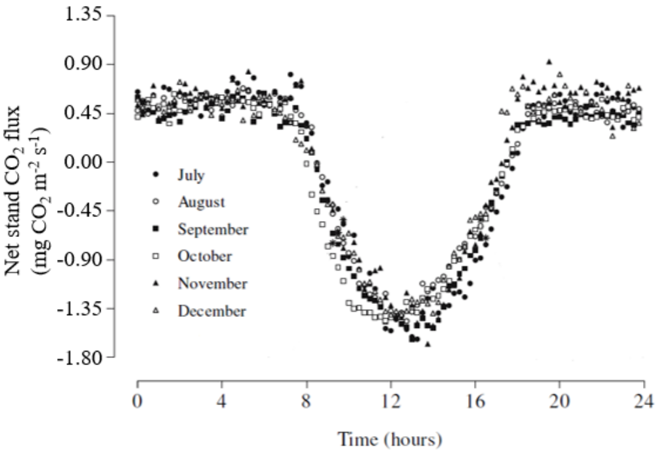

Figure 7.8: Diurnal CO_2 flux cycle of Kirinya West wetland (Lake Victoria near Jinja, Uganda). Source: Sauners et al. [195] (simplified).

For example, in case of Federseemoor peatland in Germany [145] the characteristic diurnal flux pattern starts in May, when new reeds appear and is present until October. The greatest amplitude is observed in August for CH_4 and in July for CO_2, with most positive CH_4 and most negative CO_2 fluxes between 10 AM and 1 PM (15.7 and 2360 mg m^{-2} h^{-1}, respectively). In a study of reeds, mudflats and river water in Shanyutan estuarine wetland on southeastern coast of China [197] CO_2 and CH_4 fluxes ranged from -422 to 223 and -42.3 to 49.4 mg m^{-2} h^{-1}, respectively.

Carbon dioxide flux diurnal pattern was attributed to gas-transport mechanisms in plants driven by photosynthesis and respiration, but it was also affected by the inundation levels. Meanwhile, methane flux peaked at night under mostly anaerobic conditions and decreased during day, especially during low tide. Another study looking at multiple ecosystems in the Mid-Atlantic region in the USA [194] demonstrates how different the AEC flux can be depending on a day. For carbon dioxide, that can be even a 10-fold difference. For methane the changes observed were less dramatic, but still could reach 50%.

A summary of GHG fluxes in literature is shown in Section 7.3. Kim et al. [94] provide a meta-analysis of GHG sources in sub-Saharan Africa. They show that natural terrestrial CO_2 flux ranges from 40 to 1490 mg m^{-2} h^{-1}, while natural aquatic flux stretches across even greater range: from -135 to 2645 mg m^{-2} h^{-1}. This shows what a range of CO_2 fluxes can be encountered across different types of land coverage. When it comes to methane, the study suggests, that woodland of all sort are a sink while savanna, cropland and rice fields are small to medium sources. Wetlands, floodplains, reservoirs and lagoons are the major methane sources with average flux of 10.8 ± 4.0 mg m^{-2} h^{-1}.

The most geographically relevant comparison available is an EC study of Kirinya West wetland (Jinja, Uganda) by Saunders at al. [195], see Figure 7.8. The maximum uptake observed was 6340 mg m^{-2} h^{-1} and the highest emission was 3170 mg m^{-2} h^{-1}, hence the values observed during MOYA-2 and ZWAMPS fall well into this range. It is however worth bearing in mind that the 24 h average of the flux is 320 mg m^{-2} h^{-1}.

7.4 Guide to flight planning for EC

7.4.1 Improving the PBL depth correction

Looking at the processing of AEC described in Chapter 6 it is apparent that by far the weakest point is the PBL depth correction. As mentioned before it is assumed that entrainment zone equals 80% of BLH [189]. The weakness of this assumption is that the value was derived in much more temperate climate and it might be actually different for tropical wetland. There are only few profiles empirically quantifying BLH and no attempt to quantify the

Source	CO_2 flux range (mg m^{-2} h^{-1})
MOYA and ZWAMPS AEC (this work)	604 - 630
Natural Terrestrial	40 - 1490 [94]
Natural Aquatic	-135 - 2645 [94]
Kirinya West Wetland (Jinja, Uganda)	Maximum uptake: 6340 [195] Highest emission: 3170 [195] 24h average: 320 [195]
	CH_4 flux range (mg m^{-2} h^{-1})
ZWAMPS AEC (this work)	21.4 - 29.5
Wetlands, Floodplains, Reservoirs, Lagoons	10.8 ± 4.0 [94]

Table 7.2: Comparison of carbon dioxide and methane fluxes in literature with this work.

entrainment zone / convective boundary layer border at all for the dataset used in this work. Even the very definition of the entrainment zone is rather fluid:

> In theory, it is the region in which the mean buoyancy flux is negative [...]. It effectively is impossible to measure flux profiles with sufficient precision to determine the [entrainment zone] in real atmospheres with this definition. Another possible definition is the region in which the mean [...] temperature, moisture, and/or aerosol profiles have strong gradients.[...] A third definition [...] is the region in which more than 5% but less than 100% of the air in a horizontal or temporal transect has free-troposphere characteristics such as low aerosol concentrations or low humidity [...]. In practice this definition is equivalent to finding the locations of percentiles [...] of the [convective boundary layer] top. ([191])

However, in these work the choice was between this correction or no correction at all. Ultimately an approximate correction was decided to give closer to the truth values than no correction at all. In future AEC dedicated campaigns it would be ideal to have more detailed measurements of the PBL dynamics provided by ground based radar or lidar system [191, 198, 199]. However, in absence of means to do so, it would be beneficial to sample the PBL more frequently between legs, even using high ascent rate, just to have more comparison points with the modelled BLH. This could allow making a more precise estimate of the fraction of PBL that is convective and how it changes throughout flight. Another possible approach is stacking legs at different altitudes what could give further information on how much flux is lost with altitude and help to make the correction more precise. This strategy is however very limited with BAe-146, since it is a subject to substantial (from AEC perspective) flight level limitations over ground.

7.4.2 Diurnal cycle

Especially in terms of CO_2 emissions from wetlands, there is not much agreement in the literature and this is likely impacted by the complicated mechanisms underlying its temporal variability. The diurnal patterns heavily influence the observed GHG fluxes [145, 170, 194, 195]. Since FAAM flights last at most 5h and usually take place in daylight knowing the local diurnal pattern would be beneficial in upscaling the data. In fact, lack of such proved to be one of major issues for Shaw et al. [59].

For sites with EC towers, like e.g. in studies conducted by Hannun et al. [194] or Metzger et al. [189], it would be ideal to stack one leg above the tower to have most direct comparison and at the same time monitor flux decay with altitude. This however is an infrequent luxury to have a EC tower on site, especially in sub-Saharan Africa, which is the area of particular interest for the FAAM's newly developed AEC capacity. An alternative would be a parallel chamber study or even just continuous concentration measurement. The last solution is least precise however very easy to execute.

It would require a FGGA (or even UGGA) equipped with automated calibration system and a power supply being placed on the research site for a few days, not even necessary during the flight (since no direct comparison can be made).

7.4.3 Drafting flight plan

Lac Télé / Likouala-aux-herbes and Grand Affluents Ramsar sites in the Republic of Congo were chosen for the hypothetical AEC flight (see Figure 7.9). Lac Télé or Lake Tele is a stunning nearly perfectly round lake in a middle of forested wetland created by River Likouala. Its waters are rich in organic matter and the surrounding ecosystem includes 4400 km^2 wooded swamp and savanna or floating prairies [200]. Grand Affluents is a large site surrounding Lac Télé / Likouala-aux-herbes and covering 59 000 km^2. It contains major Congo tributaries - Ubangi, Sangha, Likouala-Mossaka and Alima, and its dominant habitats are permanently flooded or wetland forests, marshes, ponds and lakes [201]. Both sites are characterised by extensive, largely unaffected by human activity wetlands, which are have not been studied for methane flux using airborne platforms.

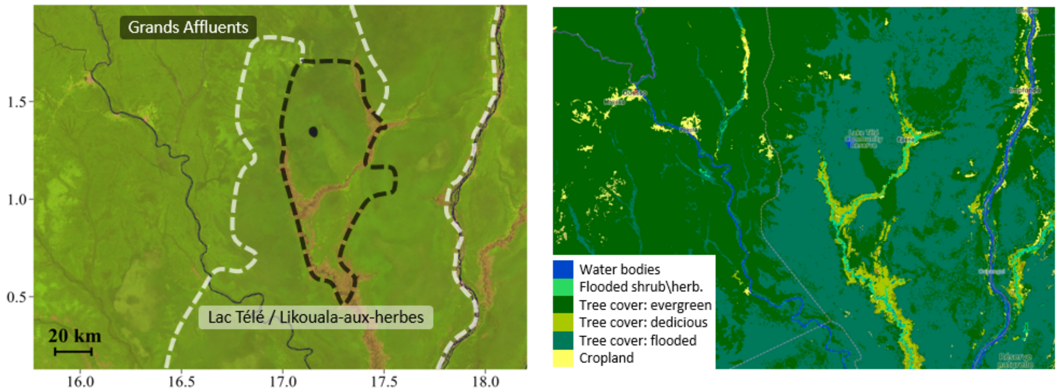

Figure 7.9: Lac Télé / Likouala-aux-herbes and Grand Affluents Ramsar sites map and land coverage map. Sources: GLAD Landsat MOSAIC 2019 map [72] and European Space Agency CCI Land Cover map [150].

On the logistic side, there is an airport nearby in Ouésso and range of other scientifically promising wetlands. The area is also very flat, so there would be no physical obstacles for long level legs. The most obvious downside is unstable political, economical and social situation in the Congo, albeit considerably better than in neighbouring Democratic Republic of Congo being home to the majority of African wetlands. Furthermore, low cloud deck and slack wind could be significant constrains.

An example of a wetland that would not be an good place for AEC flight is Elephant Marsh - a Ramsar site in south Malawi, shown in Figure 7.10. It is only approx. 10 km wide and restricted tightly by Great Rift Valley edge, what with the predominant wind direction along the Valley (rather than across). With AEC legs preferentially being perpendicular to the wind direction, the space would be highly constrained and, even though AEC-worthy data could be obtained, BAe-146 would not be the best aircraft for this location. A smaller aircraft, such as Twin Otter, could fly lower and slower, hence shorter legs and the hills limiting one side of the wetland would not be an issue. Even though small aircraft does not have such a range like FAAM, Elephant Marsh covers only 615 km^2 so it would be completely feasible to cover it with a limited range.

The day chosen for the flight was 24th July 2021, because of its stable, relatively strong for the region south-westerly wind (4-5 m s^{-1} at 100 m altitude) until 15:00 local time (L). The sky was mostly clear only with occasional fragmented cloud at 1500 m, so above the operation area. Temperature and PBL expansion could potentially be tricky, like in case of leg 5-C137. The temperature changes quite dramatically in the morning from 22° C at night and until 8:00 L to 27° C from 9:00 L onward leading to PBL development. Hence, it would be idea to reach the task area about 10:00 L and leave it by 14:00 L. This is not always possible, due to flying permissions and airborne wildlife, which might be a bit too friendly. Nevertheless, the changes in PBL should be taken into account when planning the flight.

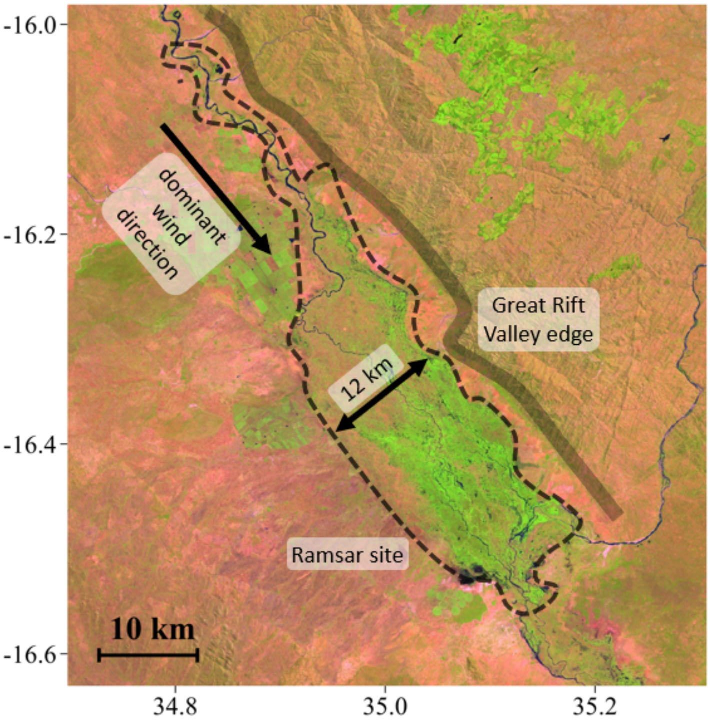

Figure 7.10: Elephant Marsh Ramsar site as an example of location unsuitable for AEC on board of FAAM aircraft. Map source: GLAD Landsat MOSAIC 2019 map [72].

Two alternative flight plans are shown in Figure 7.11 and described below. The first one is a general survey, suitable for the first flight of a campaign, especially that there are barely any measurements in the area, so there is no reference. The outline of the flight would be:

1. Take off and transit to task area. Profile down to find the BLH, arriving at WP1 at the lowest flight level (FL) that is safe and permitted and allowing 5 min for calibrations.
2. At WP1 turn to WP2 at the minimal FL following the terrain. Overall, it is necessary to stay in the lower half of PBL with 0.6 BLH being maximum. But the lower the better.
3. Turn to WP3 allowing for calibrations, and start next leg between WP3 and WP4. Same procedure for WP5 and WP6.
4. Profile up to top of PBL, turn and arrive back at WP6 at the same altitude and repeat the pattern backwards, ie. with legs WP6-WP5,

WP4-WP3 and WP2-WP1.

5. At the end profile up to top of PBL, turn and, if time allows, add a ‘half-leg’ WP1-WP7 or transit back.

This approach, however, compromises on the data quality. Such long legs (approx. 160 km or 30 min each) can be repeated only twice and at the same FL, and hence insufficient to asses flux decay with the altitude and lower the error significantly. Repeating them is important, since some data will likely fail the QA/QC process and two stacked legs decrease chances of gaps. They also demonstrate to some extent the temporal variability of the flux. The main purpose of this kind of survey is highlighting the areas of interest and providing some context for future flight planning. It could also be combined with mass balance runs in case of smaller and better defined wetlands.

The second approach is a more detailed survey of a smaller area, in this case just the Lac Télé / Likouala-aux-herbes Ramsar site. The flight plan assumes a similar ‘squiggly line’ pattern with 50-60 km legs (10 min), but thanks to shortening the distance they can be repeated 6 times. In a AEC study of NO_x and VOCs in London Vaughan et al. [193] used 7-8 repetitions of each leg, but since a wetland are considerably more homogeneous than a city, 5-6 legs are likely sufficient. Nevertheless, the way points could be moved closer together if 6 runs would prove insufficient. The way points on each side are spaced by 15-20 km allowing some space to check the BLH. Additionally, the way points are removed away from the clearings around Ball and Likouala rivers not to hassle the local farmers with low level flights directly over their heads.

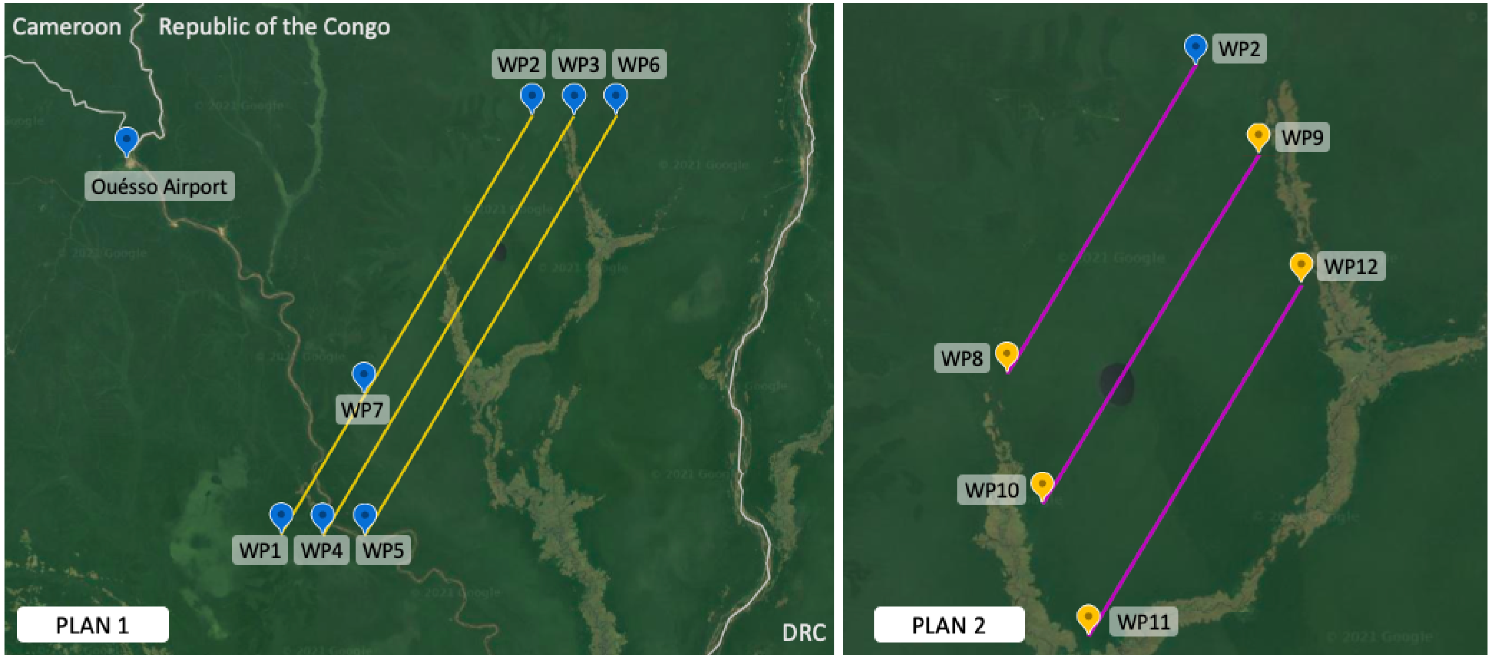

Figure 7.11: Draft flight plans for Lac Télé / Likouala-aux-herbes and Grand Affluents wetlands in the Congo for 24th July 2021 conditions (south-westerly wind, mostly clear sky). Map source: Google Earth.

Chapter 8

Conclusions: Airborne eddy covariance

The main objective of this work was calculating methane AEC flux from data obtained on board of BAe-146 and hence proving FAAM's capacity to deliver a new kind of data product. This objective was met in 100% showing that despite very early stage of development of the 'fast' FGGA mode the speed and quality of data was sufficient for AEC. Moreover, the data has proven to be exceptionally good quality in case of C137 and C138, despite the measurements being taken at relatively high altitude above the ground.

Another side of project was delivering first large scale measurements of wetland methane flux in Sub-Saharan Africa and adding to the very scarce base of airborne data in the region. This objective was also met, however the data presents a very narrow snapshot in time, hence it cannot really be treated as a self standing study and highlights need of further campaigns. The main observation that can be drawn at this stage is the noticeable heterogeneity of the wetland, described also by DelSontro et al. [158]. Open water is characterised by very low methane flux, while the shores and wetland area show much higher emissions. If the data was extrapolated it could mean significant underestimation of the models, however further work is needed to draw conclusions.

Final objective was formulating an approach to planning AEC specific flights for BAe-146. The approaches described commonly in literature usually refer to small aircraft and cannot be replicated by FAAM. However, FAAM provides much greater payload capacity and speed, making surveys of large remote areas possible. The three methane flux campaigns - MOYA-2, ZWAMPS and MOYA-Arctic were a valuable lesson of BAe-146 flux capacity and limitations. Notably, the BLH depth correction needs further work, especially if it is meant to be applied in tropical setup.

Overall, this project was taking a leap into the dark in terms of instrumentation, flight planning approach and the researched sites. It turned out to be very successful, even though at first glance it might not have delivered a straightforward outcome. It set however a precedence and hopefully it will be followed by further studies of wetlands in Zambia, Uganda and other African countries. It is unacceptable in 21st century to scientifically (and not only) ignore an entire continent in terms of GHG emissions, but also air or water quality [94, 134–136]. Moreover, I hope that future research will bring much closer cooperation with local researchers and specialists, who are often overlooked in the process.

Appendix A

Supporting Information for Chapter 3

A.1 Data overview

(a) Flight C179

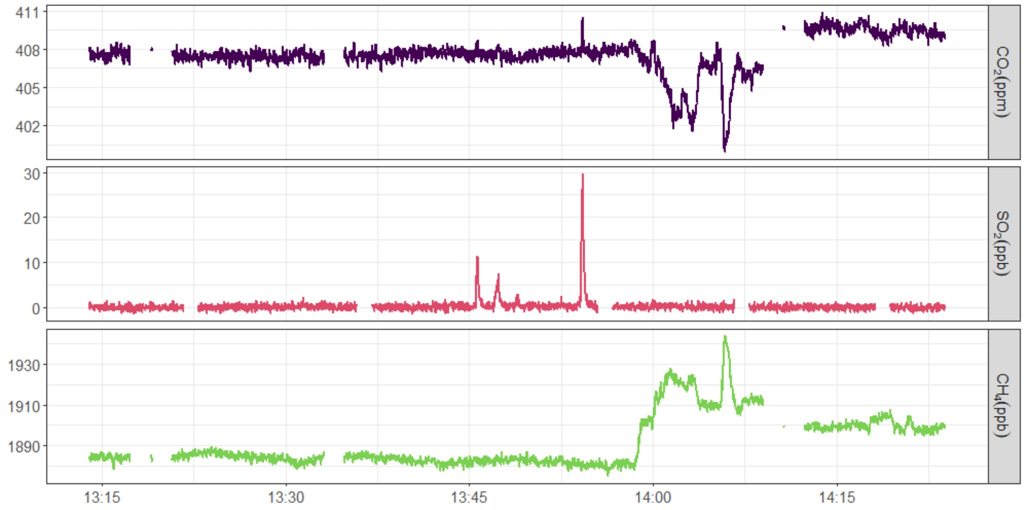

(b) Flight C180

Figure A.1: Time series for all ACRUISE-2 flights.

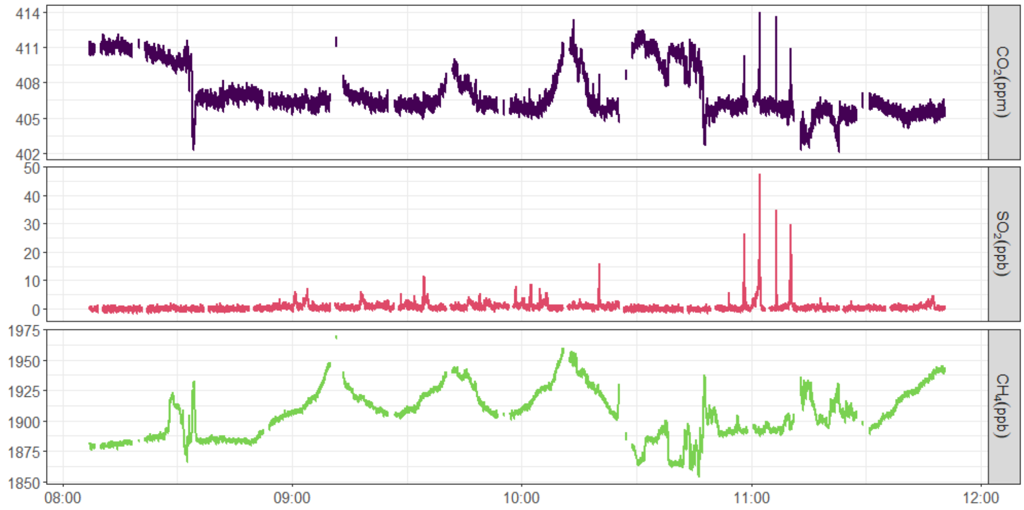

(c) Flight C181

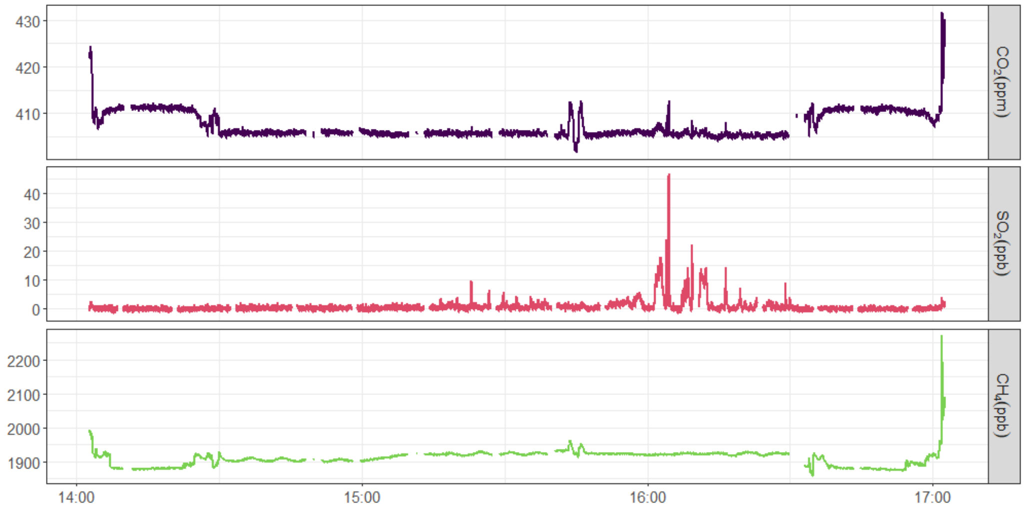

(d) Flight C182

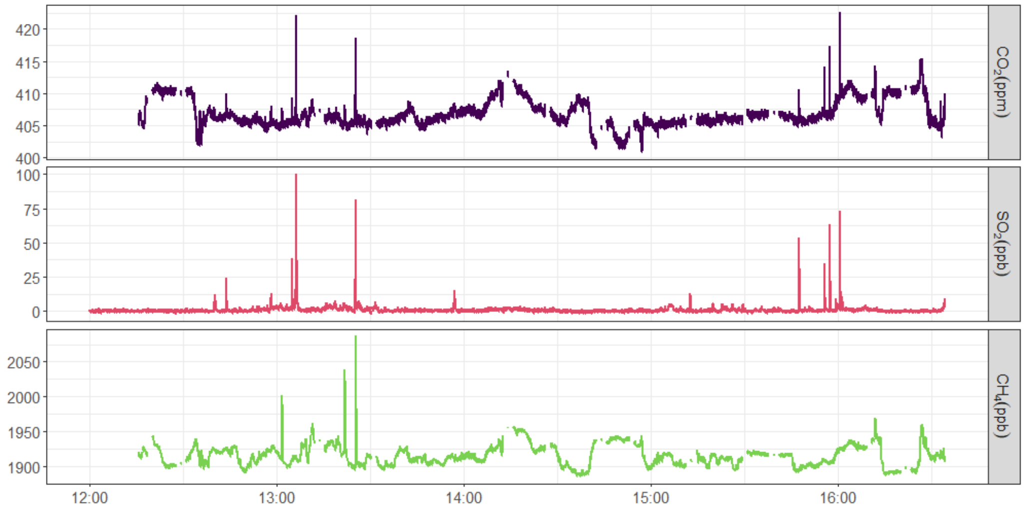

(e) Flight C183

Figure A.1: Time series for all the ACRUISE-1 flights.

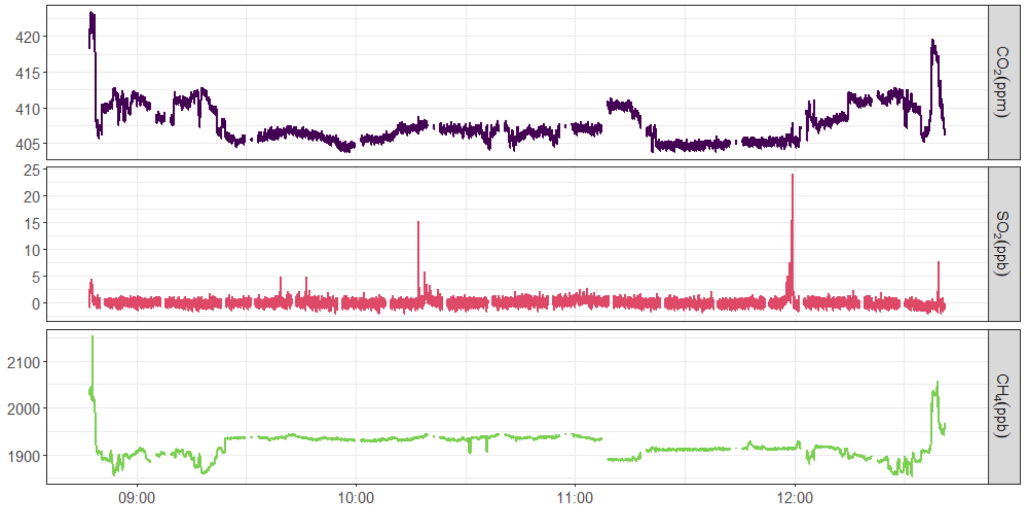

(f) Flight C184

(g) Flight C185

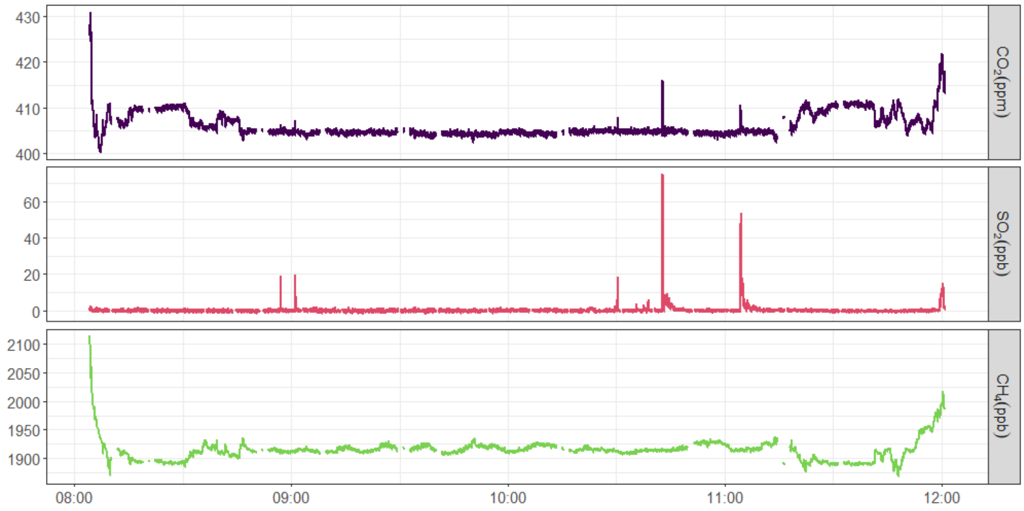

(h) Flight C186

Figure A.1: Time series for all the ACRUISE-1 flights.

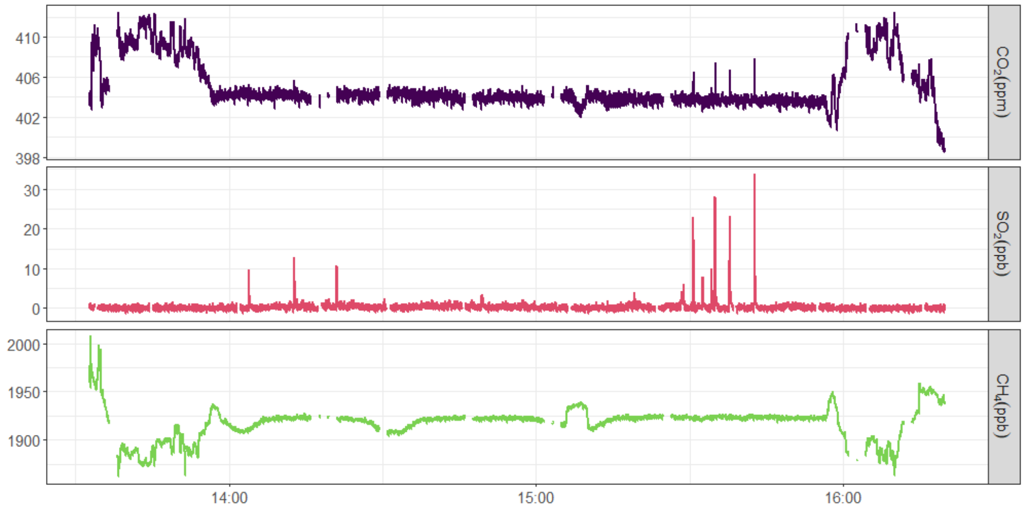

(i) Flight C187

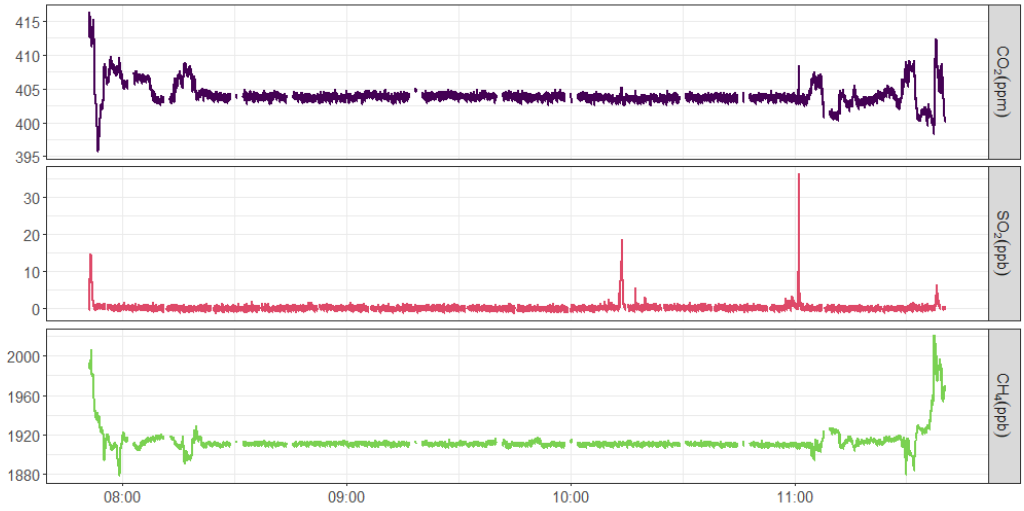

(j) Flight C188

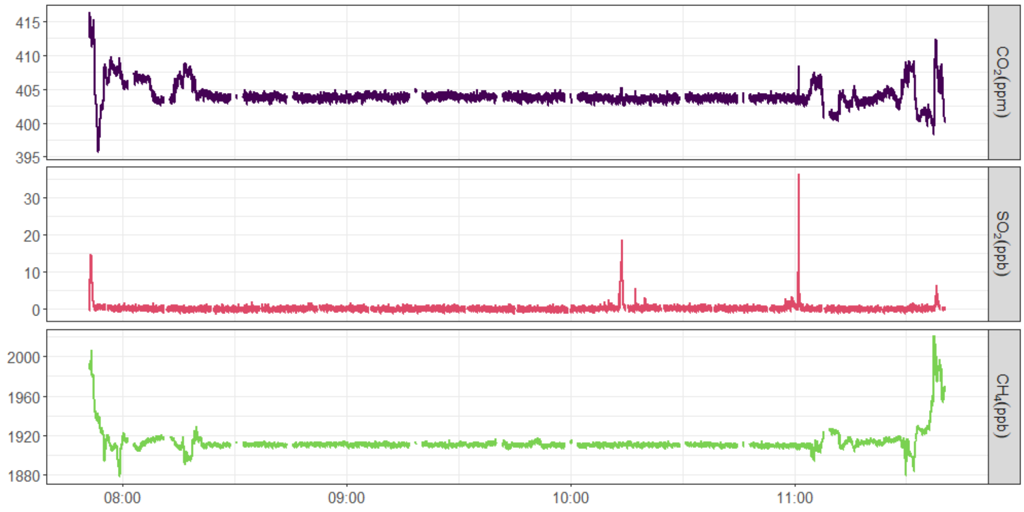

(k) Flight C189

Figure A.1: Time series for all the ACRUISE-1 flights.

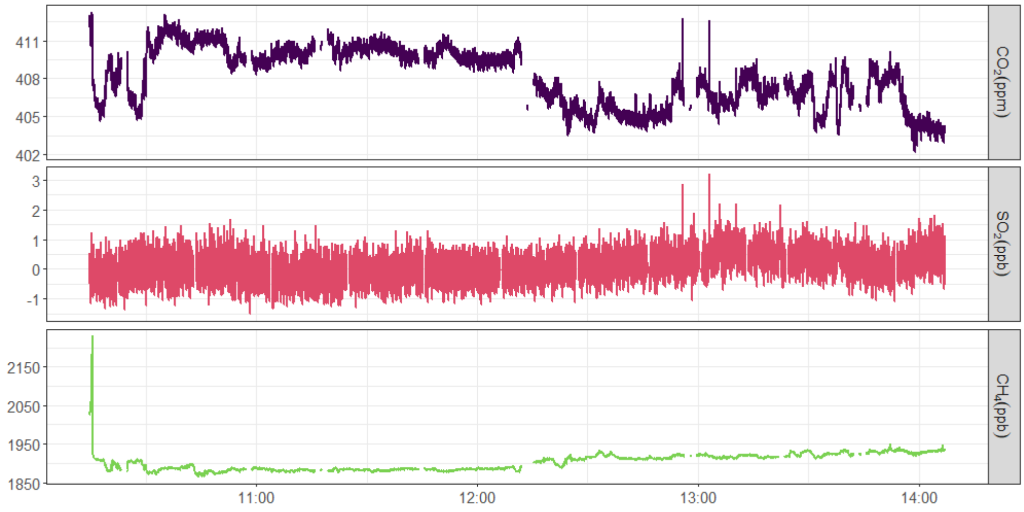

(l) Flight C190

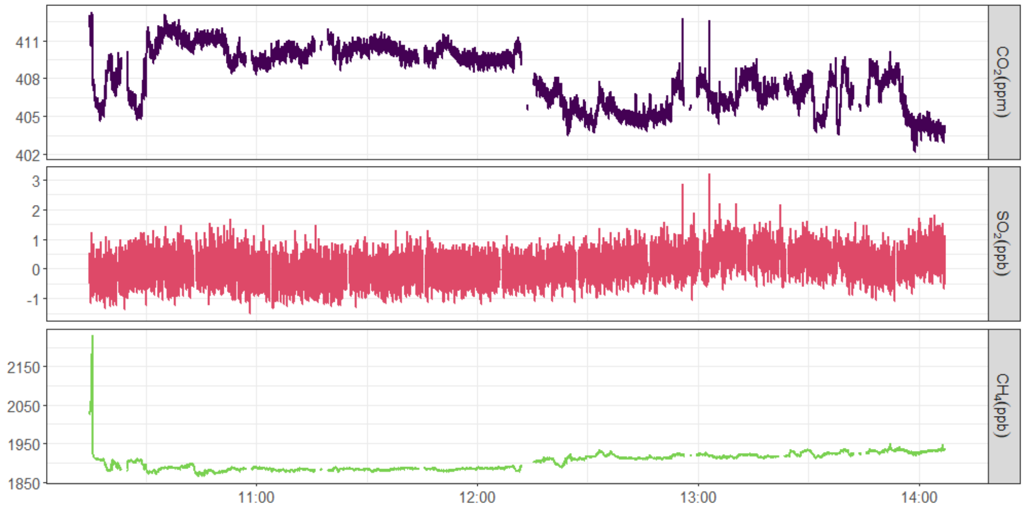

(m) Flight C191

Figure A.1: Time series for all the ACRUISE-1 flights.

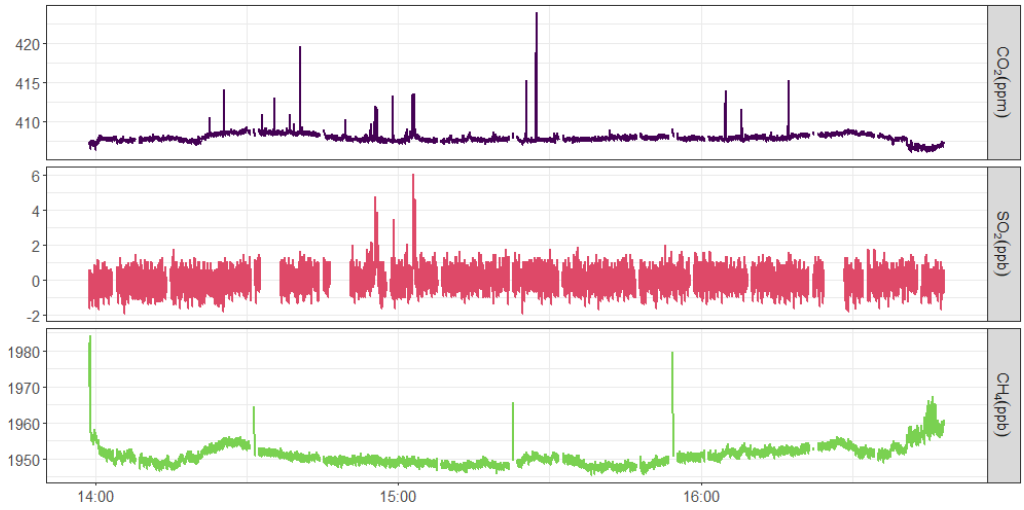

(a) Flight C253

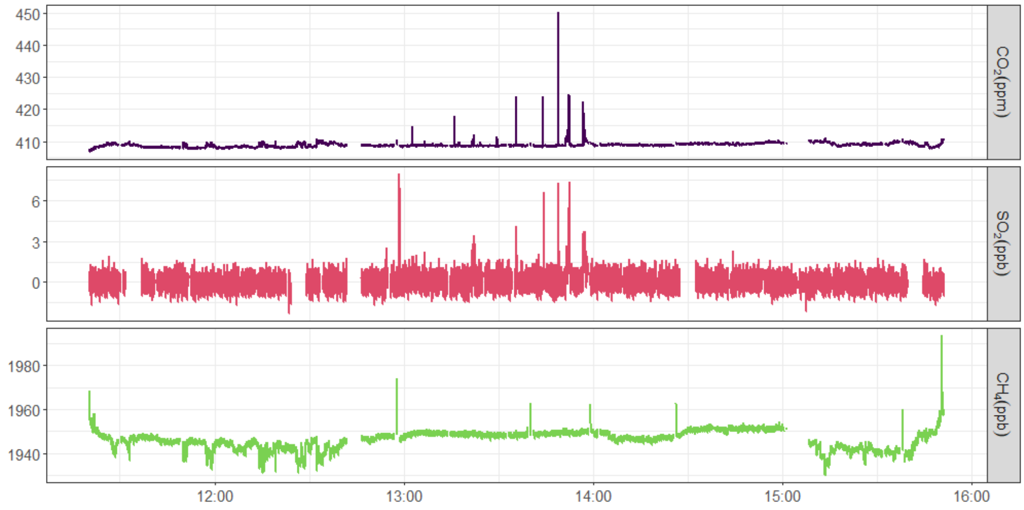

(b) Flight C254

(c) Flight C255

Figure A.2: Time series for all the ACRUISE-2 flights.

(d) Flight C256

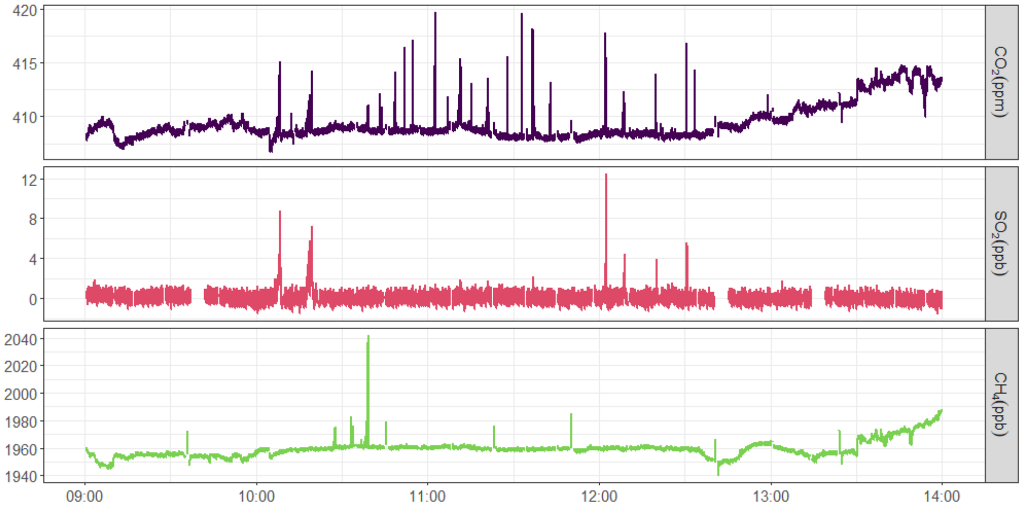

(e) Flight C257

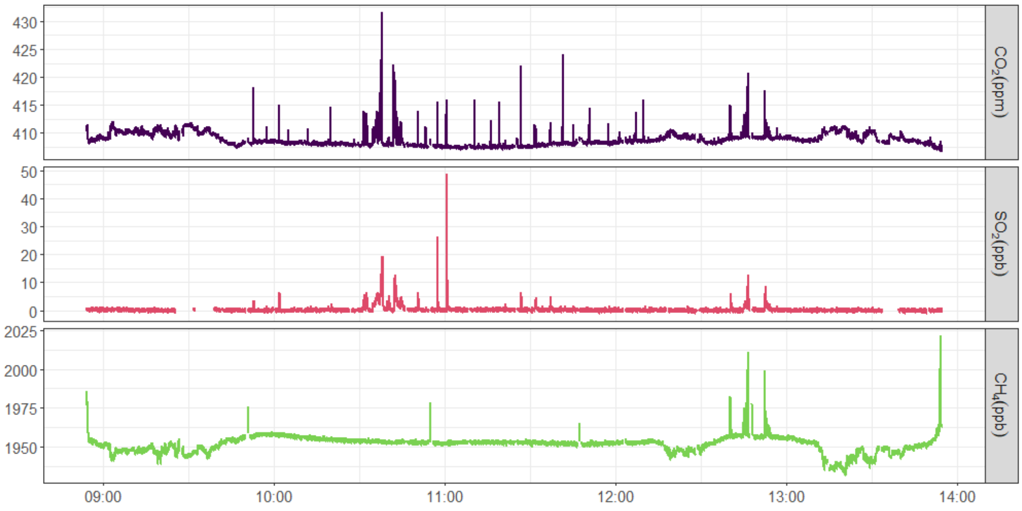

(f) Flight C258

Figure A.2: Time series for all the ACRUISE-2 flights.

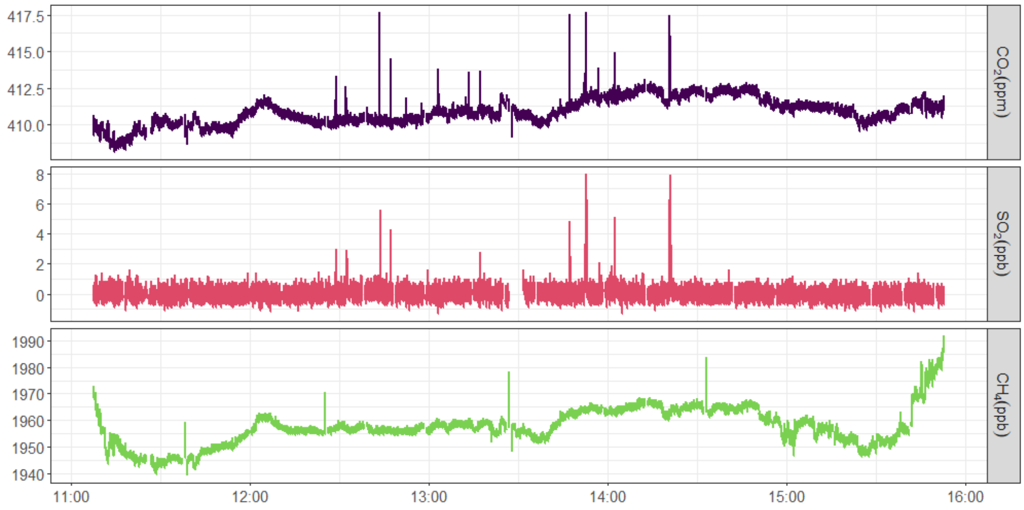

(g) Flight C259

(h) Flight C260

(i) Flight C261

Figure A.2: Time series for all the ACRUISE-2 flights.

(j) Flight C262

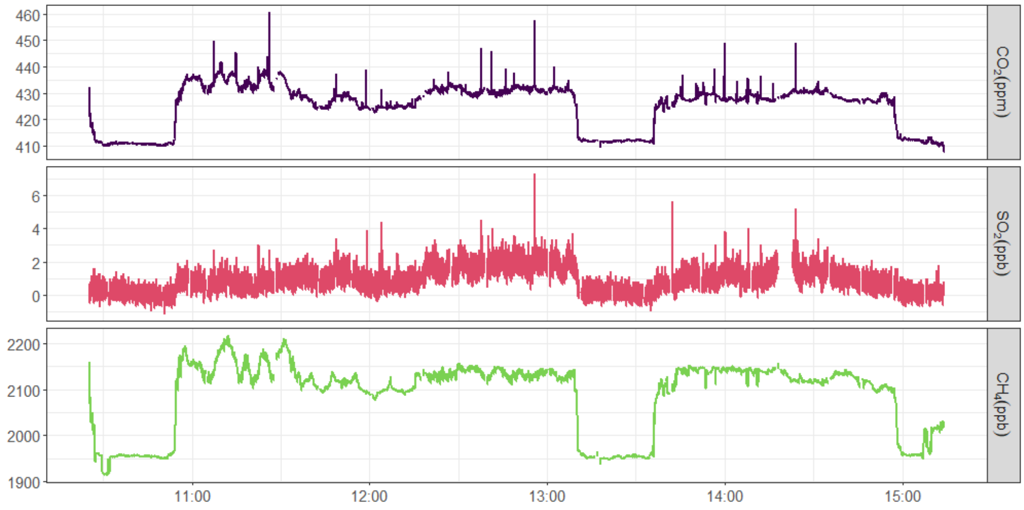

(k) Flight C263

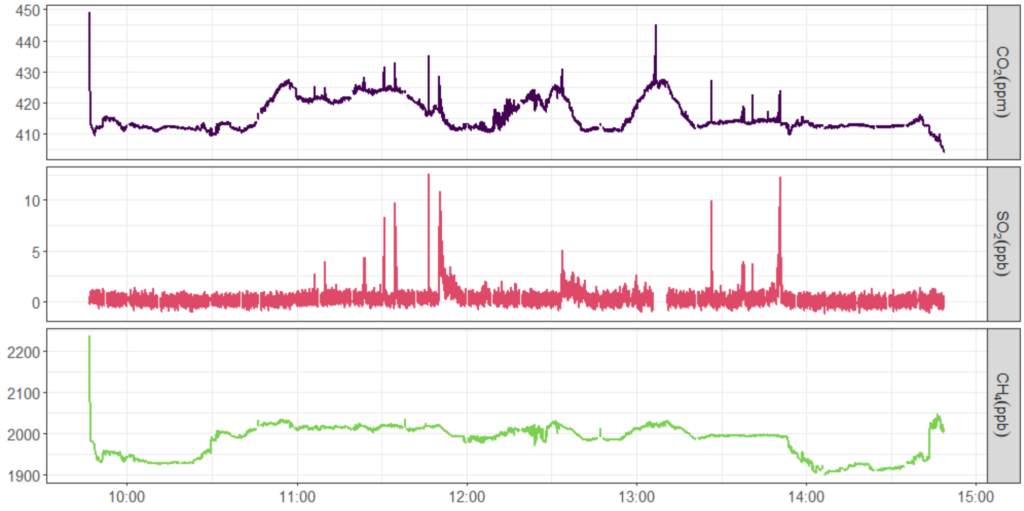

(l) Flight C264

Figure A.2: Time series for all the ACRUISE-2 flights.

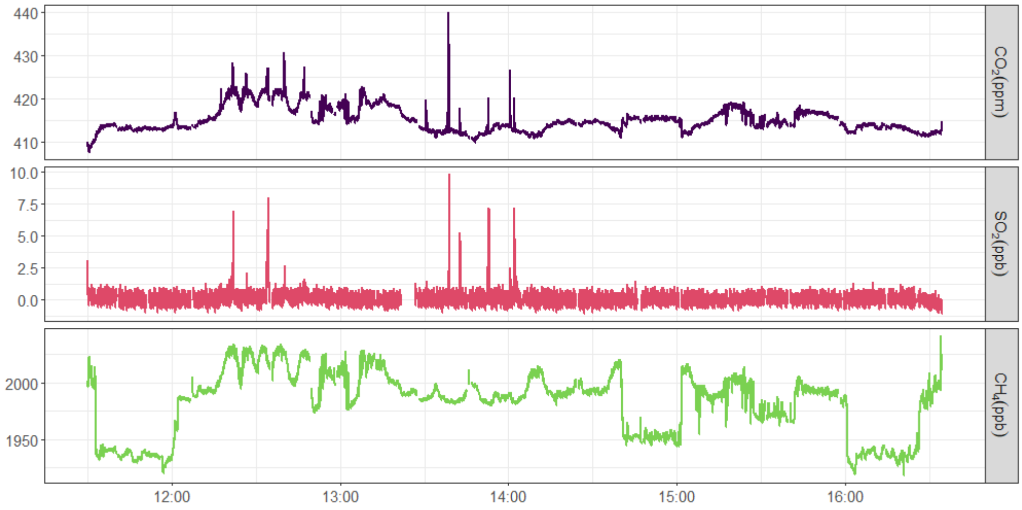

(m) Flight C265

Figure A.2: Time series for all the ACRUISE-2 flights.

(a) Flight C284

Figure A.3: Time series for all the ACRUISE-3 flights.

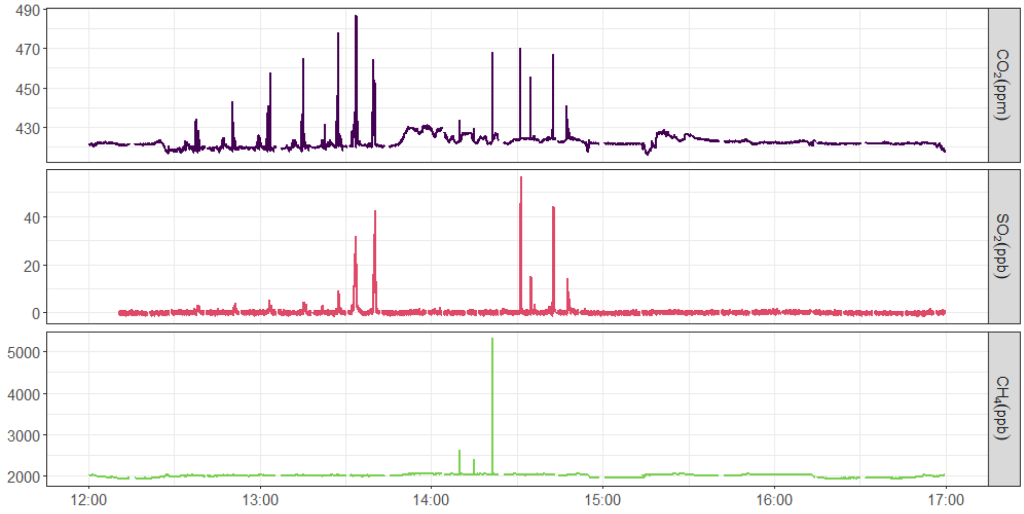

(b) Flight C285

(c) Flight C286

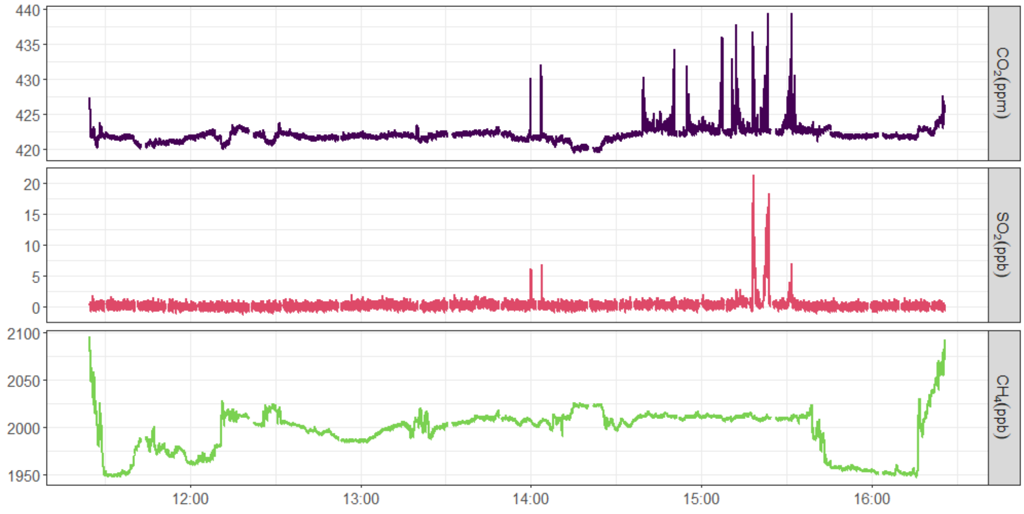

(d) Flight C287

Figure A.3: Time series for all the ACRUISE-3 flights.

A.2 Measured ships

Name	IMO	Type	Scrubber	Year built	Gross tonnage
Aegean Vision	9645437	crude oil tanker	no	2017	81300
Apl Oregon	9532783	container ship	no	2010	71800
Bow Chain	9214317	oil/chemical tanker	no	2002	23200
Bow Star	9197296	oil/chemical tanker	no	2004	30000
BTG Eiger	9731834	bulk carrier	no	2016	43200
CMA CGM Cayenne	9709192	container ship	no	2015	27300
CMA CGM Moliere	9401099	container ship	no	2009	83300
Da Li Hu	9259745	crude oil tanker	no	2004	84900
Eagle Brisbane	9795050	crude oil tanker	no	2018	113400
Elbtrader	9388534	container ship	yes	2008	8200
Grande Abidjan	9680712	ro-ro cargo	no	2015	71500
Grande Argentina	9198135	ro-ro cargo	no	2001	56700
Grande Colonia	9318527	vehicles carrier	no	2007	38700
Grande Mediterraneo	9138393	vehicles carrier	no	1998	51800
Hirado	9377420	crude oil tanker	no	2011	159800
Hoegh Detroit	9312470	vehicles carrier	no	2006	68900
Hoegh Gallant	9653678	LNG tanker	no	2014	109800
Isidor	9081356	general cargo	no	1993	2700
Jy Vincentia	9453236	bulk carrier	no	2010	32900
Kiran Anatolia	9650171	bulk carrier	no	2013	63500
KT Birdie	9597343	bulk carrier	no	2011	40300
Lake Superior	9325178	vehicles carrier	yes	2007	46800
Maersk Elba	9458078	container ship	no	2011	141700
Maersk Magellan	9447732	oil/chemical tanker	no	2010	29700
Marianna VV	9259707	crude oil tanker	no	2002	50200
Max Jacob	9188788	crude oil tanker	no	2000	81600
MSC Alabama	9123166	container ship	no	1996	37500
MSC Coruna	9480215	container ship	no	2011	61900
MSC Emma	9463047	container ship	no	2011	141600
MSC Mirja	9762338	container ship	no	2016	194300
MSC Poh Lin	9279977	container ship	no	2004	54800
MSC Tomoko	9309461	container ship	no	2006	94500
MSC Weser	9236690	container ship	yes	2001	26100
Nordic Luebeck	9483683	container ship	no	2011	10300
Seamerit	9247481	oil products tanker	no	2002	23200
St.Gregory	9414759	bulk carrier	no	2010	20800
Star Cosmo	9262637	bulk carrier	no	2005	30200
Stena Horizon	9332559	ro-ro cargo	no	2006	27500
Stena Impeccable	9693020	oil/chemical tanker	no	2017	29700
Stenaweco C Corrado	9688427	oil/chemical tanker	no	2015	50000
Sti Beryl	9658379	oil/chemical tanker	no	2013	50000
Supernova	9610212	bulk carrier	no	2012	21800
Swallow Ace	9338620	vehicles carrier	no	2007	58700

Thor Future	9326146	bulk carrier	no	2006	54200
Tian Jin	9748916	crude oil tanker	no	2015	166200
Trammo Laoura	9762912	bulk carrier	no	2017	38600
Veendijk	9346718	general cargo	no	2009	2980
Vladimir Tikhonov	9311622	crude oil tanker	no	2006	162400

Table A.1: ACRUISE-1 ships details.

Flight	**Name**	**IMO**	**Type**	**Scrubber**	**Year built**	**Gross tonnage**
C249	Aktoras	9312925	oil/chemical tanker	no	2006	23300
C249	Amazon Falcon	9779587	crude oil tanker	no	2017	44700
C249	Baltic Fulmar	9313204	container ship	no	2005	16300
C249	CL Anzi He	9890616	bulk carrier	no	2020	35800
C249	Clementine	9125384	ro-ro cargo	no	1997	24000
C249	Corn Rizhao	9883780	bulk carrier	yes	2020	4410
C249	Cosco Shipping Nebula	9795622	container ship	no	2018	215600
C249	Densa Orca	9601235	crude oil tanker	no	2012	81200
C249	Federal Shimanto	9218404	bulk carrier	no	2001	19200
C249	Grand Riviere	9733686	oil/chemical tanker	no	2015	21100
C249	Hoegh Transporter	9176395	vehicles carrier	no	1999	57800
C249	Inspiration Lake	9727376	bulk carrier	no	2015	23300
C249	Maersk Herrera	9784324	container ship	no	2018	153700
C249	Mare Siculum	9457892	crude oil tanker	no	2011	81500
C249	MP The Brady	9289972	container ship	yes	2005	54800
C249	MSC Monica	9060649	container ship	no	1993	37400
C249	Silver Sun	8519710	vehicles carrier	no	1988	39200
C249	Solero	9428085	oil/chemical tanker	no	2009	13500
C249	Tucana	9455674	general cargo	no	2008	2500
C251	Ardmore Defender	9707390	oil/chemical tanker	no	2015	23700
C251	Bulker Bee 10	9507087	general cargo	no	2010	9510
C251	CL Teresa	9721073	bulk carrier	no	2018	36400
C251	Indi	9370290	general cargo	no	2009	2550
C251	Maersk Stratus	9724556	oil/chemical tanker	yes	2017	28100
C251	MSC Lausane	9320398	container ship	no	2005	62700
C251	Silver London	9683374	oil/chemical tanker	yes	2014	29600
C251	Unity Star	9687148	bulk carrier	no	2015	22400
C251	Xin Tian Jin	9234343	container ship	no	2003	66400
C253	APL Merlion	9632014	container ship	yes	2014	168400
C253	BG Sapphire	9803699	container ship	yes	2018	12800
C253	Chemical Traveller	9804851	oil/chemical tanker	no	2019	8200
C253	Cosco Shipping Sagittarius	9783473	container ship	no	2018	194900
C253	Karita	9436783	general cargo	no	2013	4100
C253	Mont St Michel	9238337	passenger ship	yes	2002	35900
C253	MSC Eyra	8201648	container ship	no	1982	21600
C253	Nordic Lubeck	9483683	container ship	no	2011	10300
C253	NYK Rumina	9416991	container ship	no	2010	55500

C253	Preveze 1	9811127	oil/chemical tanker	no	2019	9040
C253	Songa Puma	9399789	container ship	no	2009	33000
C253	Sti Kingsway	9712852	crude oil tanker	yes	2015	63900
C254	Athiri	9457763	oil/chemical tanker	no	2010	42200
C254	Celebrity Silouette	9451094	passenger ship	yes	2011	122200
C254	Diyyinah I	9487251	crude oil tanker	no	2011	42500
C254	Elbspirit	9372860	container ship	no	2008	36100
C254	MSC Branka	9720495	container ship	yes	2016	95500
C254	NYK Vesta	9312808	container ship	no	2007	97800
C254	Texas Triumph	9737503	container ship	yes	2017	153000
C255	Arc Integrity	9332949	vehicles carrier	no	2008	71600
C255	Babylon	9878826	crude oil tanker	no	2020	154000
C255	Brussles Express*	9708784	container ship	no	2014	153200
C255	Canadian Highway	9574066	vehicles carrier	no	2010	59400
C255	Capt Eugene	9478767	bulk carrier	no	2010	55500
C255	Cosco Shipping Scorpio	9789635	container ship	no	2018	196700
C255	Delta Hellas	9406673	crude oil tanker	no	2009	81400
C255	Eco Nemesis	9719525	LPG tanker	no	2015	4750
C255	Eco Revolution	9725598	oil/chemical tanker	no	2016	24100
C255	Elbspirit	9372860	container ship	no	2008	36100
C255	Herta	9535151	container ship	no	2011	59300
C255	High Venture	9365817	oil/chemical tanker	no	2006	29900
C255	Kamome Victoria	9584102	oil products tanker	no	2011	41000
C255	MSC Branka	9720495	container ship	yes	2016	95500
C255	NYK Vesta	9312808	container ship	no	2007	97800
C255	Osgood	9368235	crude oil tanker	no	2008	62900
C255	Torrens	9293612	vehicles carrier	yes	2004	61500
C255	Umm Qarn	9732333	container ship	no	2016	153100
C255	Valentine	9166625	ro-ro cargo	no	1999	24000
C255	Visby	9223784	passenger ship	no	2003	29700
C256	Anthem of the Seas	9656101	passenger ship	yes	2015	168700
C256	Chemtrans Baltic	9298301	crude oil tanker	no	2005	42000
C256	MTM Yangon	9250165	chemical tanker	no	2003	29200
C256	Polar Argentina	9797204	container ship	no	2018	43600
C256	Stena Performance	9299159	oil/chemical tanker	no	2006	36200
C256	Uacc Mirdif	9402794	oil products tanker	no	2010	26900
C256	Vega Leader	9213818	vehicles carrier	no	2000	51500
C257	Euronike	9299678	crude oil tanker	no	2005	85400
C257	Evelyn Mearsk	9321512	container ship	yes	2007	171500
C257	Grande Texas	9796365	vehicles carrier	no	2021	65100
C257	Kyoto Express	9295256	container ship	no	2005	93800
C257	LNG Gaslog Georgetown	9864916	LNG tanker	no	2020	114000
C257	Manchester Maersk	9780445	container ship	yes	2018	214300
C257	MSC Isabella	9839272	container ship	yes	2019	228700
C257	Samuel Prospect*	9843572	crude oil tanker	no	2019	64900
C257	Thalassa Elpida	9665621	container ship	no	2014	148700
C257	Xin May	9837315	bulk carrier	yes	2019	94500
C258	Al Karaana	9431123	LNG tanker	no	2009	137000

C258	As Petronia	9286786	container ship	yes	2004	26800
C258	Asalet	9574169	bulk carrier	no	2010	17000
C258	Basic Glory	9836579	bulk carrier	yes	2020	81700
C258	Borealis	9122552	passenger ship	no	1997	61800
C258	Cosco Japan	9448748	container ship	no	2010	91100
C258	Eco Galaxy	9715555	LPG tanker	no	2015	5300
C258	Ginga Lion	9278727	chemical tanker	no	2004	16200
C258	Kapodistrias 21	9886639	crude oil tanker	yes	2021	83000
C258	Lake Superior	9325178	vehicles carrier	yes	2007	46800
C258	Maran Progress	9606754	bulk carrier	yes	2014	61700
C258	Mol Tribute	9769295	container ship	yes	2017	212200
C258	MSC Shaula	9036002	container ship	no	1992	61200
C258	Sofia Express	9450404	container ship	no	2010	93800
C258	Tarifa	9327748	vehicles carrier	no	2007	57700
C258	Ventura	9333175	passenger ship	yes	2008	116000
C258	W Kithira	9215323	container ship	no	2001	80600
C259	Aspen Spirit	9427627	crude oil tanker	no	2009	83500
C259	Cap San Marco	9622215	container ship	no	2013	118900
C259	HTK Discovery	9374349	bulk carrier	no	2007	22700
C259	Monte Olivia	9283198	container ship	no	2004	69100
C259	MSC Madrid	9480198	container ship	no	2011	61900
C259	MSC Rapallo	9484455	container ship	yes	2011	143500
C259	Navigator Yauza	9761176	LPG tanker	no	2017	18200
C259	Shannon Star	9503926	oil/chemical tanker	no	2010	8600
C259	Stroombank	9356543	general cargo	no	2009	3000
C259	Wes Gesa	9504061	container ship	no	2012	10600
C261	Al Ghuwairiya	9372743	LNG tanker	no	2008	168200
C261	Nave Velocity	9657052	oil/chemical tanker	no	2015	29700
C262	APL Merlion	9632014	container ship	yes	2014	168400
C262	Asterion	9595125	oil/chemical tanker	no	2011	23300
C262	CMA CGM Benjamin Franklin	9706891	container ship	yes	2015	179900
C262	CMA CGM Palais Royal	9839181	container ship	no	NA	236600
C262	Eagle Le Havre	9795103	oil products tanker	no	2017	62700
C262	Geographic Endurance	9842554	passenger ship	no	2020	12800
C262	Gwn 2	9859208	oil/chemical tanker	yes	2020	30100
C262	LNG Gaslog Georgetown	9864916	LNG tanker	no	2020	114000
C262	Lumphini Park	9640114	oil/chemical tanker	no	2013	11700
C262	MSC Soraya	9372494	container ship	no	2008	66400
C262	Sti Lauren	9696711	crude oil tanker	yes	2015	64800
C262	Straum	9406726	chemical tanker	yes	2010	12900
C262	Tahoe Spirit	9427641	crude oil tanker	no	2009	83500
C262	Tanja Star	9431692	container ship	no	2009	40500
C262	Troodos Oak	9875135	bulk carrier	no	2020	45200
C263	Alice	9323792	oil/chemical tanker	no	2006	25700
C263	Armorique	9364980	passenger ship	yes	2009	29500

C263	Asterion	9595125	oil/chemical tanker	no	2011	23300
C263	Dole Africa	9046538	reefer	no	1995	10600
C263	Eagle Le Havre	9795103	oil products tanker	no	2017	62700
C263	Gaschem Aachen	9257395	LPG tanker	no	2003	25300
C263	Gwn 2	9859208	oil/chemical tanker	yes	2020	30100
C263	HMM Garam	9869186	container ship	yes	2021	153200
C263	Lumphini Park	9640114	oil/chemical tanker	no	2013	11700
C263	Mol Tribute	9769295	container ship	yes	2017	212200
C263	MSC Soraya	9372494	container ship	no	2008	66400
C263	MSC Vilda	9146479	container ship	no	1998	92200
C263	Nordic Aquarius	9818216	crude oil tanker	no	2018	80800
C263	Polar Colombia	9786762	container ship	no	2017	43600
C263	Sti Garnet	9629952	chemical tanker	yes	2012	29700
C263	Sti Lauren	9696711	crude oil tanker	yes	2015	64800
C263	Straum	9406726	chemical tanker	yes	2010	12900
C263	Tanja Star	9431692	container ship	no	2009	40500
C263	Troodos Oak	9875135	bulk carrier	no	2020	45200
C264	Minerva Clara	9297333	crude oil tanker	no	2006	58200
C264	MSC La Spezia	9461403	container ship	yes	2010	153100
C264	MSC Oriane	9372482	container ship	no	2008	66400
C264	Orion Highway	9728071	vehicles carrier	no	2016	76300
C264	Sabetta	9784611	oil products tanker	no	2017	63100
C264	Seaways Shenandoah	9607966	crude oil tanker	no	2014	62700
C265	BG Onyx	9436197	container ship	no	2010	7850
C265	Elbtrader	9388534	container ship	yes	2008	8250
C265	Mindoro	9389095	crude oil tanker	yes	2009	58700
C265	Ottawa Express	9165360	container ship	no	1998	39200
C265	Sti Poplar	9696589	oil/chemical tanker	no	2014	24200

Table A.2: ACRUISE-2 ships details.

Flight	**Name**	**IMO**	**Type**	**Scrubber**	**Year built**	**Gross tonnage**
C283	BBC Iceland	9605906	general cargo	no	2013	18600
C283	CSCL Arctic Ocean	9695169	container ship	yes	2015	188600
C283	Endurance	9121273	vehicle carrier	no	1996	72700
C283	Erikoussa	9291092	bulk carrier	no	2005	75700
C283	Grande Dakar	9680724	container ship	no	2015	71500
C283	Halit Bey	9511375	general cargo	no	2008	7700
C283	Hermine	9831177	ro-ro cargo	no	2019	50400
C283	Histria Dione	9800805	oil/chemical tanker	no	2020	26300
C283	Hoegh New York	9295830	container ship	no	2005	57300
C283	Marit Maersk	9632167	container ship	no	2015	194800
C283	Siena	9577123	crude oil tanker	no	2012	42200
C283	SSI Challenger	9284300	bulk carrier	no	2004	31200
C283	W Kyrenia	9211494	container ship	no	2001	80600
C283	Yasa Pioneer	9286578	bulk carrier	no	2006	42900
C283	Yiannis	9879674	LNG tanker	no	2021	115500
C284	Al Sahla	9360855	LNG tanker	no	2008	136400

C284	Connemara	9349760	passenger ship	no	2007	27400
C284	Maran Gas Roxana	9701229	LNG tanker	no	2017	113000
C284	Nikolay Yevgenov	9750725	LNG tanker	no	2019	129000
C284	Pink Stars	9433585	crude oil tanker	no	2010	61300
C284	Tenergy	9892456	LNG tanker	no	2022	116500
C285	MSC Pilar	8715871	container ship	no	1990	52000
C286	Darya Devi	9627760	bulk carrier	no	2013	44300
C286	Queen Alesia	9573799	bulk carrier	no	2010	17000
C286	Rhea Leader	9355214	vehicle carrier	no	2008	63000
C287	APL Fullerton	9632026	container ship	yes	2014	170000
C287	Ever Act	9893905	container ship	yes	2021	240000
C287	Jose Progress	9392391	tanker	no	2009	30000
C287	Marchen Maersk	9632143	container ship	yes	2015	194000
C292	Minerva Limnos	9854375	LNG tanker	no	2021	113700

Table A.3: ACRUISE-3 ships details.

A.3 Peak integration

Flight	SO_2			CO_2			SO_2		CO_2	
	k	*a*	*b*	*k*	*a*	*b*	**peaks**	**background**	**peaks**	**background**
C179	3	2	0.5	10	3	1	high	stable	low	stable
C180	3	2	0.5	50	3	0.5	high	stable	low	variable
C181	6	2	0.5	50	3	0.5	high	stable	low	variable
C182	6	2	0.5	50	3	0.5	high	stable	low	variable
C183	20	2	0.5	50	3	0.5	high	variable	high	variable
C186	3	2	0.5	10	4	2	high	stable	high	stable
C187	5	2	0.5	10	4	2	high	stable	high	stable
C188	10	2	1	10	4	2	low	stable	low	stable
C190	10	3	1	50	3	0.5	low	stable	low	variable
C251	10	3	1	20	2	0.5	high	stable	high	stable
C253	10	3	2	20	3	0.5	low	stable	high	stable
C254	10	3	1	20	3	0.5	low	stable	high	stable
C255	10	3	2	50	3	0.5	high	stable	high	variable
C256	10	3	1	50	3	0.5	high	stable	high	variable
C257	10	3	1	20	3	0.5	high	stable	high	stable
C258	10	3	0.5	20	3	0.25	high	stable	high	stable
C259	10	3	1	20	3	0.5	low	stable	low	variable
C261	10	3	0.5	20	2	0.5	high	stable	high	variable
C262	10	3	1	50	2	0.5	high	stable	high	variable
C263	50	5	2	50	3	0.5	low	variable	high	variable
C264	10	3	0.5	50	3	0.5	high	stable	high	variable
C265	10	3	0.5	50	3	0.5	high	stable	high	variable
C284	5	2	0.5	50	3	0.5	high	stable	high	variable
C285	5	2	0.5	20	3	0.5	high	stable	high	variable
C286	5	5	0.5	20	4	0.5	low	stable	high	stable
C287	5	2	0.5	20	3	0.5	high	stable	high	variable
C292	5	2	0.5	20	3	0.5	none	stable	high	variable

Table A.4: Peak integration algorithm parameters, where *k* is smoothing parameter, *a* is standard deviation multiple describing edge of noise, *b* is standard deviation multiple describing peak threshold. Background is classified as stable or variable and peak height as relatively low or high.

A.4 SFCs with uncertainties

Number	SFC	Uncertainty limits		Ship
		Lower	Upper	
179.01	0.57%	0.02%	0.06%	MSC Poh Lin
179.02	0.95%	0.04%	0.10%	MSC Poh Lin
179.03	0.66%	0.03%	0.07%	MSC Poh Lin
179.04	0.45%	0.02%	0.05%	MSC Poh Lin
179.05	0.31%	0.01%	0.03%	Stena Horizon
179.06	0.00%			Stena Horizon
179.07	0.00%			Stena Horizon
179.08	0.11%	0.00%	0.01%	Stena Horizon
179.09	1.15%	0.05%	0.12%	Stena Horizon
179.10	1.45%	0.06%	0.15%	Eagle Brisbane
179.11	4.41%	0.19%	0.46%	Eagle Brisbane
179.12	0.98%	0.04%	0.10%	Eagle Brisbane
180.01	0.72%	0.03%	0.07%	Marianna VV
180.02	0.28%	0.01%	0.03%	Marianna VV
180.03	1.73%	0.07%	0.18%	Marianna VV
181.01	1.45%	0.06%	0.15%	Sti Beryl
181.02	1.55%	0.07%	0.16%	Sti Beryl
181.03	2.63%	0.11%	0.27%	Sti Beryl
181.04	0.83%	0.04%	0.09%	Sti Beryl
182.01	3.07%	0.13%	0.32%	Max Jacob
182.02	1.33%	0.06%	0.14%	Bow Chain
182.03	2.91%	0.12%	0.30%	Bow Chain
183.01	1.08%	0.05%	0.11%	CMA CGM Cayenne
183.02	0.72%	0.03%	0.07%	Jy Vincentia
183.03	2.15%	0.09%	0.22%	MSC Emma
183.04	2.19%	0.09%	0.22%	Hoegh Gallant
183.05	1.74%	0.07%	0.18%	Hoegh Gallant
183.06	0.60%	0.03%	0.06%	Grande Argentina
183.07	2.83%	0.12%	0.29%	Thor Future
183.08	2.44%	0.10%	0.25%	Nordic Luebeck
183.09	3.77%	0.16%	0.39%	Aegean Vision
183.10	2.67%	0.11%	0.27%	Tian Jin
186.01	2.13%	0.09%	0.22%	Star Cosmo
186.02	2.20%	0.10%	0.23%	Hirado
186.03	4.71%	0.20%	0.48%	Hirado
187.01	4.79%	0.21%	0.49%	MSC Coruna
187.02	3.45%	0.15%	0.36%	MSC Mirja
187.03	2.98%	0.13%	0.31%	MSC Mirja
187.04	2.51%	0.11%	0.26%	MSC Mirja
187.05	2.59%	0.11%	0.27%	MSC Mirja
188.01	0.96%	0.04%	0.10%	Lake Superior
188.02	2.55%	0.11%	0.26%	Lake Superior
190.01				MSC Mirja
190.02	0.13%	0.01%	0.01%	MSC Mirja
190.03	0.12%	0.01%	0.01%	MSC Mirja
190.04	0.02%	0.00%	0.00%	MSC Mirja

190.05	0.05%	0.00%	0.00%	MSC Mirja
190.06	0.00%			MSC Mirja
253.01	0.00%			
253.02	0.00%			Mont St Michel
253.03	0.00%			APL Merlion
253.04	0.00%			BG Sapphire
253.05	0.00%			Karita
253.06	0.00%			Karita
253.07	0.00%			Preveze 1
253.08	0.11%	0.01%	0.01%	Cosco Shipping Sagittarius
253.09	0.14%	0.01%	0.02%	Cosco Shipping Sagittarius
253.10	0.17%	0.01%	0.02%	Cosco Shipping Sagittarius
253.11	0.00%			Karita
253.12	0.00%			Songa Puma
253.13	0.00%			Mont St Michel
253.14	0.00%			NYK Rumina
254.01	0.00%			Texas Triumph
254.02	0.00%			Celebrity Silouette
254.03	0.02%	0.00%	0.00%	Athiri
254.04	0.11%	0.01%	0.01%	Celebrity Silouette
254.05	0.66%	0.04%	0.08%	Diyyinah I
254.06	0.84%	0.05%	0.10%	Diyyinah I
254.07	0.00%	0.00%	0.00%	MSC Branka
254.08	0.12%	0.01%	0.02%	MSC Branka
255.01	0.00%			MSC Branka
255.02	0.00%			
255.03	0.21%	0.01%	0.03%	
255.04	0.14%	0.01%	0.02%	Cosco Shipping Scorpio
255.05	0.08%	0.01%	0.01%	NYK Vesta
255.06	0.00%			
255.07	1.36%	0.09%	0.17%	Cosco Shipping Scorpio
255.08	0.00%			Capt Eugene
255.09	0.00%			Eco Nemesis
255.10	0.00%			Delta Hellas
255.11	0.00%			Brussels Express
255.12	0.00%			Delta Hellas
255.13	0.00%			High Venture
255.14	0.00%			Kamome Victoria
255.15	0.00%			Elbspirit
256.01	0.05%	0.00%	0.01%	Anthem of the Seas
256.02	0.06%	0.00%	0.01%	Anthem of the Seas
256.03	0.35%	0.02%	0.04%	Anthem of the Seas
256.04	0.85%	0.06%	0.11%	Anthem of the Seas
256.05	0.65%	0.04%	0.08%	Anthem of the Seas
256.06	0.08%	0.01%	0.01%	Anthem of the Seas
256.07	0.54%	0.04%	0.07%	Anthem of the Seas
256.08	0.18%	0.01%	0.02%	Anthem of the Seas
256.09	0.43%	0.03%	0.05%	Vega Leader
256.10	0.36%	0.02%	0.05%	Vega Leader
256.11	0.70%	0.05%	0.09%	Vega Leader

256.12	0.31%	0.02%	0.04%	Vega Leader
256.13	0.14%	0.01%	0.02%	Chemtrans Baltic
256.14	0.22%	0.01%	0.03%	Stena Performance
256.15	0.46%	0.03%	0.06%	Stena Performance
256.16	0.40%	0.03%	0.05%	Stena Performance
256.17	1.18%	0.08%	0.15%	Anthem of the Seas
256.18	0.49%	0.03%	0.06%	MTM Yangon
256.19	0.33%	0.02%	0.04%	Polar Argentina
256.20	0.22%	0.01%	0.03%	Polar Argentina
256.21	1.49%	0.10%	0.19%	Polar Argentina
256.22	0.34%	0.02%	0.04%	Anthem of the Seas
256.23	0.00%			Anthem of the Seas
256.24	0.31%	0.02%	0.04%	Anthem of the Seas
257.01	0.30%	0.02%	0.04%	Kyoto Express
257.02	0.00%			Kyoto Express
257.03	0.21%	0.01%	0.03%	Kyoto Express
257.04	0.00%			LNG Gaslog Georgetown
257.05	0.00%			Manchester Maersk
257.06	0.00%			Evelyn Maersk
257.07	0.00%			Evelyn Maersk
257.08	0.00%			Manchester Maersk
257.09	0.00%			Evelyn Maersk
257.10	0.00%			MSC Isabella
257.11	0.00%			MSC Isabella
257.12	0.00%			MSC Isabella
257.13	0.00%			MSC Isabella
257.14	0.00%			MSC Isabella
257.15	0.00%			Samuel Prospect
257.16	0.00%			Samuel Prospect
257.17	0.06%	0.00%	0.01%	Samuel Prospect
257.18	0.00%			Samuel Prospect
257.19	0.58%	0.04%	0.07%	Euronike
257.20	0.12%	0.01%	0.02%	Euronike
257.21	1.16%	0.07%	0.14%	Thalassa Elpida
257.22	0.51%	0.03%	0.06%	Thalassa Elpida
257.23	0.00%			Grande Texas
258.01	0.00%			W Kithira
258.02	0.50%	0.03%	0.06%	W Kithira
258.03	0.00%			Ventura
258.04	0.00%			Ventura
258.05	0.38%	0.02%	0.05%	Ventura
258.06	0.32%	0.02%	0.04%	Ventura
258.07	0.27%	0.02%	0.03%	Maran Progress
258.08	0.00%			MSC Shaula
258.10	2.81%	0.18%	0.35%	Maran Progress
258.11	0.00%			Lake Superior
258.12	0.00%			Lake Superior
258.13	0.00%			Lake Superior
258.14	0.00%			Cosco Japan
258.15	0.00%			Kapodistrias 21

258.16	0.00%			Kapodistrias 21
258.17	0.00%			Kapodistrias 21
258.18	0.00%			Kapodistrias 21
258.19	0.00%			Borealis
258.20	0.00%			Borealis
258.21	0.00%			Borealis
258.22	0.25%	0.02%	0.03%	Al Karaana
258.23	0.26%	0.02%	0.03%	Al Karaana
258.24	0.30%	0.02%	0.04%	Al Karaana
259.01	0.11%	0.01%	0.01%	Aspen Spirit
259.02	0.07%	0.00%	0.01%	Aspen Spirit
259.03	0.59%	0.04%	0.07%	MSC Madrid
259.04	0.25%	0.02%	0.03%	MSC Madrid
259.05	0.00%			MSC Madrid
259.06	0.00%			Navigator Yauza
259.07	0.07%	0.00%	0.01%	Navigator Yauza
259.08	0.57%	0.04%	0.07%	Cap San Marco
259.09	0.23%	0.01%	0.03%	Cap San Marco
259.10	0.20%	0.01%	0.03%	Cap San Marco
259.11	0.27%	0.02%	0.03%	Wes Gesa
259.12	0.31%	0.02%	0.04%	MSC Rapallo
261.00	0.00%			
261.02	0.00%			
261.04	0.00%			Al Ghuwairiya
261.06	0.00%			Al Ghuwairiya
261.08	0.74%	0.05%	0.09%	Al Ghuwairiya
261.10	0.33%	0.02%	0.04%	Al Ghuwairiya
261.12	0.00%			
262.01	0.00%			GWN 2
262.02	0.02%	0.00%	0.00%	Straum
262.03	0.01%	0.00%	0.00%	Sti Lauren
262.04	0.09%	0.01%	0.01%	Sti Lauren
262.05	0.00%			Tanja Star
262.06	0.00%			
262.07	0.43%	0.03%	0.05%	Asterion
262.08	0.56%	0.04%	0.07%	Troodos Oak
262.09	0.33%	0.02%	0.04%	Troodos Oak
262.10	0.38%	0.02%	0.05%	Lumphini Park
262.11	0.32%	0.02%	0.04%	MSC Soraya
262.12	0.46%	0.03%	0.06%	MSC Soraya
262.13	0.00%			CMA CGM Benjamin Franklin
262.14	0.41%	0.03%	0.05%	Eagle Le Havre
262.15	0.20%	0.01%	0.03%	Eagle Le Havre
262.16	2.13%	0.14%	0.27%	Tahoe Spirit
262.17	0.00%			Tahoe Spirit
262.18	0.00%			LNG Gaslog Georgetown
262.19	0.00%			Geographic Endurance
262.20	0.18%	0.01%	0.02%	APL Merlion
263.01	0.00%			Straum
263.02	0.00%			HMM Garam

263.03	0.00%			GWN 2
263.04	0.00%			GWN 2
263.05	0.00%			HMM Garam
263.06	0.00%			HMM Garam
263.07	0.00%			Dole Africa
263.08	0.13%	0.01%	0.02%	MSC Soraya
263.09	0.12%	0.01%	0.01%	Troodos Oak
263.10	0.00%			Alice
263.11	0.27%	0.02%	0.03%	Mol Tribute
263.12	0.00%			Mol Tribute
263.13	0.00%			Mol Tribute
263.14	0.00%			Gaschem Aachen
263.15	0.06%	0.00%	0.01%	Gaschem Aachen
263.16	0.00%			Armorique
263.17	0.00%			Eagle Le Havre
263.18	0.02%	0.00%	0.00%	Armorique
263.19	0.00%			Armorique
263.20	0.85%	0.05%	0.11%	Tanja Star
263.21	0.00%			Eagle Le Havre
263.22	0.00%			Armorique
263.23	0.19%	0.01%	0.02%	MSC Vilda
264.01	0.00%			Sabetta
264.02	0.30%	0.02%	0.04%	Sabetta
264.03	2.25%	0.14%	0.28%	MSC Oriane
264.04	0.62%	0.04%	0.08%	MSC Oriane
264.05	1.66%	0.11%	0.21%	MSC Oriane
264.06	1.74%	0.11%	0.22%	MSC La Spezia
264.08	0.26%	0.02%	0.03%	
264.09	0.00%			
264.11	0.74%	0.05%	0.09%	Minerva Clara
264.12	0.12%	0.01%	0.02%	Seaways Shenandoah
264.13	0.55%	0.04%	0.07%	Seaways Shenandoah
265.01	0.00%			Elbtrader
265.02	0.27%	0.02%	0.03%	Ottawa Express
265.03	0.00%			Elbtrader
265.04	0.19%	0.01%	0.02%	
265.05	0.04%	0.00%	0.01%	Elbtrader
265.06	0.00%			Elbtrader
265.07	0.00%			Mindoro
265.08	0.50%	0.03%	0.06%	Mindoro
265.09	0.71%	0.05%	0.09%	Sti Poplar
265.11	0.05%	0.00%	0.01%	Mindoro
265.12	0.76%	0.05%	0.09%	Sti Poplar

Table A.5: All SFCs with uncertainty.

A.5 LNG tankers

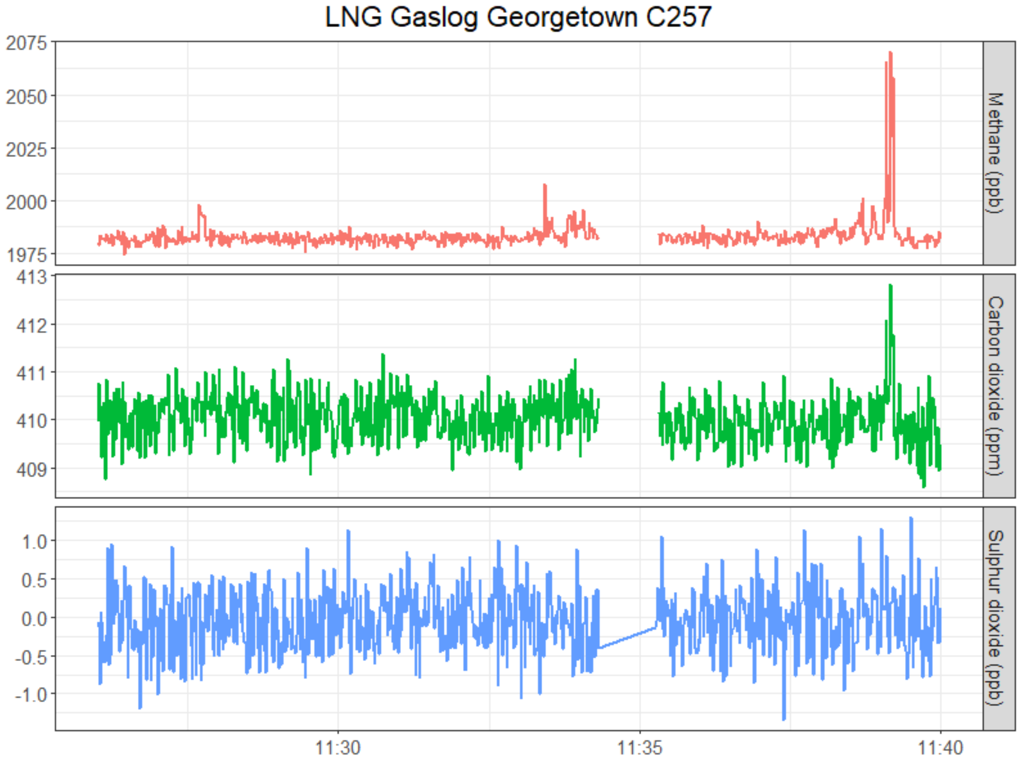

(a) LNG Gaslog Georgetown, 2020 built - first encounter

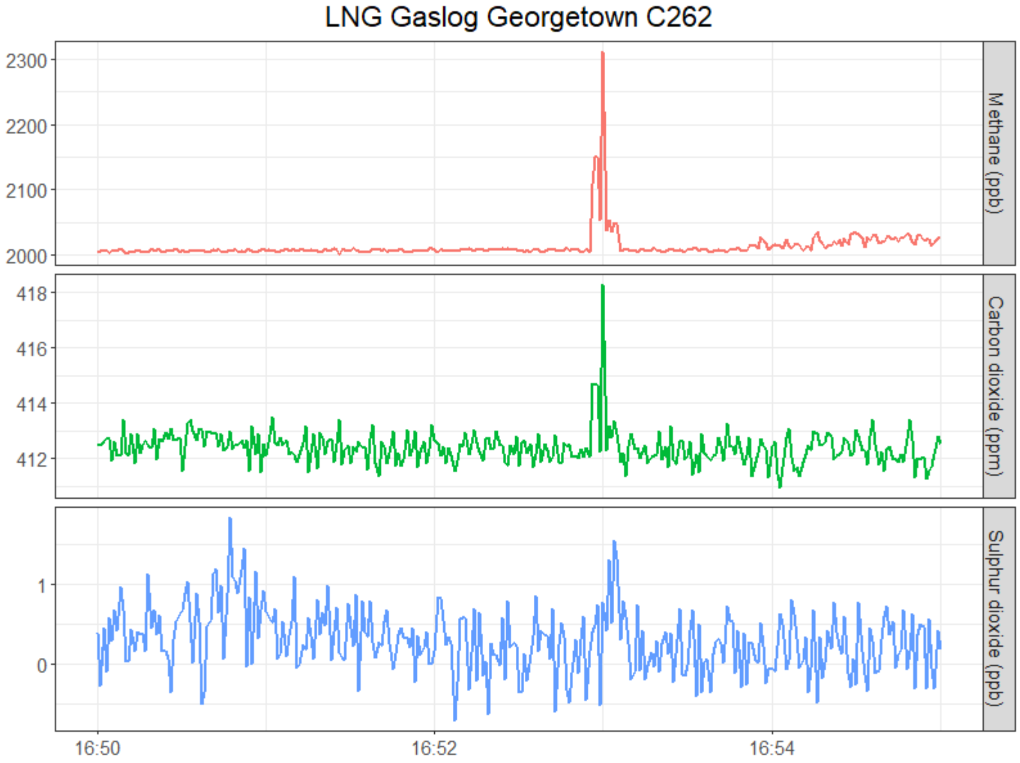

(b) LNG Gaslog Georgetown, 2020 built - second encounter

Figure A.4: Time series for LNG tankers measured during ACRUISE-2 and -3.

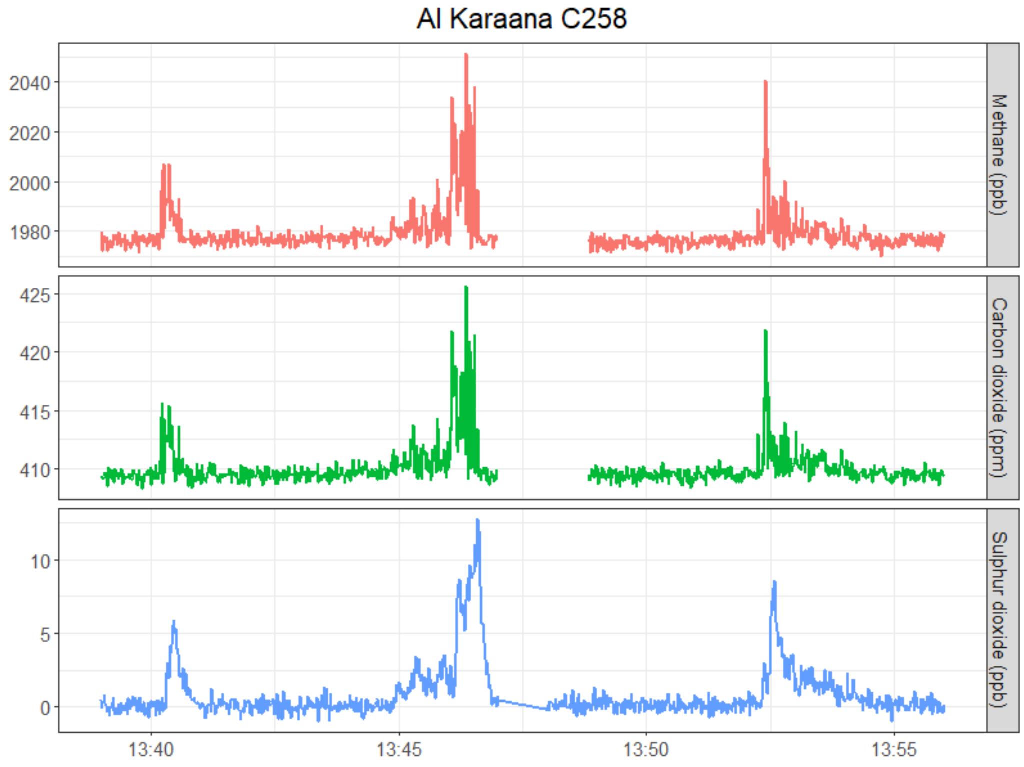

(c) Al Karaana, 2009 built

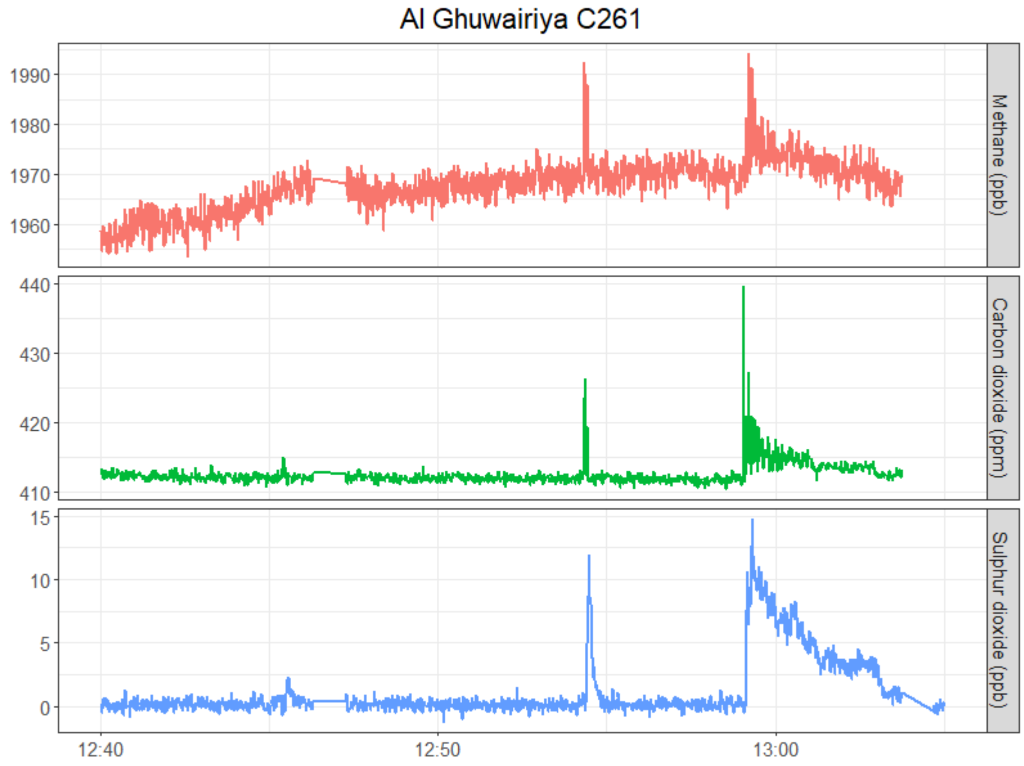

(d) Al Ghuwairiya, 2008 built

Figure A.4: Time series for LNG tankers measured during ACRUISE-2 and -3.

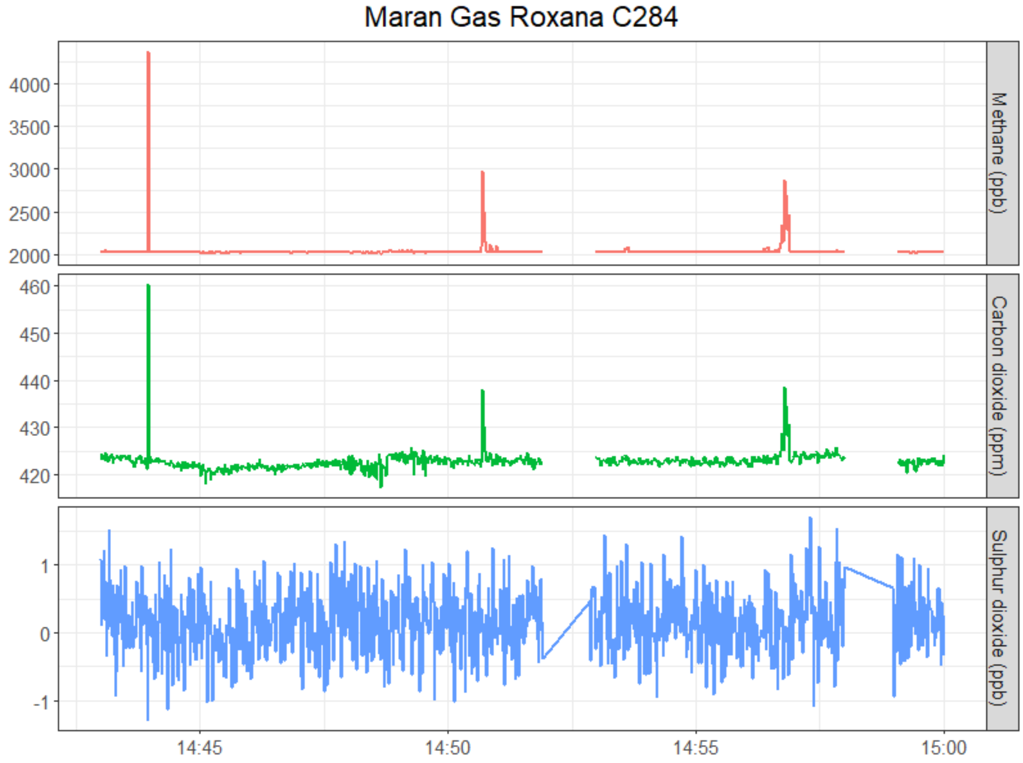

(e) Maran Gas Roxana, 2017 built

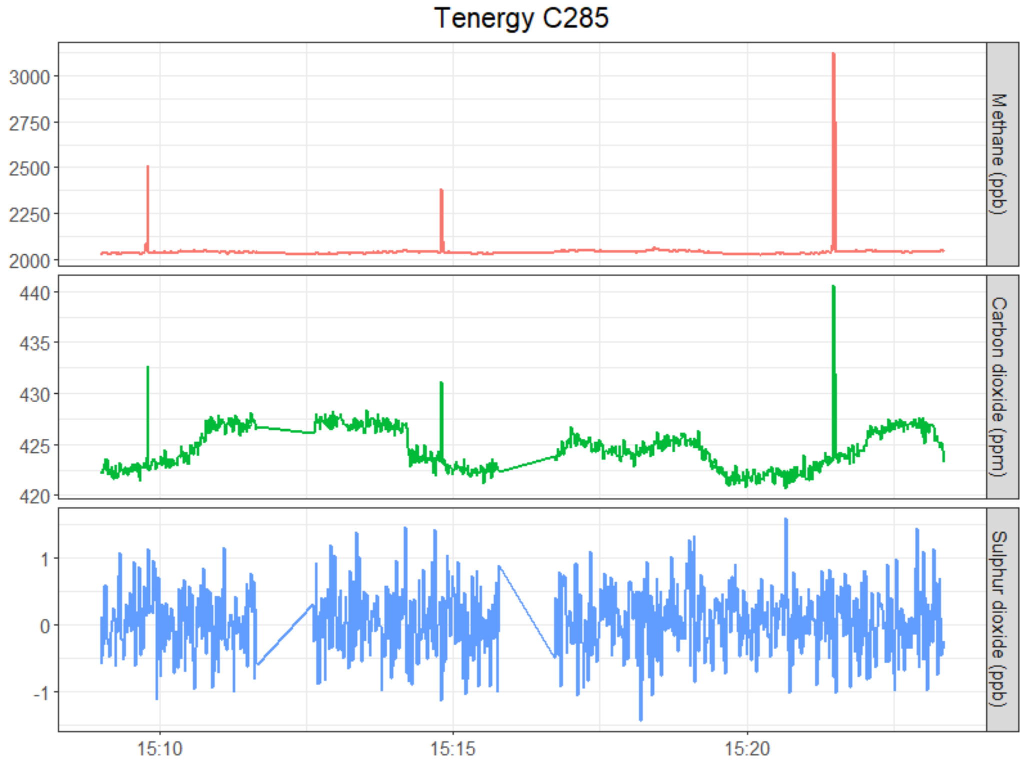

(f) Tenergy, 2022 built

Figure A.4: Time series for LNG tankers measured during ACRUISE-2 and -3.

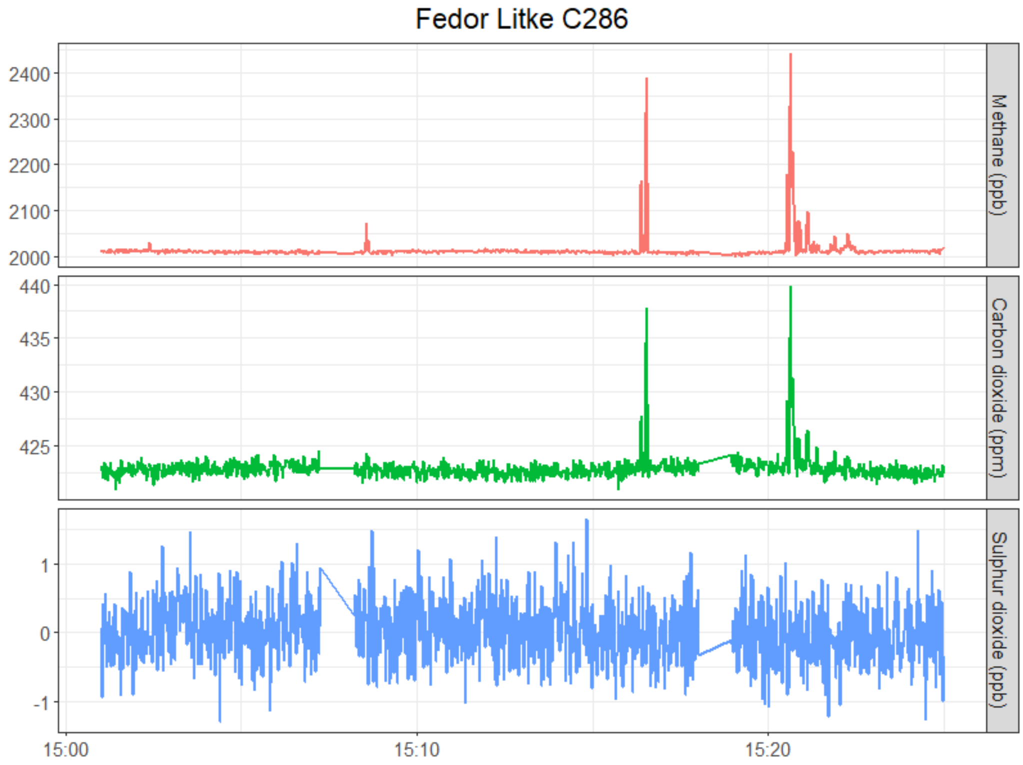

(g) Fedor Litke, 2017 built

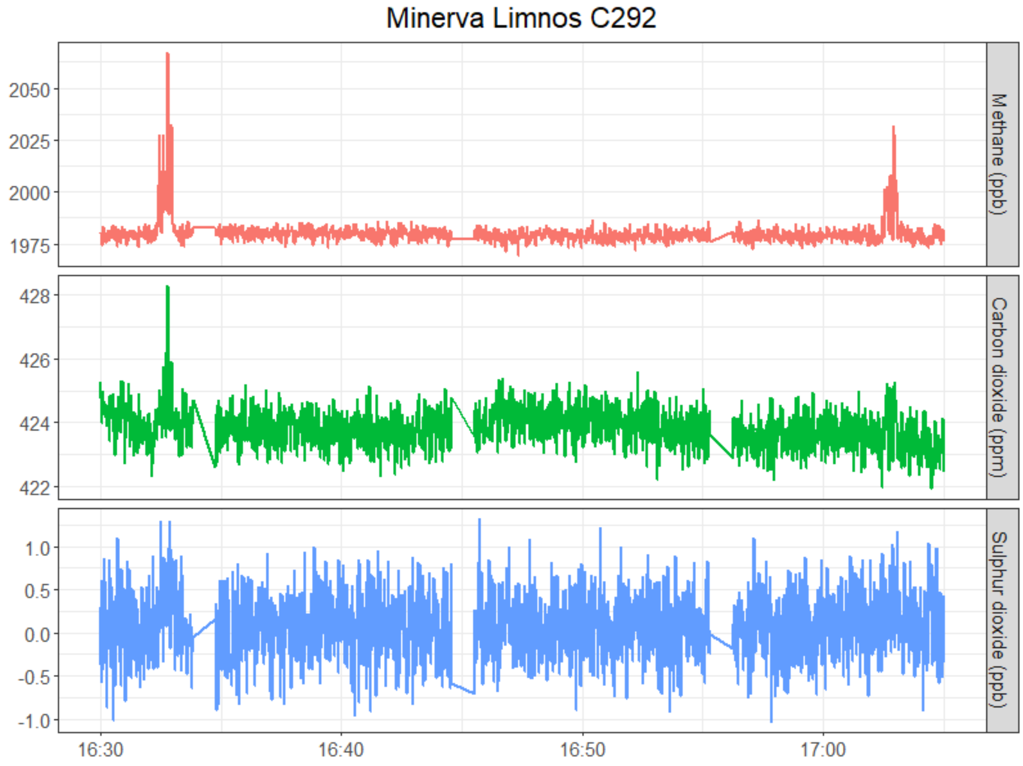

(h) Minerva Limnos, 2021

Figure A.4: Time series for LNG tankers measured during ACRUISE-2 and -3.

A.6 NOx to CO2 ratios

Flight	Number	CO2	NOx	Ratio	Ship
179	179.01	13.0	362	0.0278	Stena Horizon
179	179.02	13.0	251	0.0193	Stena Horizon
179	179.03	6.0	182	0.0303	Stena Horizon
179	179.04	14.0	409	0.0292	Stena Horizon
179	179.05	8.0	199	0.0249	Stena Horizon
179	179.06	16.0	450	0.0281	Eagle Brisbane
179	179.07	43.0	762	0.0177	Eagle Brisbane
179	179.08	11.0	281	0.0255	Eagle Brisbane
180	180.01	19.0	566	0.0298	Marianna VV
181	181.01	18.0	765	0.0425	
181	181.02	60.0	865	0.0144	Sti Beryl
181	181.03	93.0	2801	0.0301	Sti Beryl
181	181.04	30.0	587	0.0196	Sti Beryl
181	181.05	69.0	1396	0.0202	Sti Beryl
182	182.01	7.0	320	0.0457	
182	182.02	153.0	3960	0.0259	
182	182.03	25.0	654	0.0262	Max Jacob
182	182.04	47.0	1023	0.0218	Max Jacob
182	182.05	80.0	2253	0.0282	
182	182.06	21.0	640	0.0305	Bow Chain
182	182.07	23.0	615	0.0267	Bow Chain
183	183.01	19.0	783	0.0412	CMA CGM Cayenne
183	183.02	18.0	581	0.0323	Jy Vincentia
183	183.03	19.9	245	0.0123	MSC Emma
183	183.04	86.3	1499	0.0174	Hoegh Gallant
183	183.05	53.5	129	0.0024	
183	183.06	105.5	2185	0.0207	Hoegh Gallant
183	183.07	21.0	397	0.0189	Thor Future
183	183.08	20.4	212	0.0104	Nordic Luebeck
183	183.09	37.7	417	0.0111	Aegean Vision
183	183.1	54.5	863	0.0158	Tian Jin
183	183.11	6.2	0	0.0000	
184	184.01	8.3	48	0.0058	
184	184.02	12.9	388	0.0301	
186	186.01	9.0	109	0.0121	Hirado
186	186.02	35.2	203	0.0058	
186	186.03	53.9	275	0.0051	Hirado
187	187.01	9.0	181	0.0201	MSC Mirja
187	187.02	5.0	137	0.0274	MSC Mirja
187	187.03	15.2	190	0.0125	MSC Mirja
187	187.04	13.2	266	0.0202	MSC Mirja
187	187.05	22.3	437	0.0196	MSC Mirja
188	188.01	38.8	964	0.0248	Lake Superior
188	188.02	30.3	565	0.0186	Lake Superior
190	190.01	34.6	601	0.0174	MSC Mirja
190	190.02	10.2	343	0.0336	MSC Mirja
190	190.03	28.5	109	0.0038	MSC Mirja

190	190.04	12.1	119	0.0098	MSC Mirja
190	190.05	24.4	382	0.0157	MSC Mirja
190	190.06	31.7	915	0.0289	MSC Mirja
190	190.07	9.9	492	0.0497	MSC Mirja
190	190.08	28.5	74		

Table A.6: All NO_x to CO_2 ratios from ACRUISE-1 campaign.

Appendix B

Supporting Information for Chapter 7

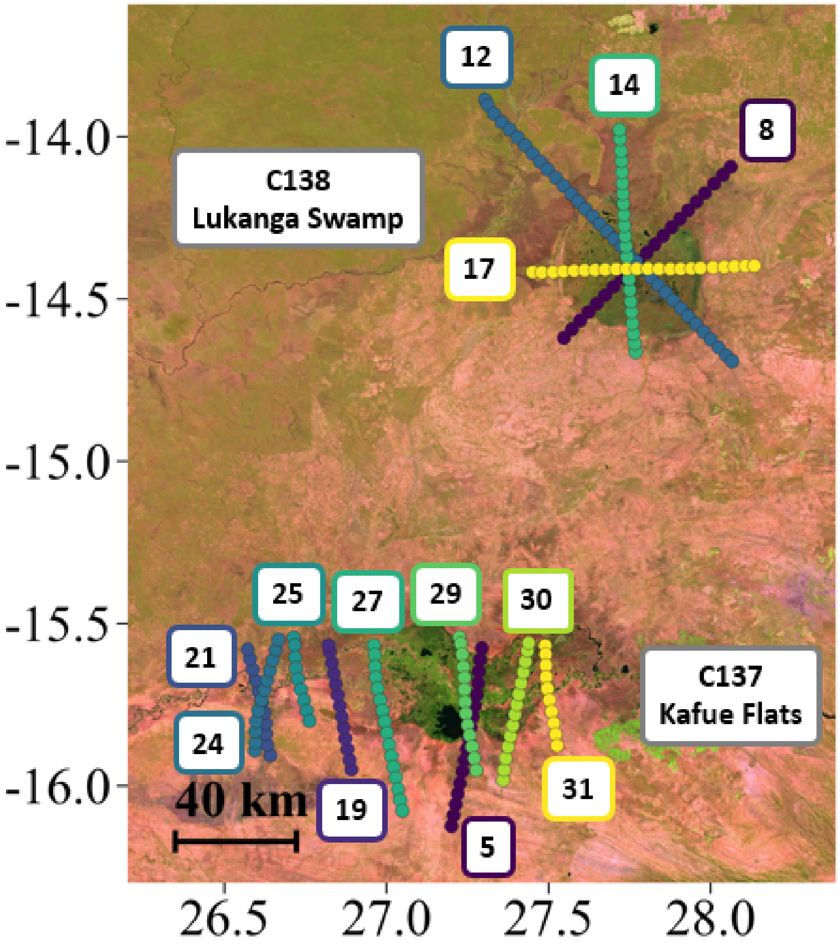

Figure B.1: C137 and C138 leg IDs, referring to the original numbering of all the legs fulfilling basic criteria. Map source: GLAD Landsat MOSAIC 2019 map [72].

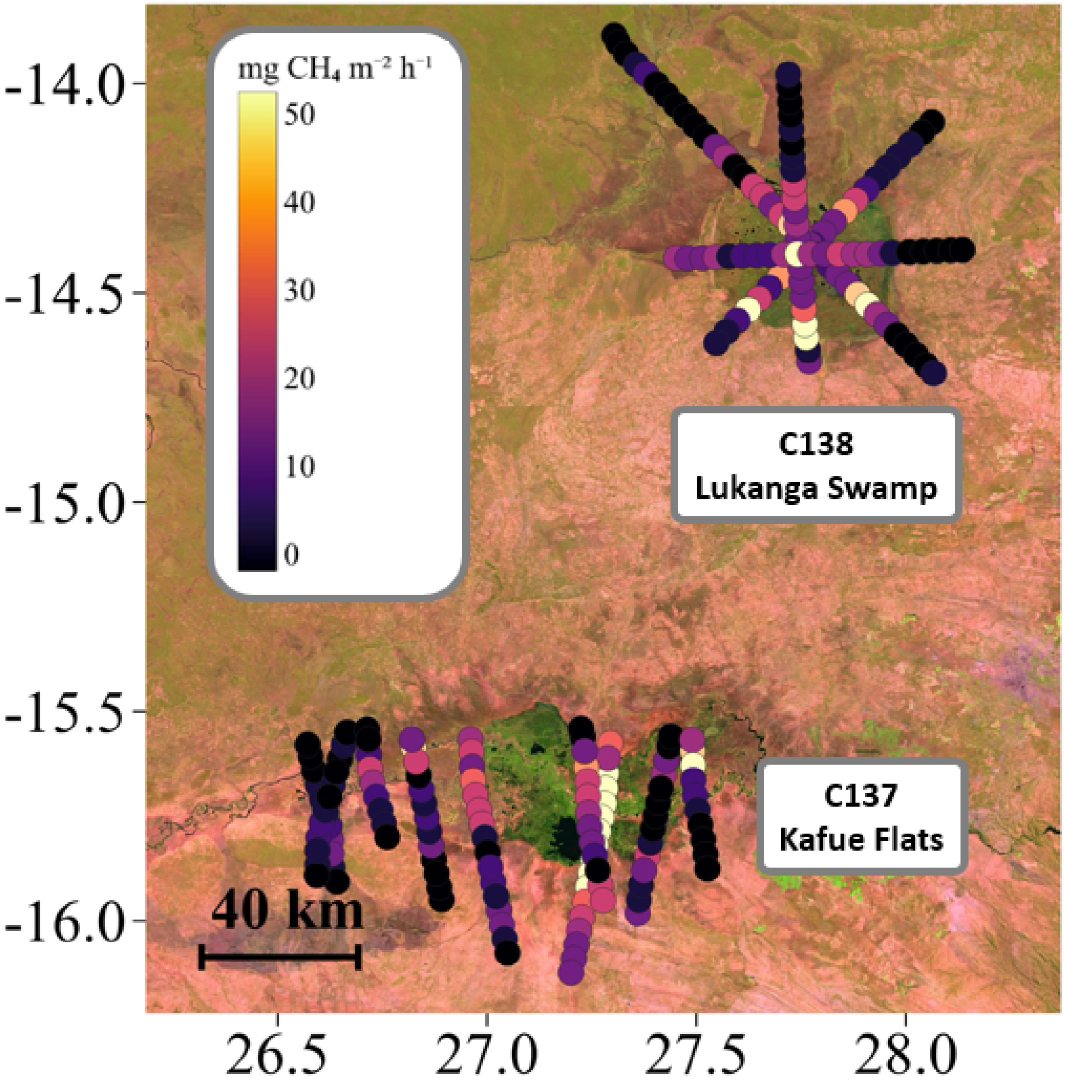

Figure B.2: Comparison between low fluxes in C137 and C138 presented on 0 - 57 mg CH_4 m^{-2} (C138's scale) at 3 km intervals. Map source: GLAD Landsat MOSAIC 2019 map [72]. [WILL LOOK BETTER IN FUTURE]

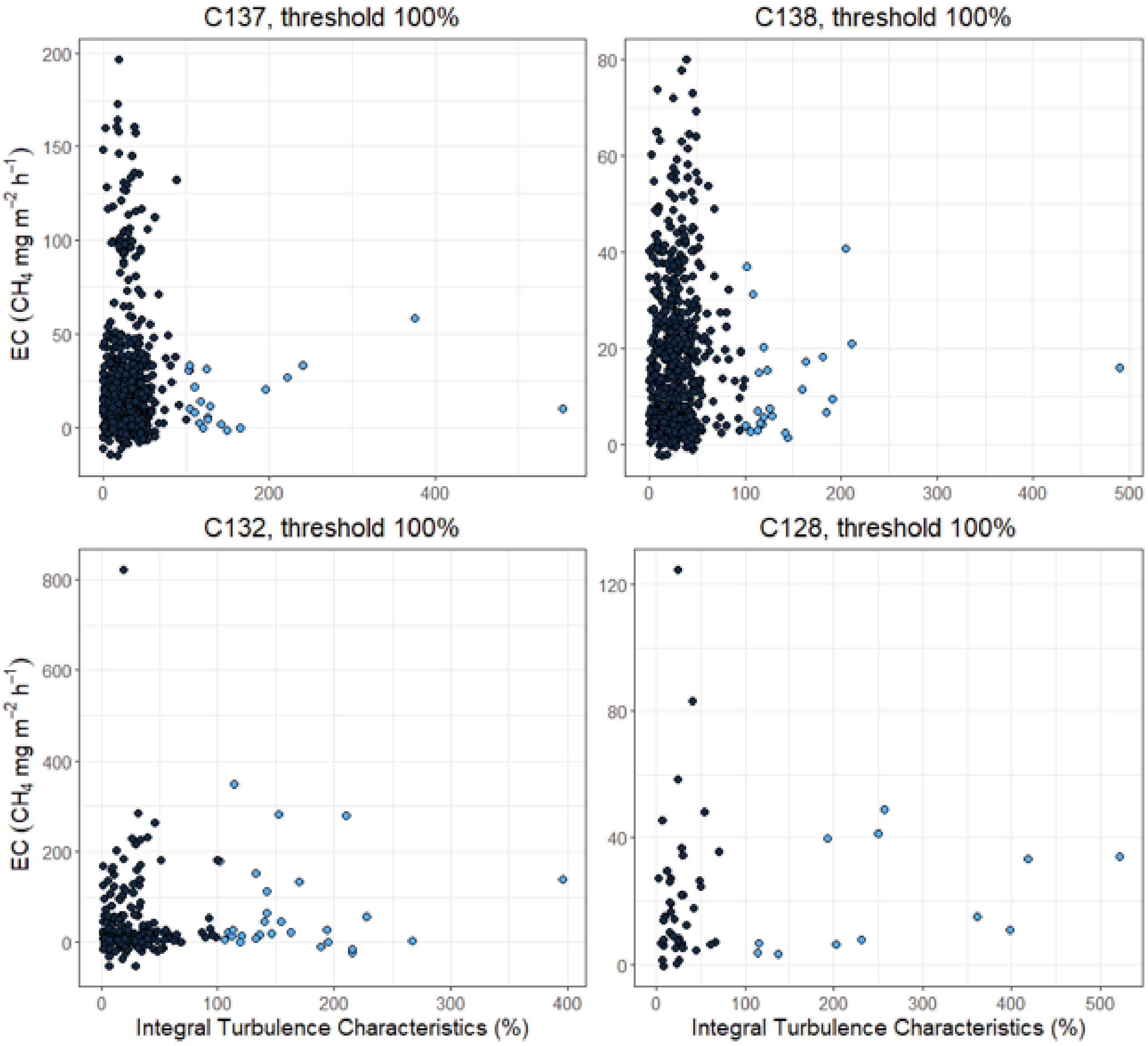

Figure B.3: ITC filtering of all the successful flights. Values in light blue exceed the 100% ITC threshold and are excluded.

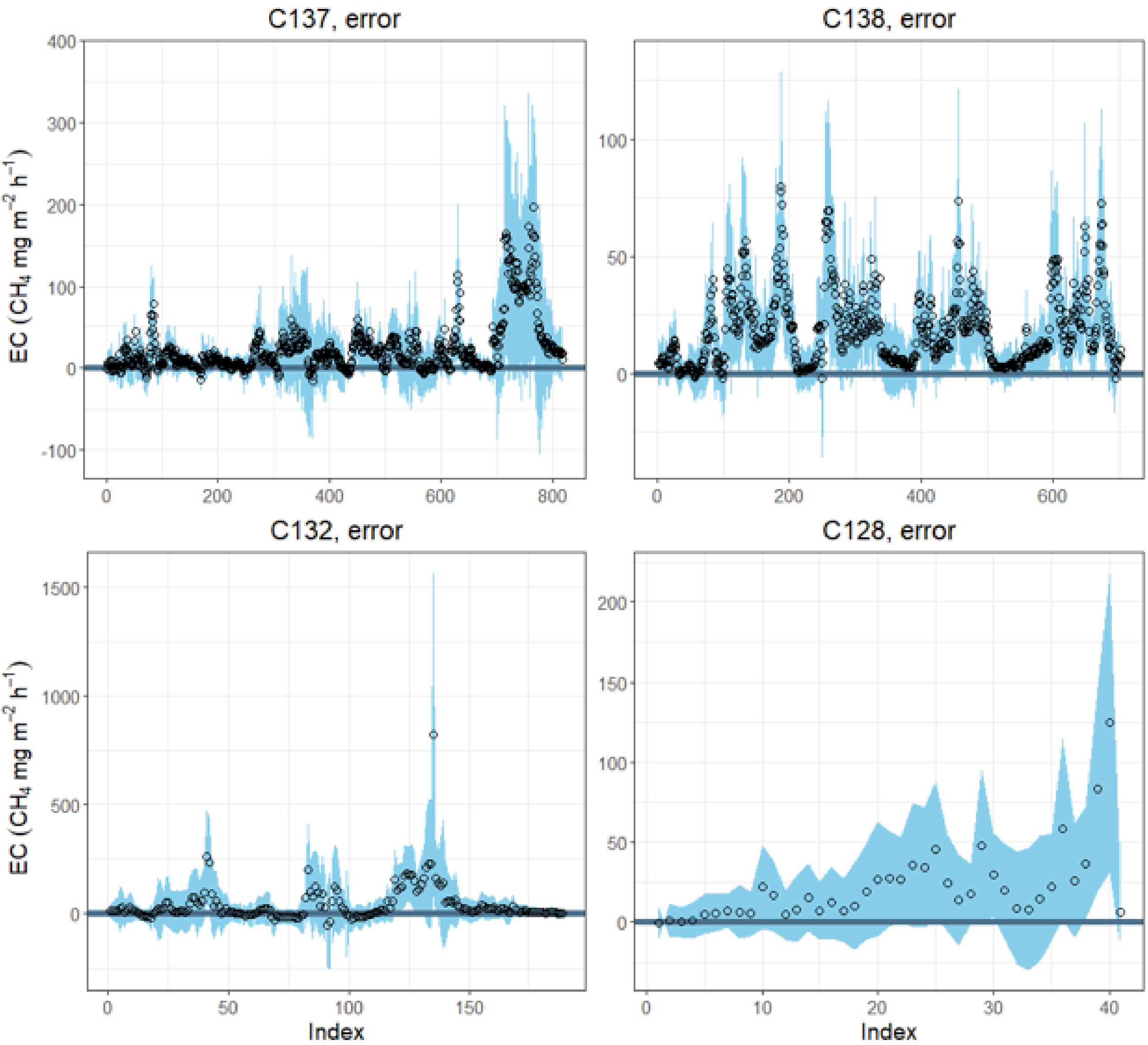

Figure B.4: Individual errors (shown in light blue) for the AEC flux values from the successful flights, plotted leg-by-leg rather than against the date for clarity.

Wetland	Leg	Length (km)	Lag vs wind (s)			LOD (mg m^{-2} h^{-1})	Mean (mg m^{-2} h^{-1})		Heat flux (W m^{-2} h^{-1})		Error	SN	Stat	NK12	Cross c
			H_2O	CO_2	T		raw	corrected	LE	H					
Wamala (C128)	21	47	-0.47	-0.50	0.00	1.1	5.7	20.9	67	9	30%	11	0	0.95	good
Wamala (C129)	*21*	39	-0.50	-0.50	**-0.56**	**2.7**	1.8	5.4	134	**-16**	**145%**	**1**	0	**0.54**	just T bad
Kyoga (C132)	12	106	-0.44	-0.44	0.00	3.8	7.6	33.4	436	23	73%	4	0	1.06	okay
	13a	37	**-5.69**	-0.44	**-0.84**	2.7	8.1	38.0	**-704**	78	51%	6	0	1.00	okay
	13b	43	-0.44	-0.38	-0.06	1.3	4.2	14.6	593	107	54%	6	0	0.97	okay
Kafue (C137)	5	65	**-1.91**	-0.41	0	4.35	35.8	71.8	1150	29	34%	17	0	1.02	good
	19	45	-0.47	-0.47	-0.03	2.21	9.1	12.7	209	72	33%	8	0	**0.79**	good
	21	40	-0.53	-0.56	0	1.80	5.8	8.9	329	38	58%	7	0	0.90	good
	24	41	-0.47	-0.41	-0.03	1.58	4.1	6.0	433	90	66%	5	0	0.99	good
	25	32	-0.50	-0.44	-0.03	3.60	6.8	11.9	354	63	72%	4	0	0.99	good
	27	61	-0.47	-0.41	0	5.42	20.4	18.9	300	72	43%	8	0	0.94	good
	29	48	-0.53	-0.50	0	2.52	15.1	21.6	639	72	38%	12	0	1.02	good
	30	50	-0.41	-0.41	-0.03	3.45	9.4	11.5	400	83	62%	5	0	1.13	good
	31	37	-0.50	-0.47	0	2.08	13.7	17.6	554	76	22%	14	0	**0.77**	good
Lukanga (C138)	8	84	-0.47	-0.44	0	0.70	10.5	18.0	334	35	18%	31	0	0.98	good
	12	123	-0.47	-0.44	0	1.01	9.9	20.0	398	52	23%	20	0	1.03	good
	14	79	-0.50	-0.47	0	1.42	13.3	15.7	424	36	22%	19	0	1.00	good
	17	76	-0.41	-0.41	0	1.13	11.6	19.7	317	19	22%	21	0	0.91	good

Table B.1: AEC CH_4 results for flights that passed the entire QA/QC process (in case of the Ugandan flights - relaxed, especially for the legs marked in italics). For the Zambian flights (C137 and C138) the aggregation window is 500 m and for the Ugandan flights (C128, C129 and C132) it is 1000 m. The values in bold fall outside of the desirable range. "Stat" = stationarity flag, "Cross correlation" refers to quality of the cross correlation plots for temperature, water and methane on scale: "good", "okay" (acceptable), "bad".

Wetland	Leg	Length (km)	Lag vs wind (s)			LOD (mg m^{-2} h^{-1})	Mean (mg m^{-2} h^{-1})	Heat flux (W m^{-2} h^{-1})		Error	Signal to noise	Stat	NK12	Cross correlation
			H_2O	CH_4	T			LE	H					
Wamala (C129)	27	21	**-1.97**	**-3.13**	0.00	4.3	**-5.9**	173	42	**102%**	**3**	**1**	1.08	**bad**
	36	23	-0.63	**-1.69**	0.00	0.4	1.2	211	5	78%	7	0	0.99	**bad**
Kyoga (C132)	3	53	**-1.94**	**-1.81**	0.00	**0.9**	**-0.4**	103	26	**256%**	**1**	**1**	**0.30**	**bad**
	4	50	**-2.09**	**-1.94**	**-4.59**	3.8	11.8	142	**-5**	48%	6	0	0.95	**bad**
	21	49	**-2.13**	**-2.09**	0.00	2.0	4.7	804	125	78%	5	0	1.07	**bad**
Sápmi (C195)	19	43	**-17.4**	**-19.3**	**-13.53**	**0.21**	-0.8	NA	NA	**161%**	8	0	1.00	**bad**
	20	246	**-15.2**	**-1.9**	**-19.88**	0.71	1.6	NA	NA	8%	**4**	0	1.01	**bad**
	24	102	**-8.1**	**-11.8**	0.00	0.08	-0.1	NA	NA	**531%**	**2**	0	0.96	**bad**
Sápmi (C196)	5	20	**-5.6**	**-9.9**	**-1.0**	0.29	0.4	NA	NA	98%	98%	0	**0.51**	**bad**
	6	26	**-4.8**	**-1.4**	**-4.3**	0.22	0.3	NA	NA	77%	77%	0	**0.55**	**bad**
	7	102	**-0.9**	**-1.0**	**-9.6**	**0.12**	0.9	NA	NA	72%	72%	0	0.86	**bad**
	9	222	**-3.7**	**-0.6**	**-9.2**	0.09	0.5	NA	NA	29%	29%	0	0.81	**bad**
	10	98	**-6.6**	**-1.2**	**-9.0**	0.24	1.8	NA	NA	93%	93%	0	0.99	**bad**
	13	40	**-5.6**	**-0.2**	**-7.1**	**0.19**	-0.5	NA	NA	109%	**109%**	0	1.00	**bad**
	15	292	**-9.5**	**-7.4**	**-5.9**	0.17	0.3	NA	NA	544%	**544%**	0	1.00	**bad**

Table B.2: Examples of AEC CH_4 results for flights that did not work. In case of Lake Bangweulu (C136) the aggregation distance was set to 1500 m, for the other flights to 1000 m. Additionally for the Bangweulu flight wind data used came from the AIMMS probe. For the two Sápmi flights, heat fluxes and positive mean are not applicable, since in the Arctic positive heat and methane flux cannot be simply assumed even in summer. The values in bold fall outside of the desirable range. "Stat" = stationarity flag, "Cross correlation" refers to quality of the cross correlation plots for temperature, water and methane on scale: "good", "okay" (acceptable), "bad".

Wetland	Leg	Length (km)	Lag vs wind (s)			LOD (mg m^{-2} h^{-1})	Mean (mg m^{-2} h^{-1})		Heat flux (W m^{-2} h^{-1})		Error	SN	Stat	NK12	Cross c
			H_2O	CO_2	T		raw	corrected	LE	H					
Wamala (C128)	*21*	47	-0.47	**-0.06**	0.00	76	**-61**	-225	67	9	**139%**	**2**	**1**	**0.73**	okay
Wamala (C129)	*21*	39	-0.50	-0.44	**-0.56**	66	-394	-1176	132	**-16**	19%	12	0	**0.86**	good
	36	23	-0.56	-0.38	0.00	90	-242	-879	207	5	77%	6	**1**	0.99	**bad**
Kyoga (C132)	12	106	-0.44	-0.38	0.00	107	254	1122	437	24	73%	5	**1**	1.04	okay
	13b	43	-0.44	-0.41	-0.06	75	280	971	594	107	37%	8	0	0.90	**bad**
Kafue (C137)	19	45	-0.03	-0.47	-0.63	310	-1497	-2178	208	72	30%	10	0	0.85	good
	24	41	-0.03	-0.47	-0.50	493	-888	-1007	433	90	**119%**	4	**1**	0.96	**bad**
	25	32	-0.03	-0.50	-0.66	287	-1503	-2194	355	63	32%	11	0	0.97	good
	27	61	0.00	-0.47	-0.41	**704**	493	-746	300	71	**225%**	**1**	**1**	**0.78**	good
	29	48	0.00	-0.53	-0.50	323	-358	-328	638	72	**217%**	**2**	0	0.82	ok
	30	50	-0.03	-0.41	**-0.28**	408	-998	-1816	401	83	60%	5	0	0.94	ok
Lukanga (C138)	8	84	0.00	-0.47	**-0.28**	226	-702	-1213	333	35	74%	6	0	0.92	ok
	12	123	0.00	-0.47	-0.47	218	-1536	-2575	398	52	30%	14	0	0.99	**bad**
	14	79	0.00	-0.50	-0.56	271	-1165	-1574	423	36	47%	9	0	0.97	good
	17	76	0.00	-0.41	-0.50	188	-361	-488	318	19	94%	4	**1**	**0.77**	good

Table B.3: AEC CO_2 results for flights that passed the entire QA/QC process (in case of the Ugandan flights - relaxed, especially for the legs marked in italics). For the Zambian flights (C137 and C138) the aggregation window is 500 m and for the Ugandan flights (C128, C129 and C132) it is 1000 m. The values in bold fall outside of the desirable range. “Stat" = stationarity flag, “SN" = signal to noise ratio, “Cross c" refers to quality of the cross correlation plots for temperature, water and methane on scale: “good", “okay" (acceptable), “bad".

Wetland	Leg	Length (km)	Lag vs wind (s)			LOD (mg m^{-2} h^{-1})	Mean (mg m^{-2} h^{-1})	Heat flux (W m^{-2} h^{-1})		Error	Signal to noise	Stat	NK12	Cross correlation
			H_2O	CO_2	T			LE	H					
Wamala (C129)	27	21	**-2**	**-1.84**	**0.00**	200	-1168	175	46	29%	12	**1**	1.01	**bad**
Kyoga (C132)	3	53	**-1.94**	**-2.19**	0.00	85	**26**	102	26	**431%**	**1**	**1**	**0.83**	**bad**
	4	50	**-2.06**	**-2.09**	**-4.59**	215	480	143	**-5**	58%	4	**1**	0.94	**bad**
	13a	37	**-5.69**	**-5.81**	**-0.84**	158	**31**	**-698**	78	**870%**	**0**	**1**	0.93	**bad**
	21	49	**-2.13**	**-1.59**	0.00	146	391	811	124	89%	7	0	1.01	**bad**
Kafue (C137)	5	37	0.0	**-1.91**	**-6.66**	532	-792	1157	29	**104%**	3	**1**	0.87	**bad**
	21	65	0.0	-0.53	**0.00**	722	-1507	328	38	87%	4	0	1.01	**bad**
	31	40	0.0	-0.50	**-2.19**	732	-970	549	76	**101%**	3	0	**0.73**	**bad**

Table B.4: Examples of AEC CO_2 results for flights that did not work. The values in bold fall outside of the desirable range. "Stat" = stationarity flag, "Cross correlation" refers to quality of the cross correlation plots for temperature, water and methane on scale: "good", "okay" (acceptable), "bad".

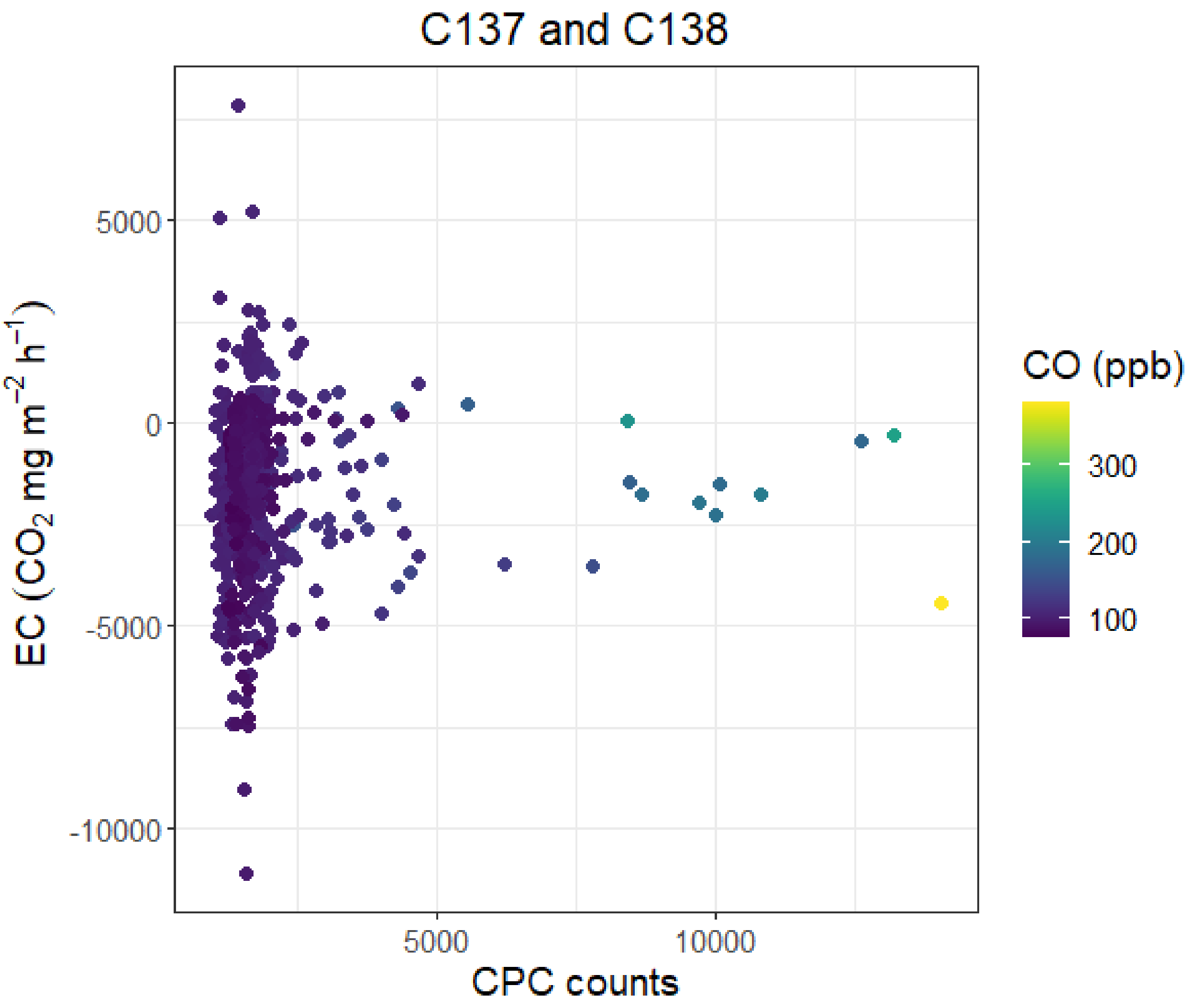

Figure B.5: Investigating potential fire effect on CO_2 flux in Zambia (C137 and C138). The high fluxes do not coincide with high CPC counts or high CO mixing ratio, hence it is safe to assume they are not caused by fires or smouldering.

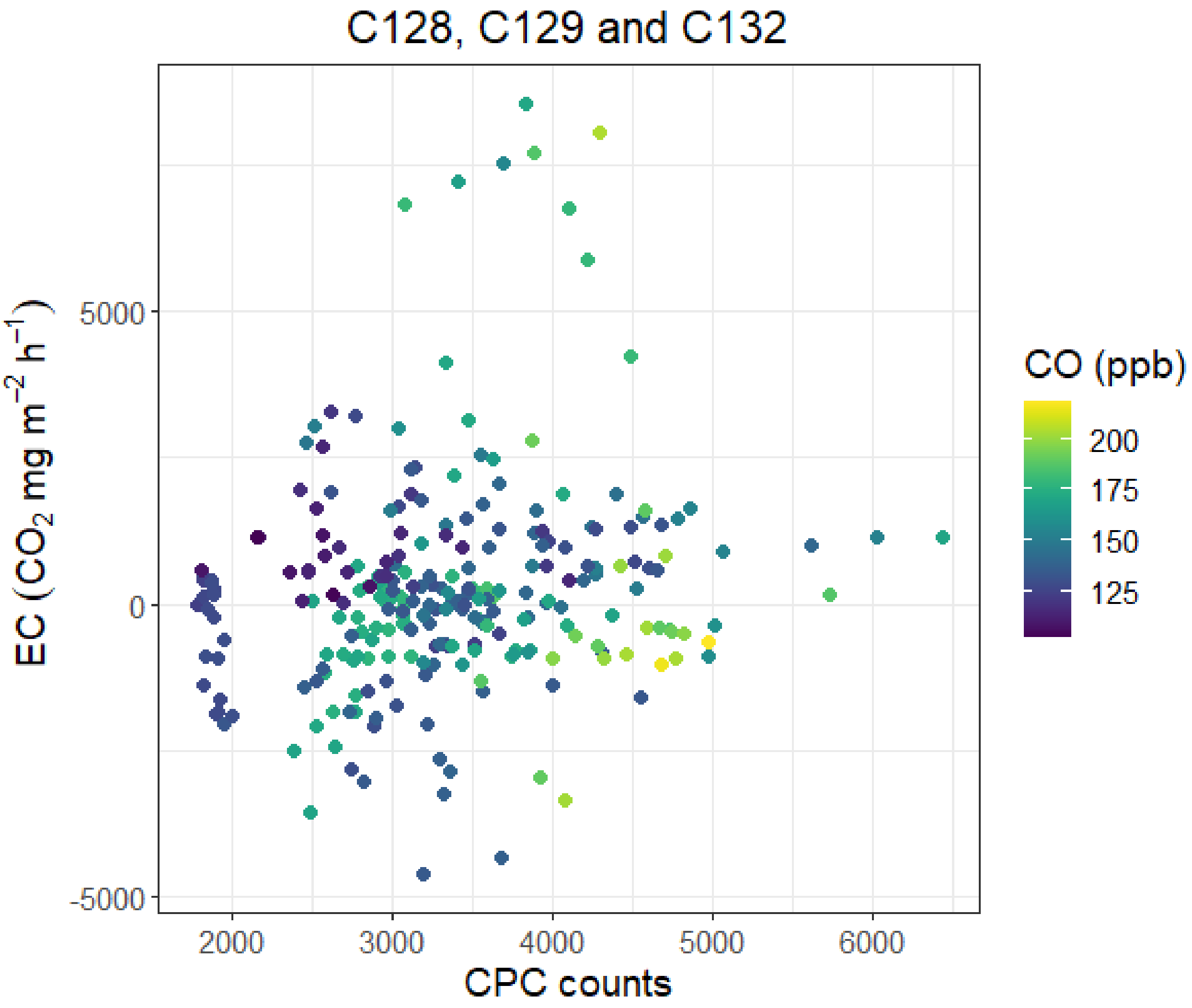

Figure B.6: Investigating potential fire effect on CO_2 flux in Uganda (C128, C129 and C132). The highest fluxes do not coincide with high CPC counts and fall in the middle of the CO mixing ratio range, hence it is unlikely that they are caused by fires or somuldering.

Sites	Wetland type	Flux (mg m^{-2} h^{-1})		Type of study	Reference
		CO_2	CH_4		
Uganda: Lake Kyoga	mixed flood levels	1052 ± 293	15.9 ± 5.6	AEC	this study
Uganda: Lake Wamala	permanently flooded	-757 ± 189	9.9 ± 3.4	AEC	this study
Zambia: Kafue Flats	seasonally flooded	-1303 ± 256	23.0 ± 1.31	AEC	this study
Zambia: Lukanga Swamps	seasonally flooded	-674 ± 241	27.9 ± 1.61	AEC	this study
Uganda: Naigombwa (Iganga district)	permanently flooded	2702	18.5	white static chamber	Were et al. 2021 [170]
Uganda: Kirinya West (Lake Victoria)	papyrus lagoon	320	NA	EC tower	Saunders et al. 2007 [195]
Congo: Congo river basin	flooded forest	NA	4.4	multiple methods	Tathy at al. 1992 [202]
Zimbabwe: Chiota (Marondera district)	dambo (seasonal)	3286	39.3	opaque static chambers	Nyamadzawo et al. 2015 [203]
Sub-Saharan Africa	all kind wetlands	1101	10.8	mata-analysis	Kim et al. 20016 [94]
China: Shanyutan (Minjiang estuary)	eustarine wetland	4530	140	transparent floating chambers	Yang et al. 2017 [197]
Brazil: Cuini, Itu and Araca	mixed flood levels	428	4.2	chambers and inverted funnels	Belger et al. 2011 [204]
Brazil: Pantanal	flooded grassland	533	7.9	meta-analysis	Sjögersten et al. 2014 [205]
Indonesia: multiple	forested peatland	3241	1.6	meta-analysis	Sjögersten et al. 2014 [205]
Malaysia: multiple	forested peatland	3319	NA	meta-analysis	Sjögersten et al. 2014 [205]
Malaysia: Alan Batu Forest (Sarawak)	undrained swamp forest	388	0.6	opaque static chambers	Ishikura et al. 2019 [206]
Germany: Federseemoor	reed peatland	102	3.4	EC tower	van den Berg et al. 2016 [145]

Table B.5: Comparison with other tropical wetland GHG flux studies.

Bibliography

[1] Lelieveld, J., Roelofs, G.-.-J., Ganzeveld, L., Feichter, J. and Rodhe, H. Terrestrial sources and distribution of atmospheric sulphur. *Philosophical Transactions of the Royal Society of London. Series B: Biological Sciences* 352.1350 (1997), pp. 149–158.

[2] Cullis, C. and Hirschler, M. Atmospheric sulphur: natural and man-made sources. *Atmospheric Environment (1967)* 14.11 (1980), pp. 1263–1278.

[3] Venzke, E. *Has volcanic activity been increasing?* `https://volcano.si.edu/faq/index.cfm?question=historicalactivity`. Accessed: 2023-05-18. DOI: `https://doi.org/10.5479/si.GVP.VOTW5-2022.5.0`.

[4] Charlson, R. J., Lovelock, J. E., Andreae, M. O. and Warren, S. G. Oceanic phytoplankton, atmospheric sulphur, cloud albedo and climate. *Nature* 326.6114 (1987), pp. 655–661.

[5] Schwartz, S. E. Are global cloud albedo and climate controlled by marine phytoplankton? *Nature* 336.6198 (1988), pp. 441–445.

[6] Quinn, P. K. and Bates, T. S. The case against climate regulation via oceanic phytoplankton sulphur emissions. *Nature* 480.7375 (2011), pp. 51–56.

[7] Smith, S. J., Aardenne, J. van, Klimont, Z., Andres, R. J., Volke, A. and Delgado Arias, S. Anthropogenic sulfur dioxide emissions: 1850–2005. *Atmospheric Chemistry and Physics* 11.3 (2011), pp. 1101–1116.

[8] Schwikowski, M., Döscher, A., Gäggeler, H. and Schotterer, U. Anthropogenic versus natural sources of atmospheric sulphate from an Alpine ice core. *Tellus B: Chemical and Physical Meteorology* 51.5 (1999), pp. 938–951.

[9] Aas, W., Mortier, A., Bowersox, V., Cherian, R., Faluvegi, G., Fagerli, H., Hand, J., Klimont, Z., Galy-Lacaux, C., Lehmann, C. et al. Global and regional trends of atmospheric sulfur. *Scientific reports* 9.1 (2019), pp. 1–11.

[10] Capaldo, K., Corbett, J. J., Kasibhatla, P., Fischbeck, P. and Pandis, S. N. Effects of ship emissions on sulphur cycling and radiative climate forcing over the ocean. *Nature* 400.6746 (1999), pp. 743–746.

[11] Dalsøren, S. B., Eide, M., Endresen, Ø., Mjelde, A., Gravir, G. and Isaksen, I. S. Update on emissions and environmental impacts from the international fleet of ships: the contribution from major ship types and ports. *Atmospheric Chemistry and Physics* 9.6 (2009), pp. 2171–2194.

[12] Liu, F., Choi, S., Li, C., Fioletov, V. E., McLinden, C. A., Joiner, J., Krotkov, N. A., Bian, H., Janssens-Maenhout, G., Darmenov, A. S. et al. A new global anthropogenic SO 2 emission inventory for the last decade: a mosaic of satellite-derived and bottom-up emissions. *Atmospheric Chemistry and Physics* 18.22 (2018), pp. 16571–16586.

[13] Wu, Z., Zhang, Y., He, J., Chen, H., Huang, X., Wang, Y., Yu, X., Yang, W., Zhang, R., Zhu, M. et al. Dramatic increase in reactive volatile organic compound (VOC) emissions from ships at berth after implementing the fuel switch policy in the Pearl River Delta Emission Control Area. *Atmospheric Chemistry and Physics* 20.4 (2020), pp. 1887–1900.

[14] Sofiev, M., Winebrake, J. J., Johansson, L., Carr, E. W., Prank, M., Soares, J., Vira, J., Kouznetsov, R., Jalkanen, J.-P. and Corbett, J. J. Cleaner fuels for ships provide public health benefits with climate tradeoffs. *Nature communications* 9.1 (2018), p. 406.

[15] Cox, R. Atmospheric sulphur and climate—what have we learned? *Philosophical Transactions of the Royal Society of London. Series B: Biological Sciences* 352.1350 (1997), pp. 251–254.

[16] Watson-Parris, D., Christensen, M. W., Laurenson, A., Clewley, D., Gryspeerdt, E. and Stier, P. Shipping regulations lead to large reduction in cloud perturbations. *Proceedings of the National Academy of Sciences* 119.41 (2022), e2206885119.

[17] Christensen, M. W., Gettelman, A., Cermak, J., Dagan, G., Diamond, M., Douglas, A., Feingold, G., Glassmeier, F., Goren, T., Grosvenor, D. P. et al. Opportunistic experiments to constrain aerosol effective radiative forcing. *Atmospheric chemistry and physics* 22.1 (2022), pp. 641–674.

[18] *Case for Support: Atmospheric Composition and Radiative forcing changes due to UN International Ship Emissions regulations (ACRUISE).*

[19] Peters, K., Quaas, J. and Graßl, H. A search for large-scale effects of ship emissions on clouds and radiation in satellite data. *Journal of Geophysical Research: Atmospheres* 116.D24 (2011).

[20] Gibbons, A. *The peopling of the Pacific*. 2001.

[21] Vance, J. E. History of ships (1998).

[22] Schob, D. E. Woodhawks & Cordwood: Steamboat Fuel on the Ohio and Mississippi Rivers, 1820–1860. *Journal of Forest History* 21.3 (1977), pp. 124–132.

[23] Madureira, N. L. Oil in the Age of Steam. *Journal of Global History* 5.1 (2010), pp. 75–94.

[24] Dahl, E. J. *Naval innovation: from coal to oil*. Tech. rep. National Defense University, Institute for National Strategic Studies, 2001.

[25] Melsted, O. and Pallua, I. The historical transition from coal to hydrocarbons: Previous explanations and the need for an integrative perspective. *Canadian Journal of History* 53.3 (2018), pp. 395–422.

[26] Endresen, Ø., Sørgård, E., Behrens, H. L., Brett, P. O. and Isaksen, I. S. A historical reconstruction of ships' fuel consumption and emissions. *Journal of Geophysical Research: Atmospheres* 112.D12 (2007).

[27] Carlton, J., Smart, R. and Jenkins, V. The nuclear propulsion of merchant ships: aspects of engineering, science and technology. *Journal of Marine Engineering & Technology* 10.2 (2011), pp. 47–59.

[28] Chiu, C.-H. History of the Development of LNG Technology. *presentation at the Annual Conference–Hundred Years of Advancements in Fuels and Petrochemicals in Philadelphia (November 18, 2008)*. 2008.

[29] Noble, P. G. A short history of lng shipping. *Texas Section SNAME* (2009).

[30] *DNV: 222 LNG-powered ships ordered in 2022*. `https://lngprime.com/europe/dnv-222-lng-powered-ships-ordered-in-2022/70166/`. Accessed: 2023-05-18.

[31] Eyring, V., Köhler, H., Lauer, A. and Lemper, B. Emissions from international shipping: 2. Impact of future technologies on scenarios until 2050. *Journal of Geophysical Research: Atmospheres* 110.D17 (2005).

[32] *IMO History*. `https://www.imo.org/en/About/HistoryOfIMO/Pages/Default.aspx`. Accessed: 2023-01-21.

[33] `https://www.imo.org/en`. Accessed: 2023-03-18.

[34] Cooper, D. A. Exhaust emissions from ships at berth. *Atmospheric Environment* 37.27 (2003), pp. 3817–3830. DOI: 10.1016/S1352-2310(03)00446-1.

[35] Kattner, L., Mathieu-Üffing, B., Burrows, J. P., Richter, A., Schmolke, S., Seyler, A. and Wittrock, F. Monitoring compliance with sulfur content regulations of shipping fuel by in situ measurements of ship emissions. *Atmospheric Chemistry and Physics* (2015). DOI: 10.5194/acp-15-10087-2015.

[36] Petzold, A., Hasselbach, J., Lauer, P., Baumann, R., Franke, K., Gurk, C., Schlager, H. and Weingartner, E. Experimental studies on particle emissions from cruising ship, their characteristic properties, transformation and atmospheric lifetime in the marine boundary layer. *Atmospheric Chemistry and Physics* (2008). DOI: 10.5194/acp-8-2387-2008.

[37] Lack, D. A., Cappa, C. D., Langridge, J., Bahreini, R., Buffaloe, G., Brock, C., Cerully, K., Coffman, D., Hayden, K., Holloway, J., Lerner, B., Massoli, P., Li, S. M., McLaren, R., Middlebrook, A. M., Moore, R., Nenes, A., Nuaaman, I., Onasch, T. B., Peischl, J., Perring, A., Quinn, P. K., Ryerson, T., Schwartz, J. P., Spackman, R., Wofsy, S. C., Worsnop, D., Xiang, B. and Williams, E. Impact of fuel quality regulation and speed reductions on shipping emissions: Implications for climate and air quality. *Environmental Science and Technology* (2011). DOI: 10.1021/es2013424.

[38] Lack, D. A., Corbett, J. J., Onasch, T., Lerner, B., Massoli, P., Quinn, P. K., Bates, T. S., Covert, D. S., Coffman, D., Sierau, B. et al. Particulate emissions from commercial shipping: Chemical, physical, and optical properties. *Journal of Geophysical Research: Atmospheres* 114.D7 (2009).

[39] Burgard, D. A. and Bria, C. R. Bridge-based sensing of NOx and SO2 emissions from ocean-going ships. *Atmospheric Environment* 136 (2016), pp. 54–60.

[40] Carslaw, D. C., Beevers, S. D., Tate, J. E., Westmoreland, E. J. and Williams, M. L. Recent evidence concerning higher NOx emissions from passenger cars and light duty vehicles. *Atmospheric Environment* 45.39 (2011), pp. 7053–7063.

[41] Schlager, H., Baumann, R., Lichtenstern, M., Petzold, A., Arnold, F., Speidel, M., Gurk, C. and Fischer, H. Aircraft-based trace gas measurements in a primary European ship corridor. *Proceedings of an International Conference on Transport, Atmosphere and Climate (TAC)*. Office for Official Publications of the European Communities, Luxembourg. 2007, pp. 83–88.

[42] Goldsworthy, L. and Galbally, I. Ship engine exhaust emissions in waters around Australia-an overview. *Air Quality and Climate Change* 45.4 (2011), pp. 24–32.

[43] Xiao, Q., Li, M., Liu, H., Fu, M., Deng, F., Lv, Z., Man, H., Jin, X., Liu, S. and He, K. Characteristics of marine shipping emissions at berth: profiles for particulate matter and volatile organic compounds. *Atmospheric Chemistry and Physics* 18.13 (2018), pp. 9527–9545.

[44] Tagliaferri, C., Clift, R., Lettieri, P. and Chapman, C. Liquefied natural gas for the UK: a life cycle assessment. *International Journal of Life Cycle Assessment* (2017). DOI: `10.1007/s11367-017-1285-z`.

[45] Lowell, D., Wang, H. and Lutsey, N. *Assessment of the fuel cycle impact of liquefied natural gas as used in international shipping*. Tech. rep. International Council on Clean Transportation, 2013. URL: `http://www.theicct.org/sites/default/files/publications/ICCTwhitepaper%7B%5C_%7DMarine%20LNG%7B%5C_%7D130513.pdf`.

[46] Shaton, K., Hervik, A. and Hjelle, H. Environmental footprint of Gas Transportation: LNG vs. pipeline. *39th IAEE International Conference*. 2016.

[47] Howarth, R. W., Santoro, R. and Ingraffea, A. *Methane and the greenhouse-gas footprint of natural gas from shale formations*. 2011. DOI: 10.1007/s10584-011-0061-5.

[48] Tamura, I., Tanaka, T., Kagajo, T., Kuwabara, S., Yoshioka, T., Nagata, T., Kurahashi, K. and Ishitani, H. Life cycle CO2 analysis of LNG and city gas. *Applied Energy* (2001). DOI: 10.1016/S0306-2619(00)00062-3.

[49] Balcombe, P., Anderson, K., Speirs, J., Brandon, N. and Hawkes, A. *The Natural Gas Supply Chain: The Importance of Methane and Carbon Dioxide Emissions*. 2017. DOI: 10.1021/acssuschemeng.6b00144.

[50] Okamura, T., Furukawa, M. and Ishitani, H. Future forecast for life-cycle greenhouse gas emissions of LNG and city gas 13A. *Applied Energy* (2007). DOI: 10.1016/j.apenergy.2007.05.005.

[51] Balcombe, P., Heggo, D. A. and Harrison, M. Total methane and CO2 emissions from liquefied natural gas carrier ships: the first primary measurements. *Environmental Science & Technology* 56.13 (2022), pp. 9632–9640.

[52] Manshausen, P., Watson-Parris, D., Christensen, M. W., Jalkanen, J.-P. and Stier, P. Invisible ship tracks show large cloud sensitivity to aerosol. *Nature* 610.7930 (2022), pp. 101–106.

[53] Mcbeath, K. The use of aircraft for meteorological research in the United Kingdom. *Meteorological Applications* 21.1 (2014), pp. 105–116. DOI: 10.1002/met.1448.

[54] Luke, W. T. Evaluation of a commercial pulsed fluorescence detector for the measurement of low-level SO2 concentrations during the Gas-Phase Sulfur Intercomparison Experiment. *Journal of Geophysical Research: Atmospheres* 102.D13 (1997), pp. 16255–16265.

[55] Bauguitte, S. *SO2 Instrument Description*. Tech. rep. 2022, p. 21. DOI: 10.5281/zenodo.7391494.

[56] Rollins, A. W., Thornberry, T. D., Ciciora, S. J., McLaughlin, R. J., Watts, L. A., Hanisco, T. F., Baumann, E., Giorgetta, F. R., Bui, T. V., Fahey, D. W. et al. A laser-induced fluorescence instrument for aircraft measurements of sulfur dioxide

in the upper troposphere and lower stratosphere. *Atmospheric Measurement Techniques* 9.9 (2016), pp. 4601–4613.

[57] Bannan, T. J., Le Breton, M., Priestley, M., Worrall, S. D., Bacak, A., Marsden, N. A., Mehra, A., Hammes, J., Hallquist, M., Alfarra, M. R., Krieger, U. K., Reid, J. P., Jayne, J., Robinson, W., McFiggans, G., Coe, H., Percival, C. J. and Topping, D. A method for extracting calibrated volatility information from the FIGAERO-HR-ToF-CIMS and its experimental application. *Atmospheric Measurement Techniques* 12.3 (2019), pp. 1429–1439. DOI: `10.5194/amt-12-1429-2019`. URL: `https://amt.copernicus.org/articles/12/1429/2019/`.

[58] O'Shea, S., Bauguitte, S.-B., Gallagher, M., Lowry, D. and Percival, C. Development of a cavity-enhanced absorption spectrometer for airborne measurements of CH 4 and CO 2. *Atmospheric Measurement Techniques* 6.5 (2013), pp. 1095–1109.

[59] Shaw, J. T., Allen, G., Barker, P., Pitt, J. R., Lee, J., Bauguitte, S. J.-B., Pasternak, D., Bower, K. N., Daly, M. C., Lunt, M., Ganesan, A. L., Fisher, R. E., France, J. L., Lowry, D., Palmer, P. I., Bateson, P., Vaughan, A. R., Cain, M., Lorente, A., Borsdorff, T., Metzger, S. and Nisbet, E. G. Globally significant methane emissions from African tropical wetlands. *TBC* 1.1 (2021), p. 1.

[60] Pollack, I. B., Lerner, B. M. and Ryerson, T. B. Evaluation of ultraviolet light-emitting diodes for detection of atmospheric NO2 by photolysis-chemiluminescence. *Journal of Atmospheric Chemistry* 65.2 (2010), pp. 111–125.

[61] Gerbig, C., Schmitgen, S., Kley, D., Volz-Thomas, A., Dewey, K. and Haaks, D. An improved fast-response vacuum-UV resonance fluorescence CO instrument. *Journal of Geophysical Research: Atmospheres* 104.D1 (1999), pp. 1699–1704.

[62] Wilson, K. L. and Birks, J. W. Mechanism and elimination of a water vapor interference in the measurement of ozone by UV absorbance. *Environmental science & technology* 40.20 (2006), pp. 6361–6367.

[63] O'Shea, S. J., Bauguitte, S. J., Gallagher, M. W., Lowry, D. and Percival, C. J. Development of a cavity-enhanced absorption spectrometer for airborne measurements of CH4 and CO2. *Atmospheric Measurement Techniques* (2013). DOI: `10.5194/amt-6-1095-2013`.

[64] Barker, P. Characterisation of FAAM's Fast Greenhouse Gas Analyser. PhD thesis. 2018.

[65] Squires, F. Modification and Characterisation of a Commercial Sulfur Dioxide Analyser for Airborne Measurements. PhD thesis. 2016.

[66] Lee, J. D., Squires, F. A., Sherwen, T., Wilde, S. E., Cliff, S. J., Carpenter, L. J., Hopkins, J. R., Bauguitte, S. J., Reed, C., Barker, P. et al. Ozone production and precursor emission from wildfires in Africa. *Environmental Science: Atmospheres* 1.7 (2021), pp. 524–542.

[67] Andrews, S. J., Carpenter, L. J., Apel, E. C., Atlas, E., Donets, V., Hopkins, J. R., Hornbrook, R. S., Lewis, A. C., Lidster, R. T., Lueb, R. et al. A comparison of very short lived halocarbon (VSLS) and DMS aircraft measurements in the tropical west Pacific from CAST, ATTREX and CONTRAST. *Atmospheric Measurement Techniques* 9.10 (2016), pp. 5213–5225.

[68] Warburton, T., Grange, S. K., Hopkins, J. R., Andrews, S. J., Lewis, A. C., Owen, N., Jordan, C., Adamson, G. and Xia, B. The impact of plug-in fragrance diffusers on residential indoor VOC concentrations. *Environmental Science: Processes & Impacts* 25.4 (2023), pp. 805–817.

[69] Andrews, S. *Atmospheric Research Aircraft Technical Specification of Scientific Equipment: Son of Whole Air Sampling Rack (UnivYork/SWAS/001)*. Tech. rep. 2018, p. 70.

[70] *MarineTraffic – Global Ship Tracking Intelligence*. URL: `www.marinetraffic.com`.

[71] Center, N. *Automatic Identification System (AIS) Overview*. Tech. rep. United States Coast Guard, U.S. Department of Homeland Security. URL: `https://www.navcen.uscg.gov/automatic-identification-system-overview`.

[72] Potapov, P., Hansen, M. C., Kommareddy, I., Kommareddy, A., Turubanova, S., Pickens, A., Adusei, B., Tyukavina, A. and Ying, Q. Landsat analysis ready data for global land cover and land cover change mapping. *Remote Sensing* 12.3 (2020), p. 426.

[73] Robinson, M. personal communication. 2021.

[74] Allabadi, A. A., Thomas, J. L., Herber, A. B., Staebler, R. M., Leaitch, W. R., Schulz, H., Law, K. S., Marelle, L., Willis, M. D., Allabadi, A. A., Thomas, J. L., Herber, A. B., Staebler, R. M., Leaitch, W. R., Aliabadi, A. A., Thomas, J. L., Herber, A. B., Staebler, R. M. and Leaitch, W. R. Ship emissions measurement in the Arctic by plume intercepts of the Canadian Coast Guard icebreaker Amundsen from the Polar 6 aircraft platform. *Atmospheric Chemistry and Physics* 16.12 (2016), pp. 7899–7916. DOI: `10.5194/acp-16-7899-2016`.

[75] Yu, C., Pasternak, D., Lee, J., Yang, M., Bell, T., Bower, K., Wu, H., Liu, D., Reed, C., Bauguitte, S. et al. Characterizing the Particle Composition and Cloud Condensation Nuclei from Shipping Emission in Western Europe. *Environmental Science & Technology* 54.24 (2020), pp. 15604–15612.

[76] Corbett, J. J. and Koehler, H. W. Updated emissions from ocean shipping. *Journal of Geophysical Research: Atmospheres* 108.D20 (2003).

[77] Johansson, L., Jalkanen, J.-P. and Kukkonen, J. Global assessment of shipping emissions in 2015 on a high spatial and temporal resolution. *Atmospheric Environment* 167 (2017), pp. 403–415.

[78] Jalkanen, J.-P., Brink, A., Kalli, J., Pettersson, H., Kukkonen, J. and Stipa, T. A modelling system for the exhaust emissions of marine traffic and its application in the Baltic Sea area. *Atmospheric Chemistry and Physics* 9.23 (2009), pp. 9209–9223.

[79] Lacy, S., Batten, S. and Sproson, D. *acruise-peakid package*. `https://github.com/wacl-york/acruise-peakid`. 2022.

[80] Barker, P. A., Allen, G., Gallagher, M., Pitt, J. R., Fisher, R. E., Bannan, T., Nisbet, E. G., Bauguitte, S. J.-B., Pasternak, D., Cliff, S. et al. Airborne measurements of fire emission factors for African biomass burning sampled during the MOYA campaign. *Atmospheric Chemistry and Physics* 20.23 (2020), pp. 15443–15459.

[81] Batten, S. An investigation of anthropogenic sulphur dioxide emissions using the FAAM Airborne Laboratory. PhD thesis. 2022.

[82] Wilde, S. E., Lee, J. D. and Carslaw, D. C. *Shipping Emissions Summary - Port of Valencia*. Tech. rep. Wolfson Atmospheric Chemistry Laboratories, University of York, 2023, p. 8.

[83] York, D. Least squares fitting of a straight line with correlated errors. *Earth and planetary science letters* 5 (1968), pp. 320–324.

[84] Wu, C. and Yu, J. Z. Evaluation of linear regression techniques for atmospheric applications: the importance of appropriate weighting. *Atmospheric Measurement Techniques* 11.2 (2018), pp. 1233–1250.

[85] *Review of Maritime Transport 2021*. Tech. rep. New York, 2021, p. 147.

[86] *The 2020 global sulphur limit. Frequently Asked Questions*. Tech. rep. 2019, p. 5. URL: `%7Bhttps://wwwcdn.imo.org/localresources/en/MediaCentre/HotTopics/Documents/2020%5C%20sulphur%5C%20limit%5C%20FAQ%5C%202019.pdf%7D` (visited on 01/02/2023).

[87] Wilde, S., Farren, N., Rebecca, W., Lee, J., Wilson, S., Padilla, L., Peters, D., Alvarez, R., Slater, G. and Carslaw, D. Mobile Monitoring to Understand Vehicle Emissions (2023). in preparation.

[88] Foken, T. and Wichura, B. Tools for quality assessment of surface-based flux measurements. *Agricultural and forest meteorology* 78.1-2 (1996), pp. 83–105.

[89] Z. Jacobson. *Atmospheric Pollution*. Vol. 1 edition. 2002, pp. 1–109. DOI: `10.1017/CBO9780511802287`. eprint: `arXiv:1206.2908v1`. URL: `http://www.citeulike.org/user/harish/article/1607807`.

[90] IPCC. Climate Change 2014: Synthesis Report. *Contribution of Working Groups I, II and III to the Fifth Assessment Report of the Intergovernmental Panel on Climate Change. In: Core Writing Team, Pachauri RK, Meyer LA (eds) IPCC, Geneva, Switzerland, 151 p.* (2014), pp. 1–112. DOI: `10.1017/CBO9781107415324`. arXiv: `arXiv:1011.1669v3`.

[91] Solomon, S., Plattner, G.-K., Knutti, R. and Friedlingstein, P. Irreversible climate change due to carbon dioxide emissions. *Proceedings of the National Academy of Sciences* (2009). DOI: `10.1073/pnas.0812721106`. arXiv: `arXiv:1011.1669v3`.

[92] Reay, D., Smith, P. and Van Amstel, A. *Methane and climate change*. 2010. DOI: `10.4324/9781849775090`.

[93] IPCC. *Climate Change 2022: Mitigation of Climate Change. Contribution of Working Group III to the Sixth Assessment Report of the Intergovernmental Panel on Climate Change*. Ed. by P. Shukla, J. Skea, R. Slade, A. A. Khourdajie, R. van Diemen, D. McCollum, M. Pathak, S. Some, P. Vyas, R. Fradera, M. Belkacemi, A. Hasija, G. Lisboa, S. Luz and J. Malley. Cambridge, UK and New York, NY, USA: Cambridge University Press, 2022. DOI: `10.1017/9781009157926`. URL: `https://www.ipcc.ch/report/ar6/wg3/downloads/report/IPCC_AR6_WGIII_FullReport.pdf`.

[94] Kim, D.-G., Thomas, A. D., Pelster, D., Rosenstock, T. S. and Sanz-Cobena, A. Greenhouse gas emissions from natural ecosystems and agricultural lands in sub-Saharan Africa: synthesis of available data and suggestions for further research. *Biogeosciences* 13.16 (2016), pp. 4789–4809.

[95] Nisbet, E. G., Manning, M., Dlugokencky, E., Fisher, R., Lowry, D., Michel, S., Myhre, C. L., Platt, S. M., Allen, G., Bousquet, P. et al. Very strong atmospheric methane growth in the 4 years 2014–2017: Implications for the Paris Agreement. *Global Biogeochemical Cycles* 33.3 (2019), pp. 318–342.

[96] Ganesan, A. L., Schwietzke, S., Poulter, B., Arnold, T., Lan, X., Rigby, M., Vogel, F. R., Werf, G. R. van der, Janssens-Maenhout, G., Boesch, H. et al. Advancing scientific understanding of the global methane budget in support of the Paris Agreement. *Global Biogeochemical Cycles* 33.12 (2019), pp. 1475–1512.

[97] Pohlman, J. W., Greinert, J., Ruppel, C., Silyakova, A., Vielstädte, L., Casso, M., Mienert, J. and Bünz, S. Enhanced CO ₂ uptake at a shallow Arctic Ocean seep field overwhelms the positive warming potential of emitted methane. *Proceedings of the National Academy of Sciences* (2017). DOI: `10.1073/pnas.1618926114`.

[98] Etiope, G. and Klusman, R. W. Geologic emissions of methane to the atmosphere. *Chemosphere* (2002). DOI: `10.1016/S0045-6535(02)00380-6`.

[99] Etiope, G., Caracausi, A., Favara, R., Italiano, F. and Baciu, C. Methane emission from the mud volcanoes of Sicily (Italy). *Geophysical Research Letters* (2002). DOI: `10.1029/2001GL014340`.

[100] Bastviken, D., Tranvik, L. J., Downing, J. A., Crill, P. M. and Enrich-Prast, A. *Freshwater methane emissions offset the continental carbon sink*. 2011. doi: `10.1126/science.1196808`. arXiv: 3533.

[101] Walter, K. M., Zimov, S. A., Chanton, J. P., Verbyla, D. and Chapin, F. S. Methane bubbling from Siberian thaw lakes as a positive feedback to climate warming. *Nature* (2006). doi: `10.1038/nature05040`.

[102] Neumann, R. B., Moorberg, C. J., Lundquist, J. D., Turner, J. C., Waldrop, M. P., McFarland, J. W., Euskirchen, E. S., Edgar, C. W. and Turetsky, M. R. Warming effects of spring rainfall increase methane emissions from thawing permafrost. *Geophysical Research Letters* 46 (2019). doi: `https://doi.org/10.1029/2018GL081274`.

[103] Lu, X., Chen, N., Wang, Y., Cao, W., Zhu, B., Yao, T., Fung, J. C. and Lau, A. K. Radical budget and ozone chemistry during autumn in the atmosphere of an urban site in central China. *Journal of Geophysical Research* (2017). doi: `10.1002/2016JD025676`.

[104] Kumar, V., Chandra, B. P. and Sinha, V. Large unexplained suite of chemically reactive compounds present in ambient air due to biomass fires. *Scientific Reports* (2018). doi: `10.1038/s41598-017-19139-3`.

[105] Saito, M., Kim, H. S., Ito, A., Yokota, T. and Maksyutov, S. Enhanced methane emissions during Amazonian drought by biomass burning. *PLoS ONE* (2016). doi: `10.1371/journal.pone.0166039`.

[106] Ribeiro, I. O., Andreoli, R. V., Kayano, M. T., Sousa, T. R. de, Medeiros, A. S., Guimarães, P. C., Barbosa, C. G., Godoi, R. H., Martin, S. T. and Souza, R. A. F. de. Impact of the biomass burning on methane variability during dry years in the Amazon measured from an aircraft and the AIRS sensor. *Science of the Total Environment* (2018). doi: `10.1016/j.scitotenv.2017.12.147`.

[107] Thompson, R. L., Nisbet, E. G., Pisso, I., Stohl, A., Blake, D., Dlugokencky, E. J., Helmig, D. and White, J. W. *Variability in Atmospheric Methane From Fossil Fuel and Microbial Sources Over the Last Three Decades*. 2018. doi: `10.1029/2018GL078127`.

[108] Schaefer, H., Fletcher, S. E., Veidt, C., Lassey, K. R., Brailsford, G. W., Bromley, T. M., Dlugokencky, E. J., Michel, S. E., Miller, J. B., Levin, I., Lowe, D. C., Martin, R. J., Vaughn, B. H. and White, J. W. A 21st-century shift from fossil-fuel to biogenic methane emissions indicated by13CH4 (2016). DOI: `10.1126/science.aad2705`.

[109] Schwietzke, S., Sherwood, O. A., Bruhwiler, L. M., Miller, J. B., Etiope, G., Dlugokencky, E. J., Michel, S. E., Arling, V. A., Vaughn, B. H., White, J. W. and Tans, P. P. Upward revision of global fossil fuel methane emissions based on isotope database. *Nature* (2016). DOI: `10.1038/nature19797`. arXiv: `0911.5180v1`.

[110] Nisbet, E., Dlugokencky, E., Manning, M., Lowry, D., Fisher, R., France, J., Michel, S., Miller, J., White, J., Vaughn, B. et al. Rising atmospheric methane: 2007–2014 growth and isotopic shift. *Global Biogeochemical Cycles* 30.9 (2016), pp. 1356–1370.

[111] Lassey, K. R. Livestock methane emission and its perspective in the global methane cycle. *Australian Journal of Experimental Agriculture*. 2008. DOI: `10.1071/EA07220`.

[112] Nichols, K. L., Del Grosso, S. J., Derner, J. D., Follett, R. F., Archibeque, S. L., Stewart, C. E. and Paustian, K. H. Nitrous oxide and methane fluxes from cattle excrement on C3 pasture and C4-dominated shortgrass steppe. *Agriculture, Ecosystems and Environment* (2016). DOI: `10.1016/j.agee.2016.03.026`.

[113] Methane generation in landfills. *Renewable Energy* (2007). DOI: `10.1016/j.renene.2006.04.020`.

[114] Observations on the methane oxidation capacity of landfill soils. *Waste Management* (2011). DOI: `10.1016/j.wasman.2010.08.028`.

[115] Cicerone, R. J. and Shetter, J. D. Of Atmospheric Methane : increases Accord-. *Journal of Geophysical Research* 86.C8 (1981), pp. 7203–7209. URL: `https://cloudfront.escholarship.org/dist/prd/content/qt30p1f1cg/qt30p1f1cg.pdf`.

[116] Han, X., Sun, X., Wang, C., Wu, M., Dong, D., Zhong, T., Thies, J. E. and Wu, W. Mitigating methane emission from paddy soil with rice-straw biochar amendment under projected climate change. *Scientific Reports* (2016). DOI: `10.1038/srep24731`.

[117] Jiang, Y., Groenigen, K. J. van, Huang, S., Hungate, B. A., Kessel, C. van, Hu, S., Zhang, J., Wu, L., Yan, X., Wang, L., Chen, J., Hang, X., Zhang, Y., Horwath, W. R., Ye, R., Linquist, B. A., Song, Z., Zheng, C., Deng, A. and Zhang, W. Higher yields and lower methane emissions with new rice cultivars. *Global Change Biology* (2017). DOI: 10.1111/gcb.13737. arXiv: 0608246v3 [arXiv:physics].

[118] Yang, J., Zhou, Q. and Zhang, J. Moderate wetting and drying increases rice yield and reduces water use, grain arsenic level, and methane emission. *Crop Journal* (2017). DOI: 10.1016/j.cj.2016.06.002.

[119] Wang, B., Xu, Y., Wang, Z., Li, Z., Guo, Y., Shao, K. and Chen, Z. Methane emissions from ricefields as affected by organic amendment, water regime, crop establishment, and rice cultivar. *Environmental Monitoring and Assessment* (1999). DOI: 10.1023/A:1006039231459.

[120] Cai, Z., Xing, G., Yan, X., Xu, H., Tsuruta, H., Yagi, K. and Minami, K. Methane and nitrous oxide emissions from rice paddy fields as affected by nitrogen fertilisers and water management. *Plant and Soil* (1997). DOI: 10.1023/A:1004263405020. eprint: 0005074v1 (arXiv:astro-ph).

[121] Rigby, M., Montzka, S. A., Prinn, R. G., White, J. W. C., Young, D., O'Doherty, S., Lunt, M. F., Ganesan, A. L., Manning, A. J., Simmonds, P. G., Salameh, P. K., Harth, C. M., Mühle, J., Weiss, R. F., Fraser, P. J., Steele, L. P., Krummel, P. B., McCulloch, A. and Park, S. Role of atmospheric oxidation in recent methane growth. *Proceedings of the National Academy of Sciences* (2017). DOI: 10.1073/PNAS.1616426114.

[122] Ambiguity in the causes for decadal trends in atmospheric methane and hydroxyl. *Proceedings of the National Academy of Sciences* (2017). DOI: 10.1073/pnas.1616020114.

[123] Saueressig, G., Crowley, J. N., Bergamaschi, P., Brenninkmeijer, C. A. M. and Fischer, H. Carbon 13 and D kinetic isotope effects in the reactions of CH4 with O(1D) and OH: New laboratory measurements and their implications for the isotopic composition of stratospheric methane. *Journal of Geophysical Research* 106.D19 (2001), pp. 127–138.

[124] Li, Q., Meidan, D., Hess, P., Añel, J. A., Cuevas, C. A., Doney, S., Fernandez, R. P., Herpen, M. van, Höglund-Isaksson, L., Johnson, M. S. et al. Global environmental implications of atmospheric methane removal through chlorine-mediated chemistry-climate interactions. *Nature Communications* 14.1 (2023), p. 4045.

[125] Allan, W., Lowe, D. C. and Cainey, J. M. Active chlorine in the remote marine boundary layer: Modeling anomalous measurements of δ13C in methane. *Geophysical Research Letters* 28.17 (2001), pp. 3239–3242.

[126] Platt, U., Allan, W. and Lowe, D. Hemispheric average Cl atom concentration from 13C / 12C ratios in atmospheric methane. *Atmospheric Chemistry and Physics* 4 (2004), pp. 2393–2399.

[127] Topp, E. and Pattey, E. Soils as sources and sinks for atmospheric methane. *Canadian Journal of Soil Science* (1997). DOI: `10.4141/S96-107`. eprint: `arXiv:1011.1669v3`.

[128] Ostler, A., Sussmann, R., Patra, P. K., Houweling, S., Bruine, M. D., Stiller, G. P., Haenel, F. J., Plieninger, J., Bousquet, P., Yin, Y., Saunois, M., Walker, K. A., Deutscher, N. M., Griffith, D. W. T., Blumenstock, T., Hase, F., Warneke, T., ZhitingWang, Kivi, R. and Robinson, J. Evaluation of column-averaged methane in models and TCCON with a focus on the stratosphere. *Atmos. Meas. Tech* 9 (2016), pp. 4843–4859.

[129] Dlugokencky, E. *NOAA/GML*. URL: `www.esrl.noaa.gov/gmd/ccgg/trends_ch4/` (visited on 10/05/2021).

[130] Lunt, M. F., Palmer, P. I., Feng, L., Taylor, C. M., Boesch, H. and Parker, R. J. An increase in methane emissions from tropical Africa between 2010 and 2016 inferred from satellite data. *Atmospheric Chemistry and Physics* 19.23 (2019), pp. 14721–14740.

[131] Turetsky, M. R., Kotowska, A., Bubier, J., Dise, N. B., Crill, P., Hornibrook, E. R., Minkkinen, K., Moore, T. R., Myers-Smith, I. H., Nykänen, H. et al. A synthesis of methane emissions from 71 northern, temperate, and subtropical wetlands. *Global change biology* 20.7 (2014), pp. 2183–2197.

[132] López-Ballesteros, A., Beck, J., Helmschrot, J. and Saunders, M. Harmonised observations of climate forcing across Africa: an assessment of existing approaches and their applicability. *Environmental Research Letters* 15.7 (2020), p. 075003.

[133] IMF. *World Economic Outlook*. 2019.

[134] Zuijdgeest, A. and Wehrli, B. Carbon and nutrient fluxes from floodplains and reservoirs in the Zambezi basin. *Chemical Geology* (2017). DOI: `10.1016/j.chemgeo.2017.07.025`.

[135] Raymond, P. A., Hartmann, J., Lauerwald, R., Sobek, S., McDonald, C., Hoover, M., Butman, D., Striegl, R., Mayorga, E., Humborg, C., Kortelainen, P., Dürr, H., Meybeck, M., Ciais, P. and Guth, P. Global carbon dioxide emissions from inland waters. *Nature* (2013). DOI: `10.1038/nature12760`.

[136] Borges, A. V., Darchambeau, F., Teodoru, C. R., Marwick, T. R., Tamooh, F., Geeraert, N., Omengo, F. O., Guérin, F., Lambert, T., Morana, C., Okuku, E. and Bouillon, S. Globally significant greenhouse-gas emissions from African inland waters. *Nature Geoscience* (2015). DOI: `10.1038/ngeo2486`.

[137] Teodoru, C. R., Nyoni, F. C., Borges, A. V., Darchambeau, F., Nyambe, I. and Bouillon, S. Dynamics of greenhouse gases (CO2, CH4, N2O) along the Zambezi River and major tributaries, and their importance in the riverine carbon budget. *Biogeosciences* (2015). DOI: `10.5194/bg-12-2431-2015`.

[138] Delmas, R., Tathy, J. and Cros, B. Atmospheric methane budget in Africa. *Journal of atmospheric chemistry* 14.1 (1992), pp. 395–409.

[139] Saunois, M., Stavert, A. R., Poulter, B., Bousquet, P., Canadell, J. G., Jackson, R. B., Raymond, P. A., Dlugokencky, E. J., Houweling, S., Patra, P. K. et al. The global methane budget 2000–2017. *Earth System Science Data* 12.3 (2020), pp. 1561–1623.

[140] Kirschke, S., Bousquet, P., Ciais, P., Saunois, M., Canadell, J. G., Dlugokencky, E. J., Bergamaschi, P., Bergmann, D., Blake, D. R., Bruhwiler, L., Cameron-Smith, P., Castaldi, S., Chevallier, F., Feng, L., Fraser, A., Heimann, M., Hodson, E. L., Houweling, S., Josse, B., Fraser, P. J., Krummel, P. B., Lamarque, J. F., Langenfelds, R. L., Le Quéré, C., Naik, V., O'doherty, S., Palmer, P. I., Pison, I., Plummer, D., Poulter, B., Prinn, R. G., Rigby, M., Ringeval, B., Santini, M., Schmidt, M.,

Shindell, D. T., Simpson, I. J., Spahni, R., Steele, L. P., Strode, S. A., Sudo, K., Szopa, S., Van Der Werf, G. R., Voulgarakis, A., Van Weele, M., Weiss, R. F., Williams, J. E. and Zeng, G. *Three decades of global methane sources and sinks*. 2013. DOI: `10.1038/ngeo1955`. eprint: `1302.3283`.

[141] Tiwari, S., Singh, C. and Singh, J. S. Wetlands: a major natural source responsible for methane emission. *Restoration of Wetland Ecosystem: A Trajectory Towards a Sustainable Environment*. Springer, 2020, pp. 59–74.

[142] Delwiche, K. B., Knox, S. H., Malhotra, A., Fluet-Chouinard, E., McNicol, G., Feron, S., Ouyang, Z., Papale, D., Trotta, C., Canfora, E. et al. FLUXNET-CH4: A global, multi-ecosystem dataset and analysis of methane seasonality from freshwater wetlands. *Earth System Science Data Discussions* (2021), pp. 1–111.

[143] Whiting, G. J. and Chanton, J. P. Greenhouse carbon balance of wetlands: methane emission versus carbon sequestration. *Tellus B* 53.5 (2001), pp. 521–528.

[144] Mitsch, W. J., Bernal, B., Nahlik, A. M., Mander, Ü., Zhang, L., Anderson, C. J., Jørgensen, S. E. and Brix, H. Wetlands, carbon, and climate change. *Landscape Ecology* 28.4 (2013), pp. 583–597.

[145] Berg, M. v. d., Ingwersen, J., Lamers, M. and Streck, T. The role of Phragmites in the CH 4 and CO 2 fluxes in a minerotrophic peatland in southwest Germany. *Biogeosciences* 13.21 (2016), pp. 6107–6119.

[146] Davidson, N. C. How much wetland has the world lost? Long-term and recent trends in global wetland area. *Marine and Freshwater Research* (2014). DOI: `10.1071/MF14173`.

[147] Taillardat, P., Thompson, B. S., Garneau, M., Trottier, K. and Friess, D. A. Climate change mitigation potential of wetlands and the cost-effectiveness of their restoration. *Interface focus* 10.5 (2020), p. 20190129.

[148] Zambia Wildlife Authority. *Information Sheet on Ramsar Wetlands, Kafue Flats*. Tech. rep. 1995, p. 4.

[149] Mumba, M. and Thompson, J. R. Hydrological and ecological impacts of dams on the Kafue Flats floodplain system, southern Zambia. *Physics and Chemistry of the Earth* (2005). DOI: `10.1016/j.pce.2005.06.009`.

[150] Agency, E. S. *Climate Change Initiative Land Cover.* 2019. URL: http://maps.elie.ucl.ac.be/CCI/viewer/index.php (visited on 19/05/2021).

[151] Zambia Wildlife Authority. *Information Sheet on Ramsar Wetlands, Kafue Flats.* Tech. rep. 2006, p. 20. URL: https://rsis.ramsar.org/RISapp/files/RISrep/ZM530RIS.pdf.

[152] Cowx, I. G., Lungu, A. and Kalonga, M. Optimising hydropower development and ecosystem services in the Kafue River, Zambia. *Marine and Freshwater Research* (2018). DOI: 10.1071/MF18132.

[153] Wamulume, J., Landert, J., Zurbrügg, R., Nyambe, I., Wehrli, B. and Senn, D. B. Exploring the hydrology and biogeochemistry of the dam-impacted Kafue River and Kafue Flats (Zambia). *Physics and Chemistry of the Earth* (2011). DOI: 10.1016/j.pce.2011.07.049.

[154] Nauer, P. A., Hutley, L. B. and Arndt, S. K. Termite mounds mitigate half of termite methane emissions. *Proceedings of the National Academy of Sciences of the United States of America* (2018). DOI: 10.1073/pnas.1809790115.

[155] Maavara, T., Parsons, C. T., Ridenour, C., Stojanovic, S., Dürr, H. H., Powley, H. R. and Van Cappellen, P. Global phosphorus retention by river damming. *Proceedings of the National Academy of Sciences of the United States of America* (2015). DOI: 10.1073/pnas.1511797112.

[156] Vörösmarty, C. J., Meybeck, M., Fekete, B., Sharma, K., Green, P. and Syvitski, J. P. Anthropogenic sediment retention: Major global impact from registered river impoundments. *Global and Planetary Change* (2003). DOI: 10.1016/S0921-8181(03)00023-7.

[157] Barros, N., Cole, J. J., Tranvik, L. J., Prairie, Y. T., Bastviken, D., Huszar, V. L., Del Giorgio, P. and Roland, F. Carbon emission from hydroelectric reservoirs linked to reservoir age and latitude. *Nature Geoscience* (2011). DOI: 10.1038/ngeo1211.

[158] DelSontro, T., Kunz, M. J., Kempter, T., Wüest, A., Wehrli, B. and Senn, D. B. Spatial heterogeneity of methane ebullition in a large tropical reservoir. *Environmental Science and Technology* (2011). DOI: 10.1021/es2005545.

[159] Zambia Wildlife Authority. *Information Sheet on Ramsar Wetlands, Lukanga Swamps*. Tech. rep. 2005, p. 12. URL: `https://rsis.ramsar.org/RISapp/files/RISrep/ZM1580RIS.pdf`.

[160] Mapedza, E., Geheb, K., Koppen, B. van and Chisaka, J. Narratives from a wetland: Sustainable management in Lukanga, Zambia. *Development Southern Africa* (2012). DOI: `10.1080/0376835X.2012.706036`.

[161] Macrae, F. B. The Lukanga Swamps. *The Geographical Journal* 83.3 (1934), pp. 223–227.

[162] Zambia Wildlife Authority. *Information Sheet on Ramsar Wetlands, Bangweulu Swamps*. Tech. rep. 1995, p. 4. URL: `https://rsis.ramsar.org/RISapp/files/RISrep/ZM531RISformer1995%7B%5C_%7DEN.pdf`.

[163] Zambia Wildlife Authority. *Information Sheet on Ramsar Wetlands, Bangweulu Swamps*. Tech. rep. 2006, p. 17. URL: `https://rsis.ramsar.org/RISapp/files/RISrep/ZM531RIS.pdf`.

[164] (UNEP), U. N. E. P. *Lake Wamala. Environmental Change Hotspots. Division of Early Warning and Assessment (DEWA)*. URL: `https://na.unep.net/atlas/webatlas.php?id=2197` (visited on 01/06/2021).

[165] Musinguzi, L., Efitre, J., Odongkara, K., Ogutu-Ohwayo, R., Muyodi, F., Natugonza, V., Olokotum, M., Namboowa, S. and Naigaga, S. Fishers' perceptions of climate change, impacts on their livelihoods and adaptation strategies in environmental change hotspots: A case of Lake Wamala, Uganda. *Environment, Development and Sustainability* 18.4 (2016), pp. 1255–1273.

[166] Natugonza, V., Ogutu-Ohwayo, R., Musinguzi, L., Olokotum, M., Naigaga, S. and Kitabona, J. Implications of climate warming for hydrology and water balance of small shallow lakes: A case of Wamala and Kawi, Uganda. *Aquatic Ecosystem Health & Management* 19.4 (2016), pp. 327–335.

[167] (UNEP), U. N. E. P. *Lake Kyoga. Environmental Change Hotspots. Division of Early Warning and Assessment (DEWA)*. URL: `https://na.unep.net/atlas/webatlas.php?id=2187` (visited on 01/06/2021).

[168] Finland (EIA Ltd.), E. I. A. C. of. *Support to the Management of Sudd Blockage on Lake Kyoga*. Tech. rep. Integrated Lake Management Project, 2004, p. 70. URL: `https://web.archive.org/web/20050512231017/http://www.eia.fi/kyoga/report/Kyoga_Model_report-EIA_Ltd.pdf`.

[169] Ojara, M. A., Lou, Y., Aribo, L., Namumbya, S. and Uddin, M. J. Dry spells and probability of rainfall occurrence for Lake Kyoga Basin in Uganda, East Africa. *Natural Hazards* 100.2 (2020), pp. 493–514.

[170] Were, D., Kansiime, F., Fetahi, T. and Hein, T. Carbon dioxide and methane fluxes from various vegetation communities of a natural tropical freshwater wetland in different seasons. *Environmental Processes* 8.2 (2021), pp. 553–571.

[171] Gunnarsson, U. and Löfroth, M. *The Swedish Wetland Survey*. Tech. rep. 2009, p. 38. URL: `https://www.naturvardsverket.se/Documents/publikationer6400/978-91-620-6618-5.pdf`.

[172] Sanna-Kaisa, J. and Tuula, K. *Finland's Ramsar Wetlands Action Plan 2016–2020*. Tech. rep. 2016, p. 20. URL: `https://www.ramsar.org/sites/default/files/documents/library/finland_ramsar_wetland_action_plan_20162020_e.pdf`.

[173] O'Shea, S. J., Allen, G., Gallagher, M. W., Bower, K., Illingworth, S., Muller, J., Jones, B. T., Percival, C., Bauguitte, S., Cain, M. et al. Methane and carbon dioxide fluxes and their regional scalability for the European Arctic wetlands during the MAMM project in summer 2012. *Atmospheric Chemistry and Physics* 14.23 (2014), pp. 13159–13174.

[174] Lagomarsino, A. and Agnelli, A. E. Influence of vegetation cover and soil features on CO2, CH4 and N2O fluxes in northern Finnish Lapland. *Polar Science* 24 (2020), p. 100531.

[175] Hargreaves, K., Fowler, D., Pitcairn, C. and Aurela, M. Annual methane emission from Finnish mires estimated from eddy covariance campaign measurements. *Theoretical and Applied Climatology* 70.1 (2001), pp. 203–213.

[176] (NERC), N. E. R. C. *Methane Observations and Yearly Assessments (MOYA)*. URL: `https://moya.blogs.bris.ac.uk/` (visited on 01/06/2021).

[177] Burba, G. and Anderson, D. Eddy Covariance Flux Measurements. *Ecological Applications* (2010).

[178] Vaughan, A. R., Lee, J. D., Shaw, M. D., Misztal, P. K., Metzger, S., Vieno, M., Davison, B., Karl, T. G., Carpenter, L. J., Lewis, A. C. et al. VOC emission rates over London and South East England obtained by airborne eddy covariance. *Faraday discussions* 200 (2017), pp. 599–620.

[179] Metzger, S., Junkermann, W., Mauder, M., Butterbach-Bahl, K., Trancón Y Widemann, B., Neidl, F., Schäfer, K., Wieneke, S., Zheng, X. H., Schmid, H. P. and Foken, T. Spatially explicit regionalization of airborne flux measurements using environmental response functions. *Biogeosciences* (2013). DOI: `10.5194/bg-10-2193-2013`.

[180] Metzger, S., Durden, D., Florian, C., Luo, H., Pingintha-Durden, N. and Xu, K. *NEON Algorithm Theoretical Basis Document (ATBD): eddy-covariance data products bundle*. Tech. rep. NEON, 2018, p. 64. URL: `https://data.neonscience.org/api/v0/documents/NEON.DOC.004571vA`.

[181] Starkenburg, D., Metzger, S., Fochesatto, G. J., Alfieri, J. G., Gens, R., Prakash, A. and Cristóbal, J. Assessment of despiking methods for turbulence data in micrometeorology. *Journal of Atmospheric and Oceanic Technology* 33.9 (2016), pp. 2001–2013.

[182] Metzger, S., Durden, D., Florian, C., Luo, H., Pingintha-Durden, N. and Xu, K. *NEON Algorithm Theoretical Basis Document (ATBD): eddy-covariance data products bundle (NEON.DOC.004571, rev. B)*. Tech. rep. National Ecological Observatory Network (NEON), 2019, p. 64. URL: `https://data.neonscience.org/documents`.

[183] Hartmann, J., Gehrmann, M., Kohnert, K., Metzger, S. and Sachs, T. New calibration procedures for airborne turbulence measurements and accuracy of the methane fluxes during the AirMeth campaigns. *Atmospheric Measurement Techniques* 11.7 (2018), pp. 4567–4581.

[184] Vaughan, A. R., Lee, J. D., Metzger, S., Durden, D., Lewis, A. C., Shaw, M. D., Drysdale, W. S., Purvis, R. M., Davison, B. and Hewitt, C. N. Spatially and temporally resolved measurements of NO_x fluxes by airborne eddy-covariance

over Greater London. *Atmospheric Chemistry and Physics Discussions* 2021 (2021), pp. 1–27. DOI: `10.5194/acp-2021-180`. URL: `https://acp.copernicus.org/preprints/acp-2021-180/`.

[185] Thomas, C. and Foken, T. Re-evaluation of Integral Turbulence Characteristics and their Parameterisations. *15th Conference on Boundary Layer and Turbulence*. 2002.

[186] Salesky, S. T., Chamecki, M. and Dias, N. L. Estimating the random error in eddy-covariance based fluxes and other turbulence statistics: the filtering method. *Boundary-layer meteorology* 144.1 (2012), pp. 113–135.

[187] Billesbach, D. Estimating uncertainties in individual eddy covariance flux measurements: A comparison of methods and a proposed new method. *Agricultural and Forest Meteorology* 151.3 (2011), pp. 394–405.

[188] Nordbo, A. and Katul, G. A wavelet-based correction method for eddy-covariance high-frequency losses in scalar concentration measurements. *Boundary-layer meteorology* 146 (2013), pp. 81–102.

[189] Metzger, S., Junkermann, W., Mauder, M., Beyrich, F., Butterbach-Bahl, K., Schmid, H. P. and Foken, T. Eddy-covariance flux measurements with a weight-shift microlight aircraft. *Atmospheric Measurement Techniques* 5.7 (2012), pp. 1699–1717. DOI: `10.5194/amt-5-1699-2012`. URL: `https://amt.copernicus.org/articles/5/1699/2012/`.

[190] Metzger, S. personal communication. 2021.

[191] Cohn, S. A. and Angevine, W. M. Boundary layer height and entrainment zone thickness measured by lidars and wind-profiling radars. *Journal of Applied Meteorology* 39.8 (2000), pp. 1233–1247.

[192] Vaughan, A. R. personal communication. 2021.

[193] Vaughan, A. R., Lee, J. D., Misztal, P. K., Metzger, S., Shaw, M. D., Lewis, A. C., Purvis, R. M., Carslaw, D. C., Goldstein, A. H., Hewitt, C. N. et al. Spatially resolved flux measurements of NOx from London suggest significantly higher emissions than predicted by inventories. *Faraday discussions* 189 (2016), pp. 455–472.

[194] Hannun, R. A., Wolfe, G. M., Kawa, S. R., Hanisco, T. F., Newman, P. A., Alfieri, J. G., Barrick, J., Clark, K. L., DiGangi, J. P., Diskin, G. S. et al. Spatial heterogeneity in CO2, CH4, and energy fluxes: insights from airborne eddy covariance measurements over the Mid-Atlantic region. *Environmental Research Letters* 15.3 (2020), p. 035008.

[195] Saunders, M., Jones, M. and Kansiime, F. Carbon and water cycles in tropical papyrus wetlands. *Wetlands Ecology and Management* 15.6 (2007), pp. 489–498.

[196] Niesbet, E. G. personal communication. 2021.

[197] Yang, W.-B., Yuan, C.-S., Tong, C., Yang, P., Yang, L. and Huang, B.-Q. Diurnal variation of CO2, CH4, and N2O emission fluxes continuously monitored in-situ in three environmental habitats in a subtropical estuarine wetland. *Marine Pollution Bulletin* 119.1 (2017), pp. 289–298.

[198] Kaimal, J., Abshire, N., Chadwick, R., Decker, M., Hooke, W., Kropfli, R., Neff, W., Pasqualucci, F. and Hildebrand, P. Estimating the depth of the daytime convective boundary layer. *Journal of Applied Meteorology and Climatology* 21.8 (1982), pp. 1123–1129.

[199] Angevine, W. M., Baltink, H. K. and Bosveld, F. C. Observations of the morning transition of the convective boundary layer. *Boundary-Layer Meteorology* 101.2 (2001), pp. 209–227.

[200] l'Environnement, D. G. de. *Fiche descriptive Ramsar, Lac Télé/Likouala-aux-herbes*. Tech. rep. 2017, p. 17. URL: `https://rsis.ramsar.org/RISapp/files/RISrep/CG950RIS_1709_fr.pdf`.

[201] Ministère de l'Economie Forestière, d. D. D. e. d. l. *Fiche descriptive Ramsar, Grands affluents*. Tech. rep. 2017. URL: `https://rsis.ramsar.org/RISapp/files/RISrep/CG1742RIS_1709_fr.pdf`.

[202] Tathy, J., Cros, B., Delmas, R., Marenco, A., Servant, J. and Labat, M. Methane emission from flooded forest in Central Africa. *Journal of Geophysical Research: Atmospheres* 97.D6 (1992), pp. 6159–6168.

[203] Nyamadzawo, G., Wuta, M., Nyamangara, J., Rees, R. M. and Smith, J. L. The effects of catena positions on greenhouse gas emissions along a seasonal wetland (dambo) transect in tropical Zimbabwe. *Archives of Agronomy and Soil Science* 61.2 (2015), pp. 203–221.

[204] Belger, L., Forsberg, B. R. and Melack, J. M. Carbon dioxide and methane emissions from interfluvial wetlands in the upper Negro River basin, Brazil. *Biogeochemistry* 105.1 (2011), pp. 171–183.

[205] Sjögersten, S., Black, C. R., Evers, S., Hoyos-Santillan, J., Wright, E. L. and Turner, B. L. Tropical wetlands: a missing link in the global carbon cycle? *Global biogeochemical cycles* 28.12 (2014), pp. 1371–1386.

[206] Ishikura, K., Hirata, R., Hirano, T., Okimoto, Y., Wong, G. X., Melling, L., Aeries, E. B., Kiew, F., San Lo, K., Musin, K. K. et al. Carbon dioxide and methane emissions from peat soil in an undrained tropical peat swamp forest. *Ecosystems* 22.8 (2019), pp. 1852–1868.